AN EXPERIMENTAL STUDY OF MIXING IN THE WAKE OF

ARCS

A Thesis submitted for the Degree of Doctor of

Philosophy of the University of London

by

Israel Jechiel Jagoda, B.Sc., A.R.C.S.

Department of Chemical Engineering

& Chemical Technology,

Imperial College of Science & Techology,

London, S.W.7.

June 1976

ABSTRACT

The turbulent wake region of the magnetically rotated D.C. plasma jet was investigated. The study was carried out because more and more industries are looking towards low temperature plasma technology in order to make use of the relatively high temperatures and fast reaction rates associated with the comparatively compact plasma and hybrid plasma-flame reactors. For successful application, however, more needs to be known about the scale of entrainment of the surrounding gases and the mixing patterns in the wake of such arcs. Shadow records obtained by one microsecond duration spark photography and by high speed cinephotography using framing rates of up to 10,000 frames/second were used to visualize the structure of the interfaces of hot and cold pockets of gas and the overall flow patterns in the wake. The extent of the influence of the arc rotation on the flow behaviour downstream was noted. A recently developed corona probe which uses the gas itself as the thermometric medium and therefore presents no thermal inertia problems was used to monitor the temperature fluctuations and thus the "mixedness" of the gas stream. A "schlieren velocimeter" was designed to measure local horizontal and vertical turbulent gas velocities throughout the test region. These velocity distributions were corrected for the effect of the integration along the optical path of the laser beam passing through the turbulent wake and other effects revealed by a statistical analysis. Flow patterns were deduced from local mean velocities and relative local densities were calculated by mass conservation. The density distribution in the wake suggests that part of the energy may be transferred from the arc to the gas in a non-translational form. The volume of air entrained from the surrounding and its distribution throughout the wake was determined.

ACKNOWLEDGEMENTS

I would like to sincerely thank Prof. F.J. Weinberg for his
consistent guidance and encouragement. His patience and availability
at all times, independent of his many other commitments, must not go
unmentioned. Many thanks are also due to Dr. A.R. Jones, who so
often acted as a "testing ground" for many ideas in conjunction
with this research. His constructive criticism contributed much
to the better understanding of the physical processes involved.

Without the technical assistance of Mr. T. Barnes, head of the
student workshop, Mr. L. Moulder, the departmental photographer
and the staffs of the electronics workshop and departmental stores,
much of this work would not have been possible.

My appreciation is due also to the Electricity Council Research
Centre for their generous financing of this project.

Last, but not least, I express my gratitude to my family for
their continued support in every form possible.

I.J.J.

LIST OF FIGURES:

LIST OF PLATES

Chapter I

INTRODUCTION

In an age of continued technical advance, but constrained by energy conservation and efficiency considerations, low temperature plasma reactors are attracting more and more interest for chemical reactions and augmentation of combustion as well as heat transfer problems. We are at present in no position to replace, purely for its thermal effect, relatively disorganized heat energy as obtained for example in combustion by highly organized and therefore thermodynamically more valuable electrical energy. This might well change in the foreseeable future with the arrival of relatively abundant electrical energy produced by nuclear fusion. Meanwhile, however, there are a number of important advantages intrinsic in the use of plasmas in technology that have caused industry to look towards them for answers to some of its more short term problems.

I.1 Plasmas - Reasons for their Use

Electric arcs exist at very high temperatures; 8,000-50,000 $^{\circ}$K depending on the atmosphere through which they pass. This makes it possible to raise reactants to uncommonly high temperatures extremely rapidly and in comparatively confined spaces. As a result many reactions will proceed very quickly, as indicated by the exponential term of the reaction rate in the Arrhenius Equation:

$$K = \exp(-E/RT)$$

where K is the reaction rate, T the temperature and R the gas constant.

The liberation of these large quantities of thermal power at such high temperatures allows the throughput of reactants to be kept at a considerable level. Products after passing through a number of intermediate, metastable stages can therefore be generated at very high rates in comparatively small plasma reactors. Careful quenching of the reacting gases can either yield the expected compounds or be used to obtain economically viable quantities of intermediate products depending on the mechanism of the reaction. In the case of the production of solids correct quenching can assure that the particle size distribution obtained lies within limits convenient for their further use as well as resulting in a particular yield.

Apart from these purely thermodynamical advantages, the arc can supply excited and dissociated species as well as ionized gases in large quantities. These species can be used to accelerate even further a given reaction or alternatively to influence the reaction mechanism to make the yield more compatible with the requirements of the industry.

Lastly, the high concentration of power makes it possible to reduce the reactors in dimensions and weight with the resulting advantages in transportation as well as the reduction in heat losses and construction cost.

Compared with high temperature plasmas, as used for example in nuclear processes, the low temperature plasma that is dealt with here can be handled and controlled using present-day technological means and a little ingenuity. Some industrial processes are already using plasma reactors while other applications are still in the laboratory or pilot plant stages. Only some of these can be covered in this introduction.

I.2 Plasmas - Their Applications

I.2.1 Formation of Gaseous Products

The formation of unsaturated hydrocarbons from methane or by the
cracking of higher hydrocarbons using an argon driven plasma jet has
been investigated (Ref: 1,2,3,4,5). The Hüls process as developed
by the Badische Anilin und Soda Fabrik (BASF) in Germany and a plant
operated in Montague, Michigan, by du Pont, already use this technique.
Acetylene is formed as an intermediate with a life-time of up to 1 msec
and temperatures of 3000-4000 °K. Careful quenching arrangements have
made it possible to achieve conversion of up to 80% of the available
carbon to acetylene. If the reaction is allowed to proceed further,
carbon black is deposited.[*] By replacing the argon in the plasma
partially or completely with nitrogen, hydrogen cyanide with conversions
of up to 30% has been obtained (Ref. 3,4,6). Both these reactions are
strongly endothermic and in both cases only correct quenching will result
in the gaseous products.

In comparable work coal has been used as a starting material to
form methane, acetylene and hydrogen cyanide gases using an argon plasma.
(Ref. 2,4,5). The coal has been introduced either by using it as an
anode material or by injecting it into the carrier gas in the form of
particles of size up to 200 microns. The formation of unsaturated
hydrocarbons is favoured at the high temperatures prevailing in the plasma.
Methane and hydrogen cyanide were produced in the main. The precise
yield of the resulting gases depended on the type of coal used (Ref. 4)

---

*The BASF electric arc furnace employs an 8000 kW arc of approximately
1 m length and is capable of producing 15 tons of acetylene per day.
(Plate 15).
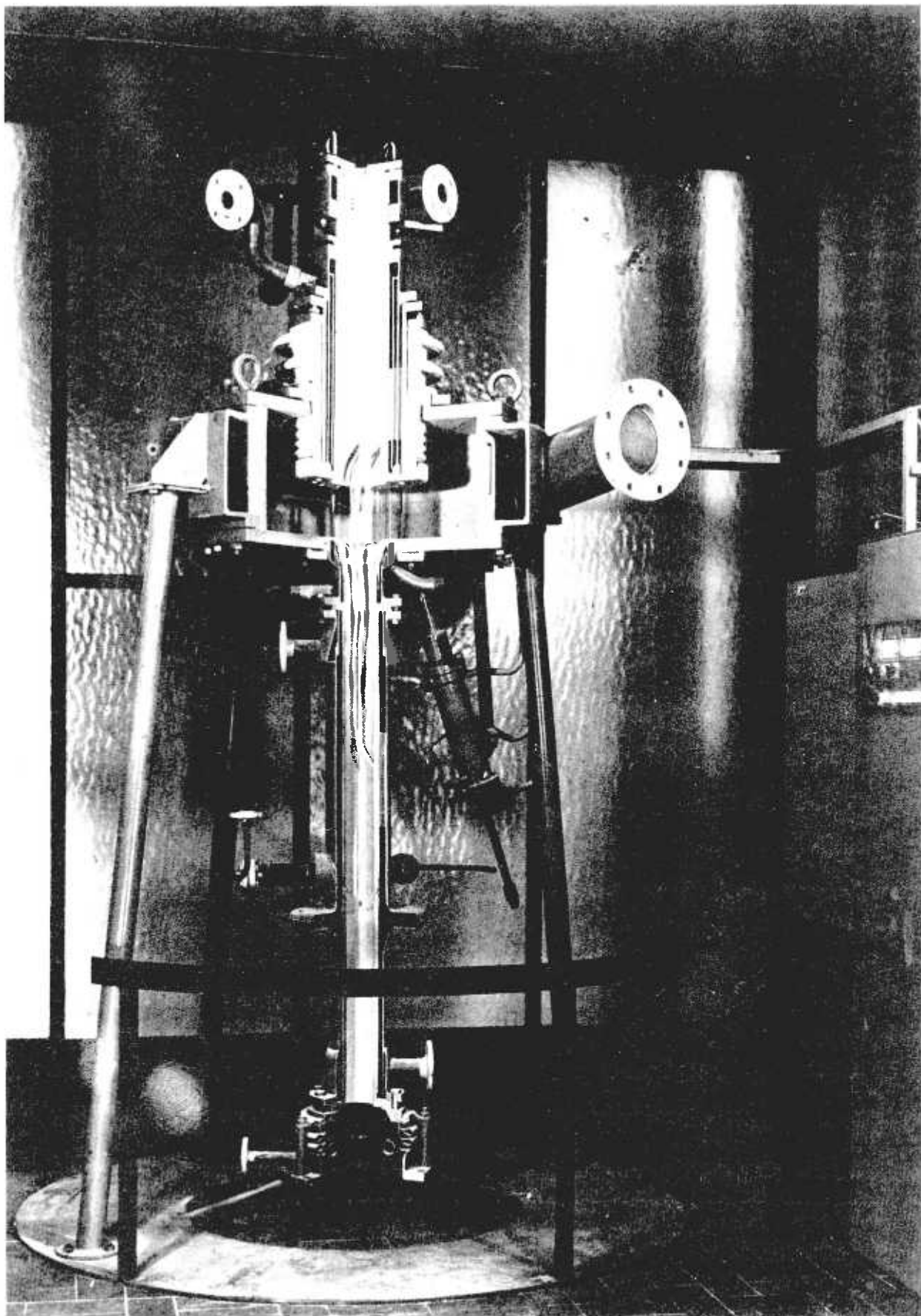
PLATE XV   HÜLS PROCESS REACTOR
(Photo: Deutsches Museum - München, W. Germany)

but acetylene production was found to be increased by the addition of hydrogen to the carrier gas, while the partial or complete replacement of argon by nitrogen favoured the hydrogen cyanide formation. As a result of dissociation, the introduction of hydrogen and nitrogen, however, always increases the minimum electrical power input required to keep the arc from extinguishing.

Another gas that can be synthesized by passing nitrogen, this time in the presence of oxygen, through a plasma, is nitric oxide. (Ref. 3,6). Where this is not a specifically desired end product this reaction causes an important air pollution problem. Work is, however, being carried out at present at these laboratories that seems to indicate that the addition of excess nitrogen might actually suppress the NO_x emission (Ref. 7).

Another process that has been investigated is the formation of acetylene and hydrogen cyanide using a nitrogen plasma. Passing these gases through a further plasma produces acrylonitrile (Ref. 3). Carbon monoxide and hydrogen have been obtained by passing methane and water vapour through a plasma. The resulting reducer gas has many uses, for example in the extraction of phosphorus from calcium phosphate or calcium fluorophosphate. If the fluorophosphate is used, calcium fluoride is a by-product (Ref. 2,3).

I.2.2 Production of Particles of Predetermined Size

A good example of the use of plasmas in the production of a solid in a desired particle size range is the oxidation of titanium tetrachloride to titanium dioxide (Ref. 2,8). Suitable quenching results in particles in the size range of around 0.25 μm. These are ideally suited for the manufacture of pigments of white paint.

Ultra-fine thixotropic silica particles for use in, for example, the manufacture of tyres and the reinforcement of fibreglass, can be

produced by injecting a mixture of moist air and pure sand into a plasma jet. The resulting particles of diameters of the order of 10^{-8} m are heavily studded in OH groups provided by the water vapour and link together via hydrogen bonding to form long chains (Ref. 2). It is these chains that encourage the thixotropic properties when added to fluids. Again it is quenching which causes the formation of the very fine particles. Similarly fine boron particles of high purity can be manufactured by reducing boron trichloride in a hydrogen plasma (Ref. 2).

I.2.3 Extraction of Metals

The use of plasmas in the extraction and purification of metals is already widely accepted (Ref. 9). Iron used in the manufacture of steel, for example, can be extracted from its ore using a hydrogen plasma or a plasma flame combination (Ref. 2). Only recently the British Steel Corporation has completed a new arc steel furnace at Llanwern. Other metal extractions at present under investigation include the reduction of zirconium trichloride to zirconium used in nuclear reactors (Ref. 2), of titanium tetrachloride to titanium for use in the aircraft and chemical industries (Ref. 2) and aluminium oxide to aluminium (Ref. 3). In the first two reactions sodium is used as a reducing agent in conjunction with a plasma-jet. Molybdenum disulphide can also be reduced to molybdenum, an important steel additive.[*]

---

[*] Very pure phosphorus for use even in the food industry has been extracted as early as 1900 by the reduction of phosphate rock with coke and silica in an electric furnace at the Chemische Fabrik Griesheim (Bitterfeld-Germany). By 1927 four 10,000 KW furnaces were in operation.

I.2.4 Flame-Arc Hybrids

A separate group of plasma applications is represented by the use of arcs in flame-plasma hybrids. Large throughputs of premixed reactants have had their flames stabilized on relatively small burners by the addition of small amounts of electrical energy in the form of arcs. Although these effects were first reported as early as 1924 by Southgate et al. (Ref. 10) it was more recently that the true extent of the possibilities presented by augmented flames had been demonstrated (Ref. 11,12,13,14). Flow rates of up to 700% of normal "blow off" rates for a given burner size were stabilized by addition of electrical energy representing only 10% of the total chemical energy liberated. This was clearly not only the result of thermodynamic effects. In fact an increase of only 50% in the reaction rate had been predicted kinetically.

An active part was played by certain radicals like OH, H and O, which were either generated directly in the plasma or by dissociated species in the carrier gas like nitrogen which was created while the diatomic gas passed through the plasma jet. Investigations have shown that flame heights remained virtually unchanged for these large flow rates, indicating that the combustion intensity had increased linearly with the raising of the volumetric throughput because of the radicals supplied by the arc.

Aerodynamic considerations along with 3 body recombinations of dissociated species enables one to arrange for high heat transfer rates in the wake region. In practice this rapid energy transfer to solid bodies can be used not only for cutting and welding, but also for rapid cooling of the reacting gas mixtures and the resulting quenching out of metastable intermediates, as in the plasma processes previously mentioned. Although the electrical energy required for the augmented combustion is lower than that for pure plasma reactions because of the

energy supplied by the combustion part, the oxygen present tends to reduce the lifetime of the electrodes considerably.

The possibility of either passing the combustibles along with the carrier gas through the plasma, or introducing them further downstream along with the choice of carrier gas, to yield specific radicals or dissociated species, makes the augmented flame a very versatile tool.

Flame plasma combinations can be expected to enable a designer to reduce the bulk of conventional combustion chambers in industry or to cope with sudden and transient increases in power requirements as in the case of the vertical take-off jet or relighting following "flame-out" at high altitudes. Augmented flames can also be used to oxidize previously non-combustible materials or lean gas mixtures below the lower limits of flammability. An investigation of the latter is presently being carried out in these laboratories. Again the arc preheats the reactants in order to allow them to pass the activation energy hump as well as providing radicals that increase the combustion intensity. Care must be taken, however, to ensure that the amount of electrical energy required does not become more substantial than the released chemical energy, unless the generation of specific chemical products keeps the process cost-effective.

Examples of chemical syntheses using flame-plasma hybrids are the production from lead of litharge used in the manufacture of batteries, ceramic cement or in oil refining and the oxidation of benzene to phenol (Ref. 3).

I.2.5 Plasmas as Analytical Tools

Plasma jets have proved powerful tools in academic and experimental investigations. They have been used in thermodynamic and reactor mechanism studies (Ref. 8). Especially for the latter the possibilities of injecting selected radicals and dissociated species have been extremely useful. The high temperatures prevailing in the arc have also been used to simulate re-entry conditions for the testing of materials to be used in spacecraft construction.

I.3 Plasmas - Problems of their Application and Solutions

Most of the above mentioned applications require the plasma effects to be distributed nearly uniformly throughout the gas flow. Unfortunately the natural behaviour of the arc does not facilitate this. As the conductivity of a gas increases with temperature, most of the arc current tends to pass through the hotter centre of the arc column, thereby heating that channel even further and thus acting as a self-focusing system. The arc further collapses into a very narrow, very hot filament. As any gas approaching the arc expands rapidly, only a small fraction passes the close proximity of the plasma. This extremely high by-pass ratio causes considerable problems as the reactions downstream of the plasma jet become controlled by the mixing of the hot and cold parts of the reactants. These mixing times are in most cases long compared with the rates of quenching discussed above. A great deal of emphasis has therefore been placed on the more uniform distribution of the plasma energy throughout the gas stream.

Attempts have been made to spread the arc by seeding the gas flow with easily ionizable materials. Some success has been obtained with caesium and potassium salts (Ref. 2) which ionize at temperatures as low

as 2500-3500 $^{\circ}$K. By choosing an appropriate seeding level all salts
could be completely ionized before any of the gas itself ionized and
a fall of ionization with increasing temperatures was observed past
a temperature of some 3000 $^{\circ}$K. This inhibited the contraction of the
arc column. Seeding may not, however, always be convenient or even
possible and attempts have been made to spread the arc using turbulent
flow (Ref. 2,11,13). In order for this to be successful, however, the
scale of turbulence needs to be of the same order of magnitude as the
arc diameter (of the order of 2 mm). Otherwise the arc might well
appear "smeared out" but is really just following the gas flow pattern
and is always in contact with the same pockets of gas. Seeding has
been used successfully to spread the arc sufficiently to make it compati-
ble in diameter with the scale of turbulence and arc columns have been
expanded by as much as a factor of ten by these combined effects.

Other more complex configurations have been used in an effort to
increase the arc width. In one particular case the arc was enclosed
along the axis of a rotating cylinder, setting up a centrifugal field
that removed the colder gases to the cylinder walls. If, however, an
appreciable gas flow was passed through this configuration the arc
was cooled by convection, or by radiation if particles were included
in the gas stream. Due to this cooling the arc then collapsed. An
attempt to cause arc spreading carried out in the course of this investi-
gation is discussed in Section III.3.

A completely different form of plasma generation is that using
induction heating (Ref. 2,5,6,13,15). A R-F coil surrounding a
quartz tube is driven by a generator capable of supplying power at a
few kW and a few MHz. A plasma that acts as a secondary, short circuited
induction winding is formed inside the tube. By introducing the gas flow
tangentially into the ionized region back pressures are set up which
cause a recirculatory flow. This reduces heat losses from the plasma,

which therefore expands. Much of the gas, however, still by-passes the plasma and while the ionized core is spread it is by no means uniform unless the gas stream is seeded. While R-F discharges have the advantage of no cooling or contamination by electrodes, their generating equipment is bulky and expensive.

As an alternative to the above mentioned arc spreading attempts, more uniform heating of the gases can be achieved by forcing the arc to move through the gas stream (Ref. 16). This has been attempted by injecting the carrier gas tangentially into an annular gap between the electrodes, in order to introduce swirl and relying on the resistance of the arc to the induced motion to cause the arc to rotate more slowly than the gas, therefore bringing it into contact with most of the gas stream. A more satisfactory, because more easily controllable, arrangement is to rotate the arc in the annulus by applying a magnetic field in the direction perpendicular to the plane of rotation of the arc (Ref. 1,8,12,13,14). By tuning the rotation rate of the arc through adjustment of the magnetic field to the flow rate of the carrier gas, it is possible to bring all parts of the gas into contact with the plasma at some time. This maximizes the evenness of the distribution of heat and radicals to the gas. Any non-uniformity remaining could be expected to be smoothed out by the extra turbulence generated by the arc which, because very little of the gas actually passes through it, behaves like a solid stirrer. The arc also induces swirl into the gas which further increases the heat transfer to surfaces in the wake region (Ref. 17). The rapid rotation rates of the arc, 2000 Hz and more, have caused investigators to even look into the possibility of using the centrifugal forces produced for isotope separation.

The expanding flow emerging from the nozzle and its turbulence causes considerable entrainment of the ambient atmosphere into the wake. Therefore a number of different possibilities of introducing reactants to the arc or its products present themselves. They could be allowed to pass through the rotated plasma jet along with a suitable carrier gas or be injected above the burner mouth. Entrainment of surrounding gases can also play an important part.

As this seems to be the most promising plasma reactor arrangement at least for a great many applications, the magnetically rotated arc was further investigated. In order to be able to ensure the most efficient flow arrangements, including entrainment, and to arrange quenching surfaces such as to maximize desired yields, something needs to be known about the flow patterns and the distribution of physical properties in the wake region. It is in order to shed some light on these previously neglected problems that this research was undertaken.

Chapter II

COMPARISON OF PROBES WITH OPTICAL TECHNIQUES

The wake region of the magnetically rotated plasma-jet analyzed in this investigation consists of a non-uniform hot argon-cold air mixture, part of which near the burner nozzle was expected to be at a temperature of a few thousand degrees absolute, and to contain ionized argon. The flows were predicted to be very turbulent, resulting in large and rapid variations of local gas conditions. The wake gases further than 1 cm downstream of the arc are non-luminous and any form of solid particles introduced into the carrier gas flow would inevitably have led to instabilities in the running of the arc.

This was borne in mind when a strategy for investigating the test region was decided upon. The use of radiation methods (radiative spectroscopy, line reversal, etc.) as well as the seeding of the gas flow for particle tracking were therefore eliminated from the start. The choices remaining could be subdivided into two main groups: probe techniques and optical methods using changes in refractive index.

II.1 Probes

While probes give measurements of very good spatial resolution they suffer from a number of disadvantages. All probes have some influence on the flow pattern around them, especially if that is of a complex nature and small scale as in this case. Because of the high temperature of the gas immediately downstream of the plasma-jet nozzle, solids would have melted in this region. A little further downstream, where average temperatures are sufficiently low not to have damaged the

probe, some pockets of ionized argon and possibly dissociated oxygen or nitrogen are nevertheless present. The probe surface would in this region have acted to promote the recombination of ions or dissociated species in the form of three-body reactions. This would, of course, have influenced the readings taken.

In the measurement of temperatures using solid thermometers, for example thermocouples, resistance thermometers or suction pyrometers, the thermal condition of their working substances rather than that of the surrounding gas is recorded. Errors are therefore introduced even under constant conditions by the imperfect convective heat transfer from the gas to the probe. This heat transfer Q_c is given by

$$Q_c = h_c (T_g - T_T)$$

where T_g is the gas temperature, T_T the probe temperature and h_c the coefficient of convective heat transfer which is a function of Reynolds and Nusselt numbers (Ref. 18). Radiation from the solid thermometer further decreases its temperature. The error ϕ_R introduced by these radiative heat losses is given by

$$\phi_R = \varepsilon\sigma (T_T^4 - T^4)$$

where ε is the emissivity of the wire and T the temperature of surrounding solids (Ref. 19). A further heat loss is caused by the thermal conduction along the leads holding the probe and connecting it to the measuring instruments. This error, E_c, is given by

$$E_c = \frac{T_T - T_B}{L(4h/d\lambda)^{1/2}}$$

where T_B is the exit temperature of the probe supports, L and d their

length and diameter respectively, and λ their conductivity (Ref. 19).

These losses are partly compensated for by the fact that the probe

measures the static temperature rather than that of the flowing gas.

Kinetic energy of the gas stream is therefore converted to heat,

increasing the local gas enthalpy. The temperature increase ΔT

resulting from this aerodynamic heating is given by:

$$\Delta T = 1/2 \; v^2/J \; c_p$$

where v is the local gas velocity, c_p the specific heat of the gas at

constant pressure and J the mechanical equivalent of heat (Ref. 18,19).

These errors are in practice minimized by making the probes as small

as possible, of material of low emissivity and possibly coating or

shielding them with such materials, making their leads long and allowing

them to follow isotherms for as long as possible. They can be further

compensated by using the equations above.

It was, however, the rapid and irregular fluctuations in the

localized temperature conditions caused by the fast flow of very small

pockets of gases of widely varying temperatures that finally made these

probes unsuitable for the present investigation. Every thermocouple

requires a finite time to allow the probe material to reach a temperature

close to that of the gas. This response time is given by the expression

(Ref. 19):

$$\frac{dT}{dt} \times \frac{\zeta c d}{4 h_c c} = T_g - T_T$$

where c and ζ are the specific heat and the density of the probe material

respectively. Although this thermal inertia can be reduced by making

the probe very small, there is a lower limit to the wire diameter if the probe is to be reasonably stable in handling and against the gas flow. Pt, 13% PtRh wires of this minimum diameter produced a thermocouple that was far too slow for the present application.

Thermocouples or resistance thermometers could not even have recorded a correct average temperature, at least if that mean $\overline{T}$ would have been defined in terms of mass fractions as

$$\overline{T} = \frac{\sum_J T_J \times M_J}{\sum_J M_J}$$

where M_J is the mass of gas present at a temperature T_J. Hot gases passing the thermocouple would have occupied a larger volume per unit mass than pockets containing an equal mass of colder gas and would therefore have been in contact with the probe for a relatively longer period of time. This would have resulted in the measured average temperature being higher than the true mean. Cox and Weinberg (Ref. 20) have dealt with the averaging properties of suction pyrometers and concluded that the average temperatures computed by the enthalpy probes deviate from the true mean temperature, indicating too high or too low depending on the flow regime within the probe. The discrepancy between measured and existing mean temperatures was found to be a function of the thermal unmixedness of the gas stream.

Hot wire anemometers of conventional design used for measuring local gas velocities have a response of approximately 100 Hz. This has been improved upon by the introduction of feedback into the electronic circuitry. However, they also suffer from the other drawbacks of probes.

A probe developed recently was used to indicate temperature fluctuations. It is based on the principle of the corona discharge and uses the

gas itself as a working substance. This eliminates any distortion in the probe output introduced by thermal inertia. The probe and its applications are described in detail in Chapter VI.

II.2 Optical Techniques

For the main body of the investigation optical techniques were used. The wake region has too complicated a structure for the use of optical interferometry which would also have been too sensitive a tool for the steep refractive index gradients that were expected there (Ref. 21). Shadow and schlieren methods were, however, found to be ideally suited. Although these are less sensitive at high temperatures (Ref. 21) the refractile index changes encountered are so sharp that sensitivity was not found to be a problem. This also influenced the precise setting up, as indicated in Chapter IV. Still and moving shadow records were obtained to give an overall qualitative structure and flow visualisation of the gases in the plasma-jet wake and a schlieren technique was adapted to yield localized velocity measurements, as discussed in the following chapters.
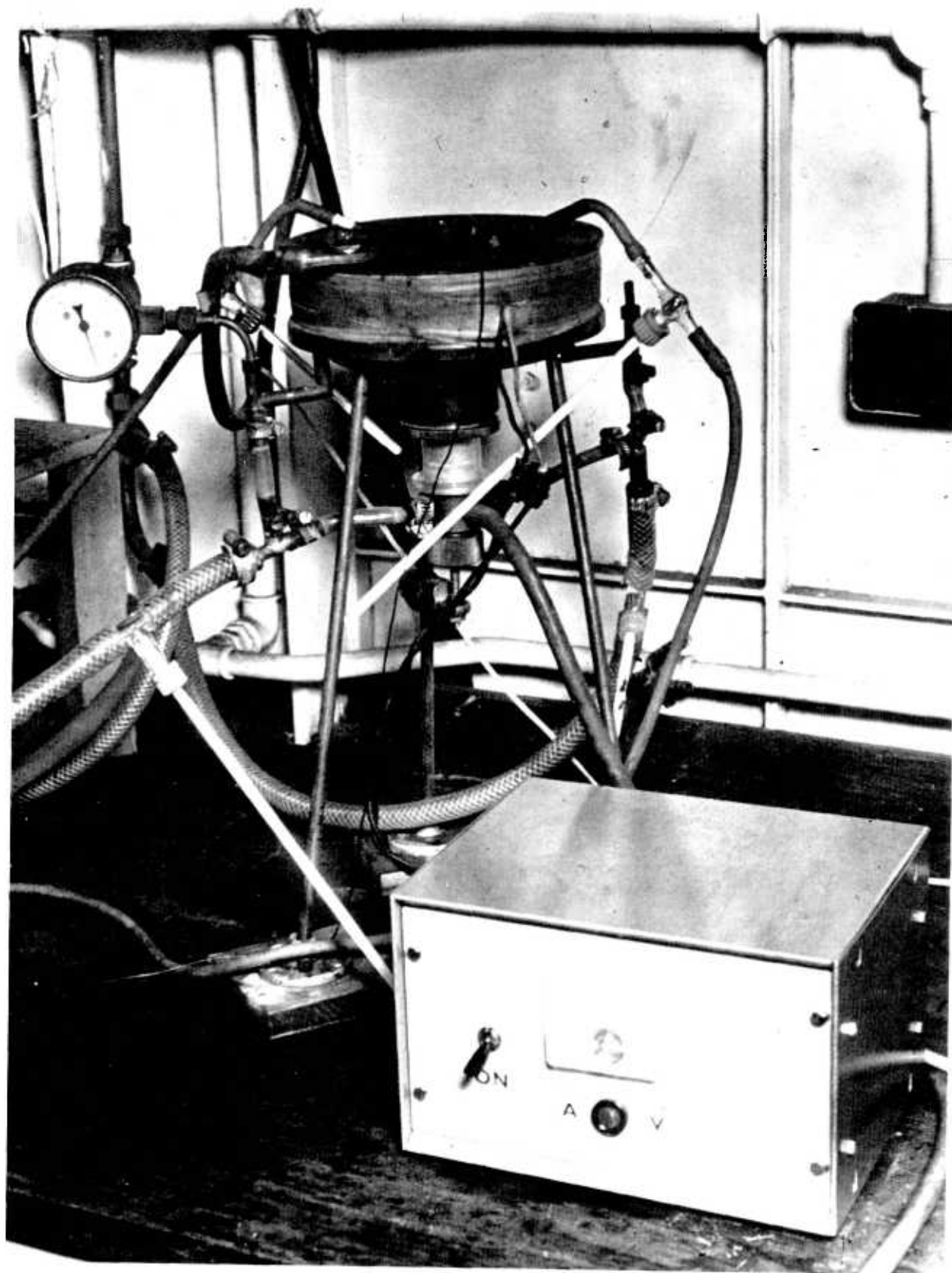
PLATE XVI   THE PLASMA-JET BURNER

Chapter III

THE MAGNETICALLY ROTATED PLASMA JET

III.1. Apparatus

The plasma jet burner consisted of two concentric electrodes and a magnetic field coil. A cross section is shown in Figure 3.1. The cathode was made up of a 2 mm diameter thoriated tungsten rod ground to a tip at the top end and fitted into a 1 cm diameter brass bar. The thorium lowers the work function of the tungsten. This improved the electrode performance, as electrons were ejected more easily. The cathode was held firmly in position at the centre of the anode nozzle by a perspex insulating block. A copper tube of internal diameter 4 mm and shaped into a cone was placed around the cathode on the perspex and served to separate the gas flow immediately surrounding the cathode from that in the remainder of the nozzle.

Two separate gas flows entered the burner through ducts in the perspex near the bottom. The inner one passing over the cathode surface left through the inside of the cone, and then out of the nozzle. This was always argon and acted to protect the cathode from chemical attack by any of the components of the main stream. That stream moved over the outside of the cone and through the nozzle. Although in this investigation this was mostly also argon, any other gas or mixture of gases could have been used as described in Chapter I.

The anode was made of copper and had a nozzle vertically through its centre, consisting of a straight hole 1 cm in diameter and 1.5 cm in depth in the upper part, opening out at an angle of 45° to a 2.5 cm hole in the lower part. This is shown in Figure 3.2. The cathode was positioned along the axis of the anode at a height such that an arc

arc position

ANODE

CONE

CATHODE

(WATER
COOLED)

MAGNETIC
COIL

PERSPEX
CATHODE
HOLDER
(WATER
COOLED)

MAIN GAS
INLET

ARGON SHEATH
INLET
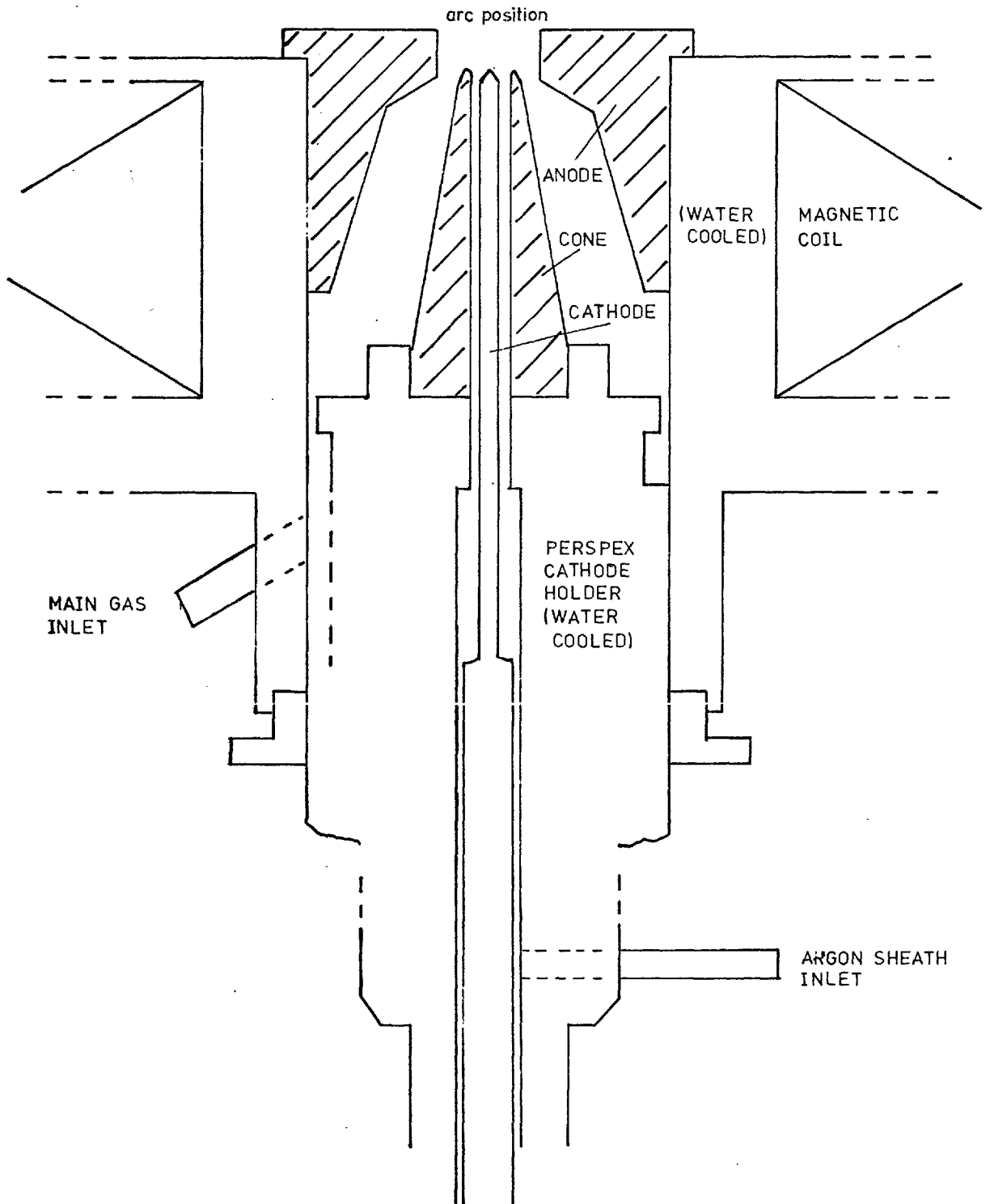
Fig. 3.1   CROSS-SECTION THROUGH THE PLASMA JET BURNER
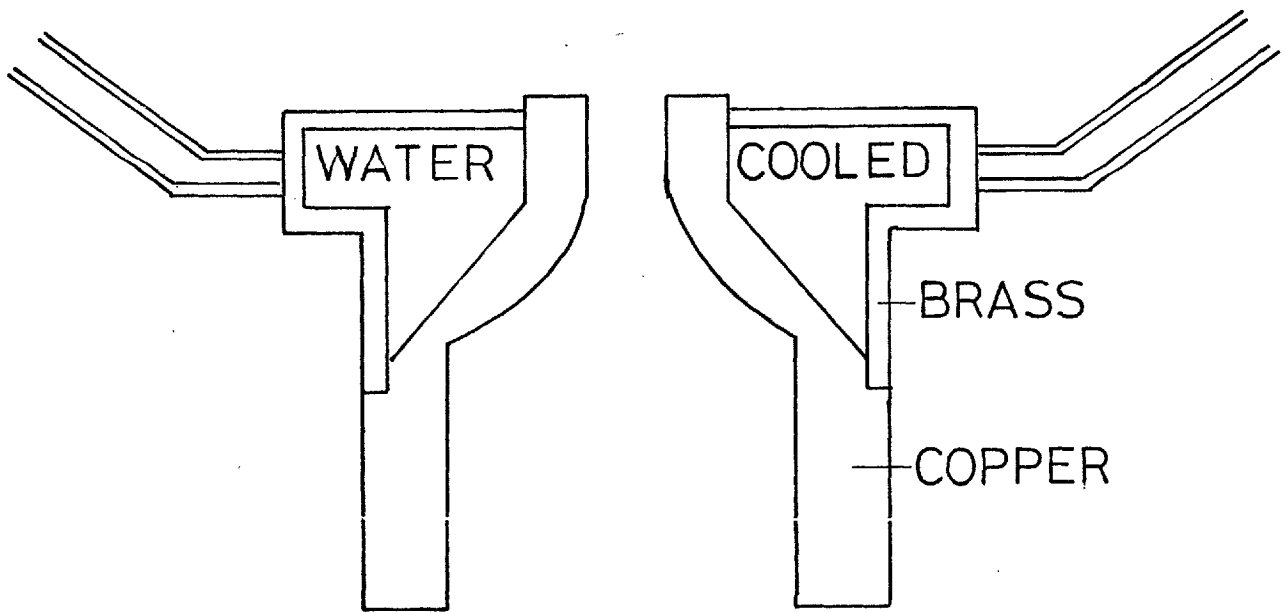
Fig. 3.2   CROSS-SECTION THROUGH THE ANODE

could be struck from its tip to the bottom end of the straight part of the nozzle.

Both electrodes were surrounded by a horizontal magnetic field coil made up of about 3500 turns of 22 s.w.g. copper wire around a cooling water jacket. The wire was cooled with high temperature insulating material. The coil as well as the cathode holder and anode were cooled using deionized water at a pressure of a few p.s.i. The water was monitored separately for coil and cathode and for the anode for flow rates using rotameters and for temperatures with mercury in glass thermometers. Deionized water was used in order to reduce the deposition of calcium salts in the cooling ducts, which would have reduced cooling efficiency. It was conveniently available at pressure at the bench.

Figure 3.3 shows the electrical connections supplying the plasma jet. A moving coil ammeter in the cathode line and a voltmeter across the electrode gap allowed continuous monitoring of current in and voltage across the plasma and thus of the power consumption of the arc. The electrical power for the arc was provided by one or two DC Miller SHR 222 welding rectifiers with power output ranges of 1 to 10 kW, capable of delivering up to 150 amps maximum each. The rectifiers had been modified to give both floating anode and cathode potentials so that they could be used coupled in series or parallel as well as singly. The anode had therefore to be earthed at the burner. The AC ripple had also been reduced by the manufacturers to less than 2%. These rectifiers are fixed power devices. For a chosen power output the ratio of arc current to arc voltage depended on the separation of the electrodes and therefore the relative vertical position of the cathode with respect to the anode.

A seirotron HF spark generator was fitted between the cathode line and earth. It worked off the open circuit voltage of the welder (75 volts

ARC CURRENT
SUPPLY

COIL CURRENT
SUPPLY

MAGNETIC
FIELD
COIL

AMMETERS

VOLTMETER

WELDERS

SEIROTRON

RECTIFIER

240 VAC
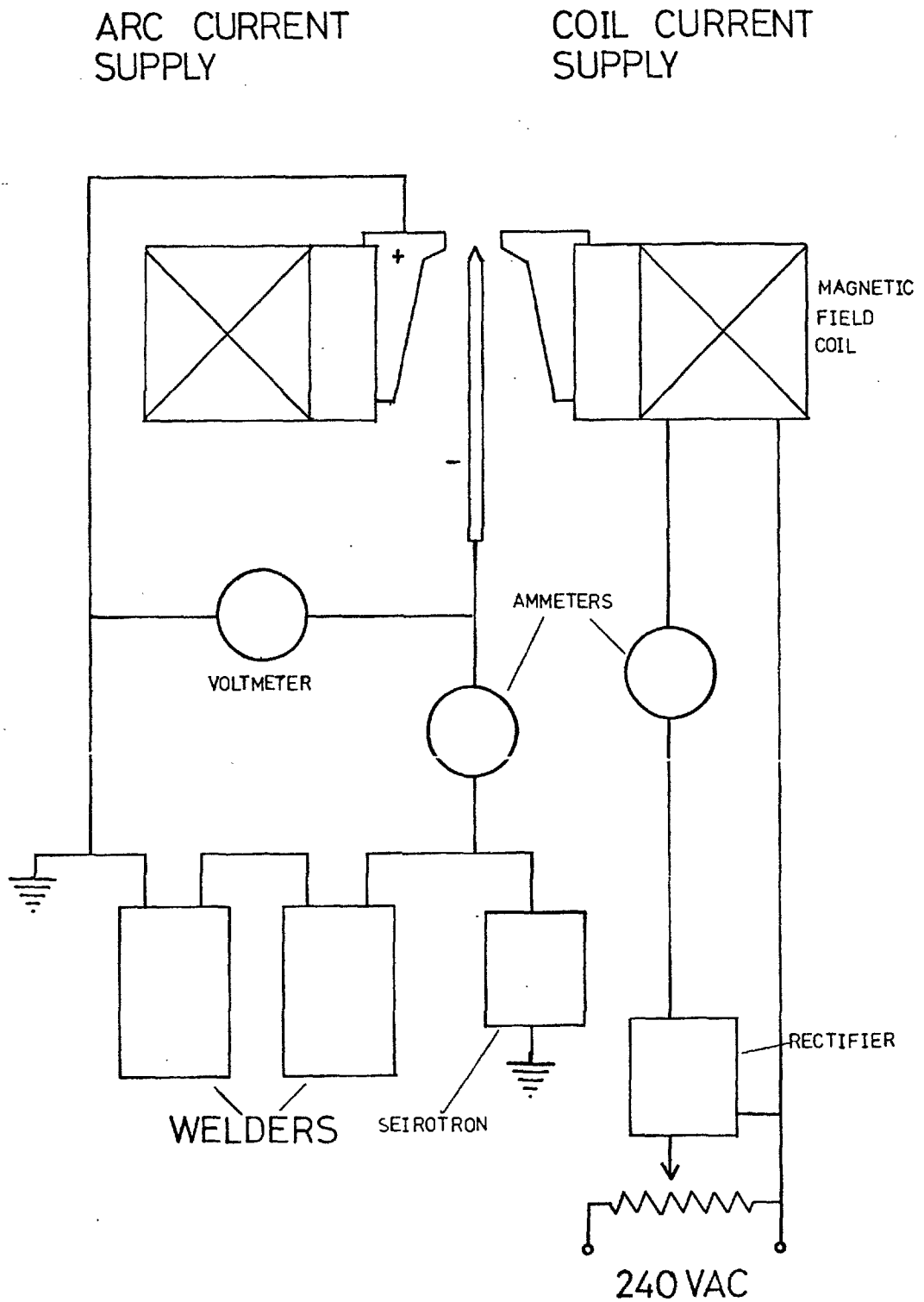
Fig. 3.3   ELECTICAL CONNECTIONS TO THE PLASMA JET

DC) and supplied a series of high frequency sparks across the electrodes
which initiated the arc. As the arc was struck, the voltage across
the welder dropped, switching the seirotron off automatically. The
seirotron could be kept on line to restrike the arc should it be
extinguished (Ref. 37).

The DC current of up to 2.5 amp for the magnetic field coil was
supplied from a rectifying and smoothing circuit as shown in Figure 3.4.
The output voltage across the coil, and thus the output current, were
adjusted by setting the input conditions from the mains voltage to a
suitable level using a rotary transformer. Both voltage and current
could be measured separately. Once the coil reached thermal equilibrium
the current supplied by the rectifier was found to be extremely stable.
No changes in current were observed even for very extended runs.
Current levels were also easily reproducible, and the AC ripple was
found to be less than 2%.

The current in the coil gave rise to a magnetic field in the region
between the electrodes in the direction parallel to their axis of
symmetry, the value of which varied in accordance with the setting on
the Variac. The directions of the field B and current in the arc I
were mutually perpendicular. They resulted in a Lorenz Force of
I B on the arc. This caused the arc to rotate in the annulus formed
by the electrodes.

When the power dissipation by the arc had been chosen by presetting
the welder, and the electrodes were in position with respect to each
other (effectively determining the arc current to voltage ratio) there
were clearly only two easily variable quantities. One was the argon
flow rate which was controlled by a needle valve and monitored by a
rotameter, a mercury manometer and a mercury in glass thermometer.
The other was the rotation rate of the arc, which was determined by the
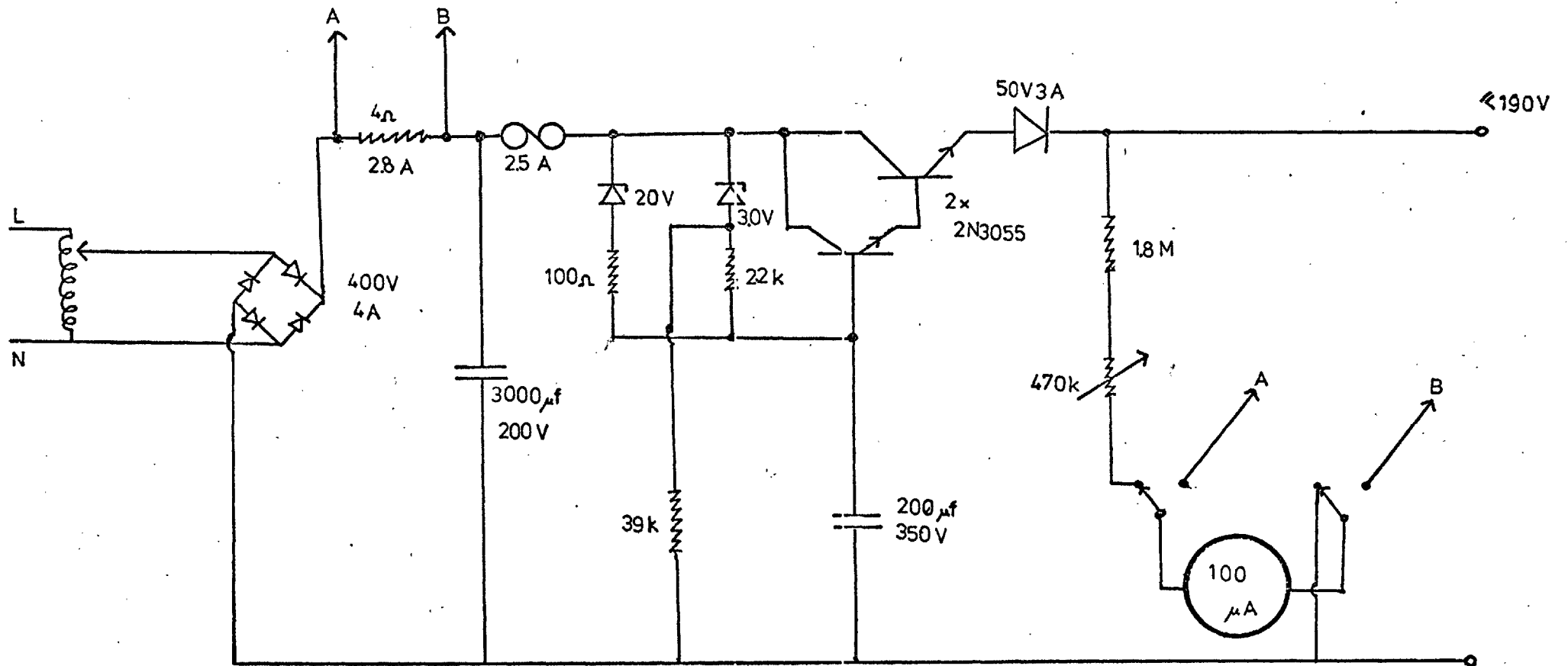
Fig. 3.4   DC SUPPLY FOR COIL CURRENT

arc and coil currents and selected by varying the magnetic field.

The rotational frequency was monitored with the aid of a small Reed Coil (Radio Spares No.2) positioned near the plasma jet and pointing towards its centre (Figure 3.5). As the arc rotated in its annulus the magnetic field associated with the arc current varied in direction. Its field lines cut the axis of the search coil with the same frequency as the arc rotation and it was this variation that was detected by the coil. The EMF induced in the coil was applied across a 1 MΩ resistor and displayed on an oscilloscope. From the recorded trace the arc rotation frequency could be obtained directly.

In the magnetically rotated arc the force exerted on the plasma by the magnetic field is balanced by the drag of the gas on the moving arc. Under equilibrium these two forces balance:

$$BI = 1/2 \zeta u \, c_D \, d$$

where B is the magnetic field, I the arc current, ζ the gas density, c_D the drag coefficient, u the linear arc velocity and d its diameter (Ref. 22). In a previous investigation (Ref. 22) the arc rotation rate was related to the magnetic field and arc current by the empirical relation

$$f \propto B^{0.6} I^{0.33}$$

where f is the rotational frequency of the arc, I its current (amps) and B the magnetic field strength (gauss) showing the rotation rate to be more sensitive to changes in the magnetic field than in the arc current. This relationship was reconfirmed in more recent measurement (Ref. 13,23). As the rotation rate is dependent on the arc current, which in turn depends on the precise electrode position for a given power

SEARCH
COIL

PLASMA JET

OSCILLOSCOPE
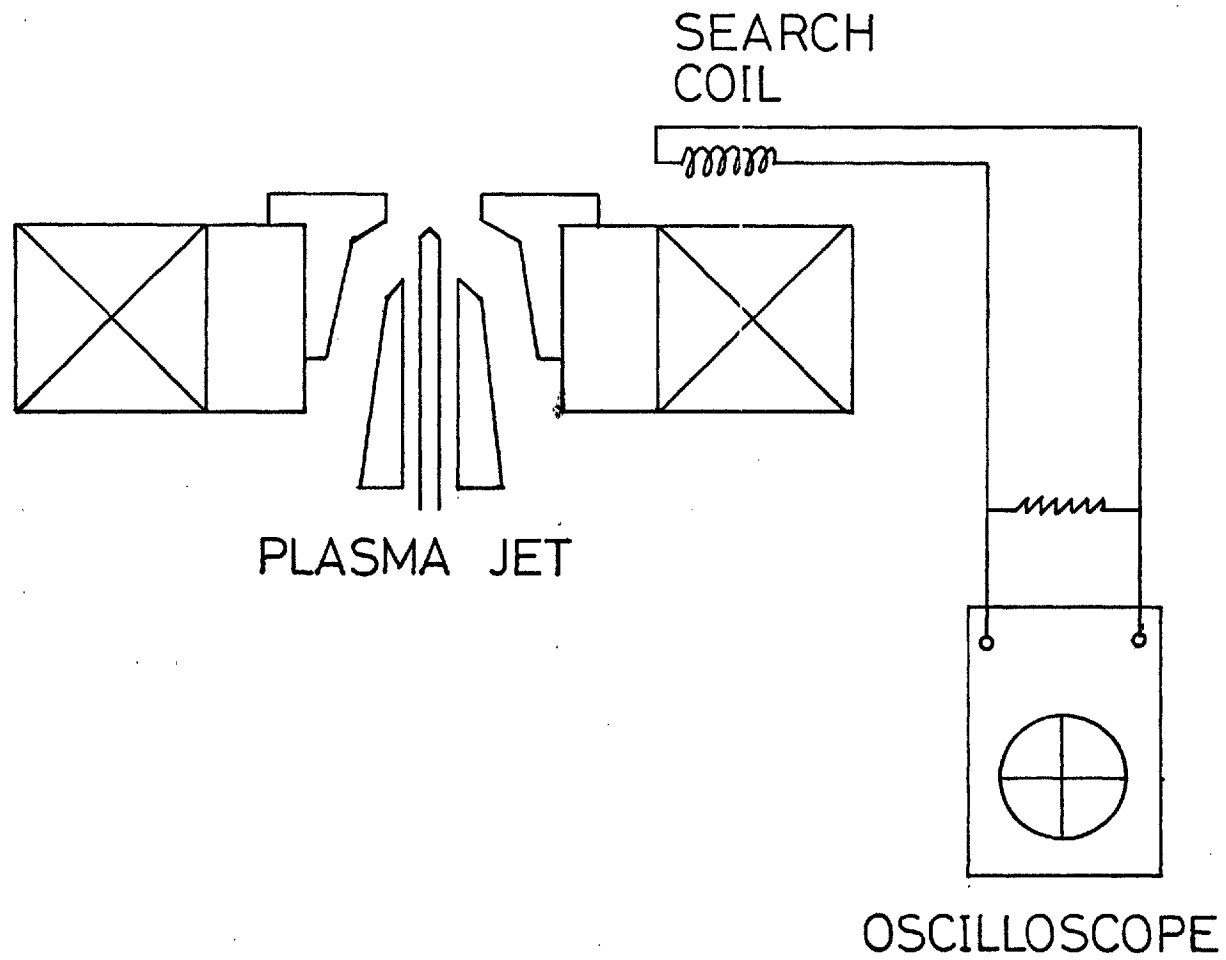
Fig. 3.5   SEARCH COIL, CIRCUIT AND POSITION

output, the arc rotation was monitored after each change in conditions and during experimental runs as well as after each dismantling and cleaning of the electrodes.

III.2 Arc Propagation

The propagation of magnetically rotated arcs has already been documented in the literature (Ref. 23,24,25); the arc in rotation remains a narrow channel of ionized gas and takes on a convolute shape. It is this shape that ensures that every part of the arc, irrespective of position, heats an equal amount of gas in any given time interval (Ref. 23,24,26). As the arc rotates the anode root remains almost stationary. The arc column stretches along the direction of rotation into the convolute shape until a condition is reached when the potential difference between some point on the column and the anode near that point is raised above the breakdown potential for that particular gap width and gas mixture. A new anode root is then formed as the arc jumps to that point and the excess length of the arc is extinguished (Ref. 22) (Figure 3.6). The process then recommences.

III.3 Attempts to Spread the Arc

So far all attempts to truly 'spread out' the arc into a diffuse disc of plasma covering the whole or even most of the nozzle uniformly have failed. Although from time to time reports are received of successful smudging of the arc they are almost always repudiated by other workers in the field using more precise techniques.

Most frequently direct optical records taken at insufficiently high shutter speeds appear to indicate a diffuse plasma. This is mostly due to the afterglow in the wake of the arc. Published material containing

arc

anode

cathode

A

B

C

D
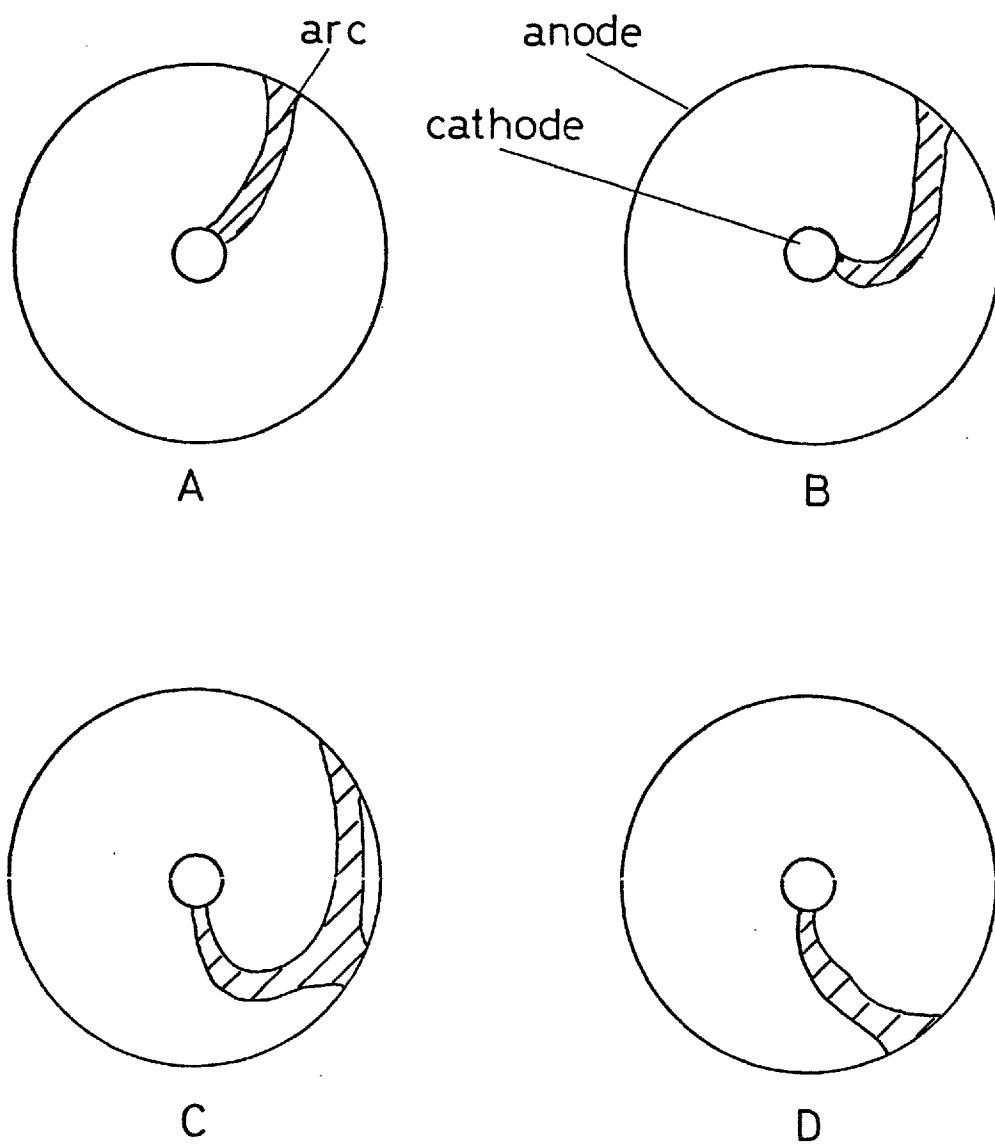
Fig. 3.6   ARC PROPAGATION (SCHEMATIC)

these photographs has in the past been amended by latter workers using faster cameras. While it might be true that a slow moving gas through the plasma jet "sees" the plasma as diffuse but turbulent, in absolute terms, however, the plasma remains in a distinct, even if expanded, channel.

It was hoped that it might be possible to spread or even diffuse the plasma by allowing it to pass through an atmosphere of ionized carrier gas. In order to test this theory the plasma jet described was slightly modified.

A second anode made of copper was placed on top of the first and electrically insulated from it, using asbestos paper. This anode consisted of two semiannular halves stuck together and insulated from each other using Araldite (Figure 3.7). The central circular hole of the second electrode was of the same size as, and was placed in line with, the lower nozzle. Each of the top anode halves was connected via a separate 10 cm long copper rod to the common positive output of one of the welders. The positive output of the other welder was connected to the lower anode. Both negative outputs were joined to the common cathode. The potential drop along one of these rods was monitored as the arc moved along the upper electrode. Although the resistance of the rod was extremely low, the high current ($\sim$ 70 amps) produced a measurable voltage along each rod. This potential was displayed on a Tektronix oscilloscope. As an arc rotated in the upper anode a positive potential was recorded as long as the arc moved on the electrode half and current flowed through the rod being investigated, while zero potential was displayed while the arc was joined to the other annulus half.

As long as only the upper arc was struck a square wave signal was displayed on the oscilloscope indicating a rotating arc spoke. Its frequency of rotation which could be varied by either changing the arc

TOP VIEW

INSULATOR

COPPER ROD

SIDE VIEW

UPPER ANODE

INSULATOR

LOWER ANODE

MAGNETIC COIL

COMMON CATHODE

PLASMA JET

OSCILLOSCOPE
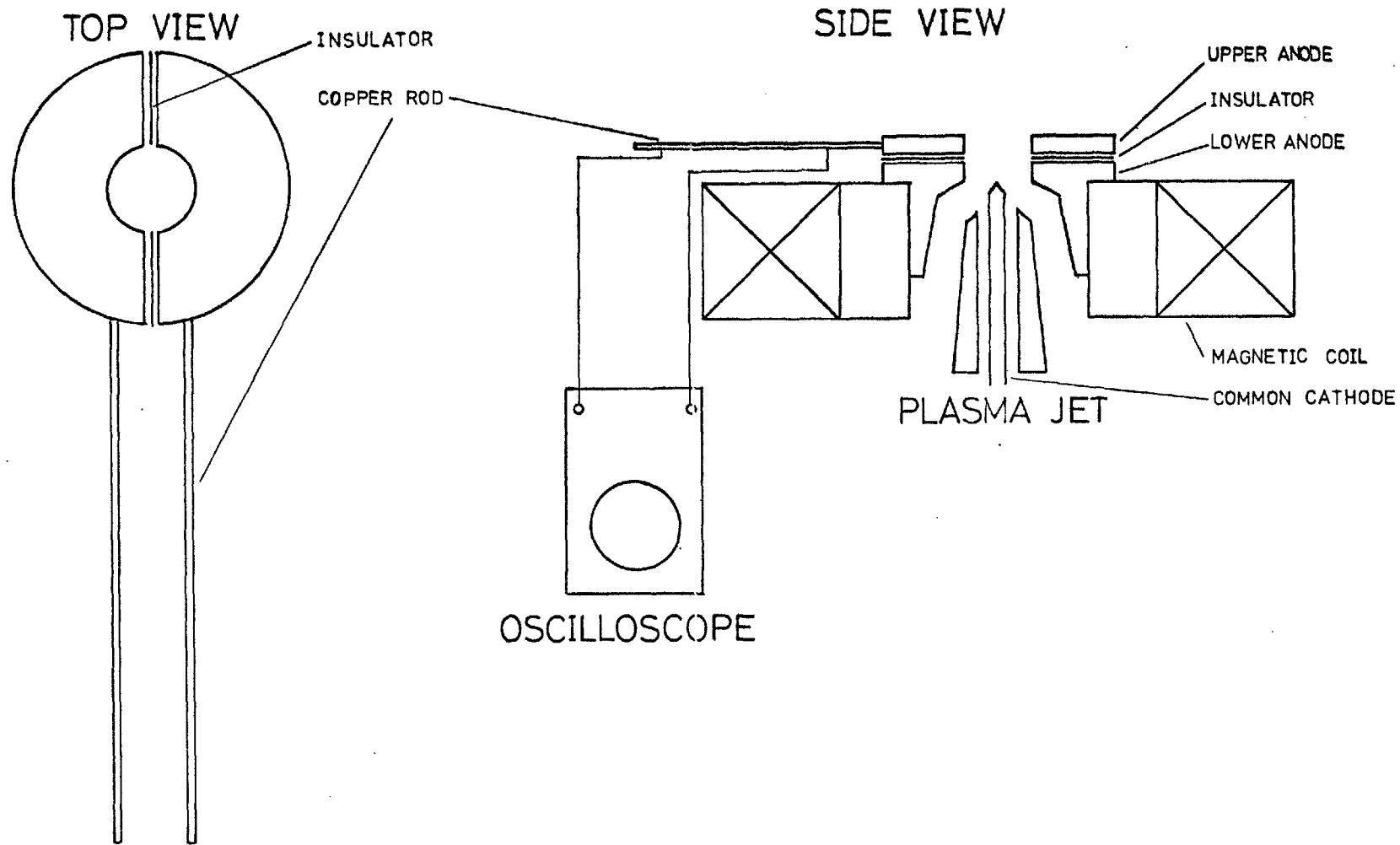
Fig. 3.7   DOUBLE ANODE CONFIGURATION

current or the DC current in the magnetic field coil was noted from both the frequency of the square wave and from measurements with the search coil. Both values were in good agreement. Plate 1 shows the change in frequency with increasing current in the upper arc as a voltage variation in one of the rods. The increase in voltage along the rod due to the higher current is also clearly noticeable from the change in signal amplitude.

When the lower arc was struck in parallel the square wave output from the upper electrode persisted. This indicates that the upper arc remained as a confined spoke. The upper rotational frequency is now found to be unaffected by the current in the upper arc at constant magnetic field (Plate 2). It varies, however, linearly with the current in the lower arc even when the upper arc remained constant (Plate 3).

It therefore appears that the upper arc hooks onto the lower one while transgressing the annulus. There could be two possible reasons for this. Either a high degree of ionization is mainly present in the immediate vicinity of the lower arc and the upper arc rather than spreading, follows the lower arc in its immediate wake. Alternatively, the ionization from the lower arc is insufficient to cause a spreading of the upper arc and the two arcs are linked together by the interaction of the magnetic fields of the two arc currents. The almost exclusive effect of the lower arc current on the rotation rate might in this case be due to the fact that this arc rotates closer to the centre of the coil experiencing a larger field effect. The predominant rotation of the lower arc does however give extra weight to the theory that the upper arc is confined to the strongly ionized immediate wake of the lower one. The true cause of the link-up is probably a combination of the two possibilities, the first playing a more important part. It is in any case clear that a diffusion of the upper arc cannot be achieved in this way. From an

ARC CURRENT
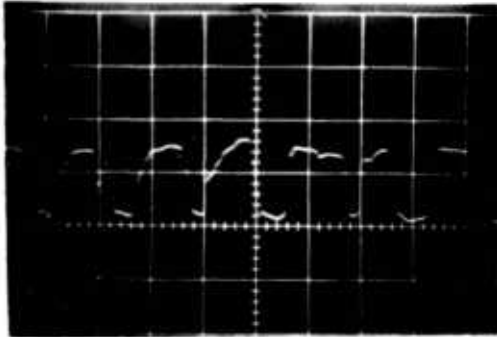
45 amps
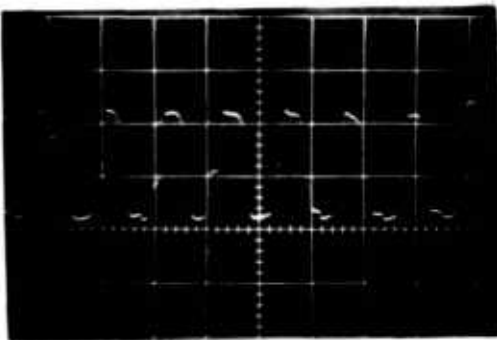
95 amps
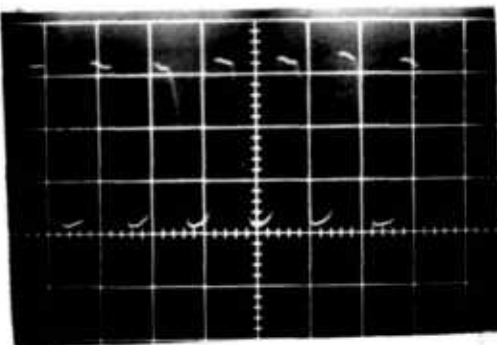
120 amps

PLATE I   VOLTAGE VARIATION ALONG LEAD SUPPLYING ONE UPPER
ANODE HALF WITH UPPER ARC CURRENT FOR UPPER ARC ONLY

ARC CURRENT

LOWER   UPPER
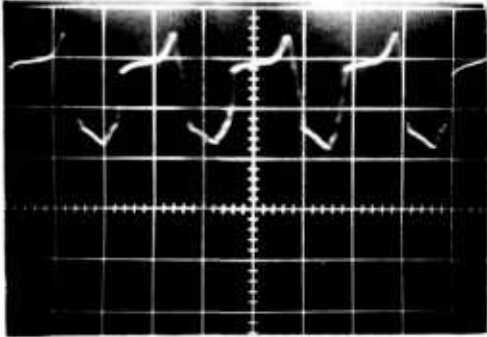
60   50   amps
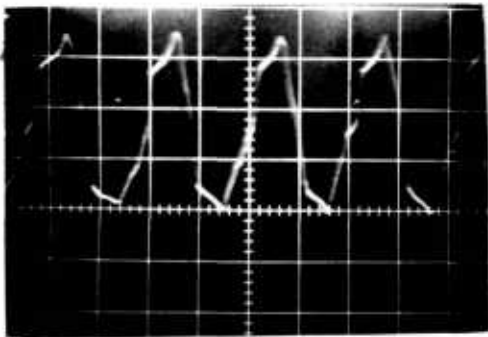
60   85   amps
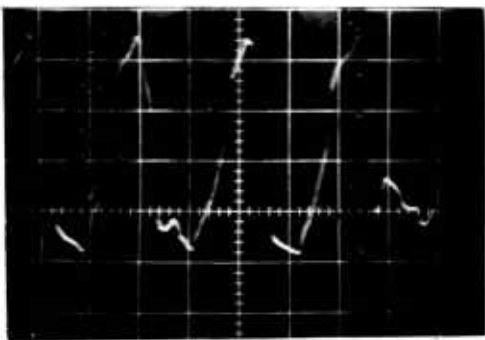
60   110   amps

PLATE II   VOLTAGE VARIATION ALONG LEAD SUPPLYING ONE UPPER
              ANODE HALF WITH UPPER ARC CURRENT FOR BOTH ARCS,
              LOWER ARC CURRENT CONSTANT

ARC CURRENT

LOWER UPPER
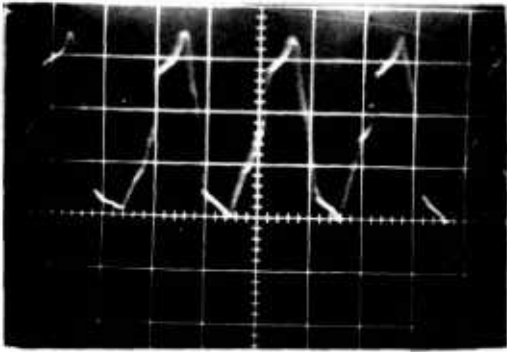
60   85   amps
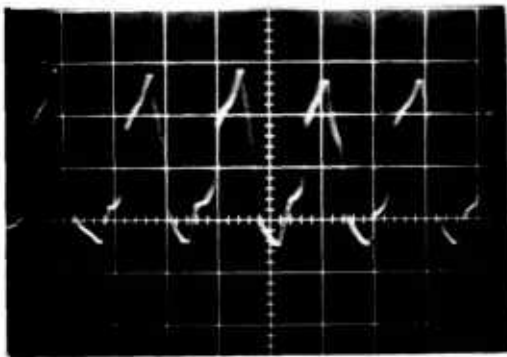
100   85   amps
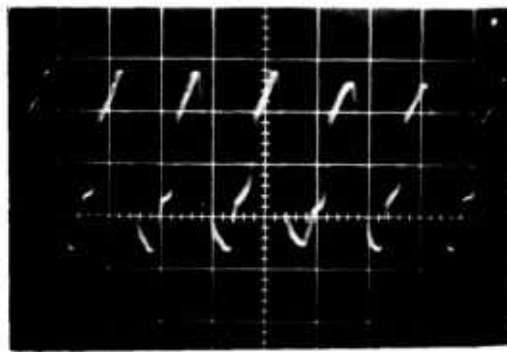
125   85   amps

PLATE III   VOLTAGE VARIATION ALONG LEAD SUPPLYING ONE UPPER
ANODE HALF WITH LOWER ARC CURRENT FOR BOTH ARCS,
UPPER ARC CURRENT CONSTANT

inspection of the rise and fall times of the square pulses it seems

clear that even any increase of the upper arc diameter is only minimal.

III.4 Interaction of Arc and Gas Flow

In addition to the arc always being confined to a thin channel of

plasma it needs to be considered that the temperature inside the column

is of the order of a few hundred times higher than that in the surrounding

gas, which results into a great expansion of the gas that is transformed

into the arc plasma. Only a relatively small amount, therefore, actually

passes through the arc core. This not only causes the arc to behave to

some extent like a solid stirrer, but also means that most of the gas

is heated by surface contact with the plasma, rather than actually passing

through it. If one therefore wanted to achieve uniform heating of the

gases passing through the plasma jet without relying on downstream

mixing, the rotation rate of the arc needs to be tuned to the flow rate

of the carrier gas through the nozzle.

For uniform heating it is desirable that each part of the gas flow

should be in contact with the arc for the same duration of time.

Theoretically, this is achieved by ensuring that in the time required for

the gas flow to move through one arc thickness the plasma completes an

integral number of revolutions. When this integer is 1 the arc is termed

to be just running into its own wake, which is clearly discernible audio-

metrically. This is the condition to be aimed for if uniform distribution

of entropy throughout the wake gases is desired at reasonable flow rates

and stable conditions. In practice, perfectly homogeneous energy distri-

bution is of course never achieved. This, however, does not greatly matter

as recent calculations (Ref. 36) have shown that the existence of small

periodic pockets of hotter gases cause an increase in the rates of many

reactions because of the exponential Arrhenius factor.

If more generally some parts of the flow are in longer contact with the arc than others, this results in a rising spiral staircase of hotter gas in an intermediate atmosphere of colder gas. Considering a volumetric flow rate (v) of argon passing through a plasma jet nozzle of radius (R) the mean gas velocity upward (u) is given by

$$u = v/\pi R^2$$

If an arc rotates in the nozzle, inducing a swirl in the gas of angular frequency (ω) the rotational velocity (s) at a distance (r) from the centre is

$$s = r\omega$$

The angle of elevation of the spiral staircase is then found to be

$$\tan \alpha = u/s = v/\pi R^2 r\omega$$

In practice, however, the spiral of hot gases is quickly destroyed by the intense turbulence in the wake region. Only a slight indication of a spiral was noticeable during this investigation.

Some of the advantages of having chosen a rotating arc configuration are now clear. On a simple plane it is clear that from the point of view of electrode conservation constantly moving arc roots are desirable as long as the electrode materials are not required to take an active part in any chemical reactions in the plasma or its wake region. Probably more important, however, is the behaviour of the arc column as a stirrer. The rotation of this stirrer induced swirl into the gas and

its angular momentum causes the jet to expand considerably on leaving the nozzle. It can be seen from the Law of Conservation of Mass, that this funnel type wake along with recirculating vortices at the nozzle mouth, causes not inconsiderable entrainment of the surrounding atmosphere into the plasma jet gases. This process would give an engineer considerable choice in the mode of introduction of reactants into the wake region of the arc. They could be injected along with the carrier gas for entropy, dissociated species or radicals through the anode nozzle, or through the walls of the nozzle, or above it. The mixing is further facilitated by the turbulence induced into the flow of the plasma jet gases by the rotating arc.

Chapter IV

SHADOW AND SCHLIEREN METHODS

Considerable work has been done on magnetically rotated arcs, including apparatus similar to that used in the present investigation. Ref. 27 gives a review of many important articles concerning the behaviour of arcs; further references were given in the introduction. Little, however, is known of the general behaviour of the gases in the wake region of a plasma jet entering an open atmosphere.

As one is dealing here basically with a phenomenon of a hot turbulent swirling gas stream entering into and mixing with a cold stationary gas, shadow and schlieren methods suggest themselves, and could be expected to lead to a better understanding of the overall shape of the wake as well as the fine structure within the emerging gas flow.

IV.1 Short Duration Photography

As high flowrates and rapid turbulent fluctuations were anticipated it was necessary to use short duration exposure photography in order to freeze the motion. Two possibilities were considered. One was the use of fast shutters (mechanical or electronic) in conjunction with continuous or long duration light sources. It will be seen later in this chapter that the optical arrangements used made a focal plane shutter preferable. Alternatively a considerable part of the optical path would have had to be screened off in order to protect the film from stray light. No such shutter was easily available and it would have had to be obtained or made up at great expense and delay.

IV.1.1 The Light Source

It was therefore decided to opt for a short duration light

source instead. The system chosen was a short duration spark, as

developed by R.J. North at the National Physical Laboratories (Ref. 28,29),

in conjunction with a slow focal plane shutter. The spark stand (Fig. 4.1)

consisted of two stainless steel cylindrical electrodes fixed in position

along a common horizontal axis of symmetry by two vertical supports. The

support carrying the live electrode was made of perspex, the other of

brass. Both verticals were fitted to a base plate, the ends of the

electrodes facing each other were ground into hemispheres. The

separation between the electrodes could be varied but was usually kept

at about 1 cm. It was in this gap that the spark was fired.

One of the electrodes had a fine hole drilled along its axis through

which argon passed via a flow indicator and a fine needle valve. The

flow was adjusted to give a fine jet in the spark gap. The argon served

two purposes, making use of its low ionization potential; it confined

the spark into a narrower channel than was otherwise possible and simul-

taneously ensured better reproducibility of the exact position of conse-

cutive sparks.

The second electrode had a somewhat larger hole drilled along its

axis. This contained a 1 mm tungsten rod held firmly in position and

insulated from the main electrode by a tube of mica. This rod was

allowed to protrude into the spark gap by about 1 mm and acted as a

trigger electrode. The other end was connected to the secondary coil

of a 300 volt pulse transformer, the primary of which was joined to the

trigger source. This pulse source consisted either of a manual or a

neon-photodiode switching circuit attached to the shutter. Figure 4.2

shows the connections to the spark stand schematically. In some cases

the trigger pulse came via an electronic delay from the light of a

Fig. 4.1   SPARK STAND

HT SOURCE   SWITCHES

CAPACITOR

CAMERA

SPARK
STAND

TRIGGER
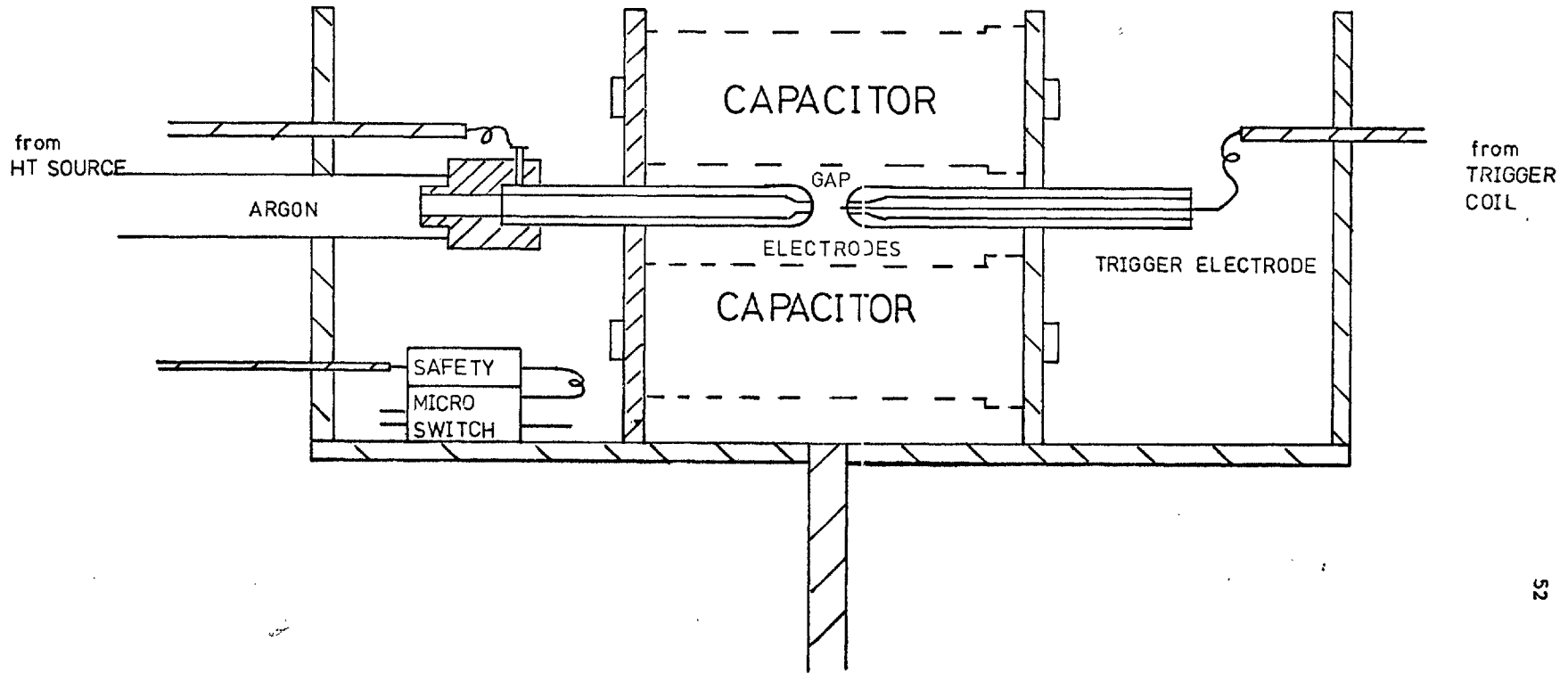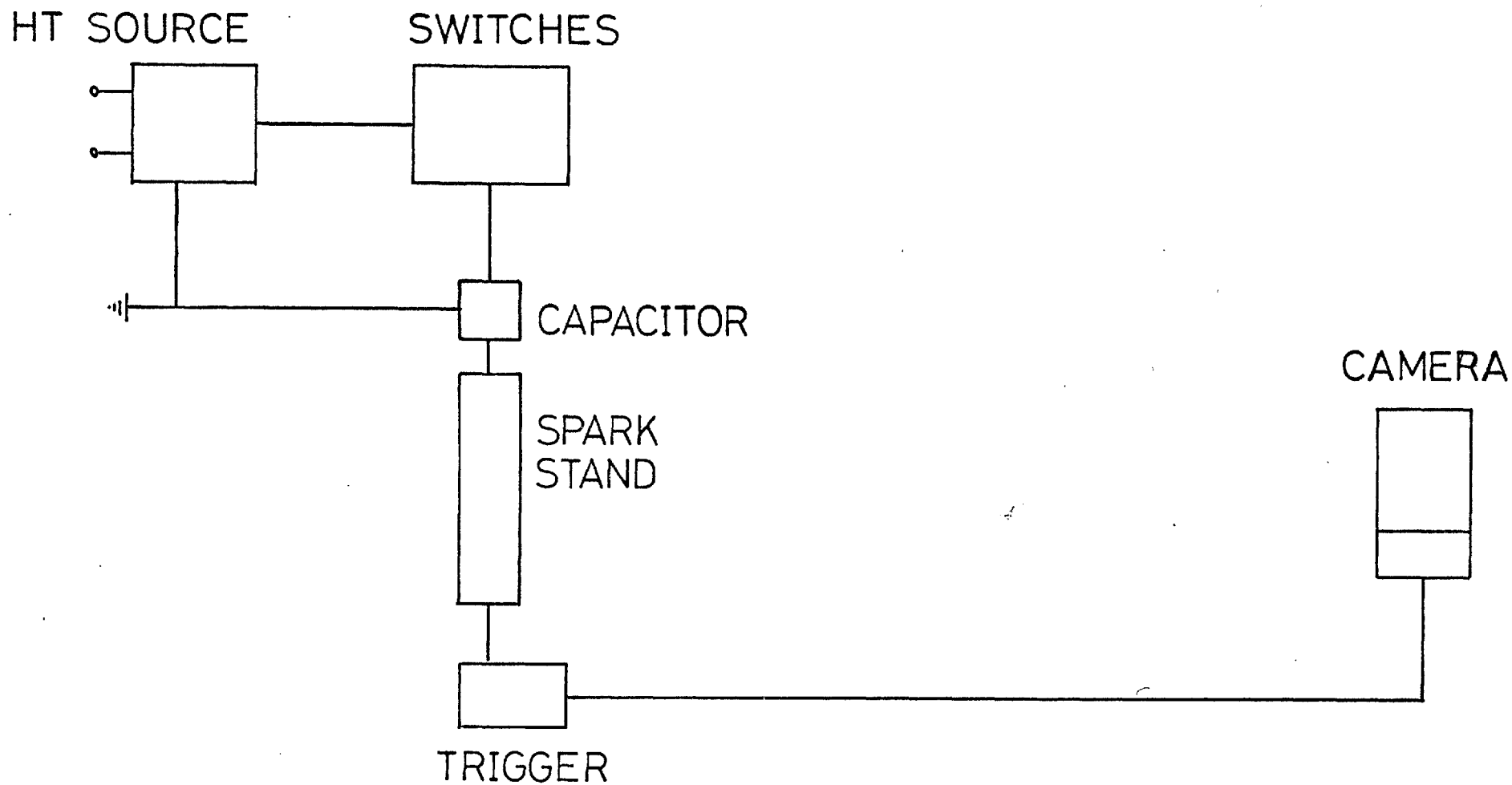
Fig. 4.2   CONNECTIONS TO SPARK STAND (SCHEMATIC)

preceding pulse, as explained later in this chapter. The pulse transformer could be replaced by an ordinary car coil if required.

The spark stand was covered by an aluminium shield with a large hole on either side to allow the light to emerge. This cover was always in place when the light source was in use in order to minimize the risks of electrocution. The shield also served to absorb some of the electromagnetic radiation liberated by the spark. This radiation caused electrical interference with other sparks - a major problem that will be discussed later.

The two electrodes were connected across a 1 μF rapid discharge capacitor with low resistance copper cable (Fig. 4.3). The electrode containing the trigger was earthed, while the other one was maintained at a potential of 8 kV. The capacitor was charged to this voltage through a series of resistors via a switching system by a current limited HT-source of the type Brandenburg MR/50R. All switches and resistors were protected in a perspex box. The box as well as the covers for the spark stands and capacitors were secured by a micro switch system. This caused immediate safe discharge of the capacitors in case of accidental removal of any of the safety devices while the system was under HT.

To operate the light source, the capacitor was charged and the Brandenburg disconnected from it. The trigger spark then supplied preliminary ionisation causing the capacitor to discharge through the main spark gap.

In the first instance the light source was triggered by the focal plane shutter. A small neon light source on one side of the shutter and a photodiode on the other along with a separate pulse generating circuit (Fig. 4.4) supplied the necessary trigger pulse for the pulse transformer. The duration of the spark discharge was measured using a

H T SUPPLY

ELECTRODES

RAPID
DISCHARGE
CAPACITOR

10 K

10 M

+ 300 V   220 K

36   2N4444

from
SHUTTER   COIL

47 K

10 K

TRIGGERING CIRCUIT
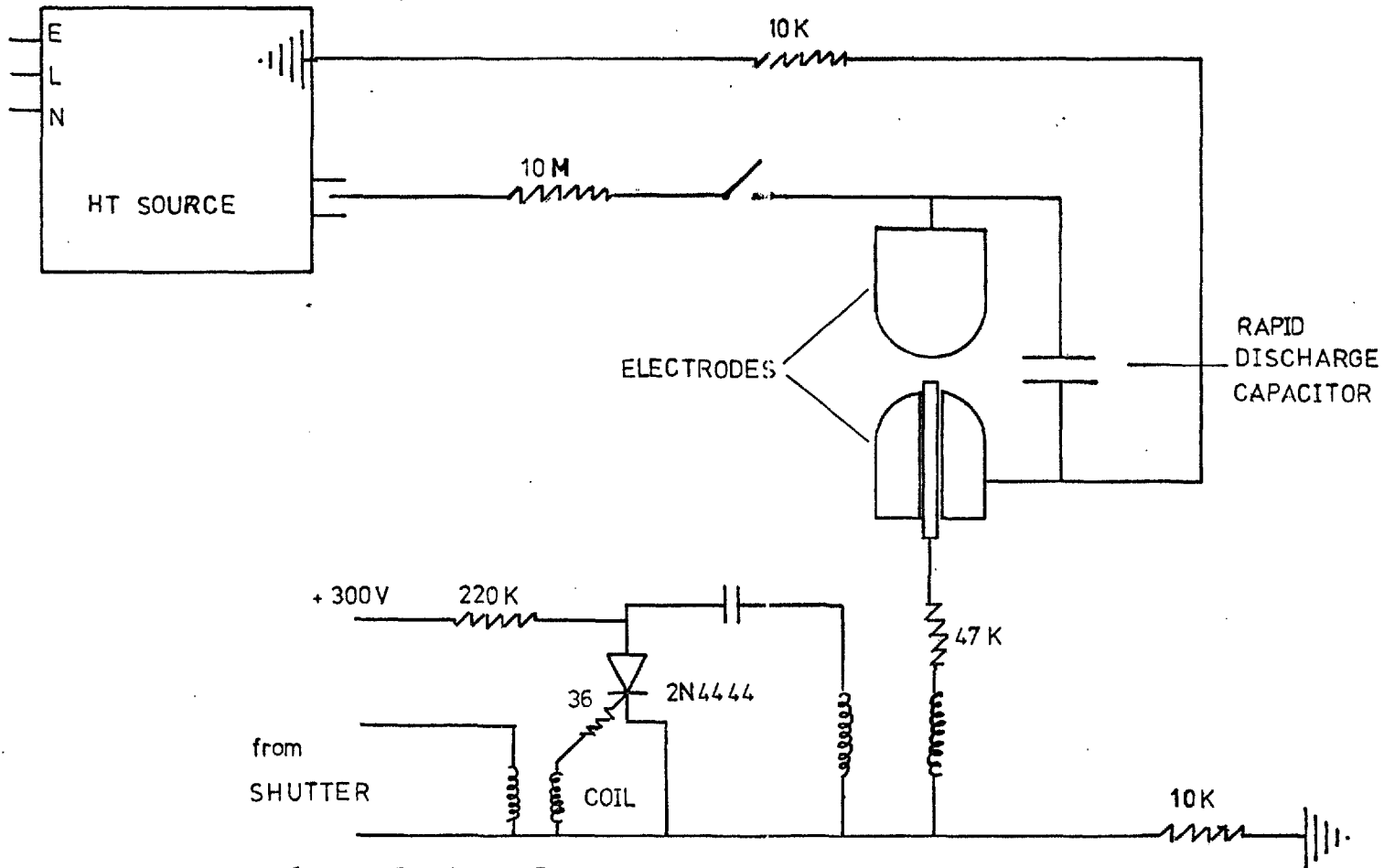
Fig. 4.3   ELECTRICAL CONNECTIONS TO SPARK STAND
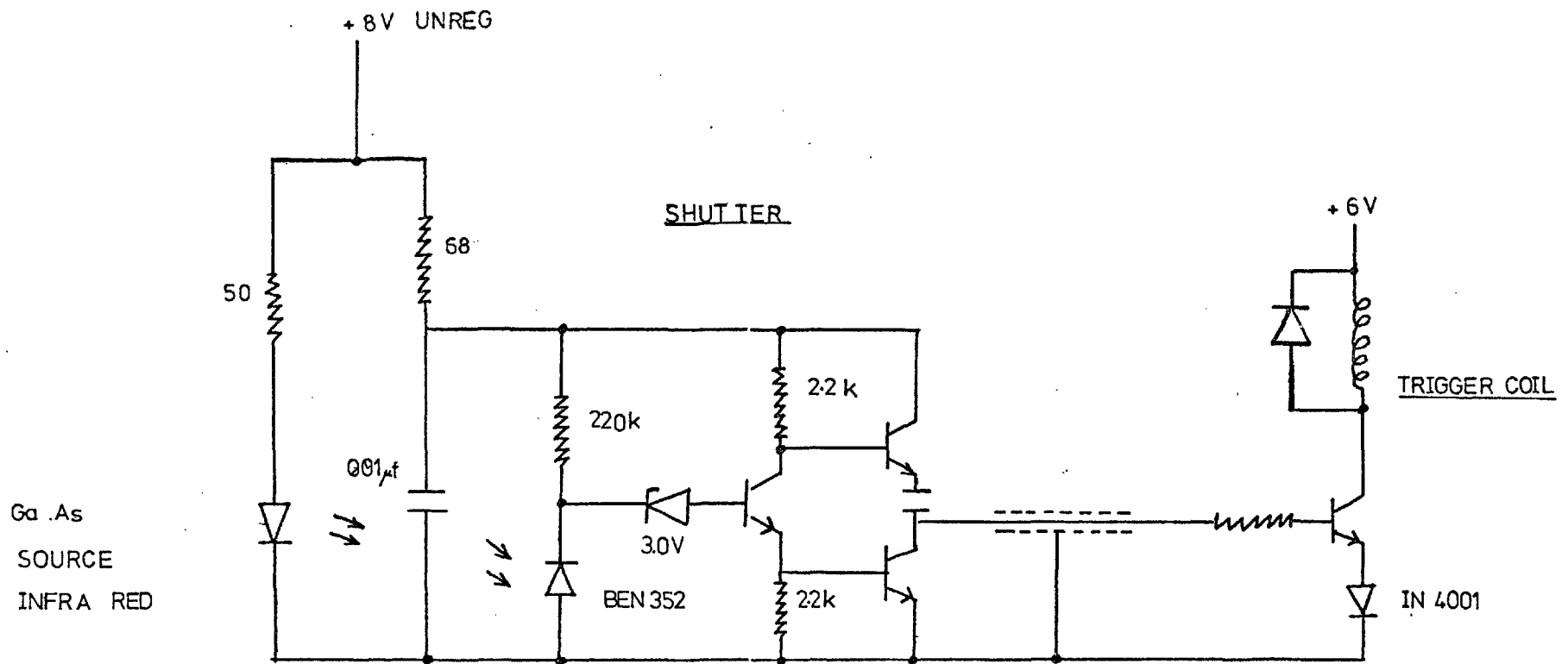
Fig. 4.4   TRIGGER PULSE GENERATING CIRCUIT
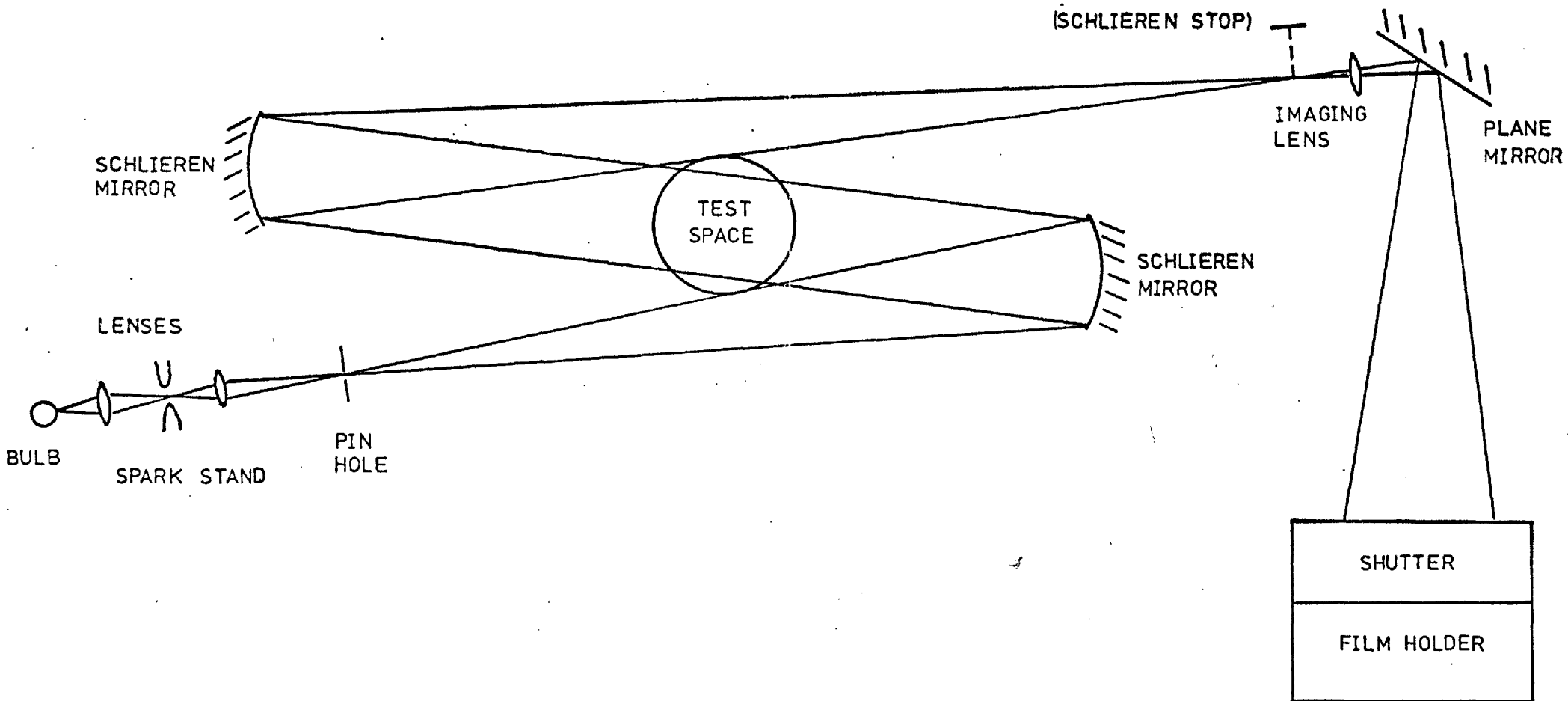
Fig. 4.5   OPTICAL ARRANGEMENT SHADOWGRAM OR SCHLIEREN
-SINGLE SPARK

photocell and an oscilloscope and the spark found to be liberating
most of its high energy within the first microsecond. It was this
that determined the exposure time irrespective of the shutter speed.

IV.1.2 The Optical System - Single Exposure

The arrangement chosen for the shadow and schlieren photography
was the standard z-shaped schlieren system using two 3 m focal length
and 0.3 m diameter schlieren mirrors with a parallel beam in the test
region (Fig. 4.5).

A quartz halogen projector bulb was used to line up the system
by focusing it onto the centre of the spark gap using a short focal
length lens. The beam was then focused with another short focal length
lens onto a pinhole placed at the focus of the first schlieren mirror
which produced a parallel beam passing through the test region above
the plasma jet burner onto the second mirror. Horizontal and vertical
brass scales with 5 mm divisions were placed in the beam at the test
region to act as a reference. The second mirror was used to refocus
the beam.

From here on the arrangement was dependent on the precise optical
system under consideration. In the case of shadowgraphy nothing was
placed at the focus and a lens of appropriate focal length past the
focus was used to provide a suitable magnification of the test region.
The 4 x 5 sheet film used was held behind the focal plane shutter - an
adapted old RAF reconnaissance camera shutter - and positioned a short
distance away from the image of the test region.

Even though in this type of arrangement the beam in the test
region is parallel, this is not strictly speaking a parallel beam
shadowgram but one of the divergent beam type as classified by Weinberg
(Ref. 21). Only the part after the focus of the second mirror contri-

butes to the sensitivity and the test region could be considered to be located at its image. From calculations in Reference 21 it can be shown that the test region, or in this case its image, should have been placed half way between the focus of the second mirror and the recording plane for maximum sensitivity to be achieved. As we are dealing here, however, with very steep refractive index gradients, a very low sensitivity was found to be quite sufficient, and the film was placed close to the image of the test region. This resulted in the much finer line markings, essential for the investigation of the fine structure that was found inherent in the shadow of the wake region. It also reduced the danger of overlapping of information from different parts of the test region. Placing the photographic plates close to the image of the test region also served to refocus the light from the arc just above the nozzle. No optical blind which might have influenced the gas flow was therefore necessary between the arc and the film to prevent fogging of the emulsion. This was especially important as radiation from the arc was not only very bright but also reached the emulsion during the entire time the shutter was open, much longer than the short duration of the spark.

The present type of arrangement using 2 schlieren mirrors, rather than an ordinary expanding shadowgraphy system, was employed for a number of reasons. It allowed easier variation of magnification without influencing the sensitivity of the shadowgrams or for that matter the line thickness of the marked record. More important, it also allowed for the film to be kept well away from the intense heat and stray light emanating from the plasma even for positions of low sensitivity and very thin lines where the film-test region (or image of test region) distance was kept small. Lastly, it was easily convertible into a schlieren system.

The predominant aberration in this arrangement is astigmatism, as is usual with the use of mirrors. As most deflections were in the vertical direction it was found that the best results were obtained by placing the film a little way behind rather than in front of the image of the test region. Most work was carried out at unit magnification.

For use as a schlieren system a stop was placed at the focus of the second mirror. This was again followed by a lens whose focal length was chosen for the required magnification of the test region. The film holder and its shutter were placed precisely in the image plane of the plasma jet wake. For this adjustment the "Method of the Disappearing Shadow" was used, which is based on the following principle. When focused, all rays from the test space return to their original position in the image. In practice a turbulent premixed flame was supported on the plasma jet burner with no plasma present and the schlieren stop removed. A finely ground glass plate was moved along the optical axis until the shadows produced by the refractive index changes in the flame disappeared.

The astigmatism inherent in the z-shaped schlieren set-up now presented some problems. It brought vertical deflections to a focus in a different plane perpendicular to the optical axis from horizontal deflections. It therefore prevented a true focal point from being formed by the beam. Instead a vertical focal line, followed by a focal disc, followed by a horizontal focal line appeared when moving the stop in the direction of the beam propagation. Attempts to correct for the aberration using cylindrical lenses (Ref. 41) were unsuccessful, as they always caused some distortion of the schlieren image. This gave a choice of three positions for the schlieren stop. In order to obtain

a stop just sufficient to cover the focal disc a photographic plate was placed at the "central focal position" and exposed to a flash of light from the spark with no activity in the test region. After development a transparent glass plate with a black spot exactly the size of the   to be excluded direct beam was obtained and this was used as a stop. Alternatively a knife edge was used at the horizontal focal line to view horizontal deflections and at the vertical focus for vertical deflections.

The stop was positioned roughly using the continuous light source behind the spark. For more precise placement, especially of the circular blind, the spark itself had to be used. The short duration of the flash however made the exact positioning of the stop very awkward. It was found, however, that a card covered with luminous paint placed behind the stop made fine adjustments easier, as the afterglow of the paint gave an indication in which direction the stop needed to be moved in order to obscure the direct beam completely.

Photographic records were obtained for all possible positions of the schlieren blind. It was found that a knife edge placed at the horizontal focal line gave the best results. The use of the circular stop did - as could be expected - not result in a uniform illumination of the schlieren image of the test region, and was also more difficult to adjust correctly. It was generally found that dark field schlieren gave better results than light field schlieren for similar conditions.

In all circumstances, however, shadow photography gave results more easily analyzed than did schlieren. As can be seen in Plate 4, the shadow method gave a very precise record of a fine line structure. Higher sensitivity or narrower line width could be obtained by moving the film away from or towards the image plane of the test regions.

The markings on these films correspond to 2nd gradients of refractive index perpendicular to that part of the beam traversing the test region which arrived at the film at this particular point. The white lines on the film therefore indicate boundaries of cold and hot gas. As the film was placed very close to the image of the test region the relative positions of the markings reflect closely the relative positions of these boundaries. A closer inspection of the records thus indicates that the wake region is made up of a number of pockets of hotter and cooler gas. A detailed analysis is presented in Chapter V dealing with the results from the qualitative analysis of the wake region.

IV.2 Double Exposure Photography

While we now have a method of obtaining a more general picture of the overall shape and the type of structure of the hot and cold gases involved in making up the wake region of the arc, we still have no estimate of the order of magnitude of velocity that was to be expected. To observe this it was decided to record two consecutive short exposures separated by a variable delay of the order of a fraction of to a few milliseconds. In order to achieve this the light source arrangement in Figure 4.5 was replaced by that shown in Figure 4.6. Here a second spark was focused with a short focal length lens into the first spark gap. The quartz halogen bulb was placed behind the second spark stand and focused on it. The second spark was arranged to be somewhat stronger than the first by increasing the discharge voltage and using a somewhat larger capacitor, until both sparks resulted in approximately the same illumination in the plane containing the photographic plate. Figure 4.7 shows schematically the charging and triggering arrangements for the double spark light source. The first
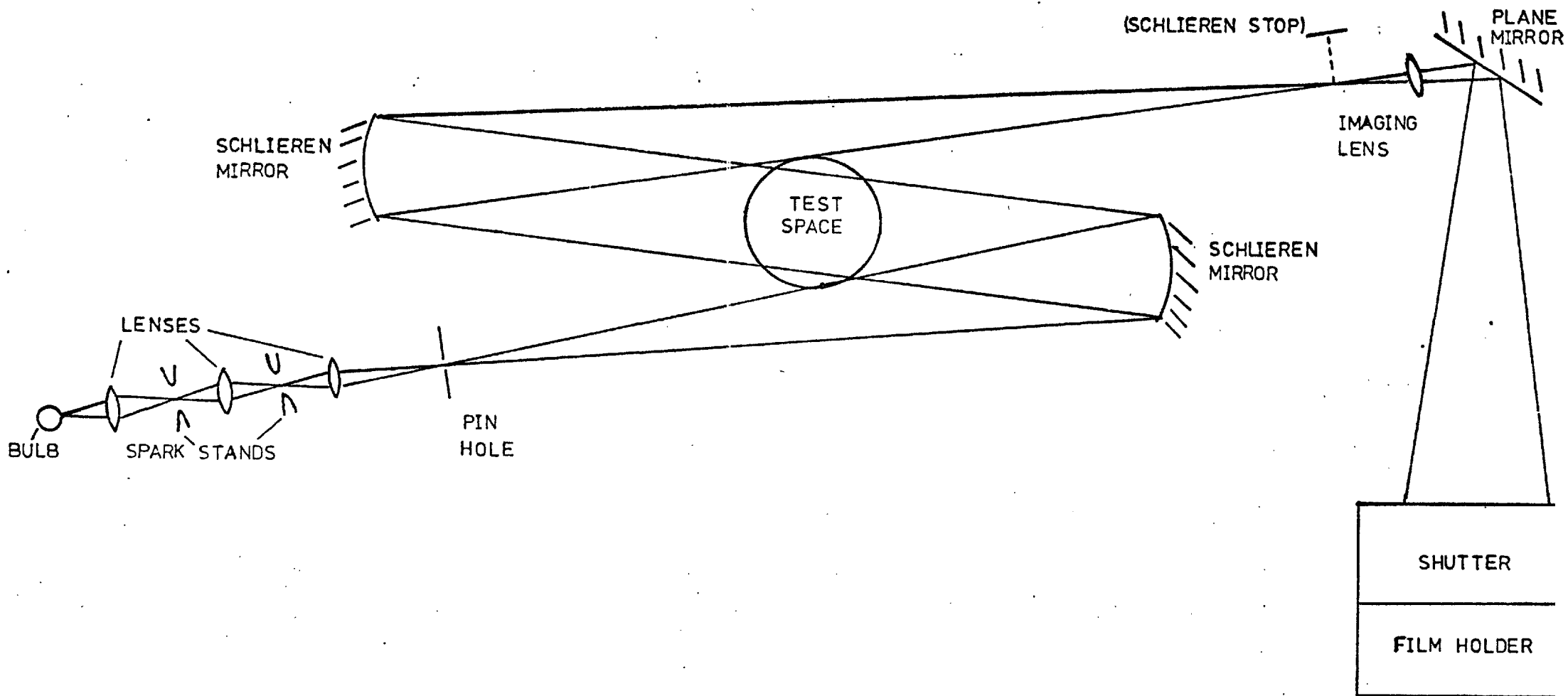
Fig. 4.6 OPTICAL ARRANGEMENT SHADOWGRAM OR SCHLIEREN
          —DOUBLE SPARK
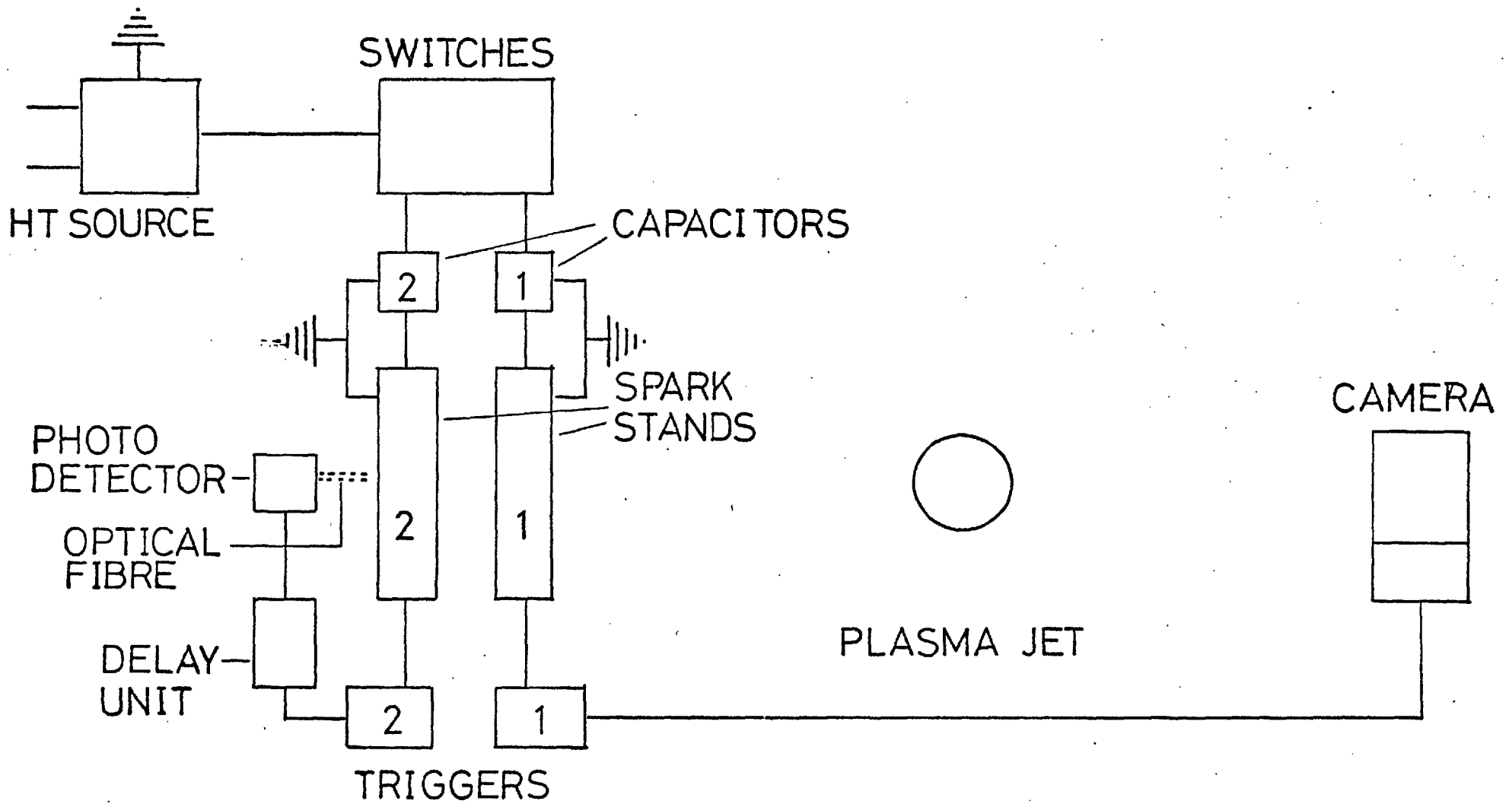
Fig. 4.7   CONNECTIONS TO SPARK STAND (SCHEMATIC)
            -DOUBLE SPARK

spark was triggered as before from the shutter. Some light from the 1st spark was ducted away using an optical fibre onto a diode, which activated a variable delay. After a preselected time this sent a trigger pulse to the pulse transformer of the second spark stand. The revised triggering circuit for both sparks is shown in Figure 4.8, that for the variable delay in Figure 4.9. The delay gave separation times between sparks of 0.1 to 10 msecs and was calibrated using an oscilloscope triggered by the output to the first spark and displaying the signal from the output of the second spark. The not inconsiderable amount of electromagnetic energy liberated by the first spark tended to cause the second one to discharge immediately. To prevent this it was found necessary to shield all components and leads as well as the electrodes themselves. Every part of the circuit was earthed separately to prevent the setting up of earth loops. All leads were kept as short as possible. It was still found that precise positioning of all components and leads was critical to prevent premature discharge of the second spark. Once a workable position was obtained by trial and error, a great number of runs could be executed before readjustment was required.

We now have a means of obtaining two superimposed shadowgrams of the wake region separated by about a millisecond. After correction for small errors in superimposition the distances through which the gas stream has advanced in the preselected time interval can be measured using the interfaces between hot and cold gas pockets as markers at various points in the wake region. As the preselected delays between exposures are known, it is possible to calculate the instantaneous magnitude and approximate direction of the velocity component perpendicular to the illuminating beam.

A closer inspection of the record obtained in Plage 4 gives an indication of some of the difficulties encountered in the analysis of
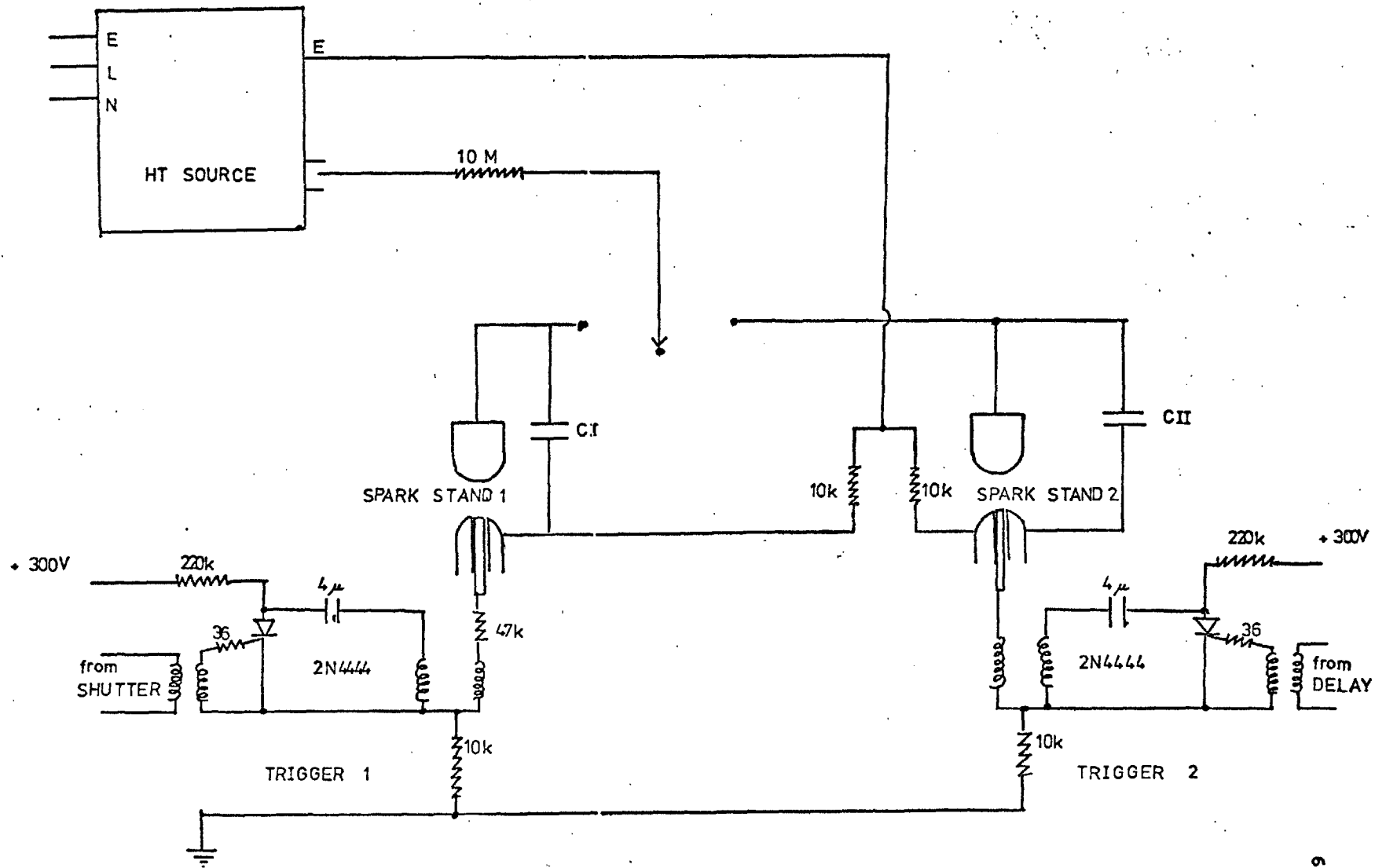
Fig. 4.8   ELECTRICAL CONNECTIONS TO SPARK STAND
-DOUBLE SPARK

PULSE WIDTH MONOSTABLES

+5V

+5V

0V

WIDTH

.1µ

22k
DELAY

470

1k

2N 3704

IN 4001

220k

3.0V

2.2k

2.2k

BEN 352

FIBRE OPTIC LINK
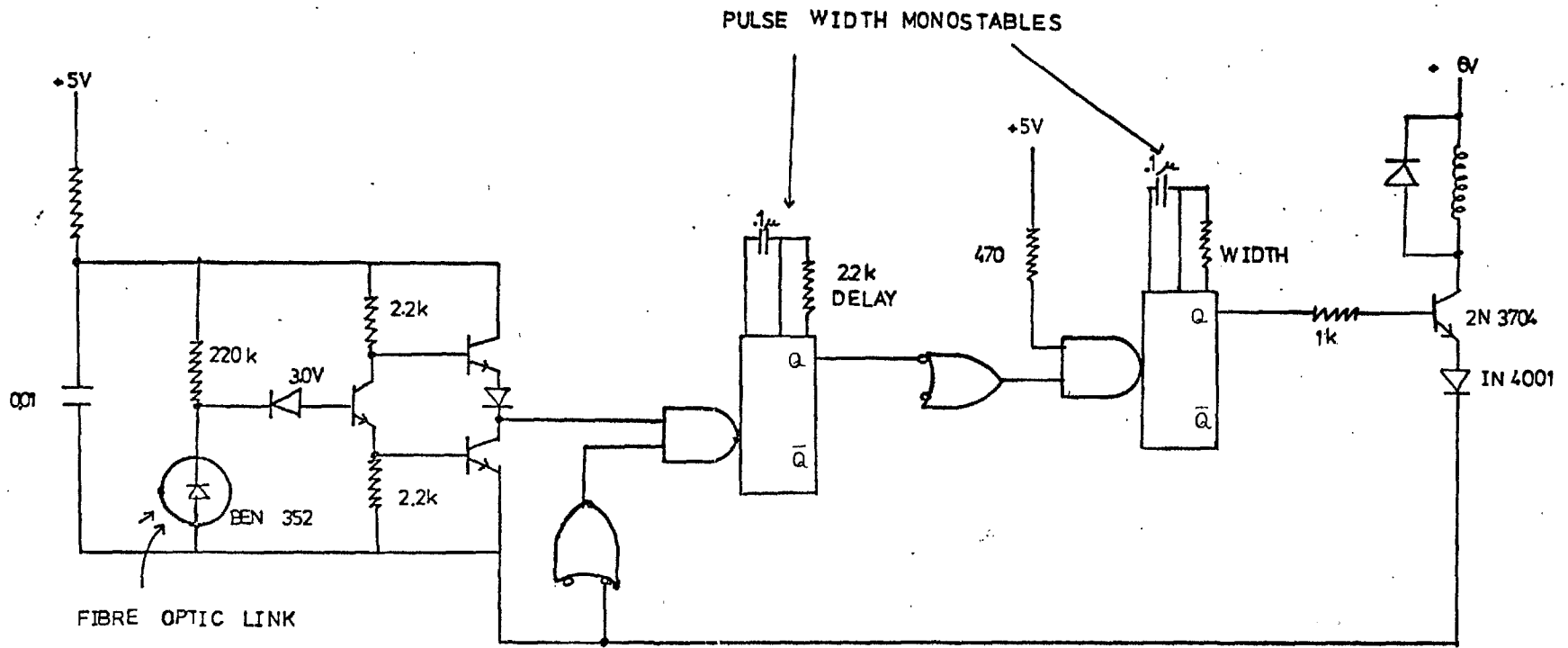
PHOTO CELL –   DELAY –   TRIGGER –

CIRCUITS

Fig. 4.9   VARIABLE DELAY AND TRIGGER CIRCUIT FOR DOUBLE
SPARK

these velocities. First it is necessary to have arranged for the
interfaces used as markers to have moved a distance within approxi-
mately critical limits of 1-3 mm between consecutive exposures.
A smaller separation gives no clear double marking but rather a
smudging of the otherwise clean lines. Too large a separation causes
two difficulties. A second marking due to a lower interface may be
too close to the first marking of a higher boundary. This causes
confusion between first and second markings due to different pockets
of gases. Pockets of gas can also be observed to change shape
drastically on moving a relatively short distance. This is confirmed
by cine records described in the next chapter. It is therefore often
difficult to decide whether a pair of markings closely spaced but of
different shape is actually a result of the same interface displaced
and transformed in the set time interval, or two entirely separate
pockets of gas. These problems are especially acute in the region of
high density of schlieren near the nozzle exit and along the axis of
the wake.

In an attempt to overcome this problem two different gases were
used in the spark gaps. One was again argon, the other a 3:1 helium
neon mixture. The later made a precise spark gap and voltage adjust-
ment essential in order to prevent familiar continuous neon discharge.
Because of the different emission spectra of the two gases differently
coloured sparks were to be expected. This was to give slightly different
colour markings due to the two sparks and simplify the analysis.
Surprisingly, the use of Polaroid Polarcolor film proved better for the
purpose of colour differentiation then either Kodak High Speed Ektachrome
or Agfa colour films. Even so, while the blue due to the argon discharge
is clear, the lines due to the neon spark are much weaker and only show

a very slight reddish tinge. This is probably partly due to the stronger emission of lines in the ultraviolet end of the spectrum at the higher temperatures predominant in the spark discharge, and the voltage limitations within which a distinct He-Ne spark could be produced.

The distribution of velocities varies at any particular instance for any one condition over the whole of the wake region by more than one order of magnitude. A delay between sparks suitable to give separations within the critical distance limits in one part of the wake region was therefore obviously not suitable in another. It was therefore necessary not only to vary the conditions in the plasma jet burner but also to produce records of different delays keeping all other factors constant in order to obtain just one value of velocity in all parts of the test region for any one condition. The wake region of the arc constitutes a turbulent flow system. A great number of readings are therefore required to obtain meaningful average values for its properties at any one point. Many hundreds of double exposure photographs would therefore have had to be taken and analyzed in order to give a distribution of mean flow velocities throughout the test region for any one set of arc conditions. This method has therefore been used to give an indication of the order of magnitudes of the velocities present only.

IV.3 High Speed Cinephotography

From the double exposure shadowgrams it is a logical extension to move on to high speed cinephotography. For this the spark light sources were replaced by a continuous 5 mW Spectra Physics Type 162 argon ion laser. It was chosen because it emits blue light. This made it possible

to use a relatively slow film even for the highest framing rates, giving higher contrast since the photographic emulsion is by far at its most sensitive in the blue region of the spectrum.

The laser beam was focused onto a pinhole after which it was allowed to expand. As in the case of spark photography, the two schlieren mirrors were placed to give a parallel beam in the test region (Fig. 4.10). The second mirror along with a short focal length lens placed beyond its focus were used to produce a shadow of the test region in the plane of the film in the camera. The lens of the camera had been removed and the laser beam allowed to fall directly onto the film, the aperture being fully open. The lens in the system was chosen and positioned such as to give a reduction of the image of the active test region down to a size that just filled the 16 mm frame of the film. The camera used was a Hitachi 16 mm High Speed Camera that provided a framing rate up to 10,000 frames per second. The camera speed was set near the upper limits of its framing rate. The film used was the Ilford Micro Neg. Pan Type 204, 16 mm, doubly perforated, cut into 100 ft lengths. Only the latter three-quarters of each film could, however, be analyzed, as the camera needed nearly 25 ft to build up to its working speed.

Cine shadow records were taken for different flow and arc rotation rates. These were repeated for various arc positions and voltage to current ratios. They were facilitated by choosing different positions for the cathode along the axis of symmetry of the burner as explained in Section III.1. The films show clearly the flow patterns in each part of the test region for the different cases. They also indicate the relative magnitudes and directions of velocities in various parts of the wake. These are discussed in detail in the next Chapter.
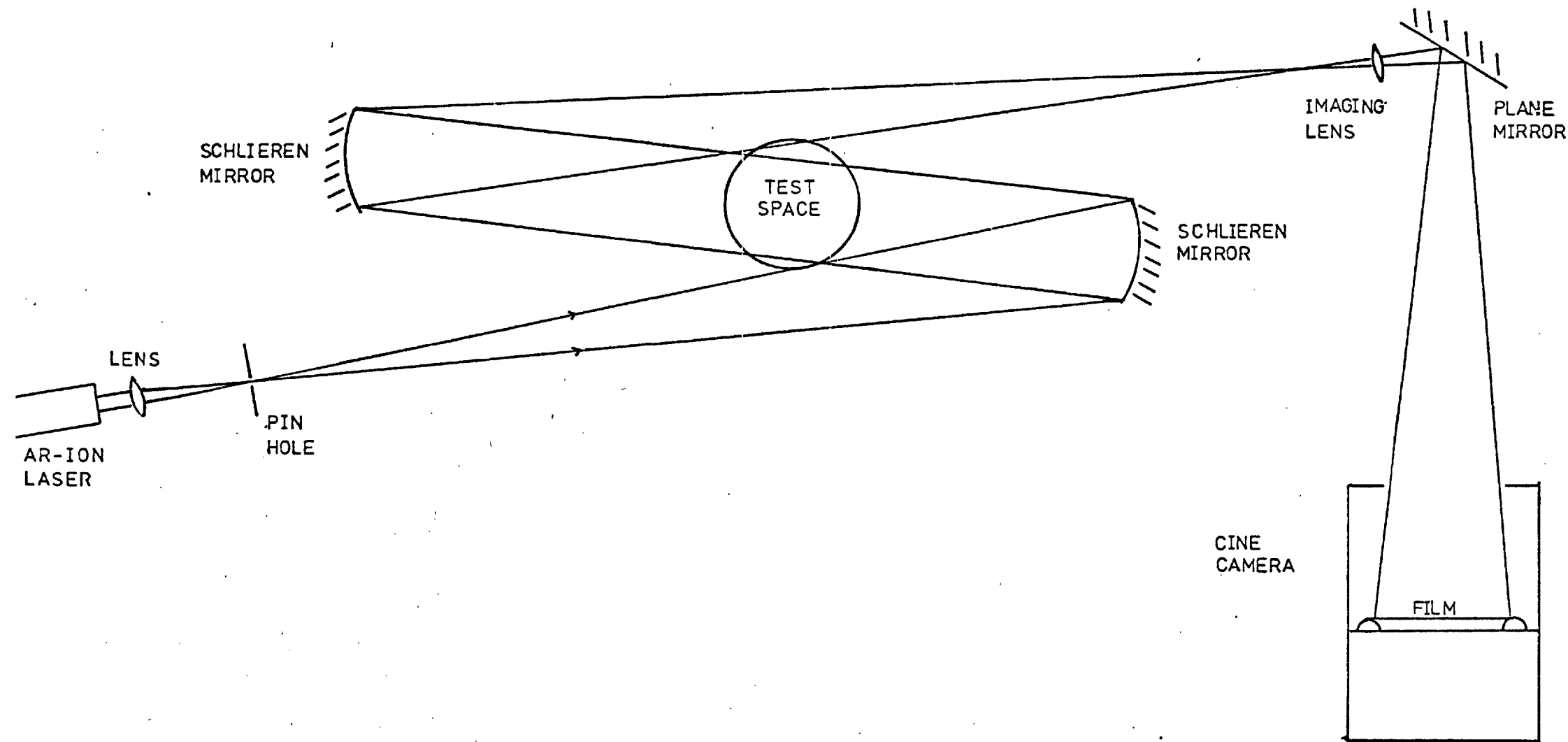
Fig. 4.10   OPTICAL ARRANGEMENT FOR SHADOWGRAM USED
IN HIGH SPEED CINEPHOTOGRAPHY

IV.4 Shock Waves as a Diagnostic Tool

The velocity of propagation of a shock front in a gaseous medium depends on the density of this medium and therefore its temperature and composition. As long as the temperature changes are considerable they have a greater effect than any variation in composition of the gas mixture (Ref. 38). It was hoped to make use of this phenomena to investigate the temperature distribution within the wake. To obtain a shock wave a spark stand was constructed similar to the ones used to produce the illuminating sparks (Fig. 4.1). The electrodes were connected across a 10 μF capacitor charged to 10 kV. The shock spark was triggered by opening the camera shutter via a small trigger electrode embedded in the earthed steel rod. The energy released in the spark created a shock wave emanating from the gap between the electrodes. Shock fronts of velocities of the order of Mach 1.4 were obtained using this technique. The optical set-up was precisely the same as for the wake region of the arc on its own. The new spark stand was placed next to the plasma jet burner with its electrodes pointing in the direction parallel to the beam in the test region. Its spark was triggered by the opening of the shutter. Two lengths of thread had small loops tied into one of their ends. Both loops were fitted loosely over one of the electrodes. The threads were pulled taut and their other two ends were tied to a vertical pole positioned on the opposite side of the test region such as to form an angle of approximately 60 degrees between the two fibres (Fig. 4.11). The intersection of their shadows extended beyond the loops provided a position for the axis of symmetry of the spark electrodes, and thus indicated the centre of the spherical shock wave. The illuminating spark was triggered by the radiation of the shock producing discharge via an optical fibre, a photodiode and a

STRING

VERTICAL
SUPPORT

LASER BEAM

IN TEST SPACE

ELECTRODE,

SPARK STAND
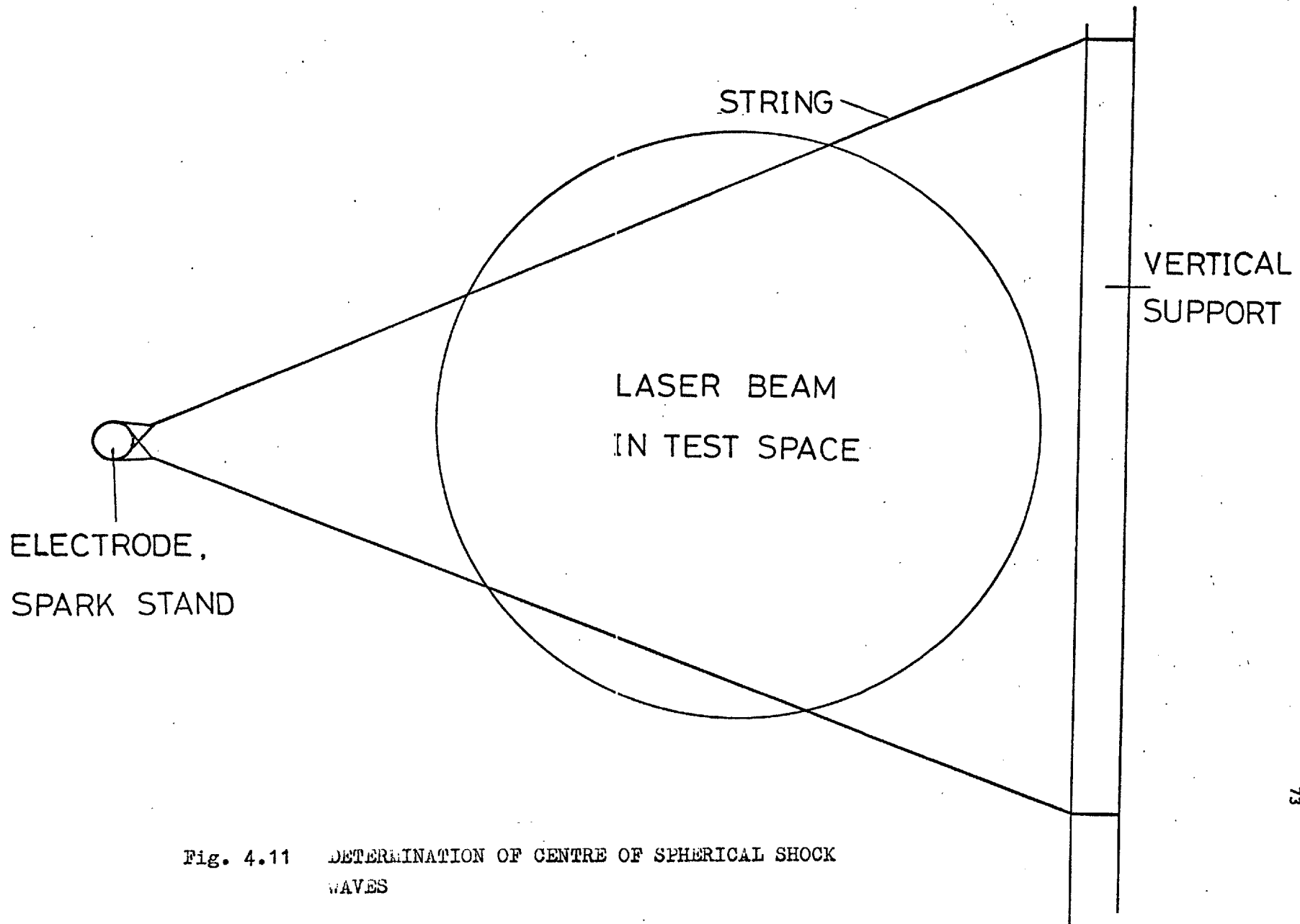
Fig. 4.11   DETERMINATION OF CENTRE OF SPHERICAL SHOCK
             WAVES

variable delay as in the case of the double exposure photography. (Fig.4.12)

By varying the delay the progress of the shock wave in the test region could be monitored in successive shots and a comparison of distance moved during different delay times gave an indication of the shock velocities. The reproducibility of these measurements was found to be quite good. The system could have been expanded to give two or more successive exposures of the same shock wave using a similar technique to that used for the double exposure wake studies. Shock velocities measured by these multiple sparks would not have suffered from errors that might have been introduced by any non-exactness of the reproducibility of the shock strength.

Records were taken of the shock front moving towards the wake and passing into it. The variation of distances moved by different parts of the shock wave was comparatively small as can be seen in the records shown at the end of Chapter V.5. Additional reasons why this method was not developed further are also discussed there.
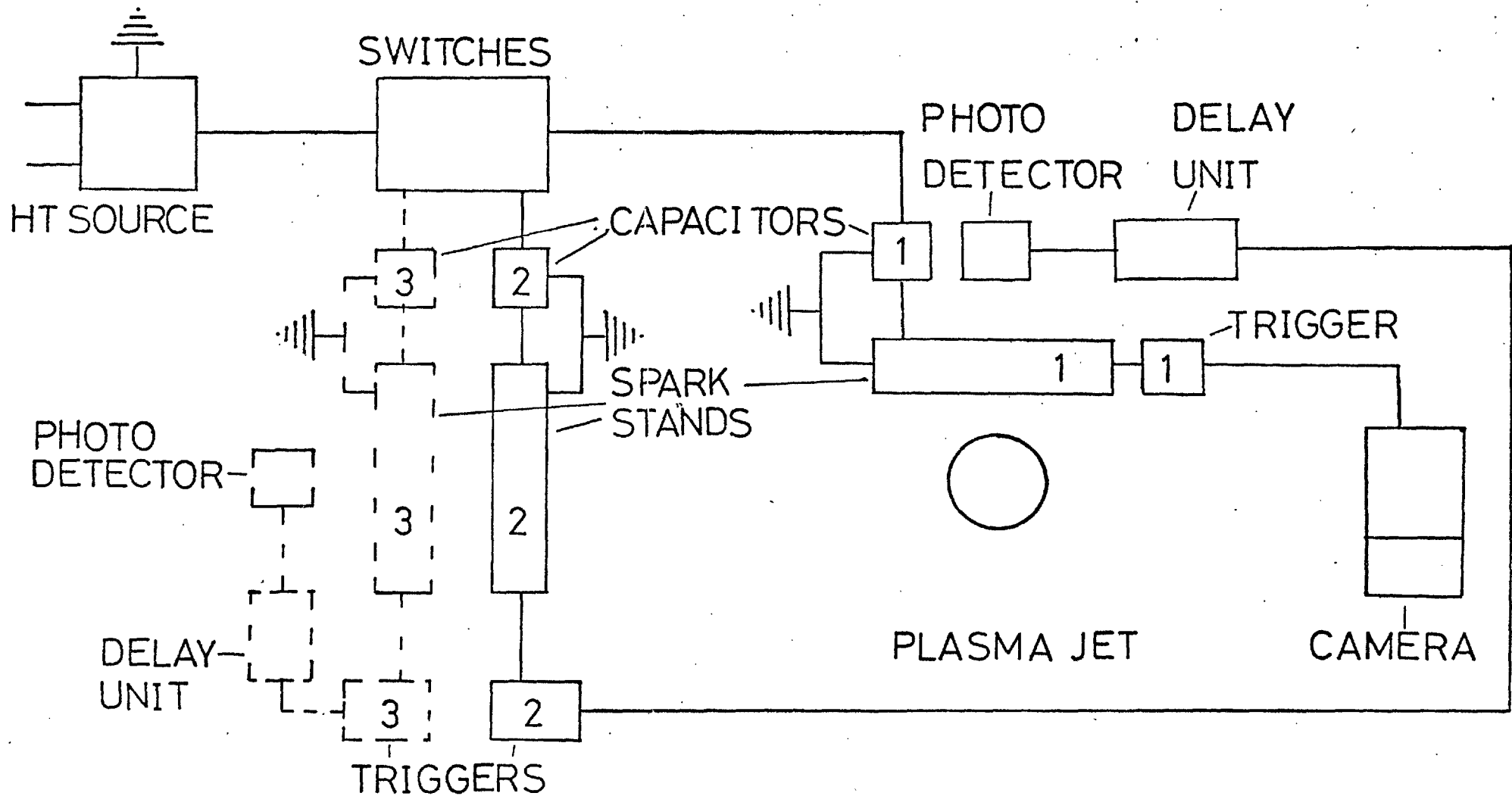
Fig. 4.12   CONNECTIONS TO SPARK STAND (SCHEMATIC)
                 – SHOCK FRONT

Chapter V

SHADOW AND SCHLIEREN RESULTS

This chapter considers some of the photographic records obtained by the use of the short duration spark photography with single and double exposures and the high speed cinephotography as described in Chapter IV.

V.1 Single Exposure Shadowgrams

Plate 4 shows an example of a shadowgram - exposure time a few microseconds - of the wake region of the arc. The optical system and the light source used are described in Section IV.1. The circular field of view was limited by the size of the schlieren mirrors. The strip shadow on the right was cast by a vertical brass scale slotted in 5 mm intervals. The nozzle shadow is clearly visible as are the inlet and outlet pipes for the water cooling of the anode. The bright brush immediately above the nozzle resulted from the radiation emitted by the rotating plasma, extended past the upper nozzle rim by the carrier gas flow. This flow expands after passing through the arc and forms a V-shaped wake region whose boundaries become less distinct with increasing height above the nozzle. The magnification of this particular record is 2:5.

As discussed in Chapter IV each of the lines in the shadowgram of the gaseous region represents a nonzero second order differential of the refractive index with respect to distance perpendicular to it. Every bright line on the record has a less easily distinguishable dark band associated with it. These markings represent boundaries formed by steep changes in refractive index and indicate how the boundaries between

the pockets of hot gas, predominantly argon, and those of the colder

gas, consisting mainly of air, are distributed throughout the wake.

Although the gases present in the test region are not only at different

temperatures, but also of different types - namely argon and air - adjacent

layers of different gases of the same temperatures could not be expected

to yield the distinct lines observed in Plate 4. This was confirmed in

a control experiment in which the shadow of an argon jet entering the

open atmosphere without the plasma was observed under equal optical

conditions. As mentioned previously, the viewing plane was chosen less

than 2 cm past the position of the image of the test region, and the

markings correspond therefore closely to the relative interface positions

in the test region. The complex structure of fine lines that makes up

the wake suggests that this region consists of a great number of pockets

of gas of various sizes and densities, some containing a hot medium,

mostly argon, and others consisting mainly of cold air.

A closer inspection of the shadowgrams on Plates 4 and 5 indicates

that the complex line structure consists of two different areas. The

inner part of the cone, closer to the nozzle exit, seems to be made up

of a great number of very small pockets of gas. Many of these do not

seem to be closed volumes, but are randomly interlinked to form rugged

chains interspaced with surfaces dividing zones of different temperatures.

The appearance of chains could be due to overlapping pockets. The outer

layer of the cone and the entire wake region further downstream show a

different picture. Here the pockets of gas are much larger and fewer in

number and seem to be inclined to form closed volumes of more or less

constant gas conditions. The markings caused by the gas interfaces also

seem to be more distinct.

The complex irregular boundary structure immediately downstream of

the nozzle is probably due to a smaller scale of turbulence in that

region where hot gases predominate with the possibility of remains of the

10.2 l/min ARGON, 1.5 kHz

PLATE IV   SINGLE EXPOSURE SHADOWGRAM OF THE STRUCTURE IN THE
WAKE REGION OF THE MAGNETICALLY ROTATED PLASMA JET

arc channel still present. The likelihood of significant entrainment
of the surrounding air into this central core region appears from
observation discussed later to be small. The lines in this region are
found to be somewhat less well defined, which might be due to less
distinct boundaries between pockets of gases of different temperature
distributions. Additional fuzziness of the lines may have been caused
at least in part by the higher gas velocities that are present there.

The shadowgrams present a 2 dimensional record of a 3 dimensional
test region. It was therefore important to determine whether the mark-
ings obtained near the centre of the wake are actually those caused by
the integration of all the interactions of the hot to cold gas interfaces
with the beam along its entire length in the test region, or whether only
effects near the outside of the wake cone are recorded. As a different
pattern is observed near the centre of the shadowgram, corresponding to
the region immediately and vertically downstream of the plasma to that
in the surrounding layers it was concluded that the activities throughout
the wake region of the plasma jet are visible on the film.

V.1.1 Variation of Argon Flow Rate

The effects on the behaviour of the wake of the two easily variable
properties of the plasma jet, the flow rate of the carrier gas and the
rotation rate of the arc, were investigated. At first the arc rotation
rate was kept fixed at about 1300 Hz and the argon flow rate was raised
from 4.2 l/min in steps to 17.6 l/min (Plate 5). The most noticeable
result of this is the gradual appearance and growth of the "plasma
brush" as the increased carrier gas flow pushed the plasma out of the
nozzle. With increasing flowrate the inner zone containing the small
scale inhomogeneities is extended further downstream. The mean size of
gas pockets in the outer regions and further downstream is also found

1·3 kHz
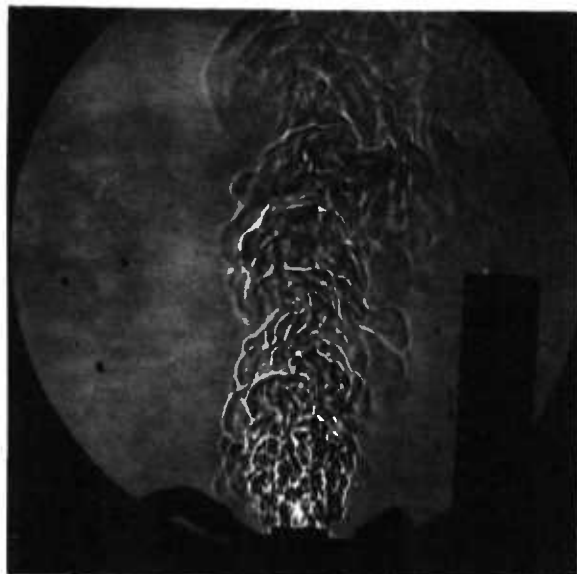
4·2 l/min
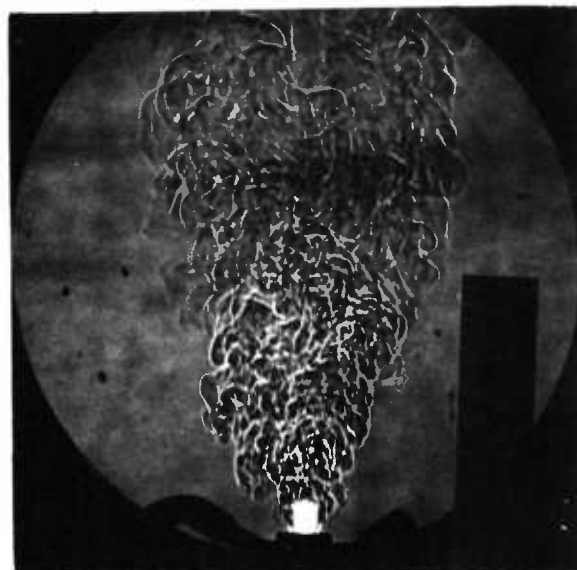
7·3 l/min
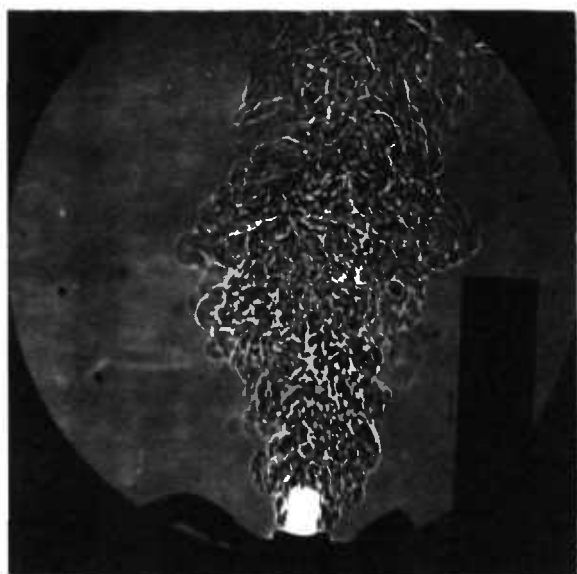
13·8 l/min
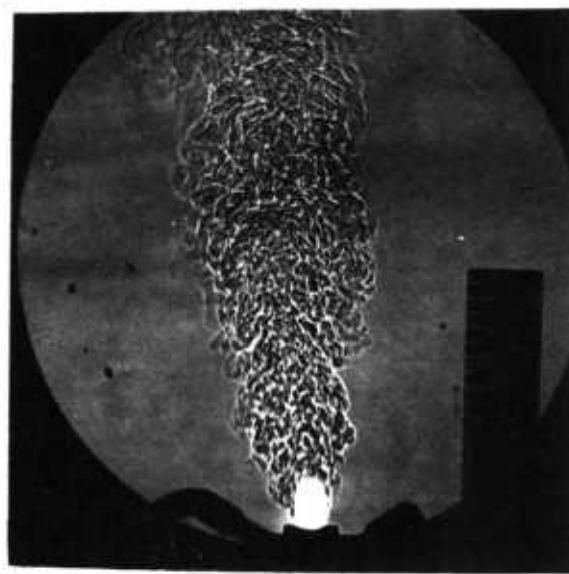
17·6 l/min

PLATE V   SHADOWGRAMS SHOWING THE CHANGES IN THE PLASMA JET
WAKE WITH INCREASING CARRIER GAS FLOW RATE AND
CONSTANT ARC ROTATION RATE

to be diminishing with increased gas flow while the number of inter-

faces and the intensity of their markings increases noticeably. This

indicates the presence further downstream of an increasing number of

pockets of gas at various temperatures and of sharper refractive index

gradient fluctuations most likely due to more abrupt temperature

changes between the various zones. The wake funnel is also noted to

have contracted with increasing argon supply at very high flow rates

(Plate 5) suggesting that entrainment is lower in the region of small

scale turbulence.

The heat losses to the plasma jet burner were monitored by recording

the flow rates and temperature rises of the cooling water. The heat

transfer rate from the arc to the gas increased with rising argon flow

rate, even though the radiative losses from the arc probably increased

because of the extended arc column length. The aerodynamic changes in

the wake region due to the greater relative velocity between the carrier

gas flow and the propagating arc are, however, at least partly masked by

the increased turbulence due to the increase in the cold flow Reynold's

number.

V.1.2. Variation of Arc Rotation Rate

To overcome this the argon flow rate was kept constant at 3.3 1/min

and the rotation rate increased from 0.8 KHz to 2 KHz by varying the

DC current in the magnetic coil from 0.8 amp to 2.5 amp. At these low

flow rates the two regions were clearly visible (Plate 6). Dealing

first with the upper part of the wake the changes in the propagation

rate of the arc appears to have little effect on that pattern. Number

density and size distribution of the pockets are relatively constant

throughout this series of shadowgrams. This, however, is not true for

the gas in the close vicinity of the plasma jet. In this region the

3·3 l/min ARGON
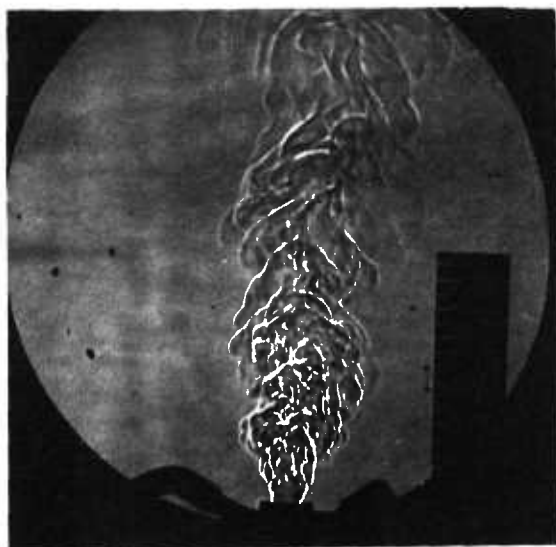
0·8 kHz
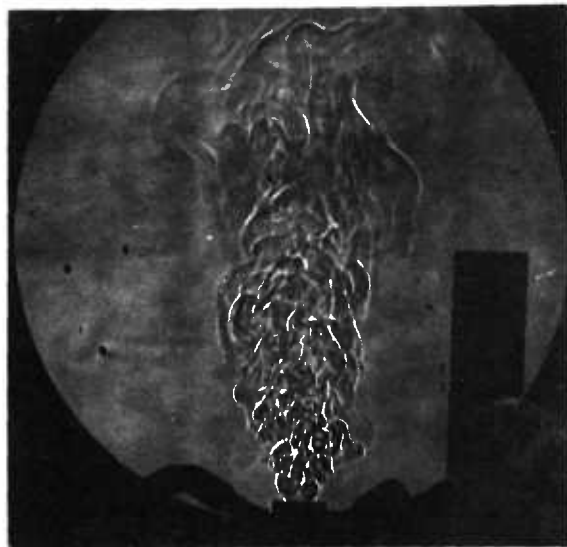
1·1 kHz

1·4 kHz
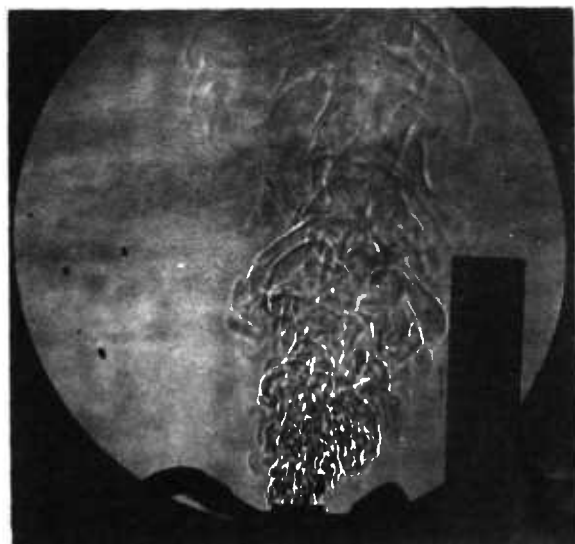
2·0 kHz

PLATE VI   SHADOWGRAMS SHOWING THE CHANGES IN THE PLASMA JET
            WAKE WITH INCREASING ARC ROTATION RATE AND CONSTANT
            CARRIER GAS FLOW RATE

number of gas pockets increases while their size decreases when the arc is allowed to rotate more quickly in the nozzle, suggesting a decrease in the scale of turbulence with frequency of arc rotation.

Comparing the effect of the variation of carrier gas flow and of the arc rotation rate indicates that the properties of the lower part of the wake region depend on both these variables. The distance that this zone extends in the downstream direction is proportional to the flow rate of the gas while the level of turbulence predominating increases with the arc rotation rate. It is this region that has its flow pattern governed by the solid stirrer-like behaviour of the rotating arc. Further downstream the flow seems independent of the activities in the nozzle, but is a function of the flow rate of the gas; a phenomena also observed by other workers investigating flow downstream of nozzles (Ref. 30).

V.2 Double Exposure Shadowgrams

In order to test the variation of the gas velocity with distance downstream, two exposures of shadowgrams separated by a known time interval were superimposed on each other. The precise optical set-up used to obtain this is described in Section IV.2. As the delay between the flashes is known, localized velocity components in any direction perpendicular to the beam can be determined. Plate 7 shows a series of double exposure photographs that was obtained by keeping the carrier gas flow rate and the arc rotation rate constant and increasing the delay between exposures after each separate shot. The double contrast edges near the top of the photographs show the motion of the second blind of the focal plane shutter, the width of the dark grey region being an indication of the time elapsed between first and second flash. The

108 l/min ARGON   1·7 kHz

1·0 msec

1·5 msec

2·5 msec

3·5 msec

PLATE VII   DOUBLE EXPOSURE SHADOWGRAMS WITH INCREASING DELAY
TIMES AND CONSTANT PLASMA JET CONDITIONS
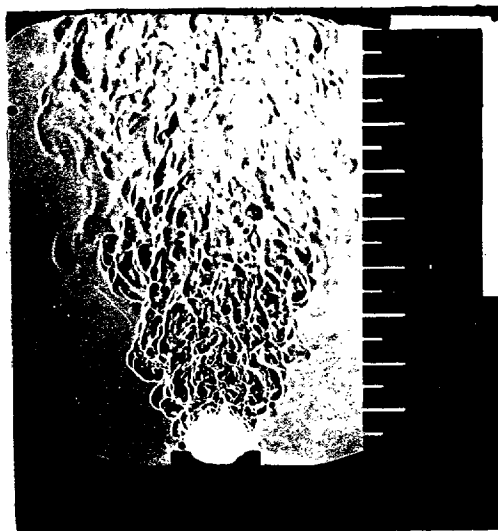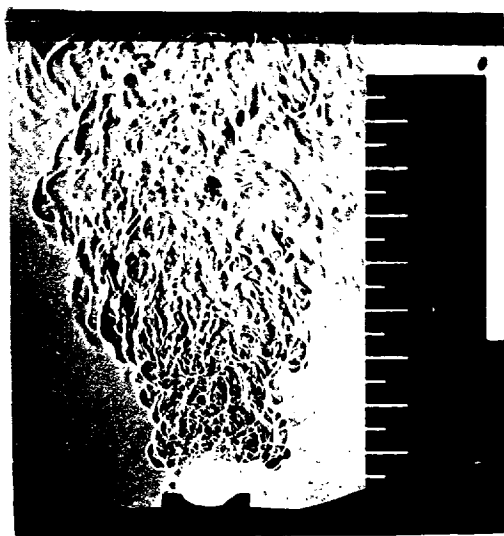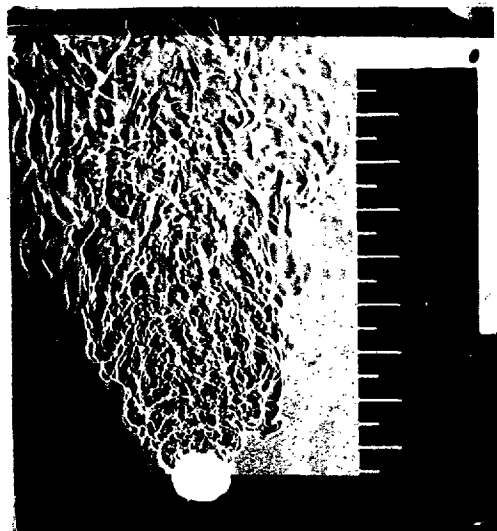
actual delay was measured by displaying the flash energies from the
sparks via two photocells on an oscilloscope, as previously discussed.
The interfaces between pockets of gases of different properties again
form bright lines on the emulsion and it is these that are used as
markers. The distance between lines resulting from successive exposures
is measured, allowing for the magnification of the optical system, and
divided by the time delay between sparks resulting in the instantaneous
local vertical components of velocity.

The double lines are only clearly discernible if the interfaces
have moved a distance within a definite range during the times between
exposures. The reason for this is discussed in section IV.2. As
increased time delays are considered, double lines therefore become
visible in regions of predominantly lower velocities. The shadow series
on plate 7 shows a shifting of the position of clearly noticeable double
lines in the downstream direction with increasing delay times. This
means that velocities decrease with distance downstream, a not entirely
unexpected result.

An opportunity to apply the optical system to a practical problem
presented itself soon after it was set up. In a parallel investigation
(Ref. 8) a nozzle was developed to fit a cylindrical quartz reactor
onto the top of the plasma jet orifice. The nozzle angles were chosen
specifically to result in the best possible mixedness of the emerging
gas stream. Plate 8 shows a comparison of the flow pattern with and
without the nozzle, the argon flow rate and the arc rotation rate
having been kept constant. The flow with the nozzle in place clearly
consists of larger pockets of gas indicating less turbulence and a more
uniform regime past the mouth of the water-cooled steel cone than without.
As not only the plasma jet conditions, but also the delay separating the
two sparks, was kept unaltered between the two exposures, the distribution

14 l/min ARGON

1 kHz
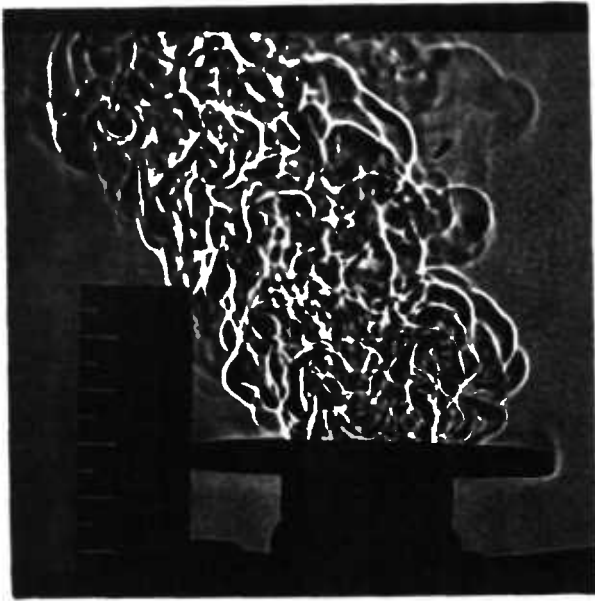
WITH NOZZLE
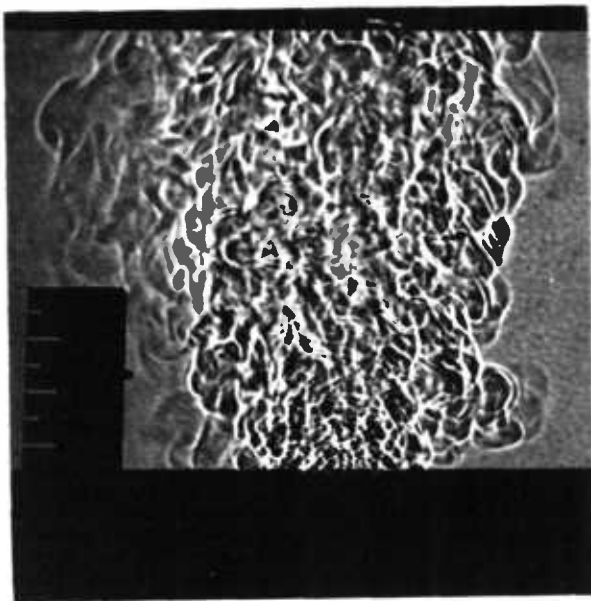
WITHOUT NOZZLE

PLATE VIII   SHADOWGRAMS SHOWING A COMPARISON BETWEEN PLASMA
JET WAKES WITH AND WITHOUT ATTACHED NOZZLE

of double lines gives some information about the velocity distribution. The fact that the dual markings are only visible in the lower part of the wake with the nozzle in place, while they are clearly discernible throughout the test region for an uncovered jet, suggests a much more rapid velocity decay in the directed flow.

It is not always possible by mere inspection of the records to determine the directions of flow as it cannot always be decided which of the two markings has been caused by the first and which by the second spark. This presents special difficulties in the case of horizontal displacements near the boundaries of the wake, where recirculation is to be expected. As mentioned in Chapter IV, an attempt was made to overcome this problem by "colouring" one of the light sources using neon as a spark gas. This only produced a faintly reddish tinge which is only just discernible on Polaroid Polarcolour film, less well on High Speed Ektachrome and not at all on Agfa Colour cut film. Polarcolour film, however, was found to be too slow to give intense markings, especially in view of the reduced light output from the neon spark. Its contrast properties are also much weaker than those of the polaroid Type 51 film that was used for the black and white records. These two facts resulted in rather smudged records. Plate 14 shows an exposure from an argon spark followed by a neon spark produced on High Speed Ektachrome. The blue and red region at the top and bottom of the record indicate the position of the shutter when the individual sparks were fired. The markings are considerably less well defined than those for the black and white records (Plate 4).
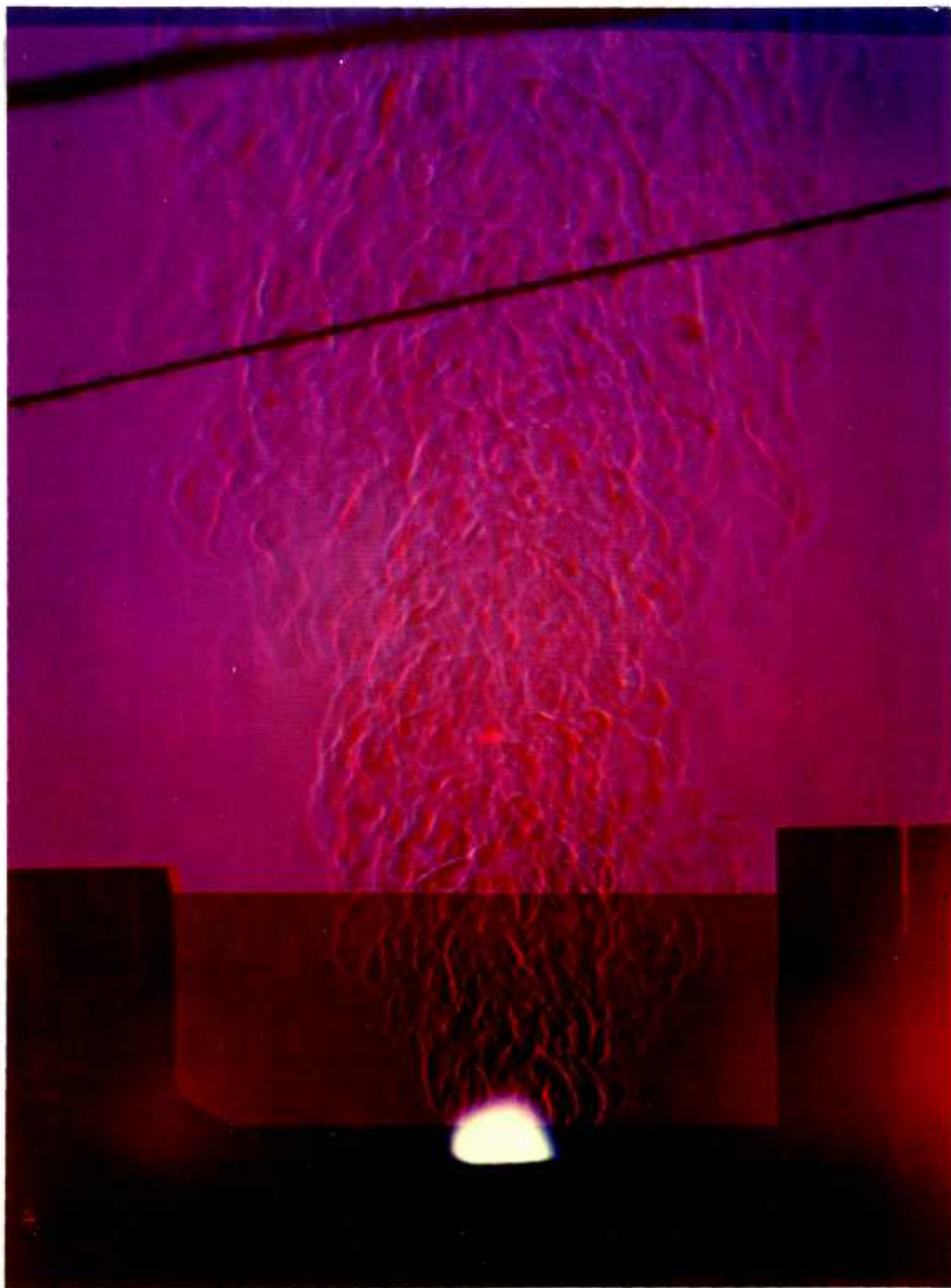
Plate XIV   DOUBLE EXPOSURE SHADOWGRAM USING BLUE
             AND RED SPARKS.

V.3 Instantaneous Schlieren Records

Plate 9 shows three schlieren records. The first one, reduced

in magnification by a factor of roughly two, was produced by placing

a horizontal knife edge at the horizontal focus as described in

Section IV.1.2. The lower two of approximately unit magnification

had their circular schlieren stop placed at the focal disc halfway

between the vertical and horizontal focal lines. All three records

are dark field schlieren. It is clear from the results obtained that

because of the non-point focus due to the aberrations, no uniform dark

field was obtainable, and that especially in the case of the circular

stop the sensitivity of the system varied with position across the test

region. This was because rays deflected through equal angles ended up

absorbed by the schlieren stop or not, depending on their position of

origin. The schlieren markings are also wider and less well defined

than those of the shadowgrams. As schlieren markings correspond to

refractive index gradients this indicates that the gas pockets do not

entirely consist of gas of uniform refractive index and therefore

density, but their properties change gradually near the limits of the

gas pockets. At the boundaries themselves these changes suddenly

become abrupt, resulting in the distinctive markings seen on the shadow

records which correspond to variations in refractive index gradients.

To re-emphasise this, it can be seen that pocket boundaries only are

visible on the schlieren photographs in regions of low sensitivity.

14 l/min ARGON   1.3 kHz

HORIZONTAL   STOP

CIRCULAR   STOP

PLATE IX   SCHLIEREN RECORDS OBTAINED USING DIFFERENT SCHLIEREN
              STOPS
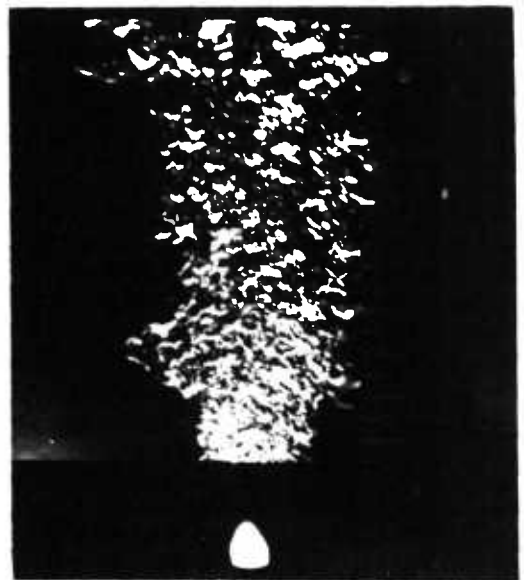
V.4. <u>High Speed Cine Records</u>

Plates 10 and 11 show prints of some consecutive frames of 16 mm

high speed cine records obtained at a framing rate of approximately

10,000 frames per second of the moving shadows produced by the plasma

jet wake. The shadowgram in each frame, while not as distinct as

those produced by the instantaneous spark photography, is clearly

legible everywhere except in the region immediately downstream of the

nozzle, where velocities are too high even for this camera. Film

records were obtained for different flow and rotation rates and were

viewed on a Specto Motion Analyser which permitted the films to be

projected at 16 or 2 frames/second or frame by frame.

The cine records enable the two separate zones of the wake to be

distinguished even more clearly than the short duration stills. The

flow immediately following the nozzle exit is seen to be very fast and

in the case of high carrier gas throughput rates the motion could not

be completely frozen. This region appears very stable in orientation

to external disturbances. A fairly rapid transition from this flow

regime to the much slower outer and downstream flows, is observed.

In the outer sections the flow velocities are considerably slower.

In the centre of the wake cone far downstream, large pockets of gas

move in an overall upward direction but with a considerable random

velocity component superimposed. Near the outside of the wake a number

of moving, recirculating eddies are observed. The regressive velocities

in these eddies are in general slower than the typical upward velocity

in those regions. The flow patterns in the slower-moving areas are far

more susceptible to outside influences like draughts. The entire plasma

jet was therefore screened off as far as possible from the remainder of

the laboratory for the quantitative measurements to be described in

Chapter VII. The screens were placed a distance of more than a foot

10.5 l/min ARGON   12 kHz

PLATE X   HIGH-SPEED CINÉ RECORDS (10 000 FRAMES/SEC.) OF THE
PLASMA JET WAKE REGION

42 l/min ARGON   1·2kHz

PLATE XI   HIGH-SPEED CINÉ RECORDS (10 000 FRAMES/SEC.) OF THE
PLASMA JET WAKE REGION
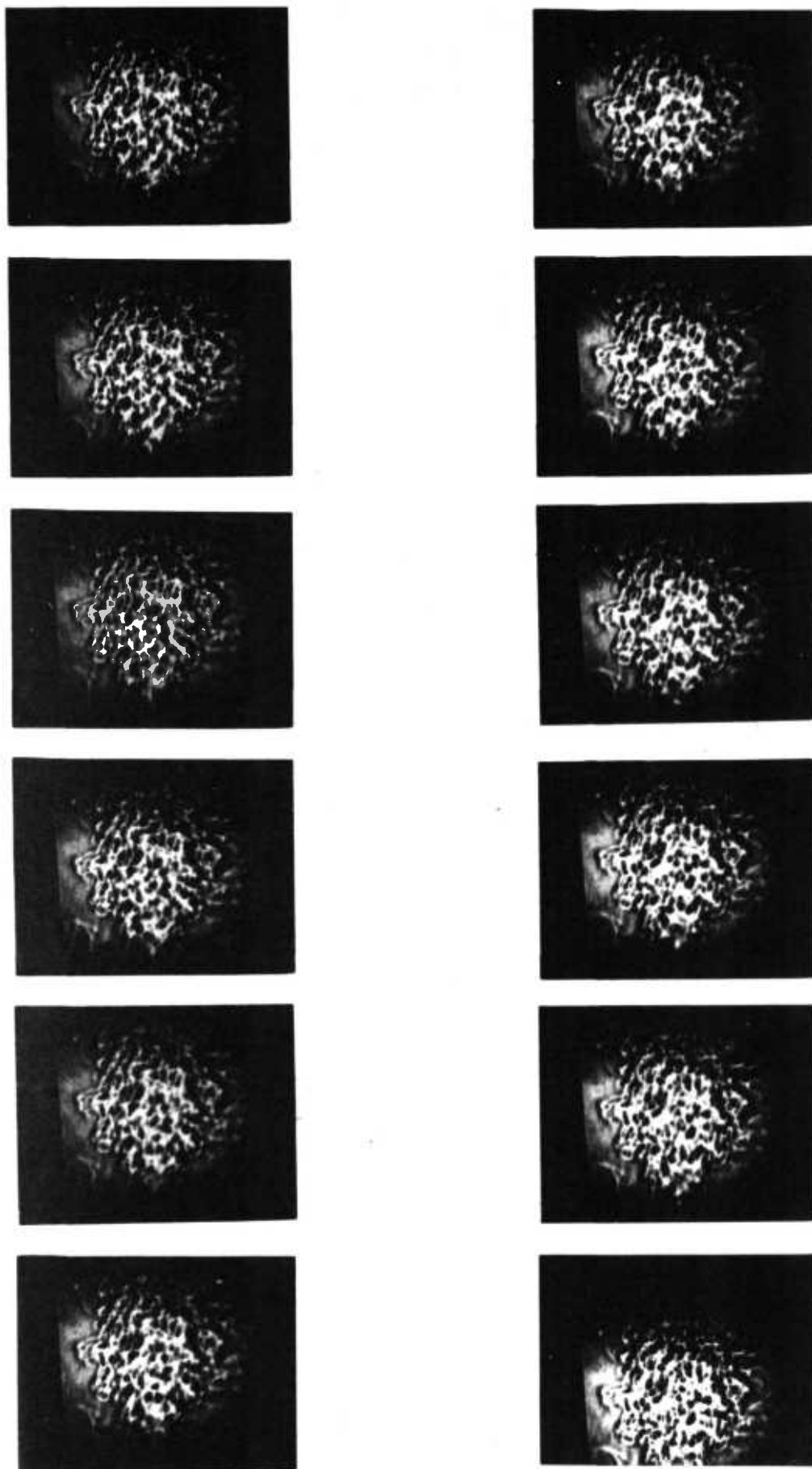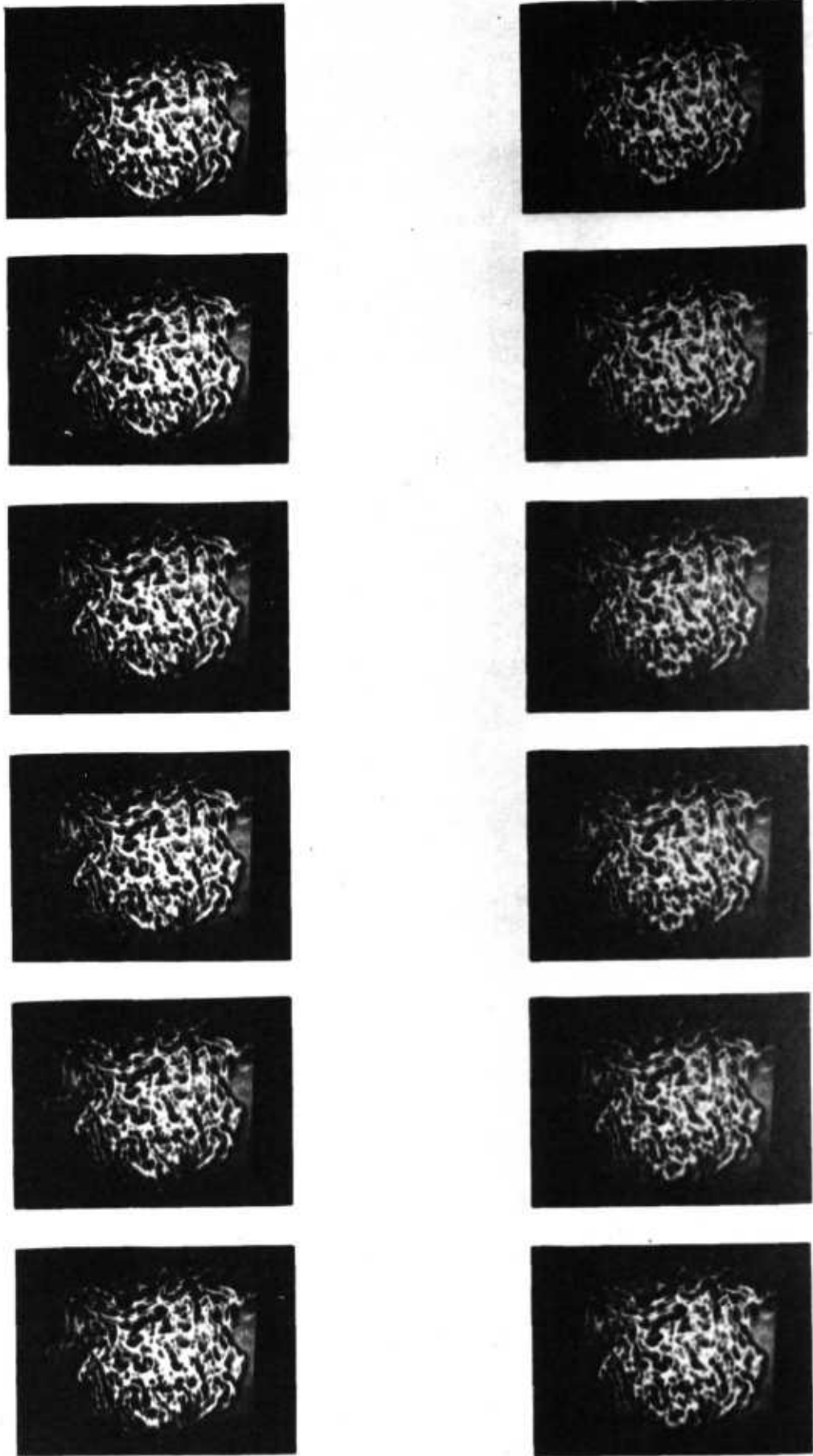
from the plasma jet burner.

As the velocity increases with decreasing distance from the axis of symmetry of the cone throughout the test region it is reconfirmed that the film received records from the entire beam integrated right through the wake region.

If the cathode is positioned such that its tip is in line with the exit edge of the anode and the arc allowed to rotate entirely on top of the nozzle mouth rather than with it, the inner fast-moving flow regime disappears completely. The entire wake region then consists of large, relatively slow-moving gas pockets. These have considerable, rapidly fluctuating horizontal velocity components and no clear conical wake shapes are therefore obtained. The erratic movement of the arc under these conditions contributes significantly to this behaviour. Anode corrosion becomes an important factor with this electrode arrangement probably due to the entrainment of air into the arc path. Good photographic records were difficult to obtain because of the large amount of radiation from the arc now completely exposed to the plates.

In past investigations it has been observed that the presence of oxygen, and to some extent nitrogen, leads to fluctuating arc behaviour and considerable electrode corrosion. The coincidence therefore of the existence of a fast inner region with a smooth arc rotation for the lower cathode position, and the absence of that central region in the case of the erratic arc motion with the protruding cathode, suggests the presence of entrained air near the arc only in the absence of the fast-flowing central region. This confirms the visual observation from the cine records that little entrainment takes place into this fast-flowing regime. What entrainment there is - a not inconsiderable amount, as discussed in Chapter IX - seems to occur in the outer layers of the wake cone.

V.5 Shock Front - Wake Interactions

Plate 12 shows a shock front approaching and entering the wake

of the magnetically rotated plasma jet obtained with the equipment

described in section IV.4. The intersecting line shadows indicate

the position of the spark that produced the shock wave. As the shock

front enters and passes through part of the wake, it changes slightly

from its spherical shape due to the random encounter of gas pockets

of varying temperatures. As the shock wave moves towards the centre

of the wake cone its records become obscured by the markings from

the refractive index gradients in the wake and it is no longer possible

to distinguish them from the complex overall pattern in that region.

Although it might have been possible to improve this by the use of

stronger shocks, meaningful measurements would still have been confined

to the outer layers of the wake. Velocity changes were also found to

be relatively small. (Temperatures experienced in the wake are relatively

low compared to those in the arc, where this method has been used in the

past (Ref. 38)). The problem is compounded by the fact that the change

in shock velocities due to varying temperatures would have had to be

integrated along the path of the shock, unless a method of determining

instantaneous shock front velocities (e.g. Laser Doppler velocimetry)

was to be used. A great number of shock speed measurements would have

been necessary to obtain the statistically significant number of

readings required by the turbulent and complex flows in this region.

A more suitable method making use of the markers conveniently supplied

by the gas interfaces was therefore developed to obtain a quantitative

analysis of the localized physical properties throughout the wake region,

as discussed in Chapter VII.

Chapter VI

PROBE MEASUREMENTS

In Chapter IV it is shown how a method was developed for determining the general shape of the wake region and its fine structure. The order of magnitude of velocities encountered in that region could also be estimated as well as the general flow pattern of the hot gases emerging from the plasma jet, all as a function of the arc conditions. We still, however, require an estimate of the homogeneity of the gas at various reference points in the wake region. For this a probe that had been developed in these laboratories and which is described later in this chapter, proved very useful.

As mentioned in Chapter II, the use of probes presents two main areas of difficulty: those present even in laminar flow conditions and those introduced by the turbulent flow of nonuniformly heated gas. The former includes the disturbance caused by the mere presence of the probe in the regime that is to be measured. Heat losses can be expected to be present, due to the radiation from solid surfaces of the probe as well as to conduction along its leads. In the absence of chemical reactions, solid probes would have acted to encourage only the recombination of ionized argon or the reassociation of possibly entrained, dissociated air. This was expected to have caused concern only in the area close to the nozzle.

Secondly, most probes require a finite time to adjust to changes in conditions. Thermocouples, for instance, can only record the temperatures of their surrounding gas correctly if their junctions are allowed to reach thermal equilibrium with these gases. They could not, therefore, have followed the rapid fluctuations present in this system. Allowing them to record 'average' values would not only have lost

information about the turbulence of the flow but also have produced

incorrect values as discussed in Chapter II. The interference

problems could not be completely overcome even with the corona probe,

although, as will be seen later, careful design helped to minimize

the inaccuracies introduced due to changes in flow pattern and

correct use resulted in no recombination of ionized gases on the probe.

VI.1 The Corona Probe - Method

The problem that results from the rapid fluctuations can be

eliminated completely by arranging for the gas whose properties are to

be measured to act as the thermometer itself. The probe that was

developed to do just this makes use of the physical properties of the

corona discharge (Ref. 8). When a conductor charged to a high potential

has at some point on its surface a much increased radius of curvature,

a discharge will occur at that point. Once the potential of the

conductor is fixed the magnitude of the discharge, as expressed by the

current through the conductor, varies inversely as the density of the

surrounding gas (Ref. 31) and thus directly as its temperature for a

fixed composition of the gaseous medium. The temperature of the

conductor has no influence on the discharge.

The probe itself consisted of two platinum wires, covered by quartz

tubing except at the tips, mounted on a calibrated rack and pinion

arrangement, mobile in a plane containing a central vertical cross-

section of the plasma jet wake. One wire had a pointed end while the

other was spherical (Fig. 6.1). The point and the sphere were separated

by about 8 mm. The two wires were part of a circuit made up of a Hewlett

Packard HP Harrison 6516A HT source, set fo 2 kV and a 10 MΩ resistor as

shown in Figure 6.1. The HT applied across the tips of the probe caused
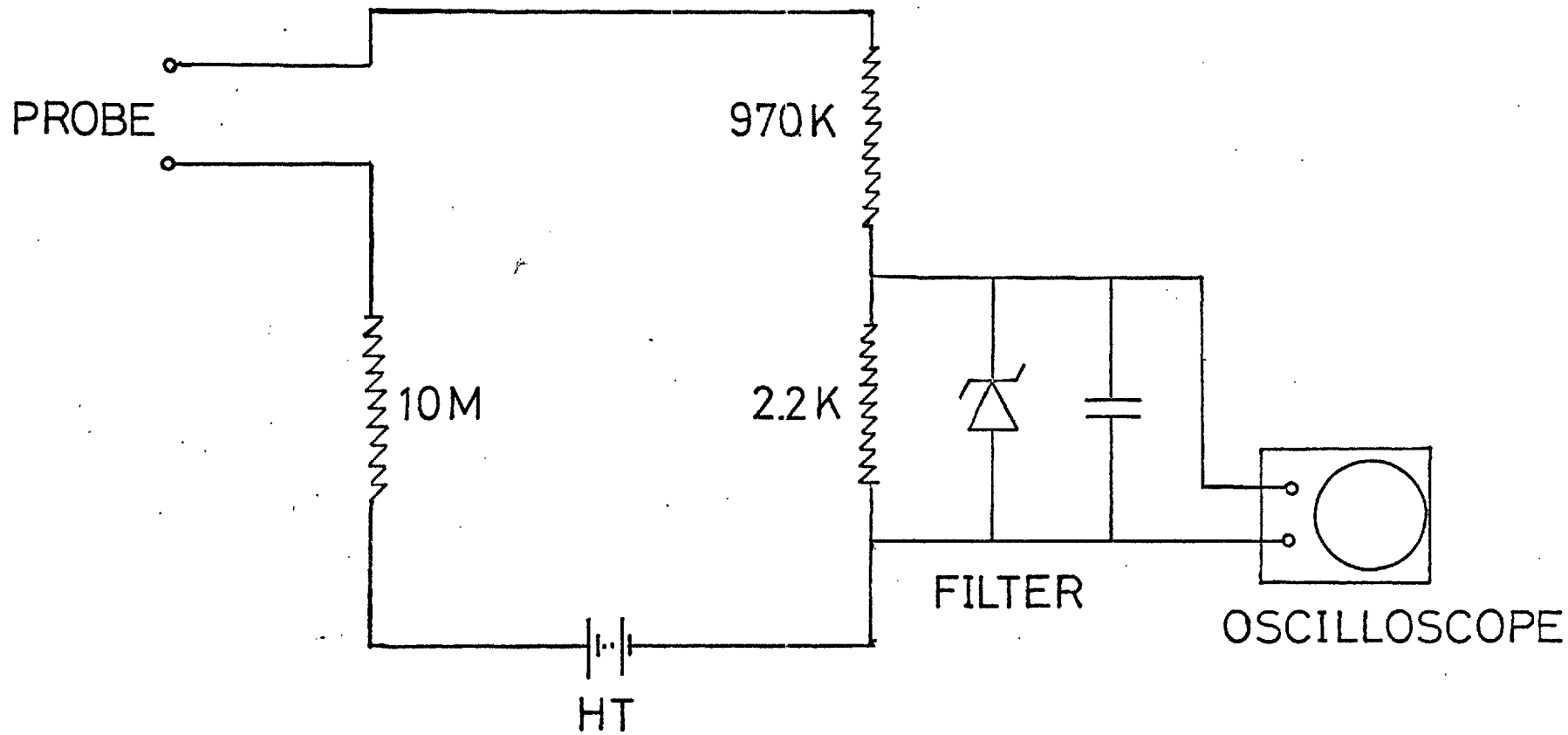
Fig. 6.1   CORONA PROBE AND CIRCUIT (SCHEMATIC)

a corona discharge to occur at the pointed electrode. Electrons emitted there were collected by the positively charged sphere allowing a current to flow in the circuit. The amount of charge emitted from the tip, and therefore the current across the 10 MΩ resistor, was a function of the condition of the gas at the probe point. The voltage across the resistor was monitored on an oscilloscope via a HF filter. The filter protected the oscilloscope from possible HT voltage surges. As conditions at the tip varied, so did the current in the circuit and the voltage displayed on the cathode ray screen. Once a given HT voltage was applied the discharge and therefore the recorded voltage were dependent on the conditions prevailing in small volume immediately surrounding the tip.

For a perfectly mixed homogeneous gas stream there would be no fluctuations in voltage, so that a straight line would appear on the oscilloscope, DC levels of which are related to the type, composition and temperature of the gas or gas mixture. As soon as pockets of gas with different properties pass the probe, however, a varying signal is displayed. The number, size, velocity and extent of the differences in properties between these pockets are reflected in the frequencies and amplitudes of the fluctuations. The degree of variation is thus an indication of the mixedness of the system. The smaller the variations, the better the system is mixed.

The difference between conditions near the nozzle where a large number of very small fast-moving, very hot pockets produced a rapidly varying signal, and conditions near the upper boundaries of the wake - where a relatively small number of large pockets passed the probe less rapidly giving a slowly changing signal - is quite clear even on a casual observation of instantaneous records of the oscilloscope screen. Analysis of more similar sets of conditions of points closer together

however, requires a quantification of the output variation of the probe. As the extent of the mixedness of the gas stream is related to the voltage fluctuations, it is these, rather than absolute DC levels, that one is primarily interested in. In order to take account of the number of deflections, their shapes and amplitude, it was decided to use the root mean square (RMS) values of the AC component of the signal as an expression of mixedness. In practice a DISA Type 55D35 Root Mean Square Voltmeter was connected across the probe output. The meter disregarded the DC output and computed the RMS value of the AC part of the output only. These in turn were recorded on a chart recorder. The longest possible integration time was chosen over which the values were determined by the meter, in order to give the best possible mean values at any one point. These values as recorded by the chart recorder were averaged again manually from the fluctuations of the trace at each point. The readings were taken with the probe tip at various positions, spaced uniformly throughout a vertical cross-section through the axis of the wake region. The values obtained were mapped out and points of equal RMS values were joined together. The resulting lines correspond to regions of equal mixedness in the wake.

The probe as used in previous investigations in these laboratories is shown in Figure 6.2. Here both wires were introduced parallel from one side of the cross-section of the wake. Preliminary investigations (Ref. 8) showed that the precise orientation of the probe, whether tip and sphere were next to each other or one above the other, is not critical. This arrangement, however, caused several problems, resulting in a seemingly unsymmetric wake as discussed in the next section. Changing the probe into a pincer type shape (Fig. 6.3) reduced these errors and resulted in the expected symmetry about the vertical axis.

The probe measures the quantity of charge emitted from the point

QUARTZ

TUFNOL

PLATINUM
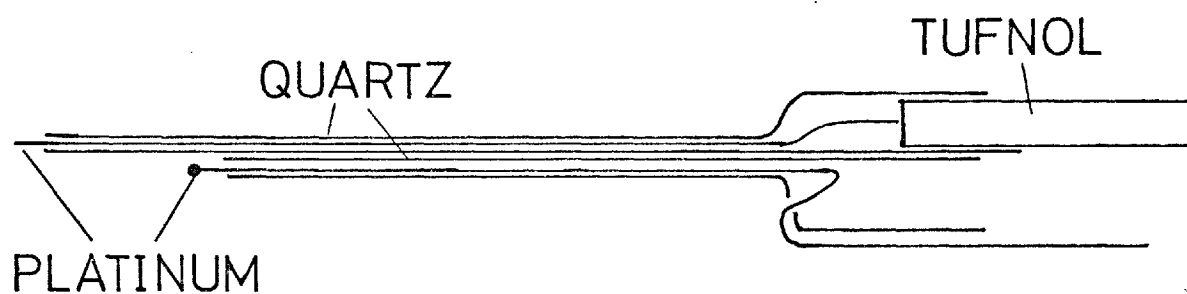
Fig. 6.2　CORONA PROBE (OROGINAL DESIGN)

STEEL　　PLATINUM　　^
　　　　　　　　　　　9mm
　　　　　　　　　　　v

REFRASIL SLEEVING
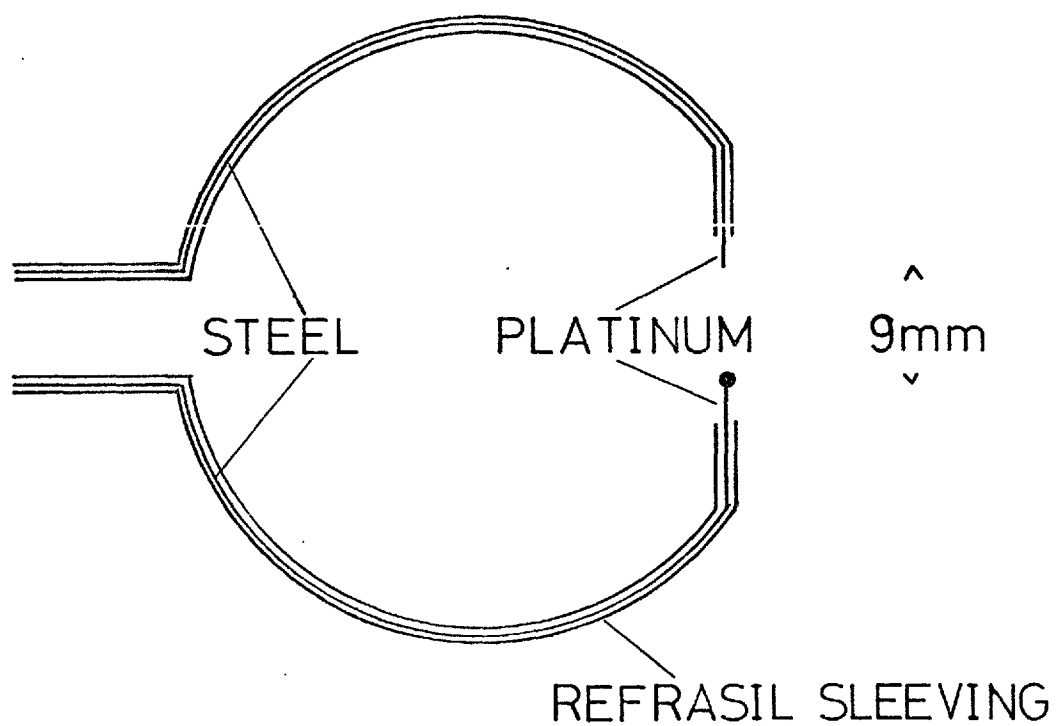
Fig. 6.3　CORONA PROBE (PINCER TYPE DESIGN)

and collected by the sphere. It was therefore important to ensure that there were no free changes from any source other than the tip present in the region of measurement or near the sphere, that could be absorbed by the probe. The probe could therefore not be used in the immediate vicinity of the arc. Only some way downstream, where temperatures were lower and charged species had a chance to recombine, are the probe results meaningful. In practice, the boundaries of the regions of useful results were obtained by temporarily switching off the HT supply when taking measurements relatively close to the arc. Unless the oscilloscope displayed a straight line, charged species or electrons were being collected by the probe from the arc, rendering that point unsuitable for measurement. In the presentation of results the region below which no valid results were obtainable is shown as a dotted line.

VI.2.   The Corona Probe - Results

The Root Mean Square values obtained by the corona probe in the wake region were assigned to each point. Iso-RMS lines and therefore contours of equal mixedness were drawn throughout the test region. In Figure 6.4 the lines obtained by the original configuration of the probe are shown. They exhibit a marked decrease in RMS value in the outer layers of the wake and in the downstream direction.

The lower part of the region opposite to the side from which the probe was introduced shows a line distribution that does not seem to fit in with the remaining pattern. Although this could be due to non-symmetry in this zone, the probe geometry could have caused the extra loop. This is suspected because in this case the probe extended right through the wake region having maximum effect on the flow pattern. The collector sphere also entered the region of maximum concentration of

ISO-mVOLT(RMS)

DISTANCES BETWEEN MEASUREMENTS
HORIZONTAL   1mm
VERTICAL   3mm

DIRECTION OF
PROBE ENTRY

DOWNSTREAM DISTANCE (cm)

RADIAL DISTANCE (cm)
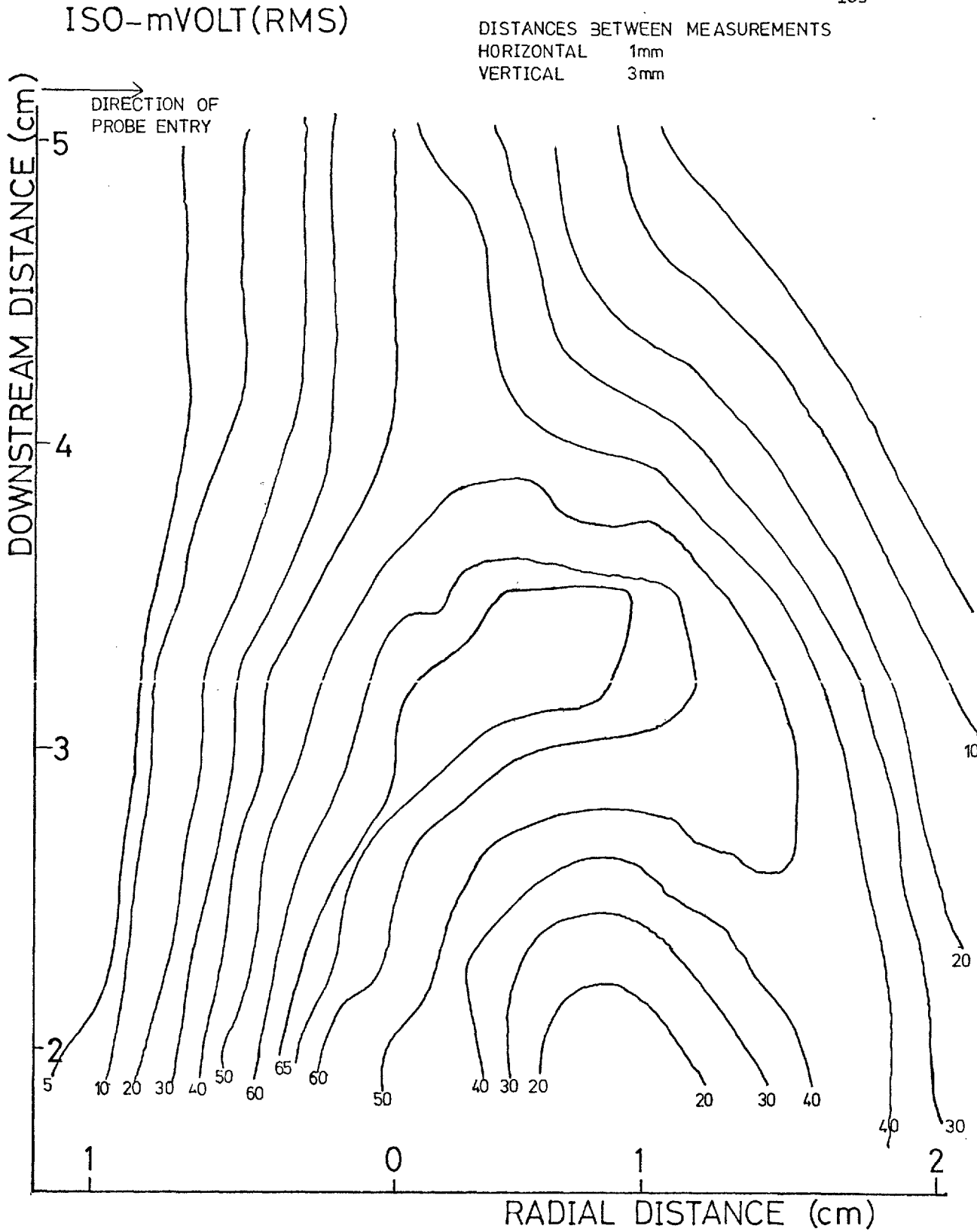
Fig. 6.4a   ISO RMS LINES (ORIGINAL PROBE)
12.4 l/min ARGON, 1.6 kHz ARC ROTATION

ISO-mVOLT (RMS)

DISTANCES BETWEEN MEASUREMENTS
HORIZONTAL   1mm
VERTICAL   3mm

⟶
DIRECTION OF
PROBE ENTRY
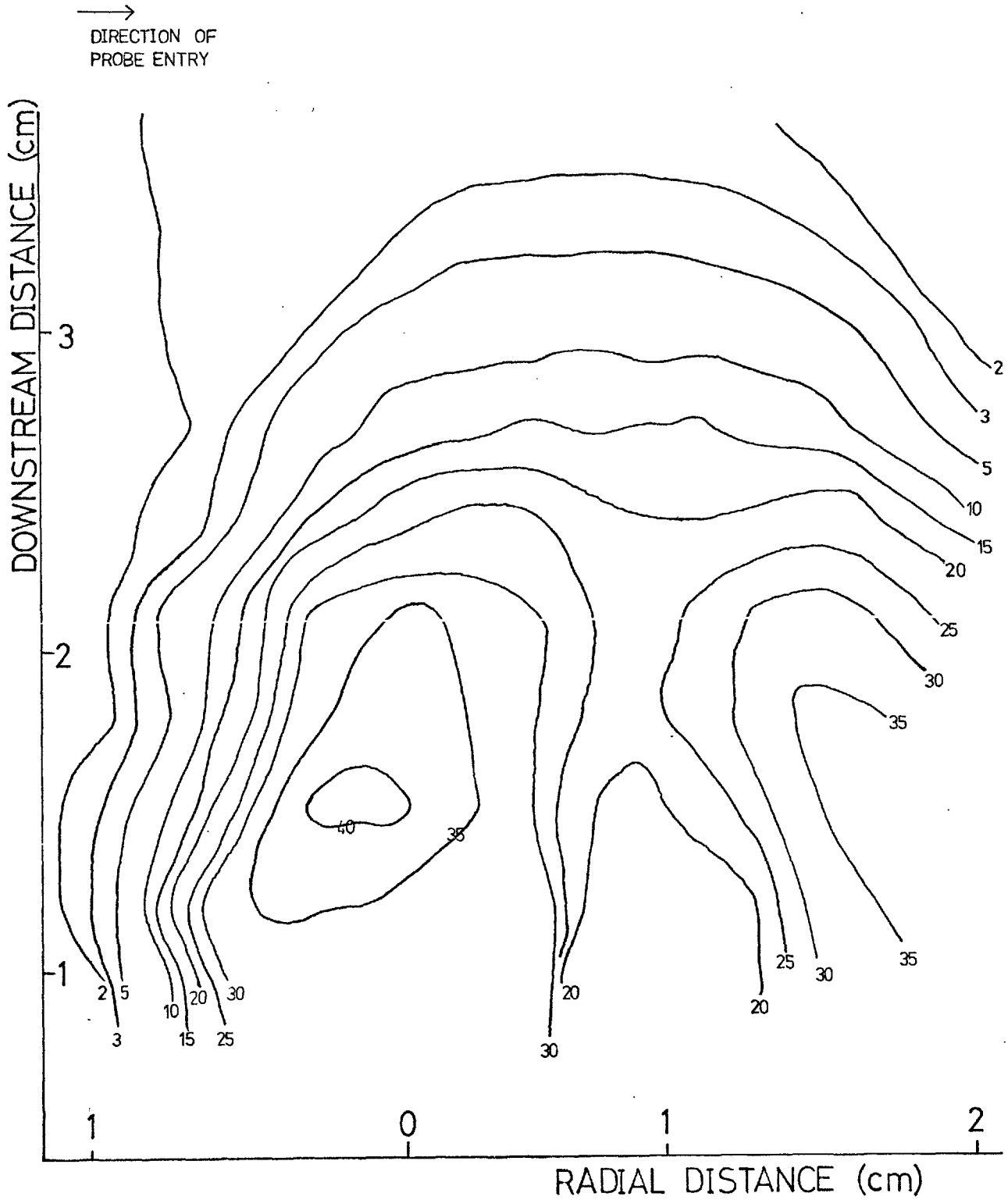
Fig. 6.4b   ISO RMS LINES (ORIGINAL PROBE)
5.7 l/min ARGON 1.6 kHz ARC ROTATION

ionized species and therefore absorbed free charges not produced by the corona discharge, even when the probe tip was in an ionization-free region. This was remedied by changing the probe to the pincer type shape mentioned earlier in this chapter (Fig. 6.3).

Figures 6.5 and 6.6 show the resulting isomixedness contours for high and low flow rates respectively. The results are now clearly symmetric and exhibit the decrease in RMS value with increasing distance from the nozzle in all directions.

The fluctuations in the probe output are dependent on size and temperature distributions of the pockets of gas passing the probe tip as well as on their flow velocity. The root mean square values can therefore not be considered to be standard deviations of velocity only. Hence they are clearly not measures of the intensity of turbulence of the flow regime, especially when one considers the much larger pocket sizes present in the outer part of the wake as compared to its centre.

VI.3 Thermocouple Probes

As discussed at the beginning of the chapter, thermocouple probes cannot follow the temperature fluctuations present in the wake region and average incorrectly, by volume rather than by mass. Nevertheless, measurements were taken in a central cross-section through the wake region at equal intervals in the horizontal and vertical direction, similar to those using the corona probe. The probe output voltage was recorded on a Phillips chart recorder which further damped the fluctuations so that a mean voltage was noted at each point. These values were constant even for prolonged measuring times. Values of mean thermocouple output are plotted in millivolts in Figures 6.7 and 6.8 for a flow rate of 12.4 1/min and 5.7 1/min of argon respectively. Positions of equal mean thermocouple voltage are joined by lines. These

ISO-mVOLT (RMS)

DISTANCE BETWEEN MEASUREMENTS
HORIZONTAL   2mm
VERTICAL   3mm
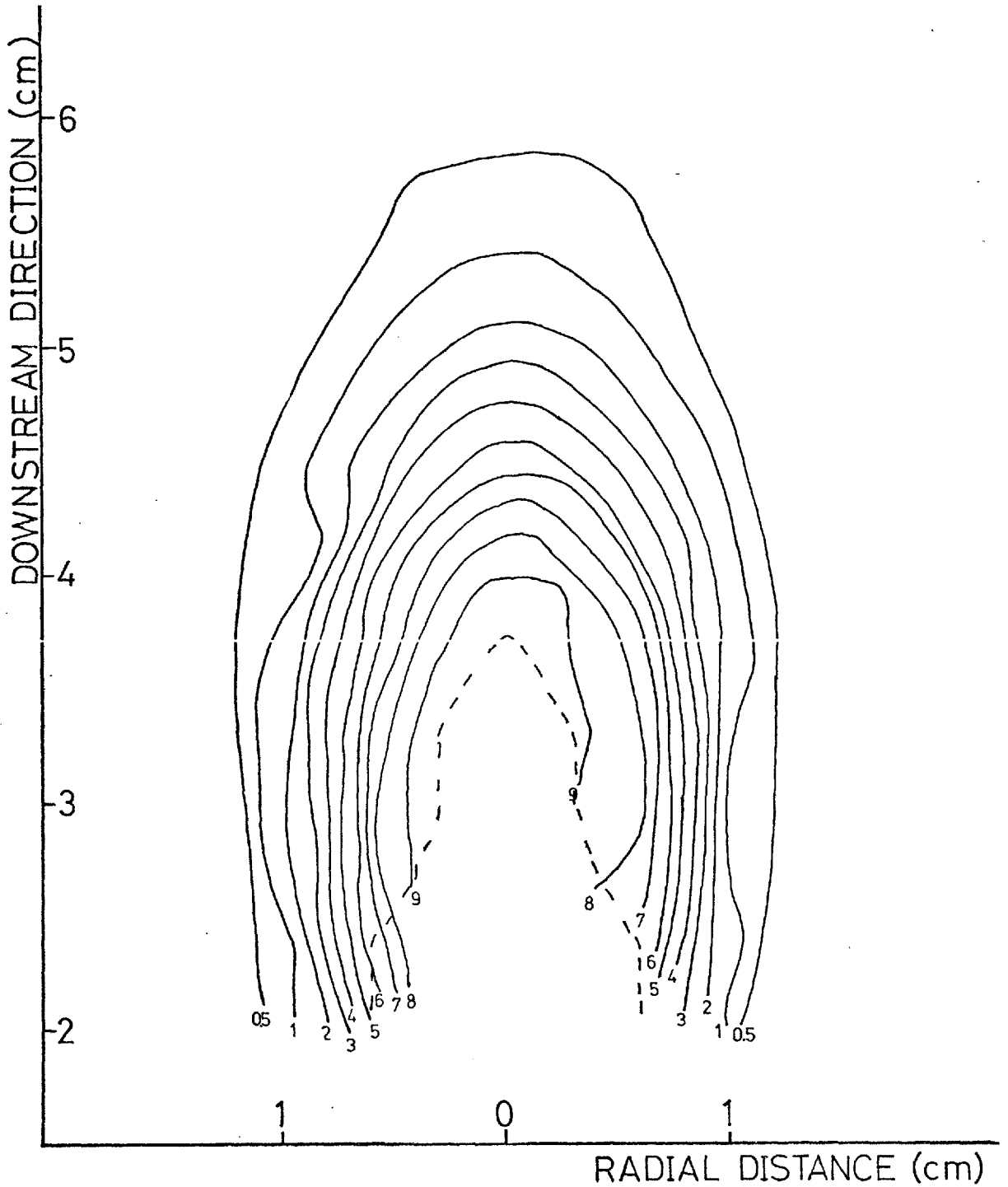
Fig. 6.5   ISO RMS LINES (PINCER SHAPED PROBE)
12.4 l/min ARGON, 1.6 kHz ARC ROTATION

ISO-mVOLT (RMS)

DISTANCES BETWEEN MEASUREMENTS
HORIZONTAL   2mm
VERTICAL   3mm
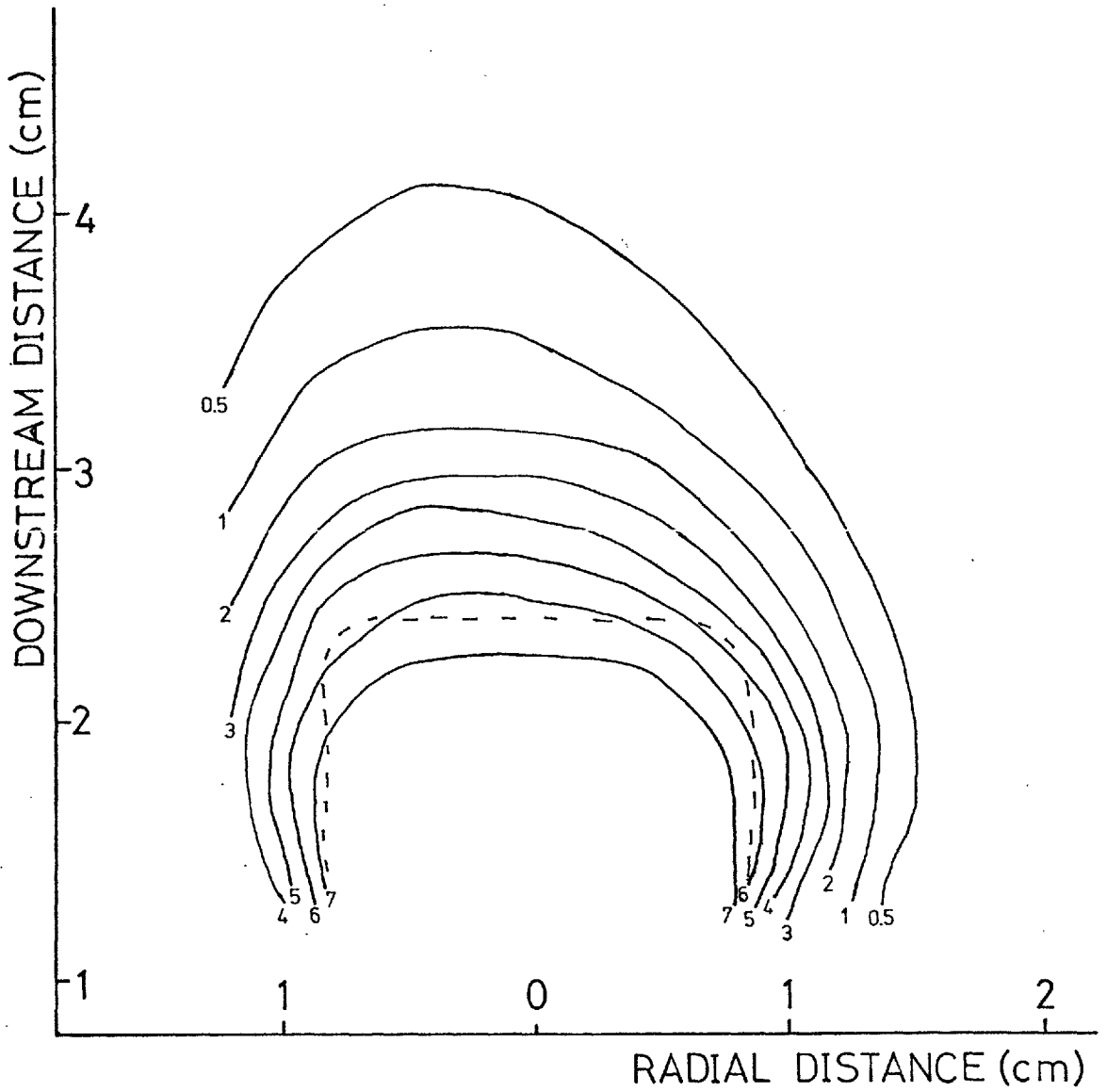
Fig. 6.6   ISO RMS LINES(PINCER SHAPED PROBE)
            5.7 1/min ARGON, 1.6 kHz ARC ROTATION

ISO-mVOLT

Fig. 6.7   ISO mVOLT LINES (THERMOCOUPLE)
12.4 1/min ARGON, 1.6 kHz. ARC ROTATION

ISO-mVOLT

DISTANCES BETWEEN MEASUREMENTS
HORIZONTAL   1mm
VERTICAL   3mm
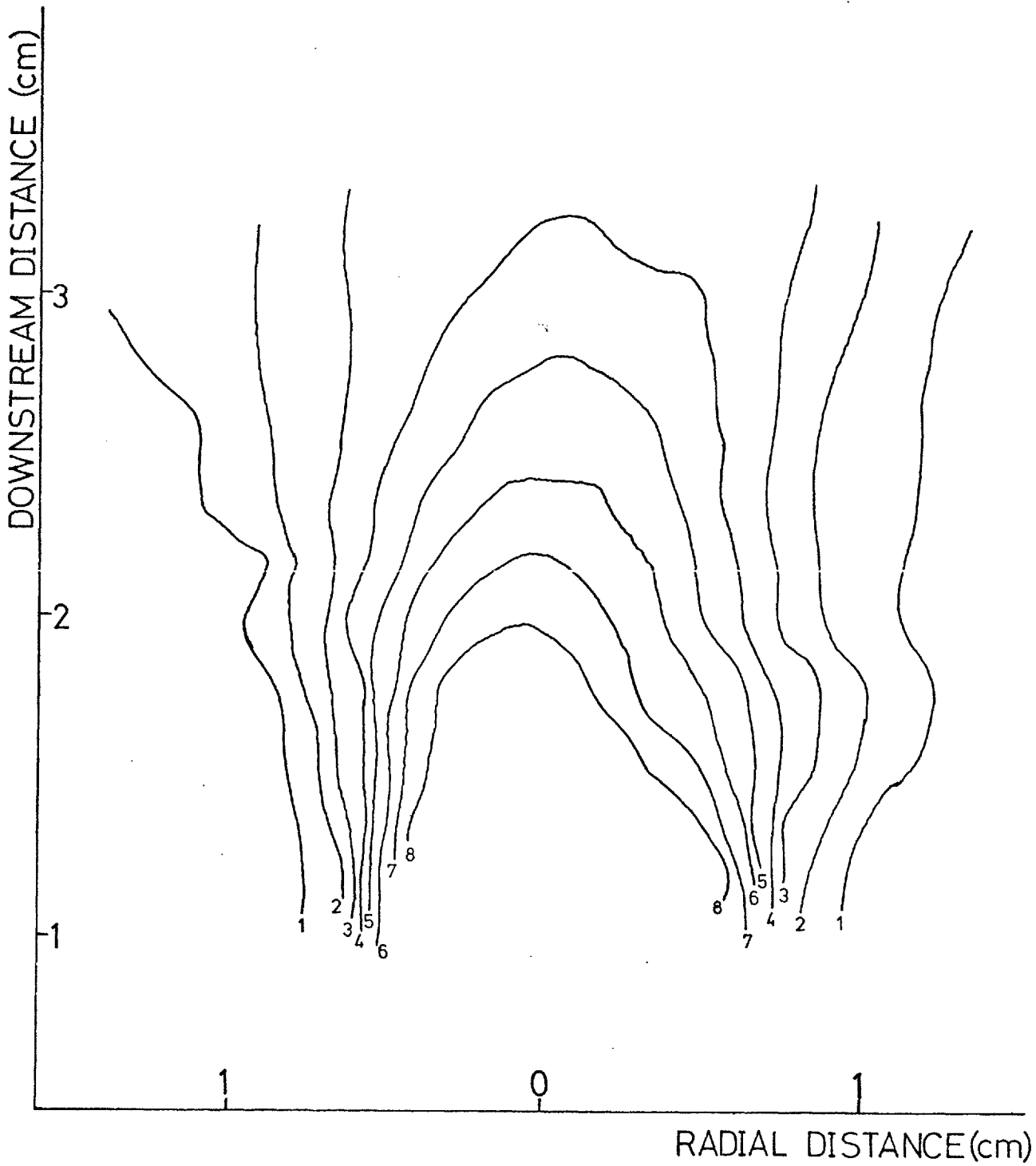
Fig. 6.8   ISO mVOLT LINES (THERMOCOUPLE)
5.7 1/min ARGON, 1.6 kHz ARC ROTATION

are labelled in terms of millivolts output rather than converted to degrees centigrade, in order to emphasize that these are not true mean temperatures.

A trend towards lower temperatures near the outside of the wake region and further downstream is, however, clearly deducible. Equally important, a high degree of symmetry is observed in the wake. This is an expected result, reconfirmed by different earlier measurements and observations, important in itself and for the analysis in Chapter VIII. As in the case of the corona probe the results immediately downstream of the nozzle are invalidated by the interference from ionized species and free electrons.

Chapter VII

VELOCITY MEASUREMENTS

Having established the general qualitative behaviour of the plasma jet gases in the wake region, we turned our attention to a more quantitative approach. It was decided to concentrate on obtaining a full range of values for localized velocity distributions at as many points in the wake as possible.

VII.1 Laser Doppler Velocimetry

VII.1.1 Theory

The method selected in the first instance was laser Doppler velocimetry. The principles underlying this technique have been extensively described in the literature (Ref. 32,33,34,39) where it is commonly applied to the measurement of shock front velocities.

Briefly a parallel laser beam is allowed to traverse the test region, (Fig. 7.1). Most of the beam does not encounter an inhomogeneity and is brought to a focus by a schlieren mirror or lens. That part of the beam that does interact with a phase object is deflected through an angle θ and brought to a focus in the same plane as the main beam, but somewhat displaced from it in a direction perpendicular to the optical axis. If the disturbance in the test region is moving with a velocity that has a non-zero component in any direction perpendicular to the direction of the beam, then the deflected part of the laser beam has its frequency Doppler shifted to a new frequency ν_2 given by

$$\nu_2 = \nu_1 [1 + (u/c) \sin \theta]$$

TEST SPACE · SCHLIEREN LENS OR MIRROR · STOP CONTAINING TWO SLITS · RECORDING PLANE

U

PHOTOMULTIPLIER SLIT

INTERFERENCE FRINGES
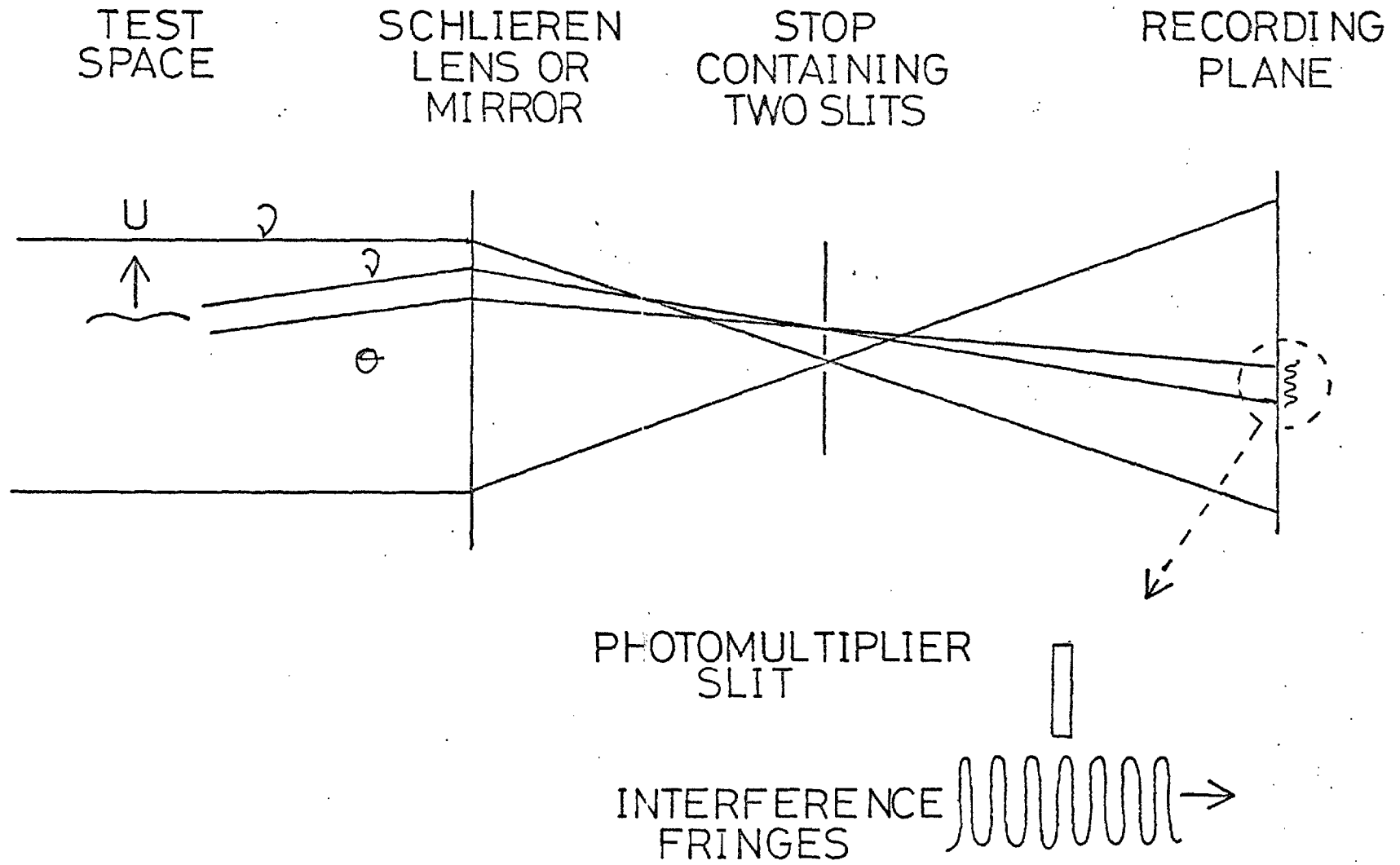
Fig. 7.1 LASER DOPPLER VELOCIMETRY (SCHEMATIC)

where ν_1 is the frequency of the incident beam, u the component of velocity of the schliere perpendicular to the beam, θ the angle of deflection and c the velocity of light. If a blind with a narrow slit cut into it is now placed on the focal point of the second lens or mirror, one can, by adjusting the relative position of the slit, select a pencil of light that has been deflected through any one suitable angle θ only. A second slit placed at the focal point of the undeflected beam allows a part of that to pass too. As the two beams expand and overlap they interfere. A white card placed in the overlapping region displays a clean interference fringe pattern. For maximum visibility of these fringes the intensity of both interfering beams must be approximately equal. The spacing of these fringes is given by the relation familiar as the Young's Double Slit expression

$$\mu = \lambda l/a$$

where λ is the wavelength of the incident beam, l the distance from the double slit to the point of observation of the fringes and a the separation of the two slits. As long as the schliere in the test region is stationary the pattern is stationary. Plate 12 shows such an interference pattern produced by a stationary glass rod. Once the disturbance moves the fringes begin to travel in the direction parallel to that of the motion in the test region. The frequency with which these fringes pass a stationary reference point is given by the beat frequency (ν_b) of the two interfering beams, i.e. by the amount the Doppler shifted beam has been changed in frequency:

$$\nu_b = \nu_2 - \nu_1 = \nu_1 \frac{u \sin \theta}{c} = u \frac{\sin \theta}{\lambda} ;$$

u can be determined from this equation directly or via the fringe
spacing. The velocity (v) of the fringes is given by

$$v = \mu \times \nu_b$$

and the velocity of the phase object in the test region by

$$u = v/M$$

where M is the magnification of the optical system. This analysis is
correct when using the undeflected beam as the reference beam. Has the
reference beam been deflected through an angle α with the optical axis,
the measured fringe velocity v_f needs to be adjusted for the off axis
position of the reference beam using the equation: (Ref. 32)

$$v = v_f [1 - (\alpha/\theta)]$$

If v is now divided by the magnification the velocity component of the
phase object perpendicular to the beam in the test region (u) is obtained.

There are two ways of explaining the formation of the moving fringes.
Either one considers the pattern to be caused by the interference of two
beams of slightly different frequencies ν_1 and ν_2 resulting in the
creation of fringes moving with the beat frequency of the two interfering
beams. Alternatively, the fringe pattern may be considered to form an
image of the phase object made up of fringes with its velocity related
to that of the object in the test region allowing for the magnification
of the system. If the undeflected beam provides the reference the fringe
system moves with the same velocity as the record of the phase object.
Otherwise the correction quoted above from Ref. 32 needs to be used.

It has been shown (Ref. 39) that these approaches are entirely equivalent.

VII.1.2 Application

In practice the optics was set up as shown in Figure 7.2. A beam from a 5 mW He-Ne laser was focused onto a pinhole and allowed to expand onto a schlieren mirror of focal length 3 m at whose focus the pinhole was placed. The parallel beam then passed through the test region and was brought to a focus by another similar schlieren mirror. The size of the test region was determined by the diameter of the two mirrors. The beam was arranged in a Z-type configuration.

A screen containing two small closely spaced slits was then placed at the focus of the second mirror. The slits were positioned either for one to be at the focus of the undeflected beam and the other at the focus of a beam deflected through a pre-chosen small angle θ, or alternatively for one slit at a point corresponding to a small upward deflection $(+\theta)$ and the other an equal deflection in the opposite direction $(-\theta)$. A piece of polaroid was placed in the path of the brighter of the thus selected beams and rotated to arrange for approximately equal intensity of the interfering beams in order to obtain maximum possible legibility of the fringes. The polaroid acted as a continuously variable ND filter of transmissivity between 80% and 3% depending on its alignment with respect to the direction of polarisation of the laser beam. This was necessary if one of the beams was the undeflected beam. If only deflected components of the laser light were used to produce the interference pattern, the polaroid compensator was not required and equal intensities could be ensured by fine adjustment of the positioning of the double slit. In both cases the intensities were compared and adjusted by covering each slit in turn and comparing
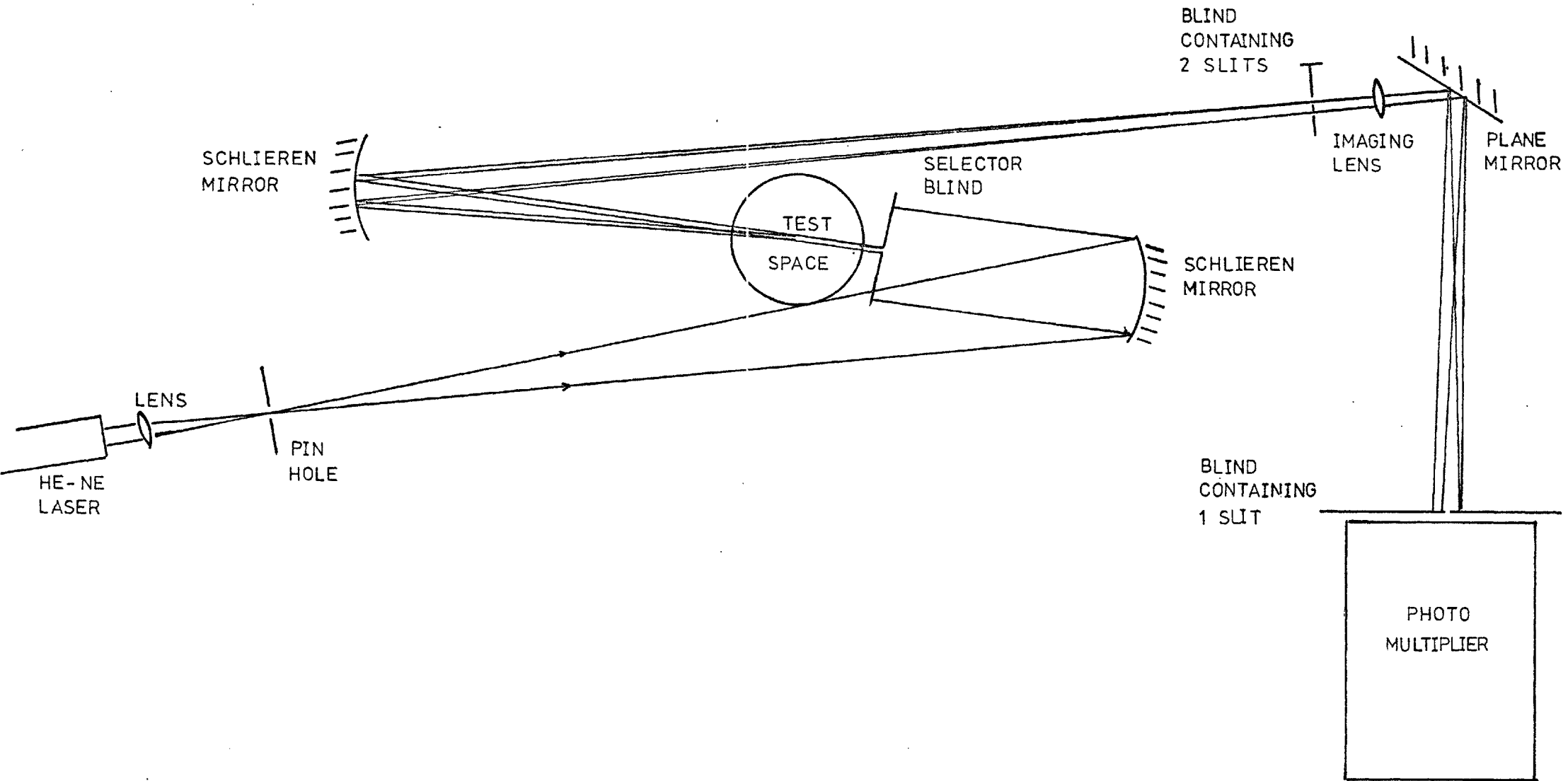
Fig. 7.2 OPTICAL ARRANGEMENT LASER DOPPLER VELOCIMETRY

the DC level displayed by the oscilloscope as a result of the light

incident on the photo-multiplier through the other slit.

The screen was followed by a lens whose focal length was chosen to

give a suitable magnification of the image. For the first half of the

measurement a focal plane shutter and a photographic plate in its holder

were placed near the image plane of the test region. A stationary

schliere, i.e., a glass rod, was placed in the test region with the

plasma jet switched off in order to produce stationary fringes. These

were recorded using Type 57 polaroid film (Plate 12). This gave a value

for μ, the spacing of the fringe pattern for the particular angle θ as

chosen by the slit position. This corresponds to a set of distance

markers.

The shutter and film were then replaced by a screen containing a

single slit or grating whose spacing distances were equal to the wave-

length of the fringe spacing. The reason for the slit width and the

possible use of the grating will be discussed later in this section. An

EMI photomultiplier was placed behind the slit and charged using a

Hewlett Packard Harrison 6516A, HT power pack. A screen containing a

small triangular aperture was placed in the parallel beam just before

the test region to select one small part of the wake region only for

investigation at any one particular time. The shape of the aperture was

chosen to give a suitable diffraction pattern at the focal point of the

second mirror, i.e. at the double slit. For a triangular aperture the

pattern was in the form of a three-pointed star.

The optical arrangement was tested by spinning a glass rod about

an axis perpendicular to itself through its centre at a rate of about

2000 RPM using a constant speed motor. The rod was allowed to cut the

beam in the test region and its linear velocity was recorded. Velocities

determined from these measurements compared well with those computed from

PLATE XII   FRINGES PRODUCED BY A STATIONARY ROD USING LASER
DOPPLER VELOCIMETRY SET-UP
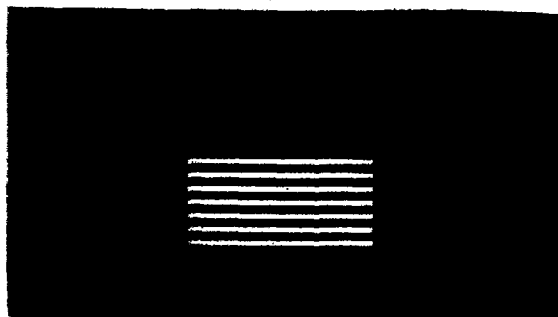
cf: GRID USED IN FRONT OF PHOTOMULTI-
PLIER TUBE

the rotational frequency of the rod. The plasma jet was then switched

on and the hot gases in the selected part of the test region produced

a moving fringe pattern on the screen in front of the photomultiplier.

As the fringes passed the slit the output from the photomultiplier as

displayed on the oscilloscope varied with the frequency ν_b, the beat

frequency of the interfering beams. This corresponds to a very accurate

clock in the normal velocity measurement techniques.

It would appear on first inspection, that the optimum width for

the slit in the image plane of the test region is half the wavelength

of the interference pattern, although a smaller slit would suffice for

bright fringes. A larger slit is equivalent to having a slit with

width (w'):

$$w' = w - n \times \mu$$

where w is the actual width of the slit, and n the number of complete

sets of dark and bright bands contained within the slit width. The

$n \times \mu$ part of the light transmitted through the slit only contributes

to the DC level of the signal produced by the photomultiplier.

As the fringes were, however, not very bright, it was necessary to

consider a way in which to amplify the AC part of the photomultiplier

output. To do this an arrangement was used which was first suggested by

Schwar and Weinberg (Ref. 40) but not actually employed at the time. The

slit was replaced by a grid of spacing equal to the wavelength of the

interference fringes. This is equivalent to allowing a number of bright

bands of width $\mu/2$ to pass an equal number of slits of equal width

simultaneously and therefore produces an amplified AC component with no

DC component at all at the output of the photomultiplier. A signal thus

produced has a higher legibility than that obtained from any other slit

configuration or width.

Problems, however, presented themselves in the use of both positions for the double slit as the focus of the second schlieren mirror. The intensity of the deflected light through any angle is a function of the refractive index gradient of that particular interface between a hot and a cold pocket of gas used as a marker at that particular instance in time. As these pockets and therefore the interfaces varied in their physical properties from one another, the intensities of successive beams refracted through a fixed angle θ were not equal. This can be seen on the instantaneous shadow photographs in Chapter V by the differences in intensity and width between various lines representing different interfaces. This obviously created a difficulty in finding a condition under which both beams were of similar intensity for all or most of the many hundreds of passing schlieren. This problem persisted even with the use of upward and downward deflected beams as there was no guarantee that rays deflected in both directions simultaneously would always be of the same ratios of magnitudes even if an entire pocket of gas would always have been contained in the small test triangle.

Another requirement was that no more than one pocket may be in the test region selected by the aperture at any one time. On the other hand if upward and downward deflected beams were to be used, two refractive index gradients opposed to each other in direction would have had to be present. The ideal condition would therefore have been one in which one closed pocket only was present at any time in the triangular beam. This was virtually impossible to achieve, although two opposing surfaces of different pockets travelling with the same velocity would have been sufficient.

It can be seen, again from the shadow photographs, that it was possible to arrange for only one interface to be considered at any time

by choosing a sufficiently small triangle (e.g. of sides 2 mm) to act

as aperture at least for regions near the slower-moving periphery of

the wake, where large pockets predominated. Simultaneous up and

downward deflections, however, were unlikely and the undeflected beam

had to be used. In the region of the small fast moving pockets near

the centre of the wake the interfaces are very close together. 'Images'

of the markers spread out into fringe patterns overlapped and it was

nearly impossible to arrange for one interface to be contained in the

test beam only. The overlapping fringe systems made meaningful

measurements in this area virtually impossible.

VII.2. Schlieren Velocimetry

It was therefore decided to make some adjustments to the optical

system and transform the Doppler velocimeter into a schlieren veloci-

meter. The optical configuration remained unaltered up to the double

slit (Fig. 7.3). That was replaced by a schlieren knife edge in a

horizontal position for measurement of the vertical velocities and in a

vertical position for horizontal velocities. The next lens was replaced

by one that gave a magnification of the test space of approximately 1:1

in the image plane. The single slit screen was removed and a screen

containing three small, narrow slits spaced closely together was

positioned in the image plane of the test region. The photomultiplier

was placed immediately behind these slits. The slits were made by

multiple photographic reductions of three 1 cm thick black lines drawn

on A4 sized papers until the entire configuration occupied a space of

less than 3 mm × 3 mm. Ilford Lithographic Film was used, the final

negative being on Ilford Lithographic plate. This optical arrangement

gives a dark field schlieren image on the screen in the image plane

of the test region. Schlieren optics in contrast to shadowgraphy or

SCHLIEREN
STOP

IMAGING
LENS

PLANE
MIRROR

SCHLIEREN
MIRROR

TEST
SPACE

SCHLIEREN
MIRROR

LENS

PIN
HOLE.

BLIND
CONTAINING
3 SLITS

HE-NE
LASER

PHOTO
MULTIPLIER
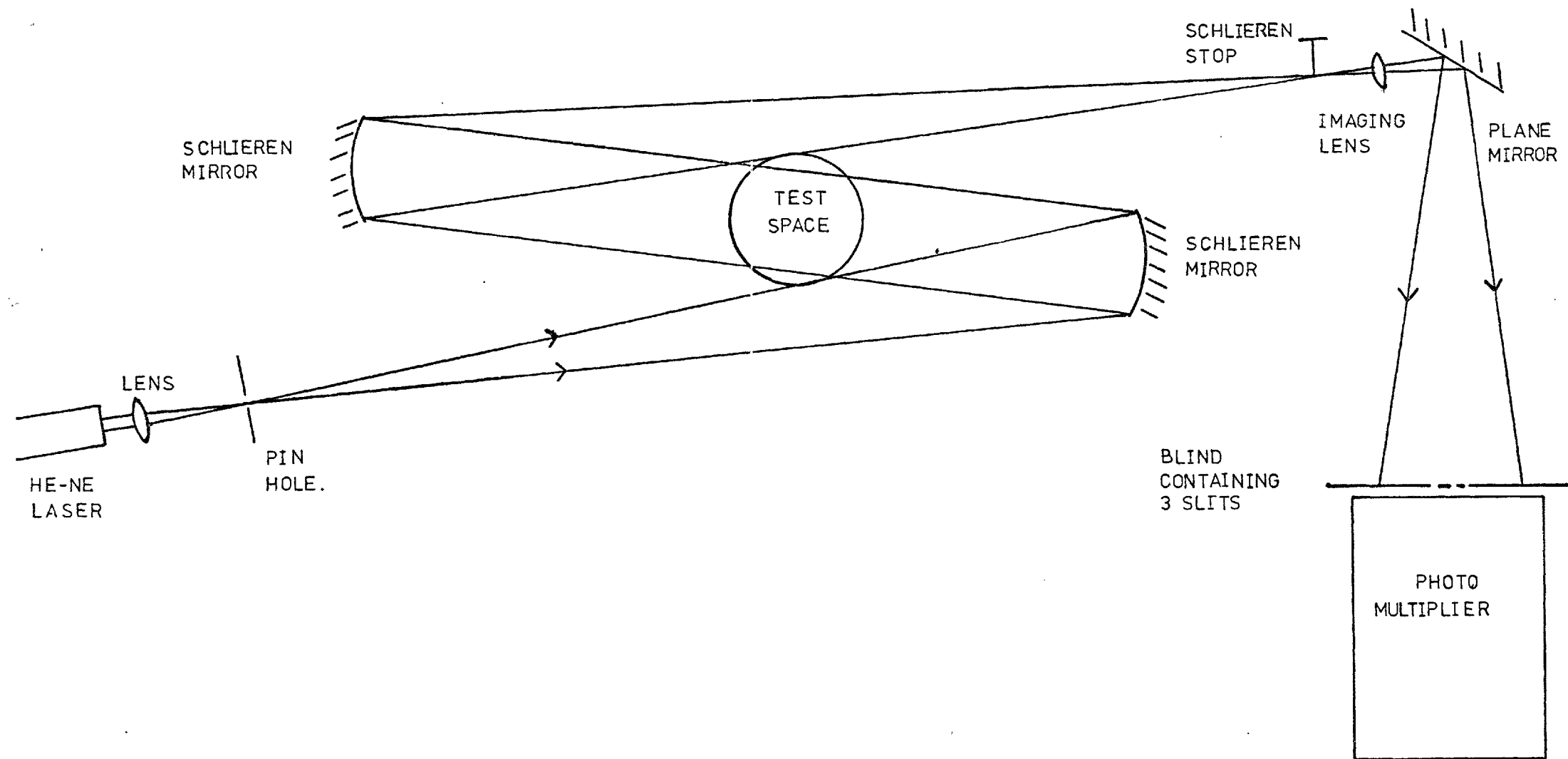
Fig. 7.3   OPTICAL ARRANGEMENT SCHLIEREN VELOCIMETRY

the production of interference fringes always produces a focused
image on the screen. All measurements executed by the three slits at
a point, or more precisely over a small area, are therefore results
of conditions that existed in the test region at the corresponding
position. We now have a way of executing localized investigations
at different points without having to preselect a part of the beam
with an aperture but by only moving the treble slit with respect to
the image of the burner. In practice this movement was achieved by
a mirror that could be tilted about a horizontal axis and turned using
rack and pinion gearing about a vertical axis, thus moving the beam
with respect to the fixed treble slit. An outer edge of the anode
was used as a reference point. In the moving schlieren image the
interfaces were once again used as markers, this time in the form of
bright lines on a dark background. As one of these lines passed the
three slits three bursts of light fell on the photomultiplier and
gave three pulses at its output which could be visualised on an
oscilloscope (Plate 13). The separation between the slits acting as
distance markers was known as was the time required for the passage
of the schlieren image across the slits from the readings from and
the settings of the oscilloscope, which again represented an accurate
clock. The magnification of the optics is easily establishable and
the local velocity of a gas pocket has therefore been measured.

The wake region of the plasma jet is a turbulent system defined
as containing a range of velocities of the form

$$V_{x,n} = \overline{V}_x + \delta V_{xn}$$

where x denotes the position and n the number of that particular measure-
ment at position x. It was therefore obviously meaningless to talk about
individual velocities and necessary to compile a large number of values
at each point. A distribution of these data could then be drawn up from

which average values of velocity for each point could be estimated.
The standard deviations of these distributions contain information
about the intensities of turbulence at the various points.

By changing the slit orientation by 90° both horizontal and vertical
velocity components could be measured separately. At first the 3 slits
were equispaced. This gave rise to a great number of groups of three
peaks. There were, however, groups of two peaks and even single spikes
recorded. This could have been due to two reasons. It is possible
that the velocity components along the slits were greater than those
across the slits preventing the markers from reaching the third or
even the second slit. This was especially likely for horizontal
measurements near the centre and for vertical measurements near the
edge of the wake cone. Alternatively the shape of the pocket of gas
had changed drastically within the time required to move past the slits,
a phenomenon not unlikely to occur, as can be seen from the high speed
cine film (Chapter V.4). Average velocities as well as standard
deviations were therefore obtained at various points in the wake from
two and three peak values separately, while the plasma jet conditions
were kept constant. A comparison between these sets of values obtained
are discussed in Chapter IX. They were found to be consistent within
experimental accuracy with the possible exception of the region very
close to the boundaries of the wake. In that region of comparatively
low velocities the effects of the change in velocities turned out to
be relatively large as these changes were considerable and even changes
in direction were not uncommon for moving pockets near the outside of
the wake, as can be seen from the high speed film. The lower velocities
and smaller concentrations also caused a smaller number of interfaces
to pass the slits. This resulted in fewer readings in the fixed time
interval over which measurements had to be taken at each point, as will

be explained later. The smaller the number of readings the larger

the statistical error introduced. Results obtained near the edges

are therefore less reliable than those near the centre. All this

considered, it was deemed justifiable to consider readings obtained

from three peaks only. This has the further advantage of enabling

the slits to be placed at different separations, the third at a

distance roughly twice that between the closer two. The peaks thus

obtained are unequally spaced which not only gives information about

the magnitude of the velocity components but also of their directional

sense (Plate 13).

As a very large number of readings were required at each point

in the wake region, the recording mechanisms were automated as much

as possible with the equipment available. The photomultiplier tube

used was a Type 9592/A manufactured by EMI in the UK. The output from

this photodetector was displayed using a Tectronix Type 561B, 10 MHz

oscilloscope. The time base sweep rate was adjusted at each point to

cope with the range of time intervals between peaks encountered.

A Vinton 16 mm cine camera was focused onto the oscilloscope screen

such that the image of the tube just filled a frame of the film. The

camera was set to expose 8 frames/sec for the faster oscilloscope

settings or 1 frame/sec using an Intervalometer for sweep rates longer

than 2 msec/cm. (The intervalometer is an instrument that allows the

Vinton camera to record single exposures of fixed duration at prechosen

intervals between 1 second and 2 hours.)

As the shutter opened a microswitch built into the Vinton power

supply along with the circuit in Figure 7.4, triggered the oscilloscope

externally causing the recording of only one complete sweep on each

consecutive frame. The film used was Ilford Micro Neg. Pan Type A403,

a comparatively slow but high contrast emulsion, available in 2000 ft

EVEN

UNEVEN

SLIT SPACINGS
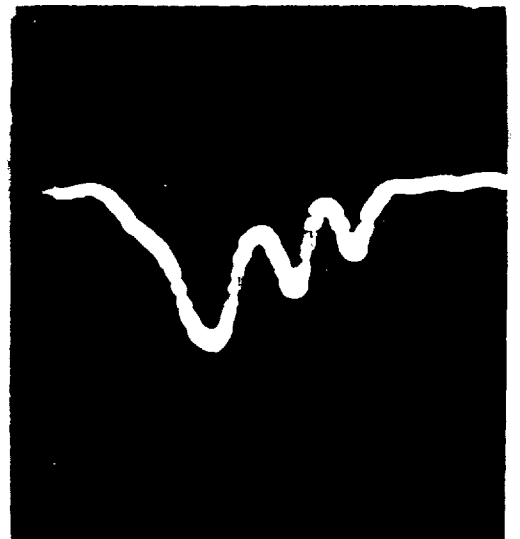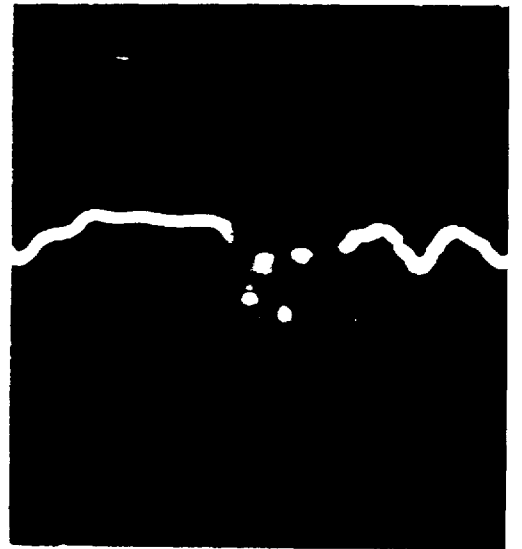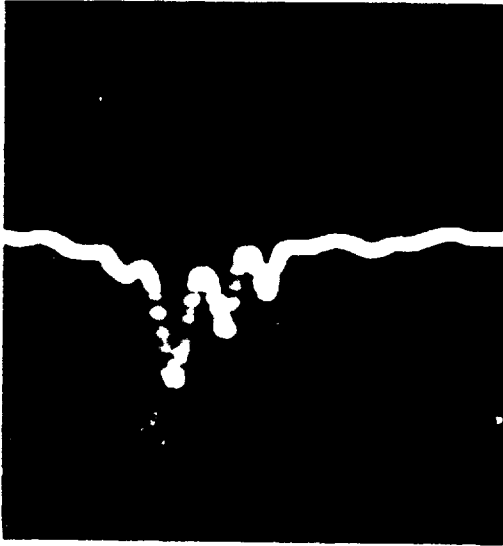
PLATE XIII   PHOTOMULTIPLIER OUTPUT FOR SCHLIEREN VELOCIMETER
USING EQUISPACED AND NON-EQUISPACED SLITS

220k

4.7k

SCOPE TRIGGER
INPUT

2000 pF
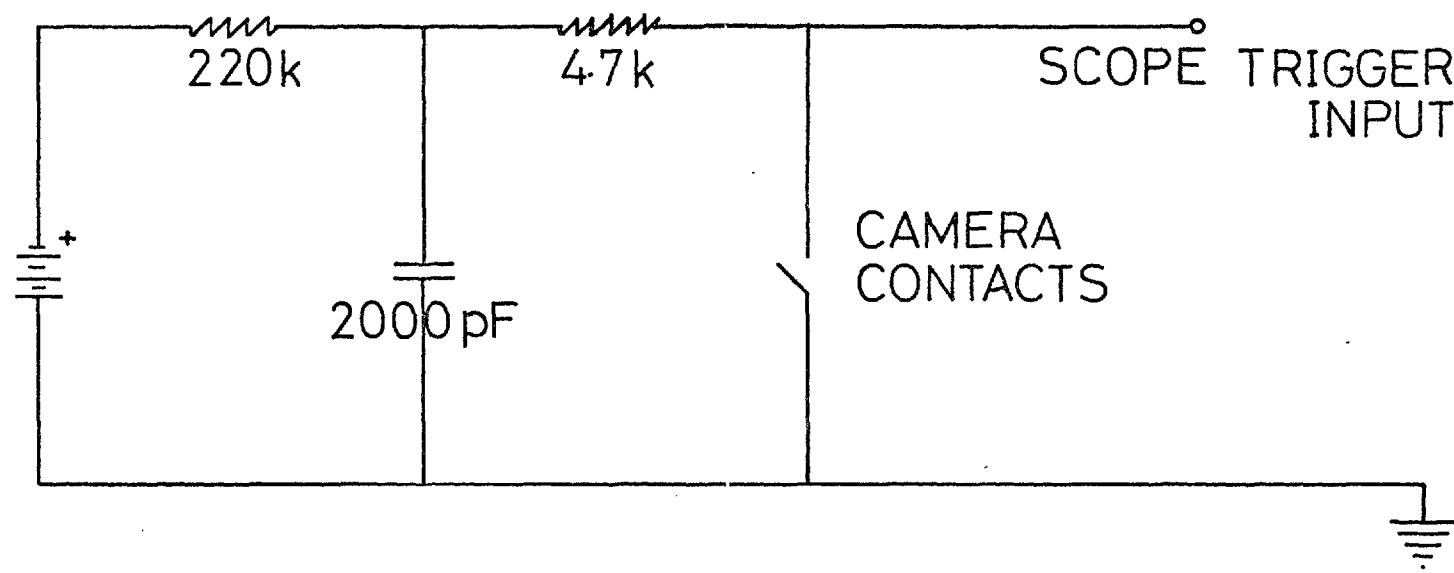
CAMERA
CONTACTS

Fig. 7.4   TRIGGER CIRCUIT VINTON — OSCILLOSCOPE

lengths at extremely competitive cost. The camera is fitted with an internal frame counter which enabled a fixed number of sweeps to be recorded at each point. Calculation of the product of number of sweeps, times the sweep duration, resulted in the total time over which readings were taken at each point. The films were developed using a 100 ft Jobo Spiral in Kodak D19 developer for 7-8 minutes. They were analyzed frame by frame using PCD-X-Y Digit Reading Equipment, which incorporates the following features. The picture to be analyzed is projected onto a ground glass screen. An x-y shift arrangement is positioned at the point to be measured - in this case the centre of one of the peaks. Its precise position is displayed digitally and can, by pressing a button, be recorded onto paper roll as well as onto Olivetti computer terminal compatible punch tape, via a Data Dynamics 390 punch. Each group of three abscissae values corresponding to a series of peaks was recorded on a separate line equivalent on the paper tape. The CDC 6400 at the Imperial College Computer Centre was programmed using FORTRAN IV to calculate the velocities corresponding to the recorded intervals, plot velocity distribution histograms, calculate mean velocities and standard deviations at every point (see Appendix 2 & 3).

Chapter VIII

STATISTICAL ANALYSIS - CORRECTION 3D TO 2D CONVERSION

In the analysis of the velocity distribution one important factor

has still to be taken into consideration, namely the fact that this,

as most optical methods, gives measured quantities that are a result

of integration along the optical path of the beam as it traverses the

test region. Near the edge of the wake this presents no real problem

as any interface giving rise to a recording must have been travelling

near the outer circumference of the wake where the laser beam is

tangential. A beam that passed through the cone of hot gases near its

centre, however, was not only influenced by disturbances in the central,

vertical plane of cross-section through the wake perpendicular to the

beam. It also recorded events in front and behind this plane. In order

to be able to map out a true velocity distribution in this central

cross-section of the test region, it is therefore necessary to deduct

these additional effects from the overall distributions of the signals

as supplied by the photomultiplier.

In order to achieve this a basic assumption needs to be made,

namely that the wake region is cylindrically symmetric about the axis

through the cathode. As shown in Chapter III the burner was entirely

axisymmetric with the exception of the gas inlets. The gases after

entering the burner passed through two flow constrictions with a pressure

drop across each of them inside the burner, as well as through the highly

turbulent arc rotation region. It is therefore unlikely that they should

have an intrinsic preferred direction, as long as they are not disturbed

by external influences like forced convection. The likelihood of that

occurring had been reduced by shielding and even switching off the

laboratory extractor system while taking readings. The symmetry of the

wake cone is illustrated by the shadowgrams in Chapter V and confirmed by probe measurements discussed in Chapter VI. It is therefore thought that the axisymmetry of the wake region is not an entirely unreasonable assumption. Once we have accepted its validity the following model can be used for the correction of the integration along the optical path.

The cone making up the wake is cut by a number of equispaced horizontal planes. All readings at any one height above the plasma jet were taken along equispaced parallel beams in these planes. The readings of interest are those that originated from the region of intersection of these horizontal planes with the vertical plane containing the central cross-section through the plasma jet at right angles to the laser beam. In order to isolate these the circular disc, formed by the intersection of the horizontal plane with the cone of the wake, is divided into a number of concentric annuli of equal thickness leaving a small disc of radius equal to one and one half times that thickness in the centre, such that one and only one beam passes through each annulus tangentially to the inner boundary of the ring (Fig. 8.1). The central ray passes through the centre of the disc in the middle. This arrangement is preferable to allowing each beam to pass through the centre of one annulus as now each beam averages over a complete ring near its intersection with the central vertical plane. Every resulting mean value, however, corresponds to the middle of its ring. Therefore each, except the centre reading, needs to be assigned to a point one half of an annulus thickness closer to the outside of the wake than the position of intersection between the central vertical plane and the beam from which it resulted (Fig. 8.2).

The width of the annuli and therefore the separation between the beams is limited by theoretical as well as practical considerations.
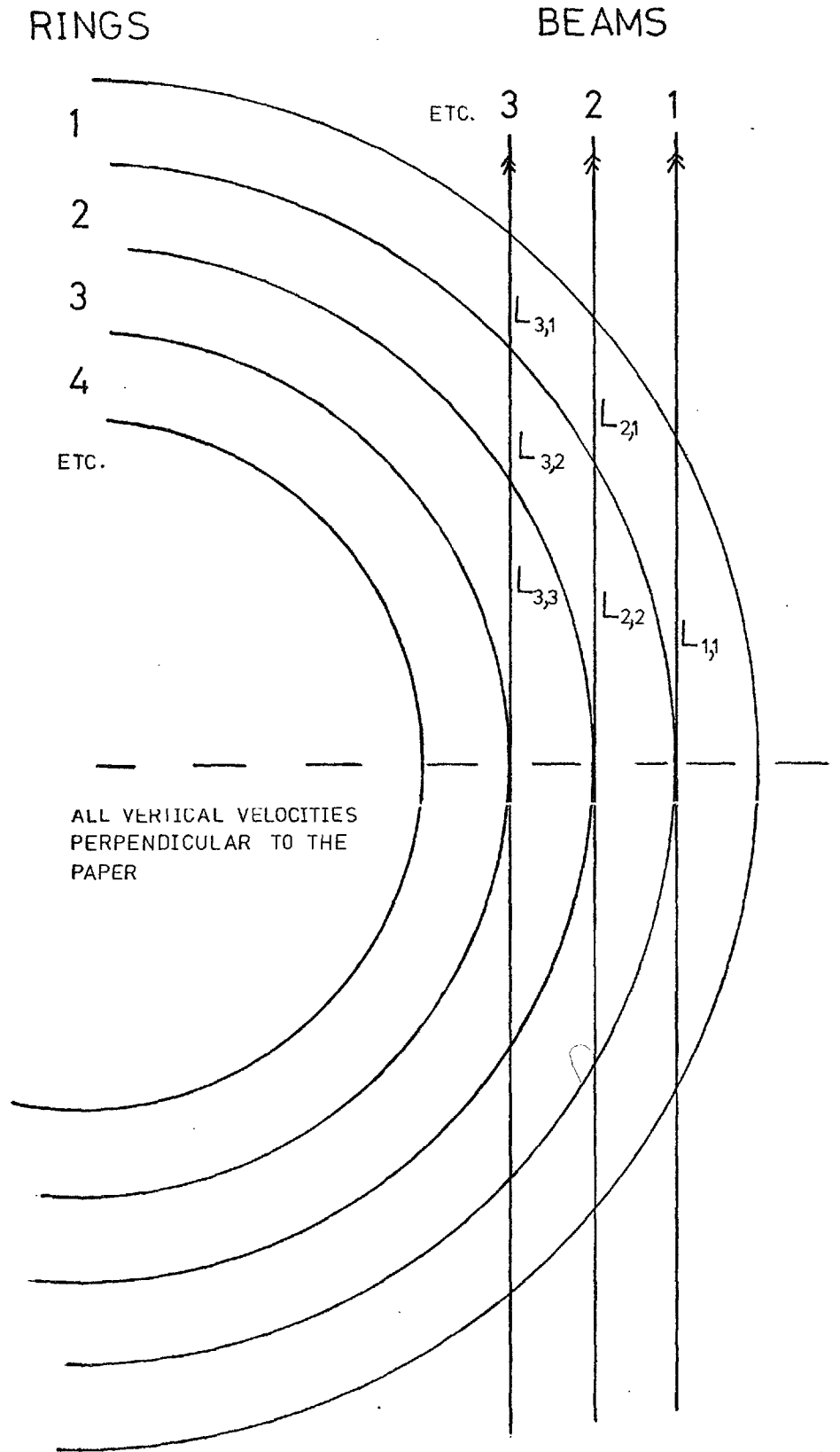
Fig. 8.1   CONCENTRIC RING MODEL – VERTICAL VELOCITIES

BEAM n

RING n

X

MEASUREMENT from
BEAM n assigned to
POINT X
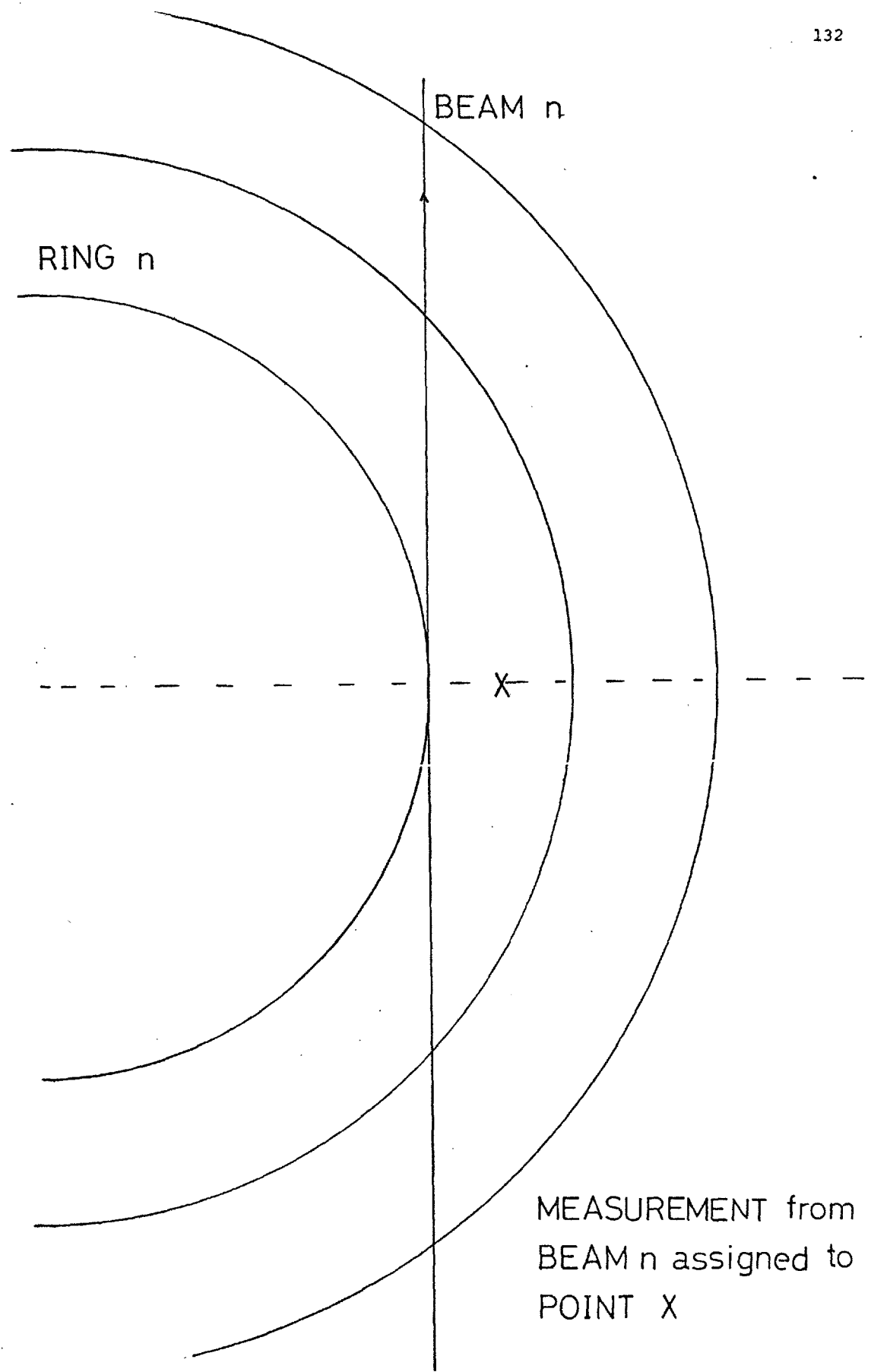
Fig. 8.2   MEASURED VALUES AND THEIR ASSIGNED POSITIONS

As we shall attempt to obtain local average values for the physical

properties of the wake region in each of these annuli, it is obviously

desirable to keep them as small as possible for maximum accuracy. This

does not only make the values obtained more truly localized, but also

reduces the probability of errors due to averaging over a region of steep

gradients of the physical quantities to be measured. On the other hand,

it is of little use to make the thickness of these rings less than the

length or total separation of the three slits, allowing for optical

magnification, as the readings were naturally averaged over the area

covered by the slit system. It is, however, important that this area

size is selected such that it is meaningful to speak in terms of

average values of quantities like velocity and density. In this case

for a slit area of approximately 3 mm square an annulus thickness of

5 mm was chosen.

Vertical measurements were taken throughout the entire cross-section

to check for the symmetry of the wake and to give a better average value

for each annulus. Horizontal measurements were taken on one half of the

wake only as just that part was visible with a vertical schlieren blind

(the remainder of the wake had its schlieren markings deflected into the

stop). As the conditions are different for horizontal and vertical

velocity measurements, each case is treated separately.

VIII.1 Vertical Velocity Analysis

Dealing first with vertical velocity components, these are all

either in an upward or a downward direction and are at all stages

perpendicular to the direction of the laser beam. The outermost part

of the beam in each horizontal plane presents few problems, as shown

by ray No.1 in Figure 8.1. That only passes through the outermost

annulus and all signals in that part of the beam are due to that region

representing a range of velocities encountered in that part of the wake.

They were recorded for a fixed duration of time and a histogram of

a continuous series of small velocity intervals versus the number of

times velocities in each interval occurred was plotted.   In order to

normalize this frequency distribution, each term of the histogram is

divided by the relative length of the optical path of that beam in

the annulus $(L_{1,1})$. A term in the histogram is defined in this

context as the number of times velocities in a given interval occurred.

The next bundle of rays, shown in Figure 8.1 as number 2, passes

through both the annuli 1 and 2. The distribution in this beam due to

annulus 1 per unit length of optical path and measured over an equal

period of time - keeping the selected velocity intervals the same as

before - is known from the previous measurement. The contribution due

to annulus 1 towards the total distribution of measurements in beam 2

is found by multiplying each term of the normalized histogram for

region 1 by the total path length of beam 2 in annulus 1 $(L_{2,1})$. This

distribution is then subtracted from the overall histogram obtained

for beam 2 by subtracting each term in turn (Fig. 8.3). If the

remaining histogram is then divided by the optical path of beam 2 in

zone $2(L_{2,2})$, the normalized distribution of velocity in ring 2 is

obtained.

A similar course of action is followed for all further parts of

the laser beam. The overall distribution for each set of rays has all

the normalized distributions due to rings outside the zone to which

these rays are tangential, multiplied by the relevant optical path

lengths in these areas, subtracted from itself. The resultant histogram

is then divided by the optical path in the region to which that part of

the beam is tangential. All these values can be calculated from the

interval between consecutive photomultiplier output peaks and a number

of calibration values like slit separation, magnification and the size of

BEAM 1

H_1

TOTAL DISTRIBUTION BEAM 1 RING 1

$H_1/I_{1,1}$

DISTRIBUTION/UNIT OPTICAL PATH RING 1

BEAM 2

$H_1 \times I_{2,1}/I_{1,1}$

DISTRIBUTION BEAM 2 RING 1

BEAM 2

H_2

TOTAL DISTRIBUTION BEAM 2 RINGS 1&2

$H_2 - H_1 \times I_{2,1}/I_{1,1}$

TOTAL DISTRIBUTION BEAM 2 RING 2

$(H_2 - H_1 \times I_{2,1}/I_{1,1})/I_{2,2}$

DISTRIBUTION/UNIT OPTICAL PATH RING 2
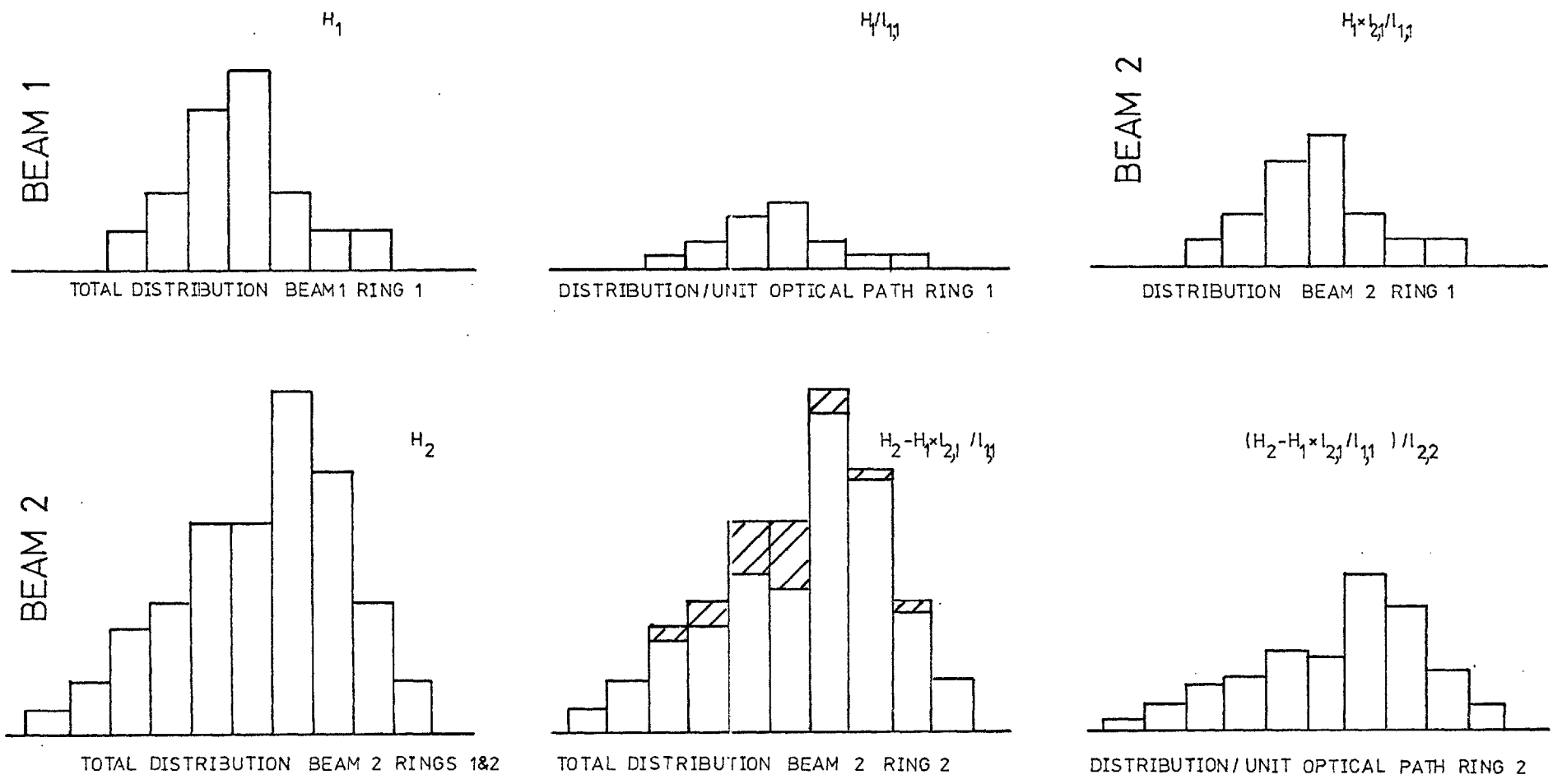
FIRST SUBSCRIPT - BEAM, SECOND - RING   H - MEASURED DISTRIBUTIONS   I - OPTICAL PATH LENGTH

Fig. 8.3   SUBTRACTIONS OF HISTOGRAMS

the concentric annuli selected by program "Veloc", (Appendix 2). It

should also now be clear why it was important to measure velocities

for the same (or at least a known) time duration at each point in any

one horizontal plane. It was necessary to obtain velocity distributions

not only per unit length of optical path but also per unit time before

carrying out the above-mentioned subtractions, in order to attach the

correct weighting factors to the measurements due to every ring. This

was ensured by measuring at each point for the same fixed amount of

time as described in Chapter VII. As discussed in the same chapter

the unequal slit separation provides a means of determining directions

of velocities as well as their magnitudes. This enables one to draw

up separate velocity distributions in the upward and downward directions.

Alternatively, it is possible to consider both sets of velocities in one

distribution by regarding all velocities in one direction as positive and

in the other as negative. It is therefore possible to obtain average

values as well as standard deviations and thus intensities of turbulence

for either case. The directional sorting of velocities, their conversion

into histograms and their correction in accordance with the annular model

discussed above as well as the calculations of the statistical properties

of the resultant distributions were carried out by program "Veloc".

(Appendix 2). The program was written in Standard FORTRAN IV.

VIII.2 Horizontal Velocity Analysis

Turning now to the horizontal velocities, the treatment of these is

somewhat more difficult as there are two different mutually perpendicular

components of motion (Fig. 8.4). They are also not always perpendicular

to the direction of the laser beam. One motion is in the radial direction.

This carries pockets of gas across the ring boundaries towards or away

from the centre of the wake. The other is a rotational motion - a result
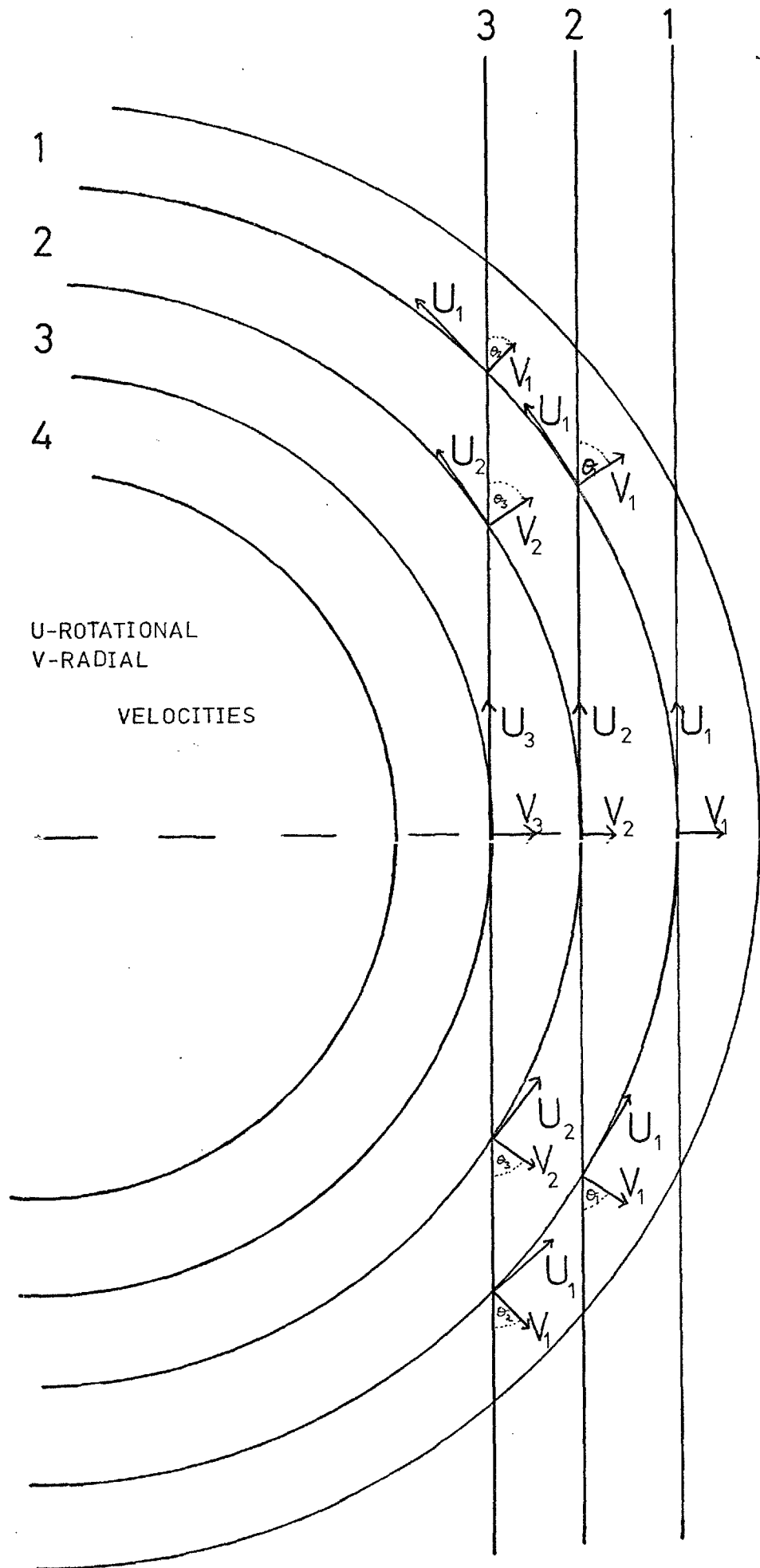
Fig. 8.4 CONCENTRIC RING MODEL – HORIZONTAL VELOCITIES

of the swirl induced by the arc rotation. As this project is mainly

concerned with the details of the distribution of the gases from the

plasma jet and from the surrounding atmosphere within the test region,

primary attention was focused on the radial motion, although the

rotational velocities of the wake region are of interest also.

VIII.2.1 Radial velocities

The part of the beam that touches the outermost zone of the wake

only presents no problems. Here the radial components of velocity are

perpendicular to the direction of the beam, while the rotational ones

are along it (Fig. 8.4). A pocket moving along the beam caused no signal

and was therefore not recorded. The distribution obtained is therefore

that of the radial velocities in that zone only. In order to normalize

it the distribution is again divided by the optical path of the beam

in that annulus. This is the case for all rings over the area in which

they interact with their respective beams tangentially. However, when

one comes to subtract the effects of the outer annuli, it becomes

necessary to allow for the angles $\theta_{N,M}$ between the directions of radial

velocity and the laser beam (Fig. 8.4). To do this the normalized

velocity histogram for each outer ring ($H_{N,A}, H_{N,B}$.....) has its value

intervals multiplied by the sine of that particular angle θ ($\theta_{N,A}, \theta_{N,B}$....)

that the beam makes with the radial direction in that particular zone.

The first subscript denotes the beam and the second the ring being

considered. The values from this distorted histogram are then fitted

into a new distribution with intervals equal to those chosen in the first

instance. Each of these new distributions is then multiplied by the

relevant optical path length (ℓ_{NA}, ℓ_{NB}....) and subtracted from the overall

histogram obtained by measurement from that beam.

VIII.2.2 Rotational Velocities

It is important to note here that while the effects of the radial velocity components in the outer rings have now been removed, contributions from the rotational velocities have so far been entirely neglected. They are, however, present in each set of non-tangential interactions between beams and rings. To be precise each rotational velocity has been multiplied by a cos θ before being recorded due to the geometry (Fig. 8.4). (Only the rotational velocity component perpendicular to the beam resulted in a reading.) Rotational components due to outer rings so far remain in the histograms belonging to all except the outermost ring, and as the distribution in each annulus is used in the calculation of all rings lying within it, the effect of the rotational velocities is cumulative. More exactly, each rotational velocity component from an outer beam has been multiplied by a sin θ in the "distortion" of the histograms before being subtracted when the distributions for the outer rings were calculated as discussed in the last section.

On the removal of these rotational components the help of the symmetry of the wake region is again enlisted. The rotational velocity has the same sense about the axis and a uniform distribution within each ring. Each part of the beam traverses every non-tangential region twice, once nearer the point of entry into the test region and once nearer the points of exit. The velocity distributions due to these traverses - as can be seen on closer inspection of Figure 8.4 - are equal in magnitude but opposite in direction when resolved into a component perpendicular to the laser beam. The velocity component along the laser beam is again not measured. As both path lengths in any one zone, as well as the duration of measurement, are equal, the distributions of velocity in either direction due to the rotational motion can be

expected to be equal. If we now consider motion in an outward direction
to be positive and motion towards the centre of the jet to be negative,
then every histogram for horizontal velocities in each ring so far
obtained is a distribution of radial velocities in each annulus with
another histogram superimposed on it. The second distribution which is
symmetric about the point of zero velocity is made up of the various
rotational velocity components multiplied by their respective trigono-
metric functions. These distributions were accumulated by successive
additions due to beams traversing the outer regions and subtractions
due to connections for effects of radial velocities in the outer rings,
as discussed above. It is important to note again that these additions
and subtractions do not cancel out as in the case of the radial velocity,
because here on each addition the distribution, (i.e. each of its inter-
vals) is multiplied by the cosine of the angle $\theta_{N,M}$, while in the case
of every subtraction this factor becomes $\cos \theta_{N-K,M} \times \sin \theta_{N,M}$ (Figure
8.4) leaving a symmetrical histogram formed by the rotational velocity
distributions, times the trigonometrical factors.

If, however, the negative section of every histogram is subtracted
from its positive counterpart, the symmetrical part is eliminated, and
a distribution is obtained, that consists of radial velocity components
only. In this process some of the radial velocity components are also
cancelled out, and it is therefore not possible to assert the actual
number of interfaces that have passed in each direction under the
influence of radial motion. It is, however, possible to calculate a
mean net velocity from each of the resulting histograms.

The subtraction was carried out by deducting each term on the
negative side of the distribution from its respective positive term.
It is therefore possible to have a negative number count for some velocity
intervals. Physically this means that a net number of velocity measurements

in this interval equal to the absolute value of that term was measured in the negative direction.

The mean velocity of each net distribution can either be calculated by considering positive and negative frequency counts of positive velocity intervals only, or by allowing only positive frequencies for positive and negative velocities. As the mean is calculated by the summation of terms made up of products of number frequency times velocity intervals, both approaches result in equal average values. (Law of Commutation of Multiplication.)

However, it is not possible to compute a true standard deviation for the total horizontal velocity component in any of the rings, as the true total velocity distribution for radial plus rotational velocities is not known anywhere. Even in the outermost zone the standard deviation for radial components, in the innermost that for rotational components only can be calculated as the other components, are in both cases along the beam.

It is re-emphasized that the standard deviation in this case is not an indication of the uncertainty in the measurement, but rather a measure of the degree of turbulence for the system exhibiting a velocity distribution of the form:

$$V_J = \bar{V} + \Delta V_J$$

where V_J is the Jth term of distribution, $\bar{V}$ the mean velocity and ΔV the fluctuating velocity component.

Mean net horizontal radial velocities were calculated by program "Veloc 2" listed in Appendix 3.

Chapter IX

RESULTS AND DISCUSSION OF 'SCHLIEREN VELOCIMETER'

MEASUREMENTS

All measurements obtained using the 'Schlieren Velocimeter" as described in Chapter VII underwent the analysis as outlined in Chapter VIII. All values referred to in this chapter as velocities at a point are in fact mean velocity values computed from those corrected velocity distributions.

IX.1 The Effect of Two Peak Measurements

As previously mentioned, a number of oscilloscope traces exhibited only two rather than three peaks. These measurements could not give any indication about the direction of velocity. It was therefore necessary to determine what influence an omission of the two peak measurements would have on the overall measured mean velocity. Measurements were taken for a fixed flow rate at a number of points in the wake and average values were determined separately for two and three peak measurements. Directions of flow were disregarded as two peak readings could not yield an indication of directional preference. Both mean velocities were plotted for points at various distances above the nozzle and off axis in Figure 9.1.

This shows that the values obtained for two and three peak measurements are generally in good agreement with the possible exception of points near the boundary of the wake. Reasons for these discrepancies are suggested in Chapter VII. It was therefore decided that the consistent use of three peak readings only could be expected to yield acceptable results.
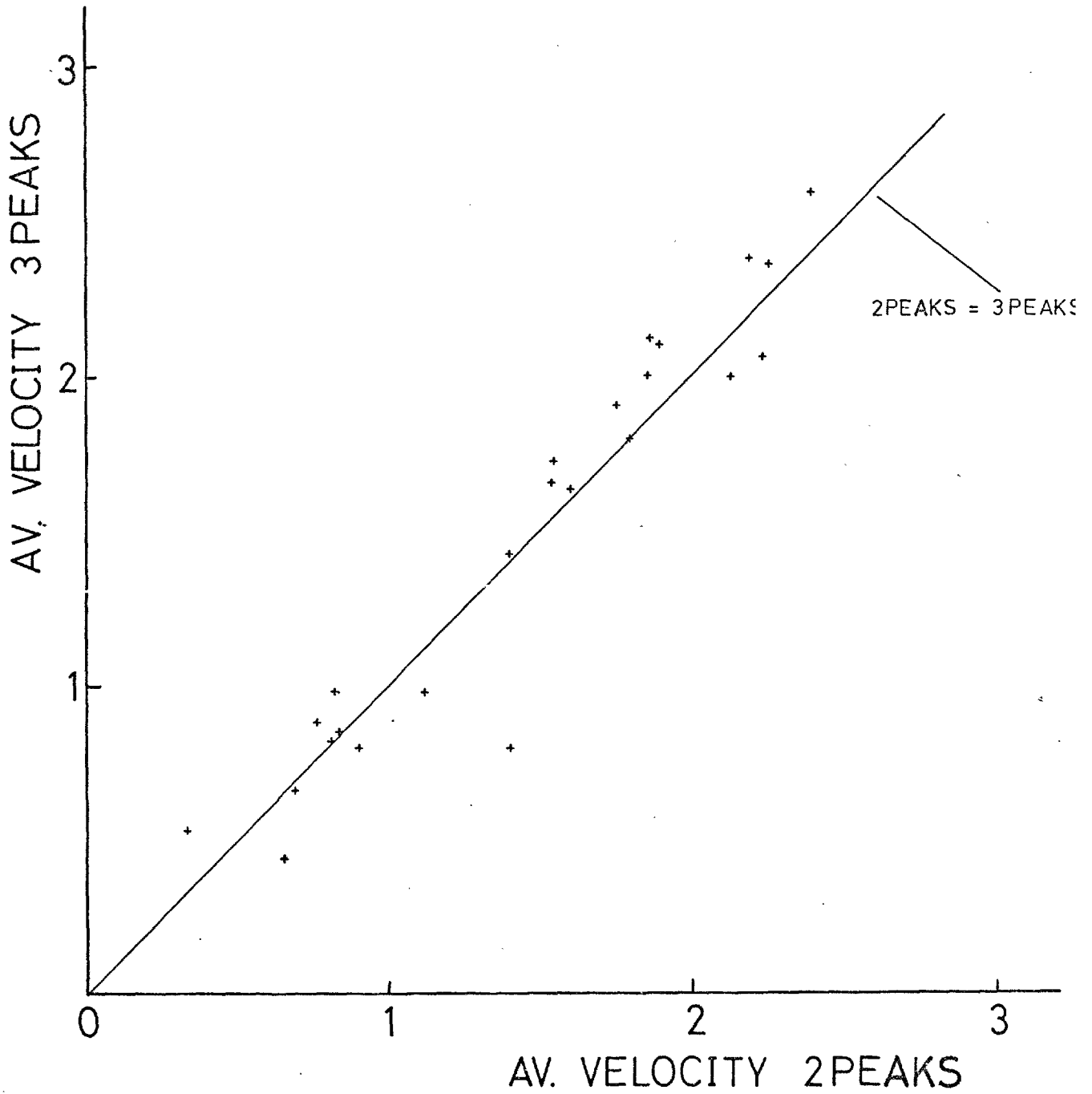
Fig. 9.1   COMPARISON OF 2 PEAK AND 3 PEAK RESULTS

IX.2 Measurements in the Complete Wake

Complete analyses were carried out throughout the wake for horizontal and vertical velocities with high and low carrier gas flow rates. For the high argon flow rate at 13 l/min and a cold flow Reynolds number of 2225, the region between 2 and 8 cm above the nozzle was measured at points 5 mm apart in the horizontal direction in rows 10 mm above each other. For the low flow of 4.4 l/min and cold flow Reynolds number of 750 measurements were taken at the same intervals from 1 to 7 cm above the plasma. High speed shadow cine records (Chapter IV) obtained at these flows show that for the higher carrier gas flow rate the entire central part of the wake region in the laser beam is made up of the "fast flow region" in which the effect of arc rotation predominates, as discussed in Chapter V. For the case of argon supplied at 4.4 l/min the test region contains the transition from the arc rotation controlled zone to the slower outer flow which had previously been found to be independent of the events in the nozzle.

Mean vertical velocities were computed from the average upward and downward velocities at each point, whereby, especially in the inner segments of the wake, the more prominent flow direction by far was found to be upward. The mean velocity values of all points in every row were fitted to a quadratic function of velocity in terms of radial distance from the centre of the wake, using the Method of Least Squares. The maximum of this velocity function was determined and the radial distance at which it occurred is plotted in Figure 9.2 for the high and Figure 9.3 for the slow flow rate. (It is not claimed that this quadratic is the best fit of velocity versus distance. It is used only to confirm the symmetry of the wake.) The same calculations were executed for the number of measurements obtained per unit time at all points at various
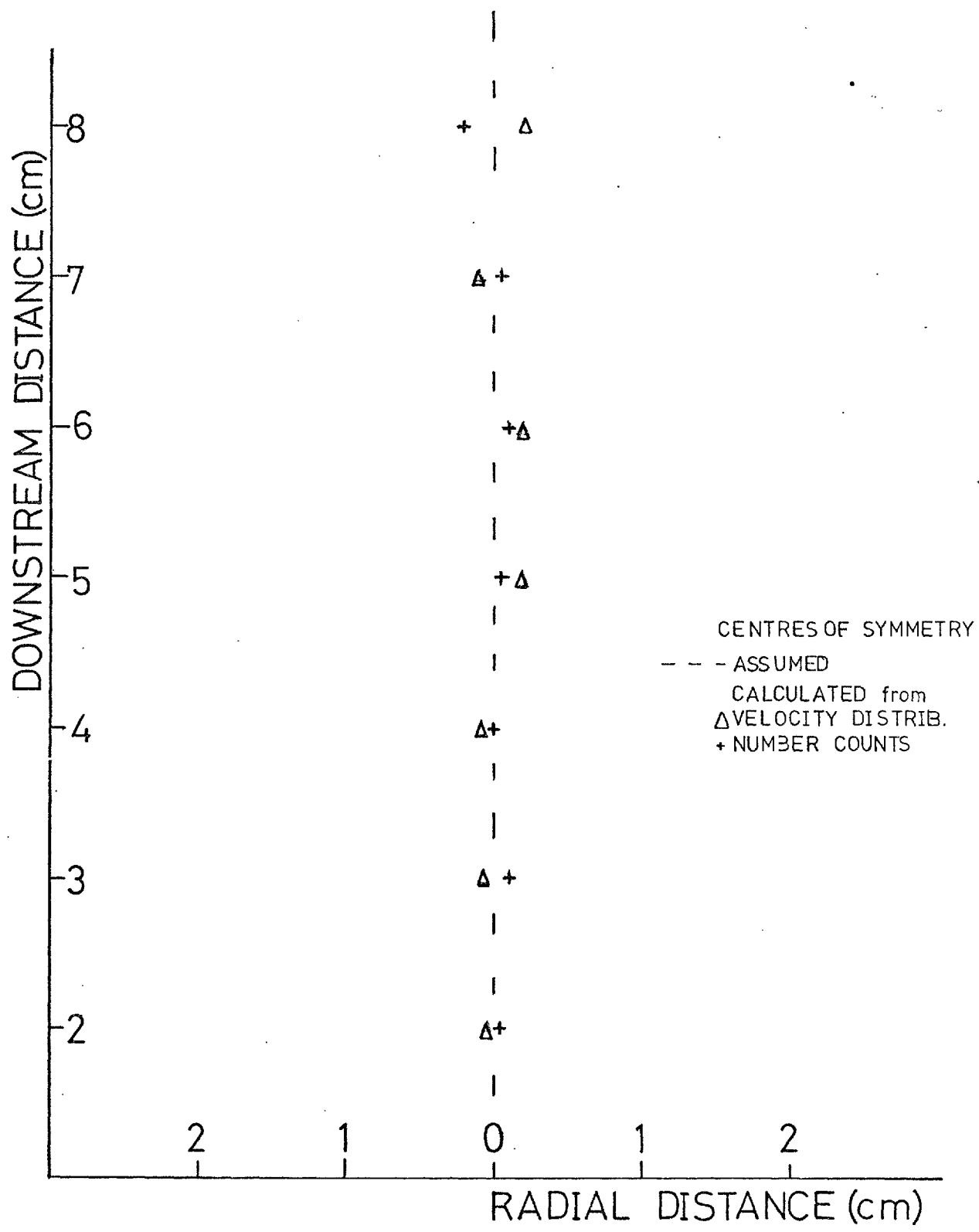
Fig. 9.2   CENTRES OF SYMMETRY FROM VELOCITY AND NUMBER
          DENSITY VS. RADIAL DISTANCE
          13 1/min ARGON, 1.1 kHz ARC ROTATION

Fig. 9.3   CENTRES OF SYMMETRY FROM VELOCITIES AND NUMBER
            DENSITIES VS. RADIAL DISTANCE
            4.4 1/min ARGON, 1.1 kHz ARC ROTATION
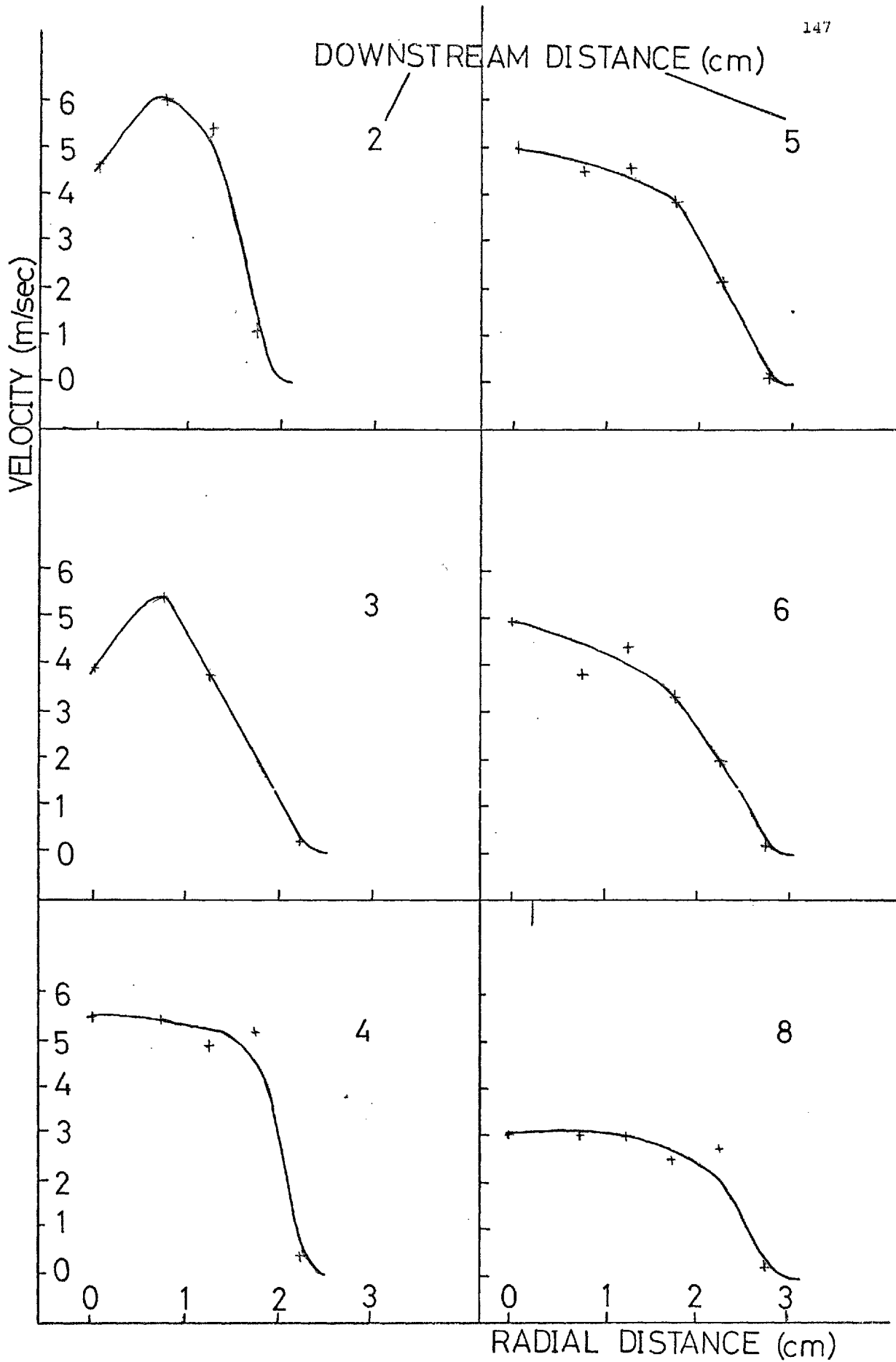
Fig. 9.4 VELOCITY VS. RADIAL DISTANCE
13 l/min ARGON, 1.1 kHz ARC ROTATION
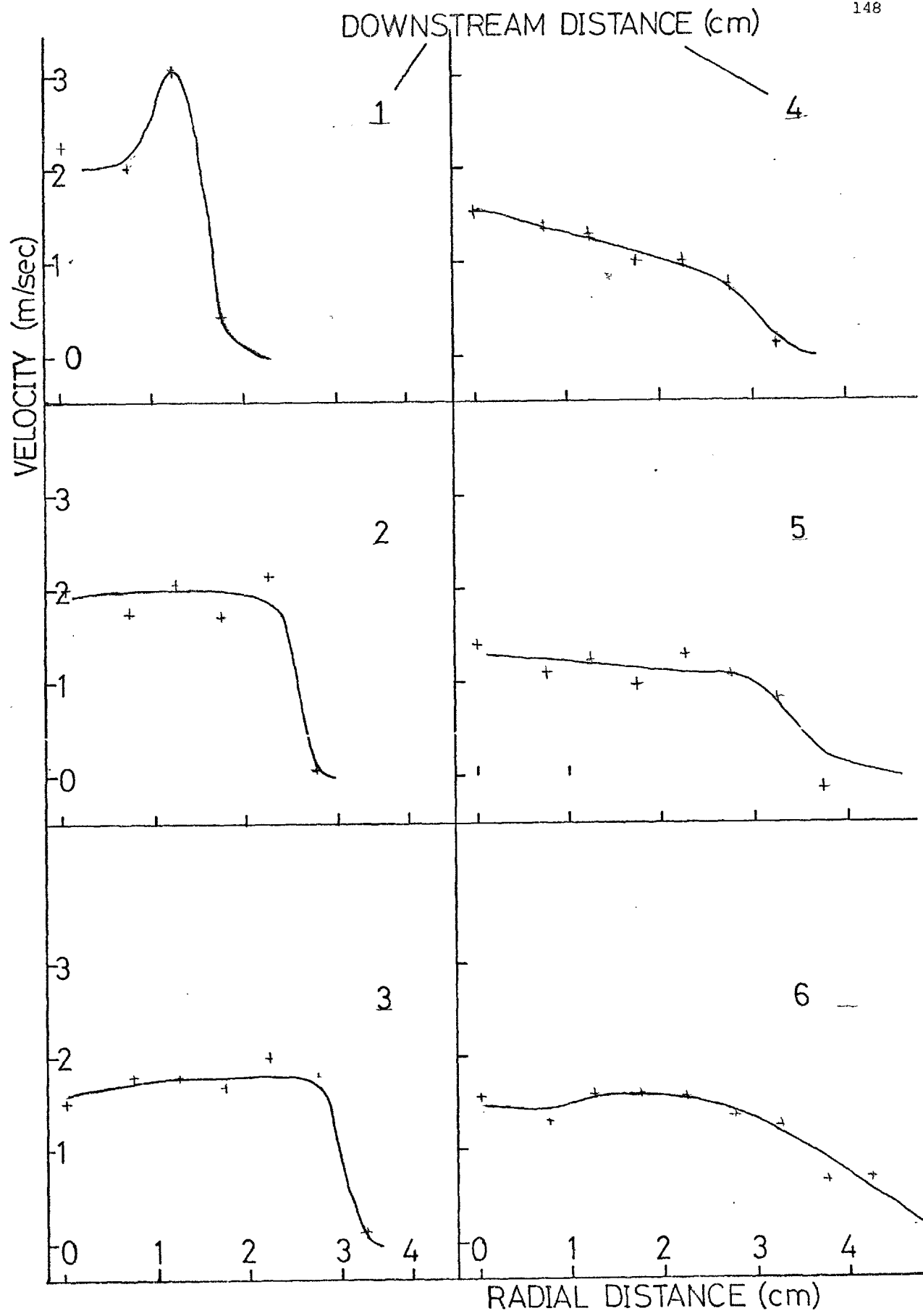
Fig. 9.5   VELOCITY VS. RADIAL DISTANCE
4.4 1/min ARGON, 1.1 KHz ARC ROTATION

heights above the nozzle and the positions of their maxima are included

in Figures 9.2 and 9.3. These frequency counts give an indication of

the number of interfaces passing each point in the test region. Each

of the four sets of maximum positions are seen to lie within 2 mm of

the central axis of the wake. This emphasizes further the cylindrical

symmetry of the test region, previously observed in Chapters V and VI.

The variations of the vertical velocities with radial distance

in the wake for various heights above the nozzle are plotted for both

carrier gas flow rates. Figure 9.4 shows this variation for the high

carrier gas throughput, while Figure 9.5 gives the same information for

the lower argon flow. In both cases the plots show an increase in

vertical flow velocity as one moves away from the centre with a maximum

mean flow velocity about 1 cm from the axis of symmetry of the wake.

Past this maximum value the velocity falls almost linearly to zero at

the outer limit of the wake. This is true up to a height of a few

centimetres above the nozzle. Further downstream the central dip in

the magnitude of the velocity is smoothed out, resulting in a velocity

value plateau near the centre of the wake reducing to zero near its

boundaries.

IX.3 Errors and their Corrections

Mean velocity measurements in the vertical as well as horizontal

direction are liable to both statistical, i.e. random, and to systematic

errors. These errors are relatively more important in the case of the

horizontal results for a number of reasons. The horizontal velocity

distributions actually measured have smaller mean values and larger

relative standard deviations. It is, however, important to re-emphasize

that because of the turbulence of the system, the standard deviations are

not direct measures of the error in determining velocities. Horizontal

velocities, as the main flow is in the upward direction, also resulted

in fewer measurements per unit time, because a smaller number of pockets

passed the three horizontally spaced slits in every time interval.

For the same reason relatively fewer interfaces actually completed their

horizontal journey across all three slits within the time of their

presence in the small test area defined by the slits. Last, but not

least, the statistical analysis required to obtain the horizontal mean

gas velocity at each point rather than only its component perpendicular

to the laser beam is far more complex than that for the vertical motion

which is entirely at right angles to the beam, as discussed in Chapter

VIII. This is compounded by the fact that each horizontal velocity

distribution obtained is made up of radial and rotational velocities

of which the rotational components need to be cancelled out, which

makes the calculation of only net mean velocities possible.

The horizontal mean velocities only are therefore corrected. The

correction is made on the basis that for symmetric flow the net horizon-

tal velocity at the centre of the wake is required to be zero. As the

systematic error is expected to predominate, the error in the mean

velocity obtained along each beam (E_n) is taken as fixed. (The

condition of a mainly statistical error, i.e. E_n is a function of the

number of readings per unit time, gives very similar results.) The

error in mean velocity for the nth segment, ε_n, is calculated by the

following formula:

$$\varepsilon_n^{\,2} = E_n^{\,2} + \sum_{J=1}^{n-1} \varepsilon_J^{\,\prime\,2}$$

where n is the number of the ring counted from the outside and $\varepsilon_J^{\prime}$ is a

function of the error in the Jth ring. This is because the mean velocity

value in each ring contains errors from that beam and all the outer

rings. Even though the effects of the outer rings were subtracted

(Chapter VIII) the resulting errors need to be computed by obtaining

the square root of the sum of the squares of the contributing errors.

As discussed in Chapter VIII in the case of the horizontal velocities

each measurement contains only the radial velocity component perpendi-

cular to that laser beam, i.e. the radial velocity times the sine of

the angle (θ_J) between the velocity direction and the beam. Each error

term in the summation due to the outer rings (ε'_J) therefore contains

the relevant sine for that beam, i.e.

$$\varepsilon'_J = \varepsilon_J \sin \theta_J$$

For the central beam, for example, all θ_J's are zero and $\sin \theta_J$'s

therefore zero.

Given the boundary condition of no horizontal velocity at the

centre and constant error (E_n) along all beams it is possible to obtain

a value of the error of mean velocity in each segment (ε_n) from the

above equations. The precise causes of the errors are contained in the

term E. It is not necessary for them to be known for this analysis as

long as they are systematic in nature.

All horizontal mean velocity values were corrected accordingly and

these values are used in all further calculations and discussions.

IX.4 Velocity Distribution and Streamlines

The velocities assigned to each point were plotted throughout the
test region in their vertical and horizontal components and were combined
to yield resultant velocities at each point, using the rules of vector
addition. As described in Chapter VIII mean velocity values obtained
for each beam are assigned to the centre of the annulus to whose inner
boundary that beam is tangential. Figures 9.6 and 9.7 show the velocity
distributions obtained throughout the test regions for the fast and slow
carrier gas flows respectively. The starting position of each arrow
indicates the locality at which that mean velocity was determined, while
the lengths and orientations of the arrows represent the magnitudes of
the velocities in the indicated directions.

From an inspection of these flow vectors it can be seen that the
main velocity occurs in an upward direction near the centre of the wake,
and that it decays relatively slowly as one moves downstream. Near the
wake boundaries the vertical velocities are much lower and no longer
dominate. The horizontal flows, which result in the expansion of the
wake and the entrainment of the surrounding air, become apparent in that
region.

These velocity distributions are joined to give streamlines covering
the test region in Figures 9.8 and 9.9. While the magnitudes of the
velocities are not discernible from these flow lines an overall flow
pattern is established for each wake region, showing the main central
flows as well as the entrainment of the surrounding gases, the latter
especially in the case of the lower carrier gas throughput rate.

The pattern for the larger argon flow (Fig. 9.8) shows a pronounced,
slightly wavy central flow region, mainly upwards in direction, with a
small amount of expanding flow and relatively little indication of
recirculation and entrainment in the area covered by the laser beam
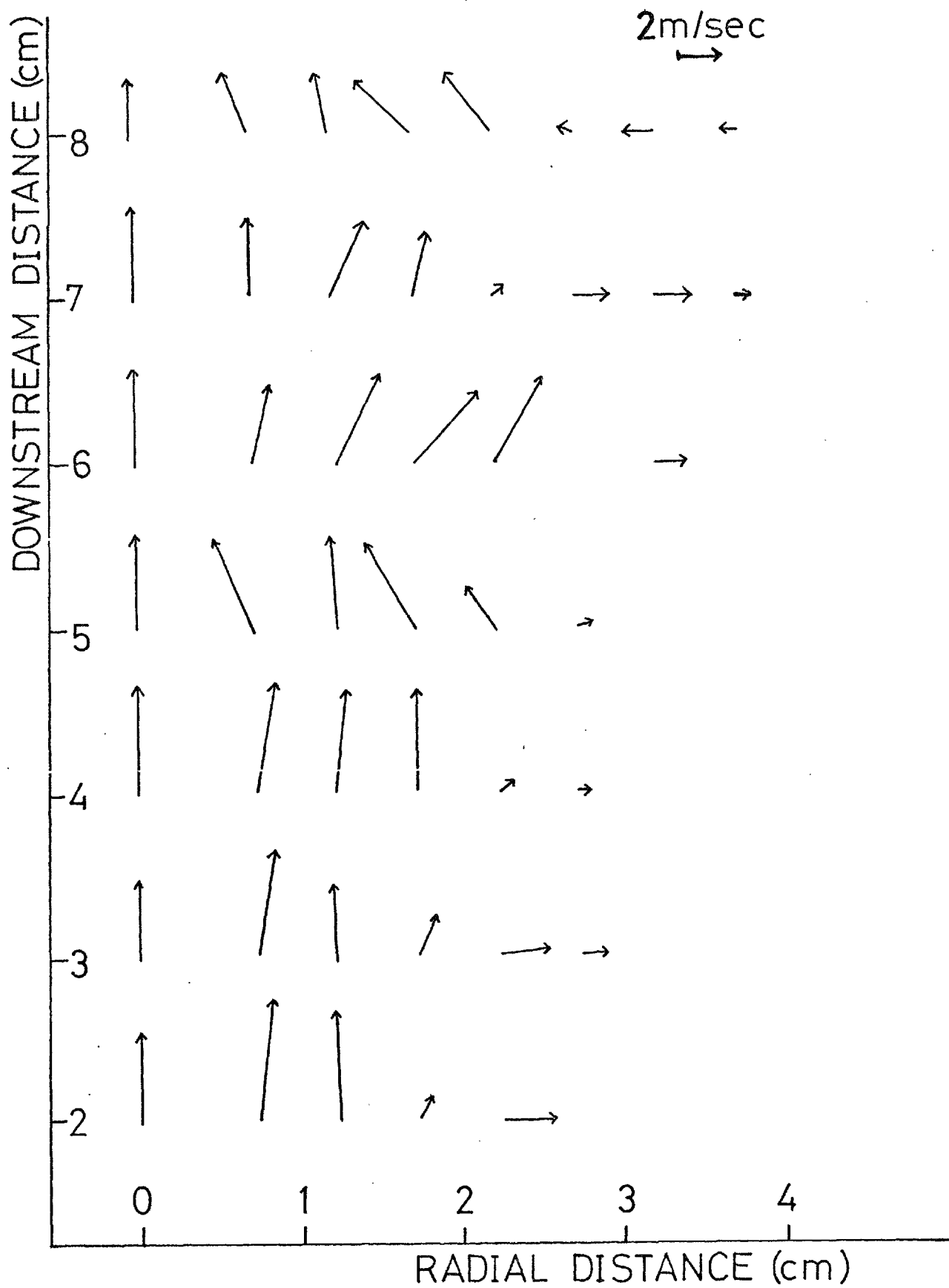
Fig. 9.6 VELOCITY VECTOR DISTRIBUTION
13 l/min ARGON, 1.1 kHz. ARC ROTATION
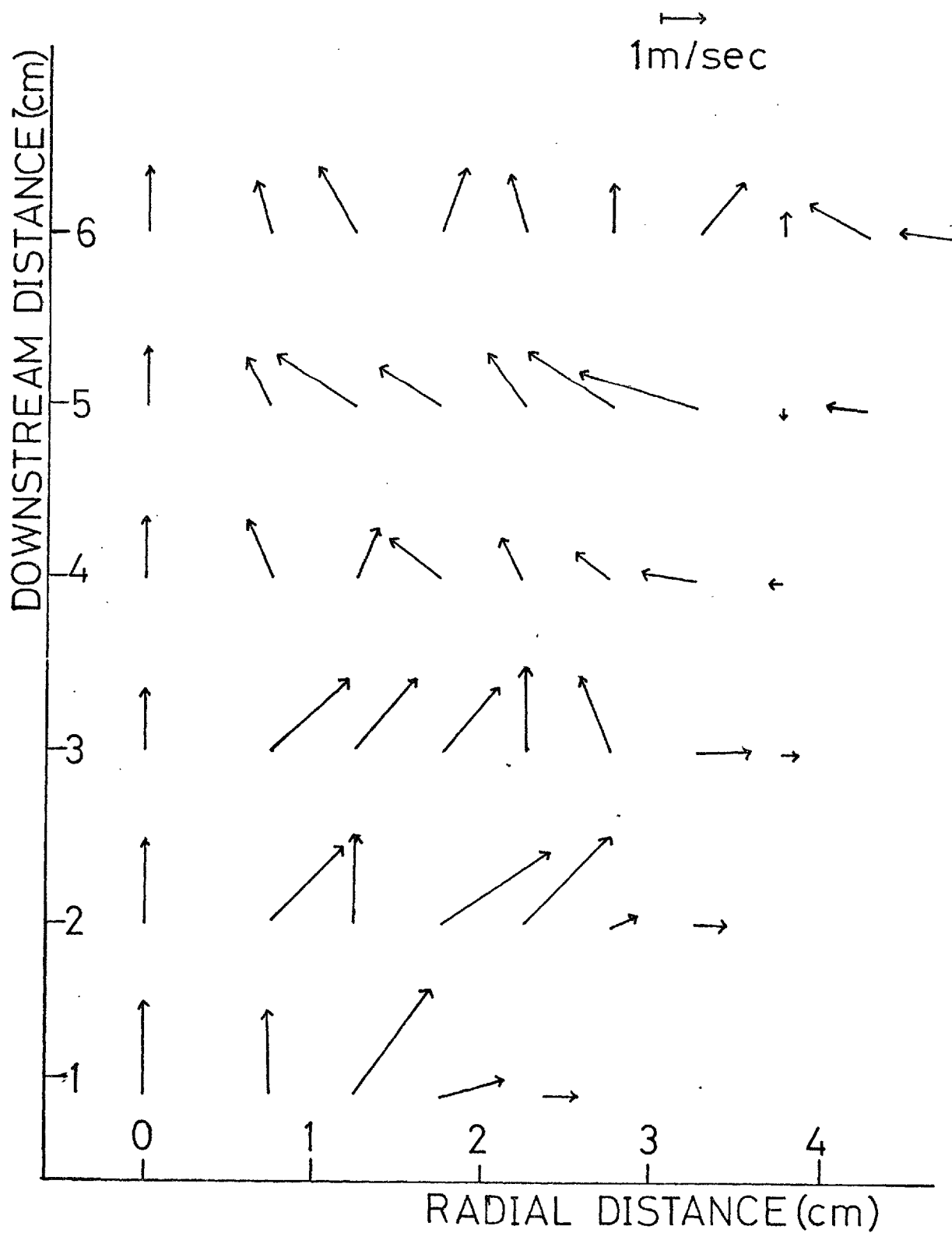
Fig. 9.7   VELOCITY VECTOR DISTRIBUTION
4.4 l/min ARGON, 1.1 kHz. ARC ROTATION
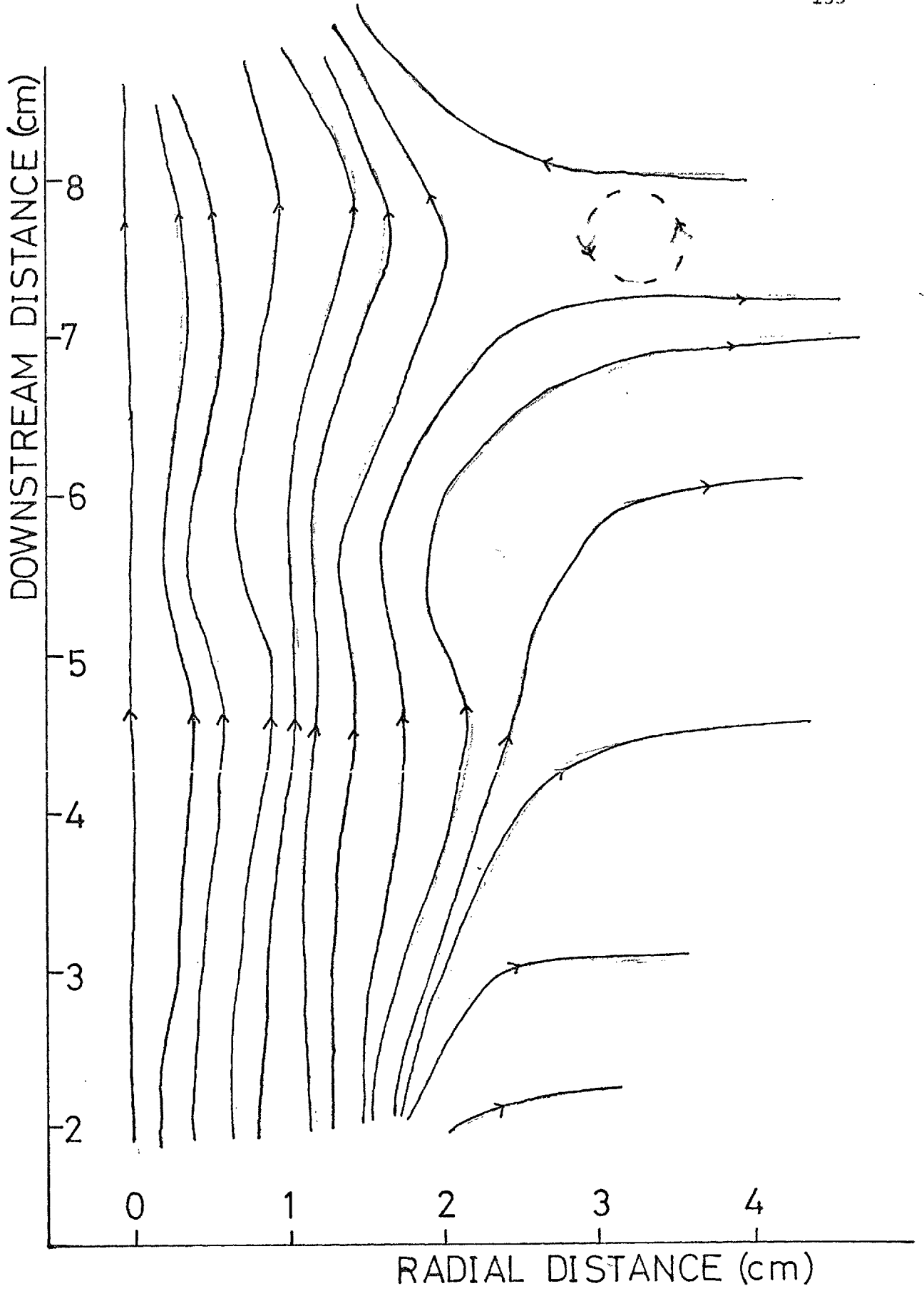
Fig. 9.8   STREAMLINES
13 l/min ARGON, 1.1 kHz. ARC ROTATION
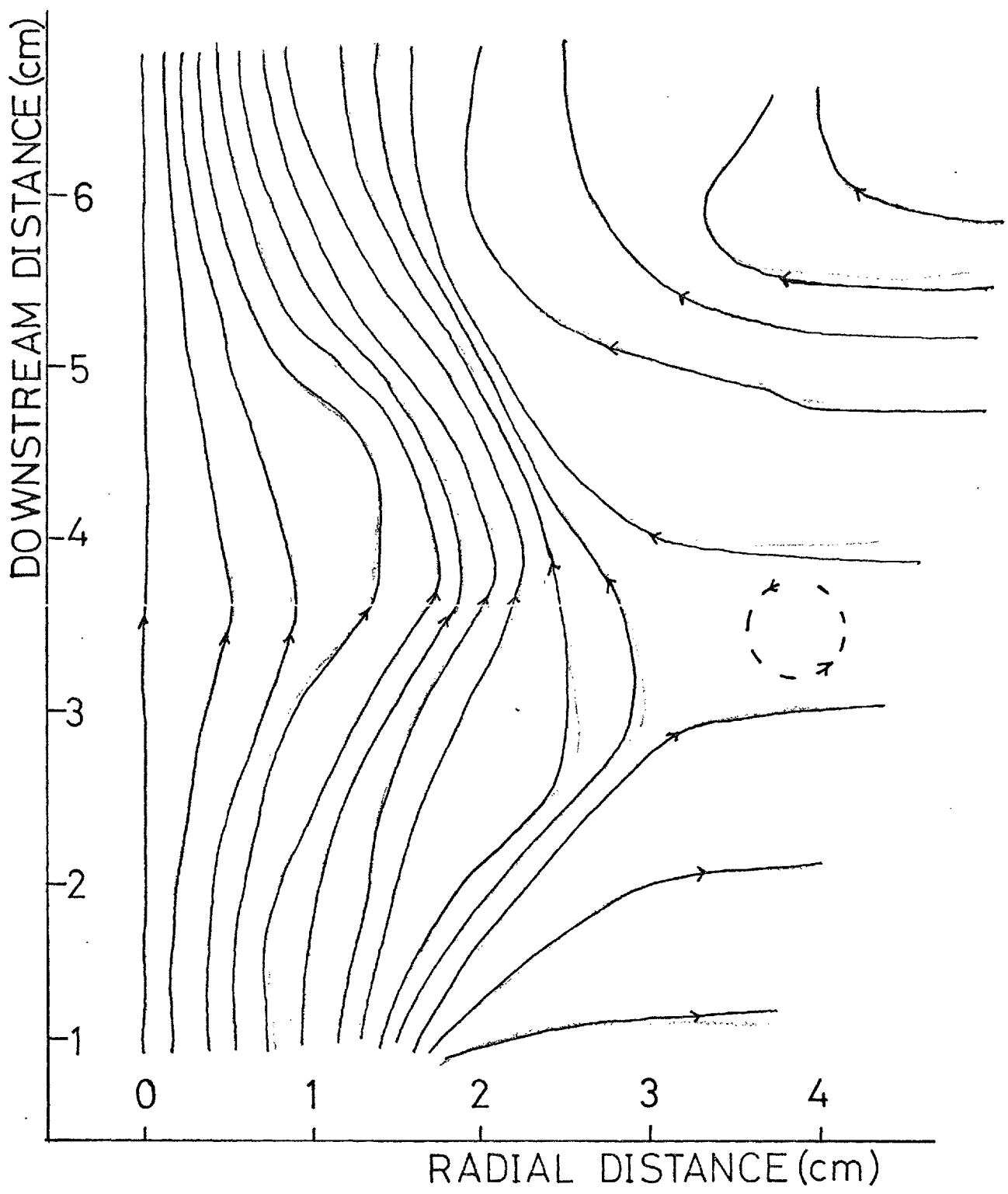
Fig. 9.9   STREAMLINES
. 4.4 l/min ARGON, 1.1 kHz. ALC ROTATION

(from 2 cm to 8 cm downstream of the nozzle) except near its top end. In the case of the slower flow (Fig. 9.9) the pattern shows a more rapidly expanding jet counteracted by considerable entrainment flow 4 cm and further downstream of the burner nozzle, and the resulting recirculating eddies.

Eddies of a diameter of less than 1 cm - the vertical separations between positions of consecutive measurements - are not discernible. Also, because these are time averaged velocity measurements, laterally moving eddies cannot be resolved, although they were clearly visible on the high speed cine shadow records (Chapter IV).

IX.5 Estimation of Entrainment in the Immediate Vicinity of the Nozzle

A system of tight fitting concentric rings, similar to the one used to correct for the effects of the integration along the optical path of the laser beam in Chapter VIII, is again superimposed on each wake region. Each ring has a thickness of 5 mm, the central regions consist of cylinders of radii 7.5 mm and all heights are 10 mm. Six layers of such rings, each following immediately on the previous, are considered for the high and the low carrier gas throughput. The inter-section between a plane containing one half of a central cross-section through the wake and the concentric ring system, results in a grid made up of rectangles of width 5 mm (7.5 mm nearest the centre of the wake) and height 10 mm, as shown in Figure 9.10. The grid is positioned such that the centre of each vertical segment coincides with an assigned position of velocity measurement.

From the horizontal and vertical velocity components of each point as measured and plotted in Figures 9.6 and 9.7, the average vertical mean for each horizontal grid section and the average horizontal mean

Fig. 9.10   VELOCITIES AT GRID CENTRES
13 l/min ARGON, 1.1 kHz ARC ROTATION

DOWNSTREAM DISTANCE (cm)

Top row: 1·34 → 1·18 → 1·33 → 1·39 → 1·37 → 1·15 → ·9 → ·58 → ·22 →

Row 6: ·47 ← 1·28 ← ·12 ← ·54 ← ·47 ← ·02 → 1·23 ← 1·02 ←
1·3 ↑ 1·28 ↑ 1·34 ↑ 1·34 ↑ 1·33 ↑ 1·14 ↑ ·65 ↑ ·32 ↑ ·24 ↑

Row 5: ·55 ← 1·49 ← 1·16 ← ·81 ← 1·4 ← 2·01 ← ·05 ← ·95 ←
1·35 ↑ 1·26 ↑ 1·11 ↑ 1·05 ↑ 1·05 ↑ ·71 ↑ ·2 ↑   ·01 ↓

Row 4: ·11 ← ·12 ·85 → ·56 ← ·98 ← 1·19 ← ·15 ←
1·55 ↑ 1·56 ↑ 1·44 ↑ 1·41 ↑ 1·4 ↑ ·71 ↑ ·06 ↑

Row 3: 1·51 → ·98 → 1·32 → ·26 ·38 ← ·79 → 2 →
1·76 ↑ 1·86 ↑ 1·82 ↑ 1·88 ↑ 1·51 ↑ ·5 ↑ ·03 ↑

Row 2: 1·6 → ·53 → 2·4 → 1·66 → ·42 → ·77 →
2·01 ↑ 2·11 ↑ 1·71 ↑ 1·07 ↑ 0·6 ↑ ·02 ↑

RADIAL DISTANCE (cm) 0 1 2 3 4 5

VELOCITIES IN m/sec
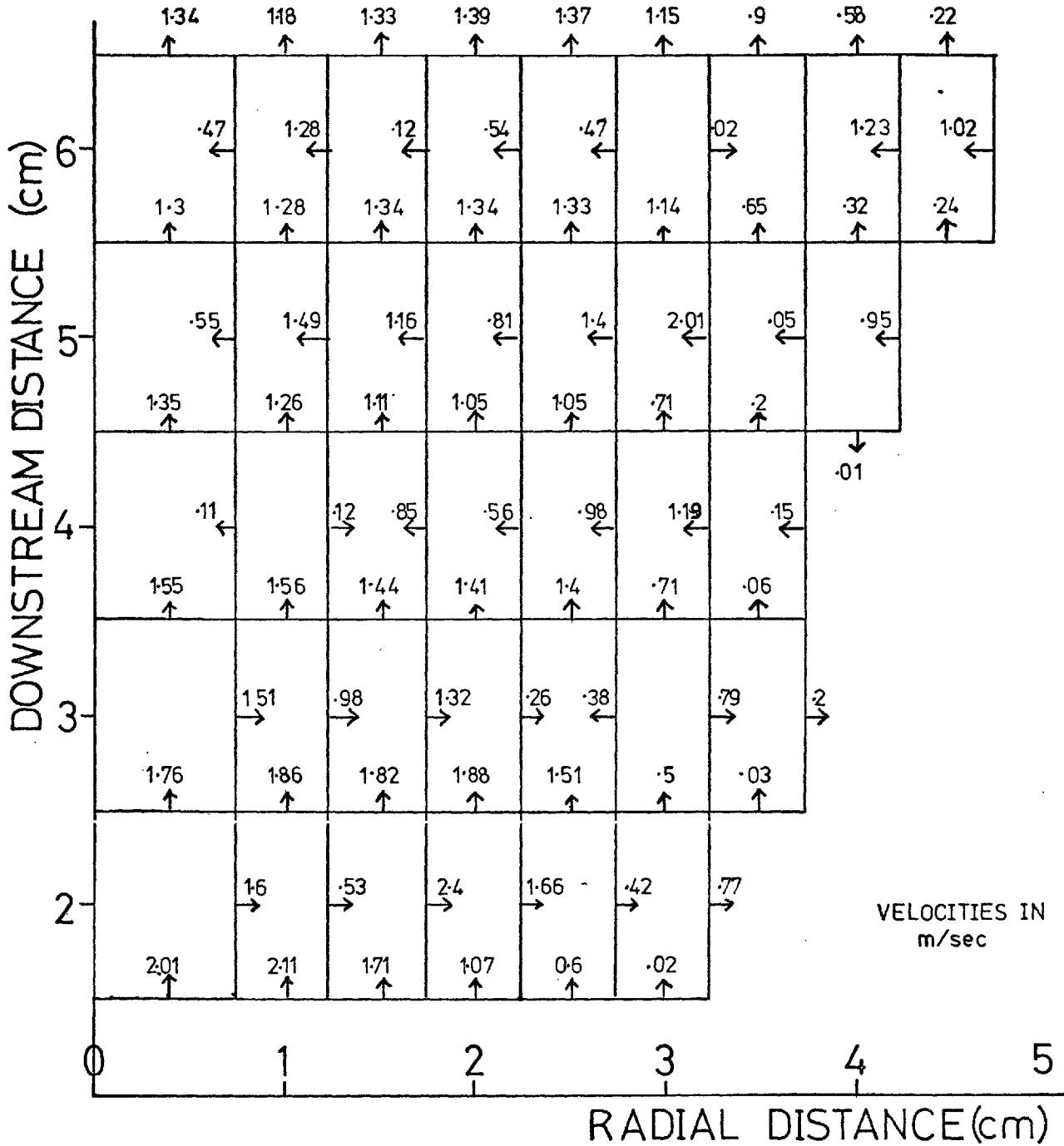
< 1·77 × 3·14 × 4·71 × 6·28 × 7·85 × 9·42 × 11·0 × 12·57 × 14·14 >

4·71 7·85 11·0 14·14 17·28 20·42 23·56 26·70 29·85

GRID AREAS

Fig. 9.11 VELOCITIES AT GRID CENTRES
4.4 l/min ARGON, 1.1 kHz ARC ROTATION

$V_{M,N+2}$ $V_{M+1,N+2}$

$U_{M,N+2}$ $U_{M+1,N+2}$

$N \uparrow V$

$U \rightarrow$ M

$(V_{M,N+1} + V_{M+1,N+1} + V_{M,N+2} + V_{M+1,N+2})/4$

$(U_{M,N+1} + U_{M,N+2})/2$ $(U_{M+1,N+1} + U_{M+1,N+2})/2$

$V_{M,N+1}$ $V_{M+1,N+1}$

$U_{M,N+1}$ $U_{M+1,N+1}$

$(U_{M,N} + U_{M,N+2})/6 + U_{M,N+1} \times 2/3$ $(U_{M+1,N} + U_{M+1,N+2})/6 + U_{M+1,N+1} \times 2/3$

$(V_{M,N} + V_{M+1,N} + V_{M,N+1} + V_{M+1,N+1})/4$

$(U_{M,N} + U_{M,N+1})/2$ $(U_{M+1,N} + U_{M+1,N+1})/2$

$V_{M,N}$ $V_{M+1,N}$

$U_{M,N}$ $U_{M+1,N}$
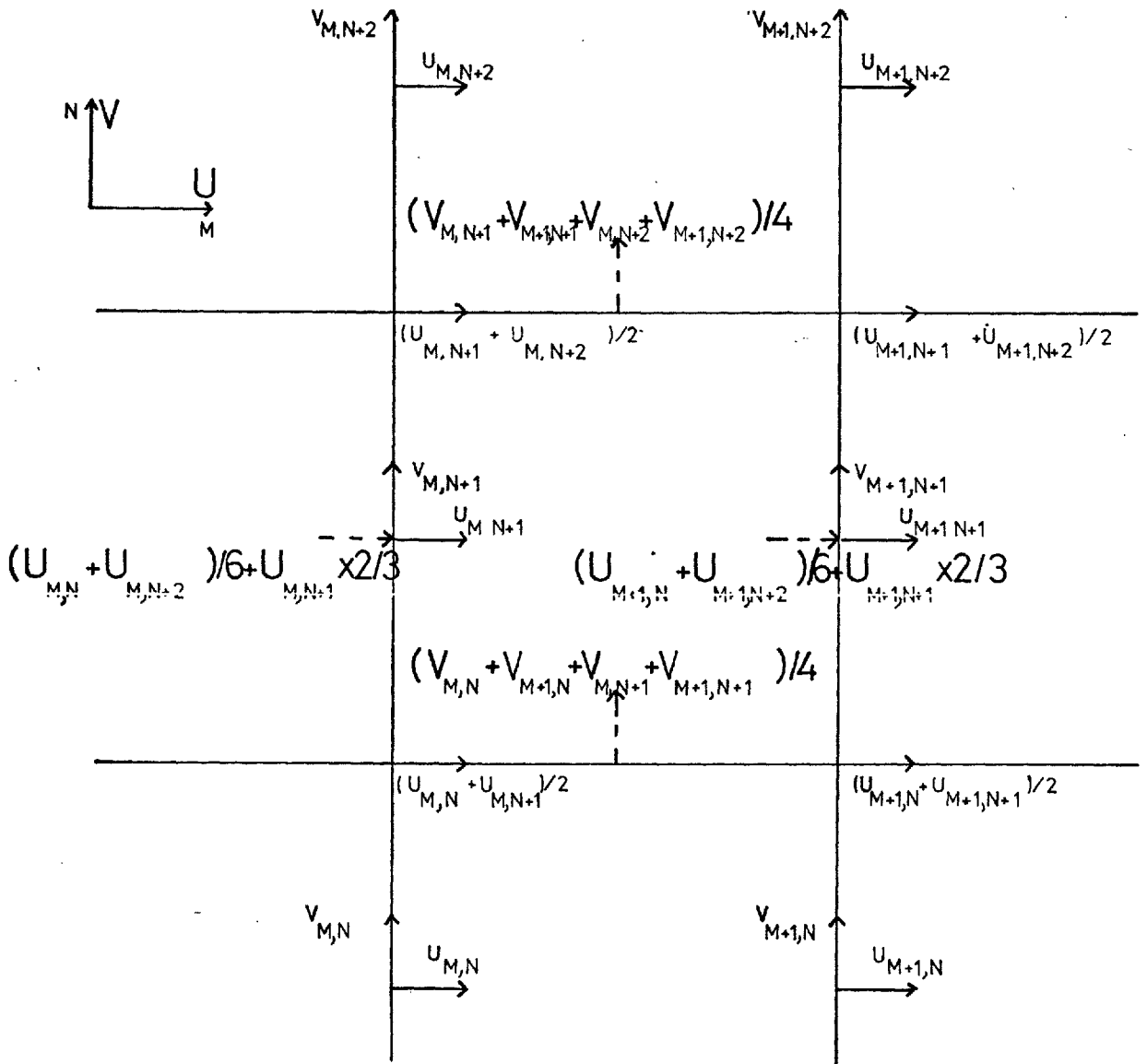
U,V GRID CENTRE VELOCITIES   U,V MEASURED VELOCITIES

Fig. 9.12   DETERMINATION OF MEAN VELOCITIES AT GRID
CENTRES

velocity for each vertical segment, were calculated and plotted for both argon flow rates (Figs. 9.10 and 9.11). Average vertical velocities were obtained by determining the mean of the four vertical velocities closest to the midpoint of each horizontal segment, while the horizontal velocities were computed by finding the mean horizontal velocity at each corner of each grid area and then averaging that with the relevant velocity component measured at the grid centre (Fig. 9.12).

As long as there are no abrupt velocity changes away from the central section of any grid segment, the product of the mean velocity component perpendicular to a grid line, times the area of the concentric ring surface, whose intersection with the central cross section results in that line, determines the net volumetric flow through that surface. As the surfaces containing the outer annuli are much larger than those near the centre, any errors in velocity measurements introduced near the wake boundaries by the lower flow velocities and fewer measurements per unit time encountered there, are emphasized in determining these flow rates.

The total flows through the surfaces which limit the grid systems at the upstream end (1 cm downstream of the nozzle for the slow flow and 2 cm for the fast argon flow) are considered first. The total flow rates through these surfaces are determined by adding the products obtained from the multiplication of each surface element times the mean vertical velocity assigned to its midpoint.

$$\text{Flow Rate} = \sum_{n=1}^{m} \pi(R_n^2 - R_{n-1}^2) \times V_n$$

where R_n is the outer limit of the nth ring, V_n the vertical velocity assigned to its centre, and m the number of sections contained in the surface considered. This flow is compared for both throughput rates

with the volumetric argon flow rates out of the nozzle. The volumetric

flow rates at the nozzle at room temperature are known from the

rotameter and gas temperature measurements. The energy transferred

from the arc to the gas was calculated as the difference between the

electrical energy supplied to the arc and the heat losses to the

cooling water of the plasma jet burner, which were constantly monitored.

Radiative losses were neglected. Dividing the heat transfer rate to

the gas by the mass flow rate of the argon, results in the mean heat

input per unit mass. From this and the specific heat at constant

pressure c_p - a quantity constant up to temperatures of 8000 $^\circ$K of

0.127 cal/l $^\circ$K in the case of argon (Ref. 35) - the mean temperature

of the gas leaving the plasma was calculated. Using the Ideal Gas Laws

the volumetric flow rate (V_o) at the exit of the plasma jet is given as

$$V_o = V_R \times T_o/T_R$$

where V_R is the volumetric flow rate at room temperature (T_R) and T_o

the nozzle exit gas temperature. It is, however, not necessary to

assume a uniform distribution of energy from the arc to the gas. It

has been shown (Appendix 1) that the volumetric expansion is the same

whether the externally supplied energy is equally distributed to heat

all the gas to a uniform final temperature or is concentrated into a

fraction of the gas raising that part to a higher temperature and leaving

the remaining argon at room conditions, as long as the pressure remains

constant and the Ideal Gas Laws are observed.

In the case of the high argon flow rate 39% by volume of the gas

passing the first surface, i.e. the first line of measuring stations,

is entrained gas; similarly 46% for the slower flow rate. By mass the

ratios of entrained air to total gas are even higher, 85% for the first

case and 93% for the second, because of the much higher temperature

of the argon compared to the entrained air. If heat transfer from

the hot argon to the colder air is allowed for, the proportion of

entrained gas increased yet further because the specific heat of air

is nearly twice that of argon and a given quantity of energy therefore

causes less expansion of air than of argon.

This indicates a very high level of entrainment of surrounding

air into the plasma jet wake in the immediate vicinity of the nozzle

for both high and low flow rates. There is, however, no reason to

believe that this entrainment was uniform across the wake. Most of the

entrained gas must have passed near its boundaries, as determined in

Section V.4 dealing with high speed cine records. As these entrainments

took place upstream of the test regions they are not indicated in

Figures 9.8 and 9.9.

IX.6   Relative Densities in the Wake

Every ring in the system is now considered to contain a gas mixture

of mean density ζ_J. As there is no source or sink of gas in any of the

rings the Law of Conservation of Mass can be expressed in the form of an

integral around the total surface surrounding each ring:

$$\oint \zeta_x \, v \, dA = 0$$

where ζ_x is the density of gas flowing into or out of the surface and v

the velocity perpendicular to the surface dA. In practice, the products

of all surfaces times the mean velocities perpendicular to them were

added for each ring. Applying this to every section of the wake gives

a set of simultaneous equations equal to the number of rings present.

Solving these equations results in a value for the mean density for each

DOWNSTREAM DISTANCE (cm)

	DA	DB	DC	DD	DE		
7	·65 DA+ ·35 DB	·08 DA+ ·13 DB	·10 DA+ ·19 DB+ ·16 DC+ ·01 DD	·08 DA+ ·17 DB+ ·25 DC+ ·02 DD+ ·01 DE	·02 DA+ ·06 DB+ ·10 DC+ ·01 DD+ ·01 DE	·02 DA+ ·05 DB+ ·09 DC+ ·01 DD+ ·01 DE	·07 DA+ ·16 DB+ ·29 DC+ ·03 DD+ ·03 DE
6	·55 DA+ ·29 DB	·13 DA+ ·22 DB	·07 DA+ ·14 DB+ ·19 DC+ ·01 DD	·05 DA+ ·13 DB+ ·25 DC+ ·02 DD+ ·01 DE	·07 DA+ ·19 DB+ ·37 DC+ ·04 DD+ ·02 DE	·02 DA+ ·05 DB+ ·10 DC+ ·01 DD+ ·01 DE	
5	·68 DA+ ·36 DB	·16 DA+ ·36 DB	·03 DA+ ·11 DB+ ·35DC+ ·01DD	·02 DA+ ·07 DB+ ·23 DC+ ·01 DD+ ·01 DE	·01 DC+ ·01 DD+ ·01 DE	·01 DC+ ·01 DD+ ·01 DE + ·04 DF	
4	·53 DA	·22 DA+ ·91 DB	·02 DA+ ·10 DB+ ·49 DC+ ·01 DD	·03 DC+ ·06 DD	·02 DC+ ·05 DD+ ·03 DE	DF	
3	·68 DA	·17 DA+ 1·01 DB	·03 DB+ ·57DC	·08 DC+ ·13 DD	·14 DC + ·23DD + ·03DE		
	DA	DB	DC	DD	DE		

0   1   2   3   4

RADIAL DISTANCE (cm)

Fig. 9.13   RELATIVE DENSITY DISTRIBUTION
13 1/min ARGON, 1.1kHz ARC ROTATION

DOWNSTREAM DISTANCE (cm)

	DA	DB	DC	DD	DE	DF			
6	·62 DA+ 1·05 DB+ ·83 DC+ ·64 DD+ 38 DE+ ·59 DZ	·21 DA+ ·47 DB+ ·43 DC+ ·34 DD+ ·20 DE+ 32 DZ	·03 DA+ ·07 DB+ ·10 DC+ ·08 DD+ ·05 DE+ ·08 DZ	·04 DA+ ·06 DB+ ·10 DC+ ·11 DD+ ·09 DE+ ·27 DZ	·01 DA+ ·01 DB+ ·03 DC+ ·04 DD+ ·04 DE+ 18 DZ	·09 DZ	·09 DZ	6·86 DZ	94 DZ
5	·43 DA+ 63 DB+ ·44 DC+ ·33 DD+ ·20 DE+ ·30 DZ	·24 DA+ ·51 DB+ ·39 DC+ ·30 DD+ 18 DE+ ·27 DZ	·09 DA+ ·19 DB+ ·22 DC+ ·17 DD+ 10 DE+ ·15 DZ	·03 DA+ ·06 DB+ ·10 DC+ ·10 DD+ ·07 DE+ ·15 DZ	·01 DA+ ·02 DB+ ·06 DC+ ·07 DD+ ·07 DE+ ·24 DZ	17 DZ	12 DZ	4·76 DZ	
4	·15 DA+ ·06 DB	15 DA+ 28 DB	25 DA+ ·50 DB+ ·51 DC+ 34 DD+ 16 DE+ 13 DZ	07 DA+ 15 DB+ ·22 DC+ 19 DD+ ·09 DE+ ·07 DZ	·03 DA+ ·06 DB+ 16 DC+ 18 DD+ 19 DE+ ·14 DZ	13 DZ	·13 DZ		DZ
3	·10 DA	·17 DA+ ·31 DB	·07 DA+ 14 DB+ ·09 DC	·10 DA+ ·22 DB+ 26 DC+ 18 DD	·05 DA+ ·09 DB+ ·24 DC+ ·26 DD+ 28 DE	·01 DB+ ·01 DC+ ·01 DD+ ·01 DE	·03 DB+ ·03 DC+ ·03 DD+ ·03 DE+ ·06 DG		
2	·33 DA	·25 DA+ ·66 DB+	·03 DA+ ·08 DB+ ·23 DC+	·02 DA+ ·06 DB+ ·17 DC+ 19 DD	·02 DA+ ·07 DB+ ·21 DC+ ·23 DD+ ·25 DE	·01 DA+ ·03 DB+ ·08 DC+ ·08 DD+ ·09 DE+ ·01 DF	DG		

(Right-side labels: DZ, DG)

RADIAL DISTANCE (cm)

Fig. 9.14   RELATIVE DENSITY DISTRIBUTION
4.4 l/min ARGON, 1.1 kHz ARC ROTATION
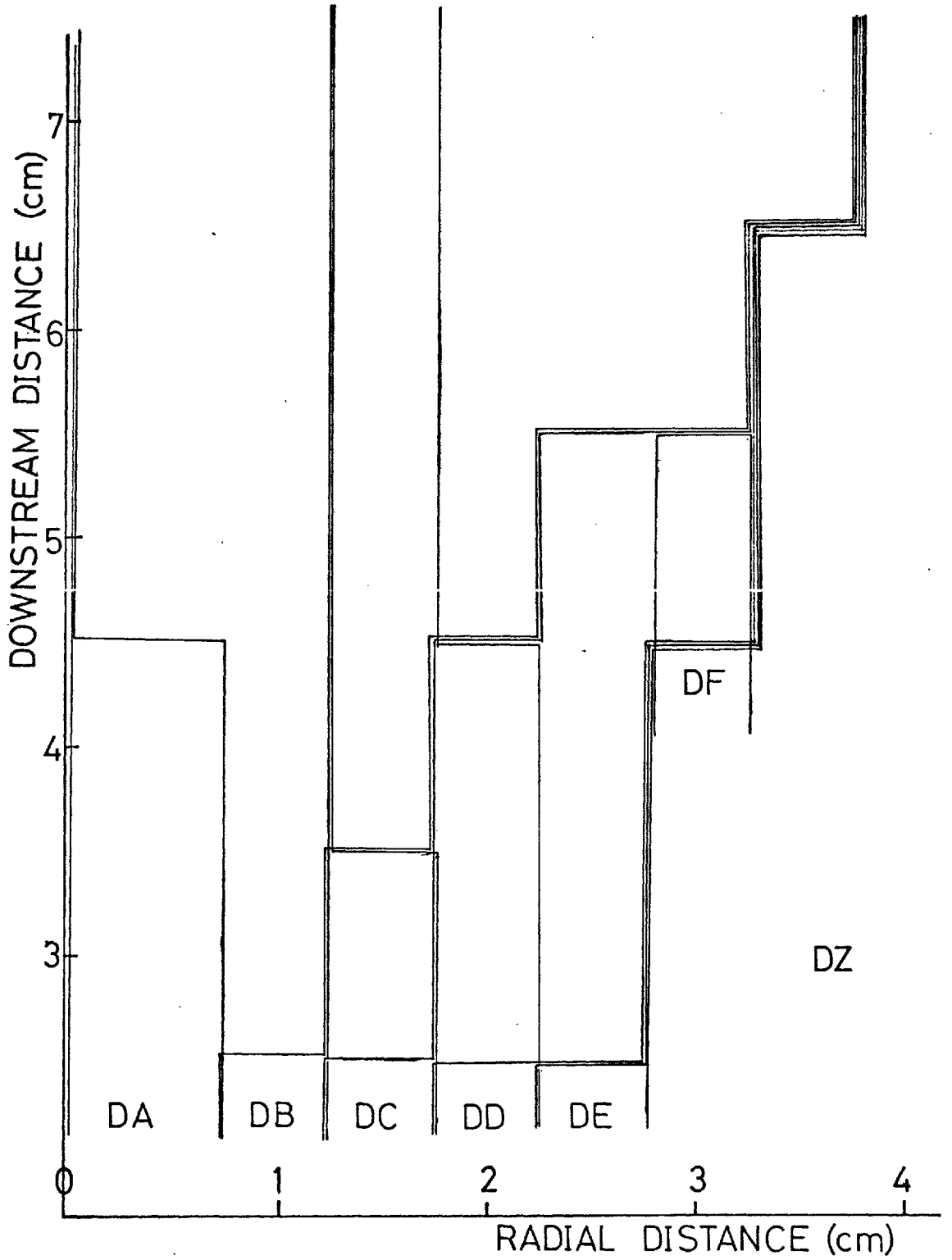
Fig. 9.17   "SPHERES OF INFLUENCE"
13 l/min ARGON, 1.1 kHz ARC ROTATION
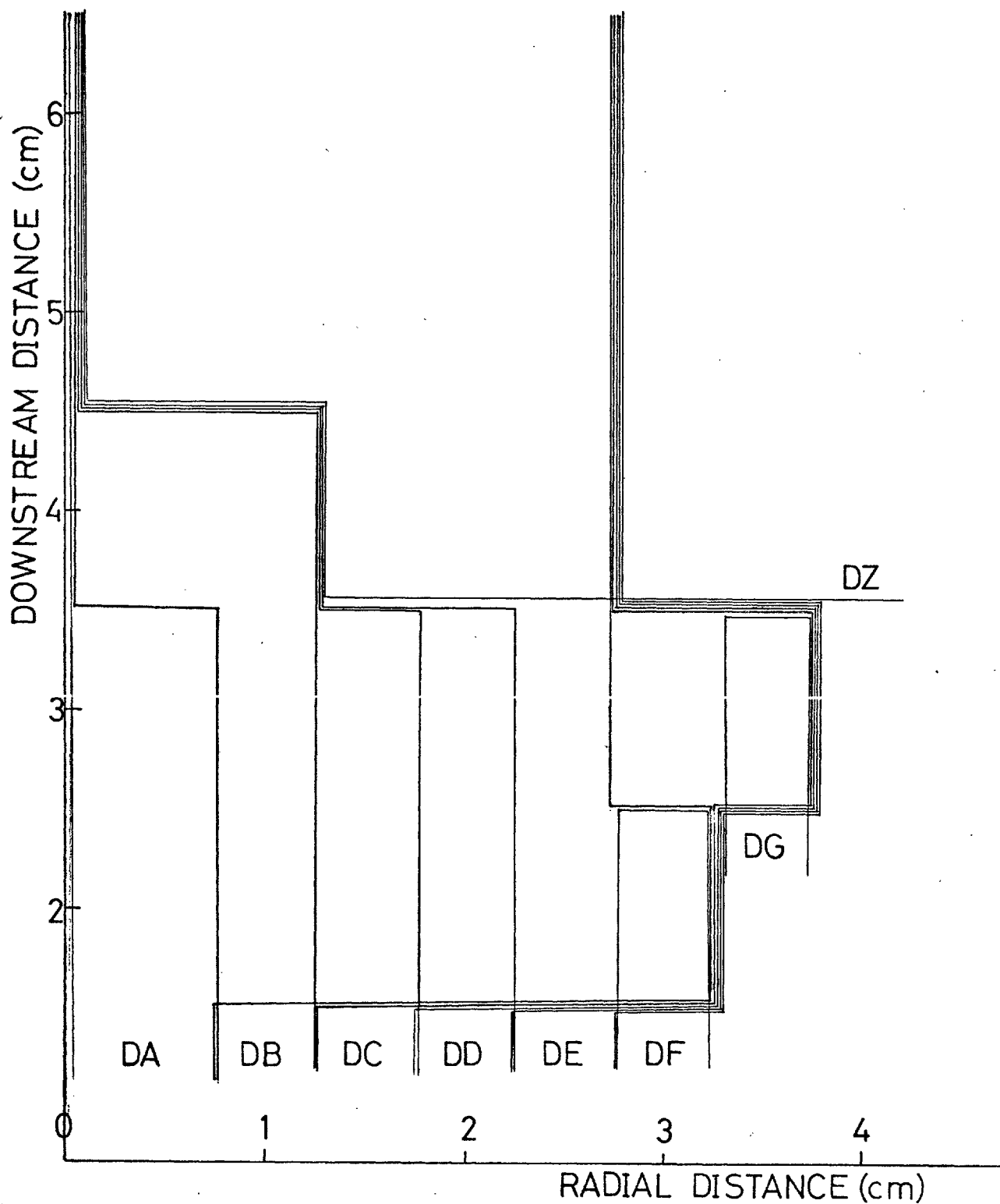
Fig. 9.18 "SPHERES OF INFLUENCE"
4.4 l/min ARGON, 1.1 kHz ARC ROTATION

segment in terms of the densities at the various positions from which the gases enter the test space. These density distributions were computed for all segments and plotted for both flow rates in Figures 9.13 and 9.14. The densities of the gases entering the test volumes are denoted as DA to DZ. It is important to note that the computed values are only relative densities with respect to the specific gravities at the boundaries of the test volume considered.

As the density in each grid section is expressed in terms of the density of the various parts of the inflowing gases, it is possible to determine the source and the relative quantity of each part of the gas mixture in every ring. Conversely a "sphere of influence" for each section of the inflowing gases can be mapped out throughout the test region. Figures 9.17 and 9.18 show this for fast and slow argon flow rates respectively. Comparisons of these two figures show the difference in entrainment pattern in the wakes for the two cases. There is comparatively little sideways entrainment in the test region for the case of the fast flow. The two innermost columns are not at all affected by the flow in the outer columns throughout the portion of the wake investigated. At lower flow rates, however, there is considerably more entrainment in this region and after a distance of 4 cm downstream of the nozzle the influence of the outer gas flows extends throughout the entire horizontal cross-section.

These conclusions confirm earlier qualitative observations made with the use of high speed shadow cinephotography and described in Chapter IV. The entire innermost two columns for the high argon flow (Fig. 9.13) and the same columns up to 4 cm downstream of the rotating arc for the slow flow (Fig. 9.14) correspond to the regions of high flow velocities in which the flow regimes are governed by the rotation of the arc in the nozzle as discussed in Chapter V. The absence of horizontal inwards

flow into the central wake core observed in that chapter is confirmed here by the measurement of zero entrainment into the inner columns in the sections of the wake region under observation.

IX.7 Discussion of Density Anomalies in the Wake

Considering the parts of the two innermost columns showing no entrainment, a closer inspection reveals an apparent decrease in density in the downstream direction if DA is assumed equal to DB. If no such assumption is made a density decrease is nevertheless observed in some innermost grid squares containing terms in DA only (Figs. 9.13 and 9.14). The rise in temperature that would account for this behaviour could have been a result of thermal eddy diffusion into the centre. The thermal gradient required for this to occur could have been caused by a deviation from the condition of uniform heating of the gas by the entire length of the arc as postulated by Chen and Lawton (Ref. 23), because the cathode acts as a heat sink. Alternatively, the centrifugal force resulting from the gas swirl induced by the arc rotation forces pockets of cooler, heavier argon away from the centre of the wake. These two possibilities are not mutually exclusive. As it is only possible to determine net horizontal flow rates these flow regimes could be masked by motion in the outward direction.

In order to establish an indication of the effects of eddy diffusion in the various parts of the wake the relative turbulence energy for the vertical velocities was plotted point for point for both flow rates throughout the wake. Horizontal standard deviations are not known (Chapter VIII) and their RTEs can therefore not be obtained. The relative turbulence energy (RTE) is defined as

$$RTE = s^2/(s^2 + \bar{v}^2)$$
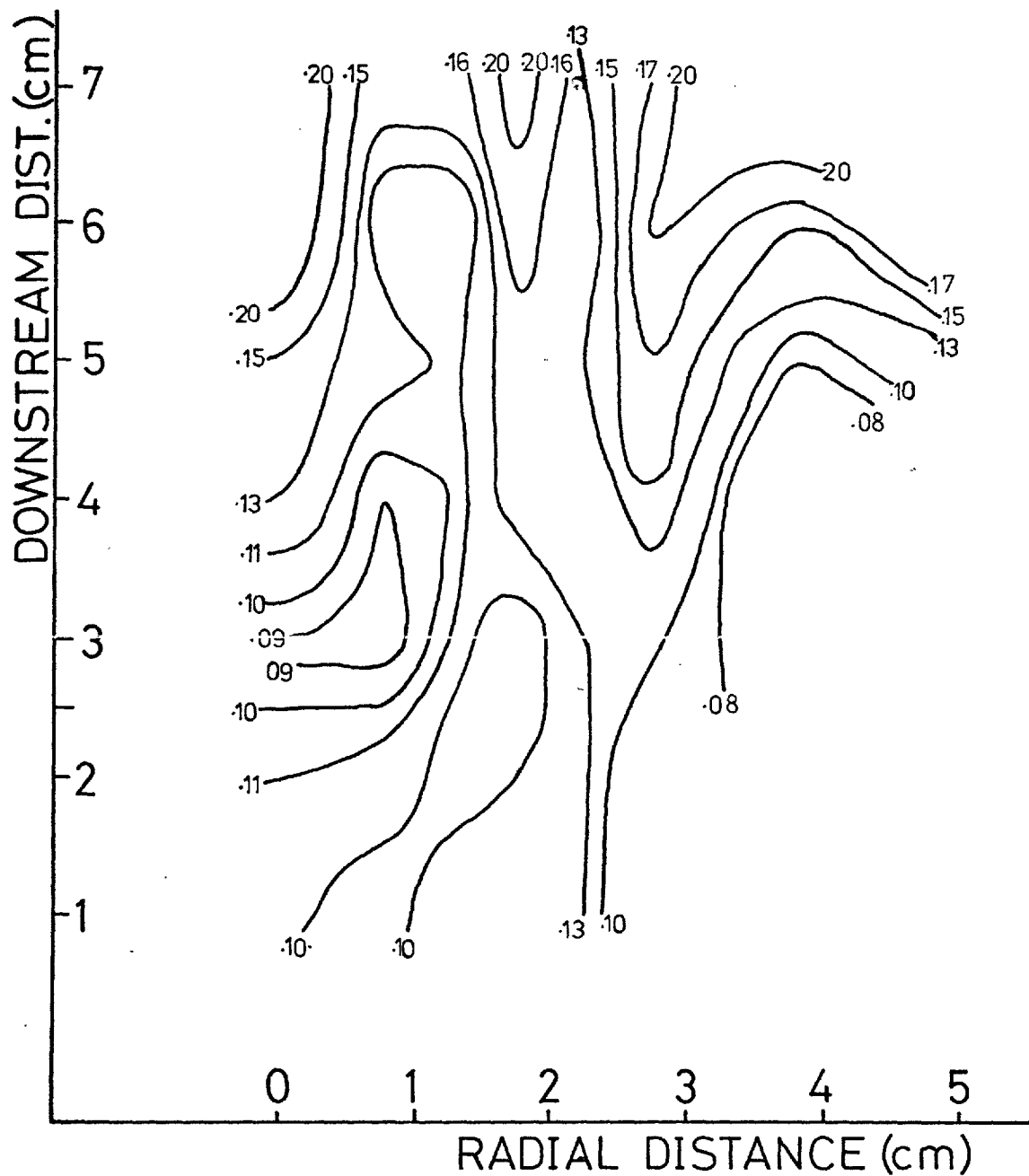
Fig. 9.19   RELATIVE TURBULENCE ENERGY
13 l/min ARGON, 1.1 kHz ARC ROTATION
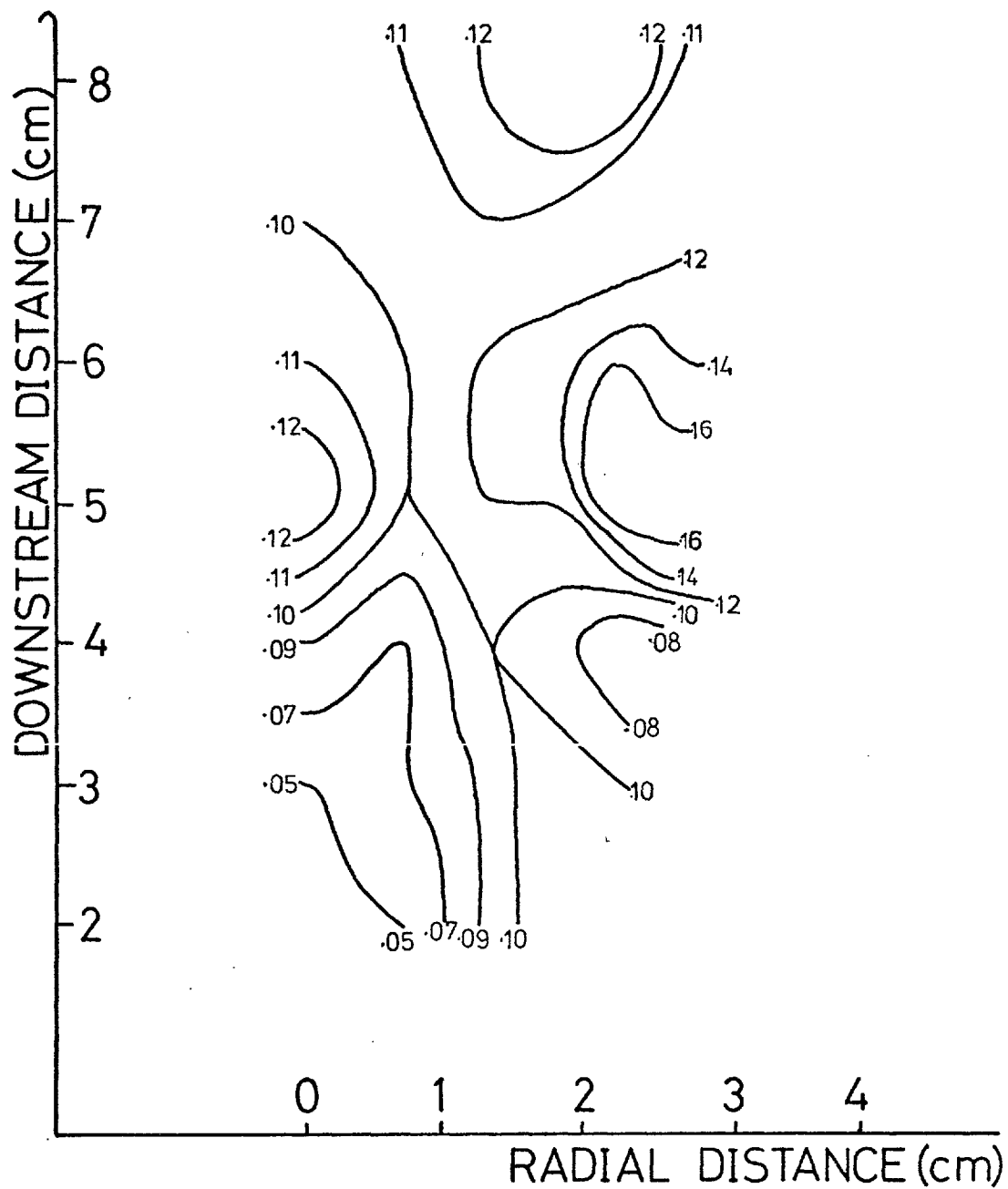
Fig. 9.20   RELATIVE TURBULENCE ENERGY
4.4 1/min ARGON, 1.1 kHz ARC ROTATION

where s is the standard deviation of vertical velocity and $\bar{v}$ its

mean value. Lines of equal fractional energy in turbulent motion were

drawn as shown for the high flow velocities in Figure 9.19 and for the

low flows in Figure 9.20. On a time scale the region up to 4 cm

downstream of the nozzle in Figure 9.20 corresponds to the entire test

region for the fast flow. The patterns are quite complex but a comparison

of equivalent wake sections on a time scale shows some similarity in lay-

out including two separate loops in the inner part of the wake.

Even casual inspection of Figures 9.19 and 9.20, however, shows

that in the inner zones of the test regions lower relative turbulence

energies at least for the vertical velocities predominate. These values

are more substantial in the outer regions and downstream where hot argon

from the nozzle encounters and mixes with the surrounding or entrained

air. It is in these areas that large shear forces between hot and cold

gas flows as well as overshooting gas pockets can be expected. As

larger gas pockets also predominate in these regions it is here that

thermal eddy diffusion may be expected to play a more important part

in the distribution of physical properties in the wake.

The density distribution in the centre of the test region, however,

appears more like that, which one would expect in an area in which heat

is released by a reaction. This behaviour could be caused by pockets of

excited and ionized argon carried downstream, for example in the form

of fragments of the arc channel. This supposition is supported by the

presence of pockets of ionized gas in this region, detected by the corona

probe (Chapter VI). Traces of dissociated air entrained in the vicinity

of the arc may also contribute. These species would act as a carrier of

energy in a non-translational mode which is transferred into translational

energy in the wake. This change in the number of degrees of freedom has

not been accounted for in the above analysis, which allowed for heat

transfer by normal convection only.

In order to check the plausibility of this explanation the "rate of heat release" is calculated that would be required to raise the gas flow in the innermost columns to the temperature needed to attain the measured density distributions. This release rate is compared with the energy supplied per unit time by the arc.

Each central grid cylinder was combined with the first ring at the same height above the nozzle and the new mean density for every one of the resulting cylinders of 1.25 cm radius and 1 cm height computed. DA = DB = D_0 is assumed. The translational mean temperature (T_t) in terms of the temperature of the gas entering the grid system (T_0) for each cylinder was calculated using the Ideal Gas Law:

$$\zeta_M \times T_t = \zeta_0 \times T_0$$

where ζ_M is the measured density and ζ_0 the density of the gas entering the column (= DA = DB). From this the rate of heat release (R) required in each cylinder to maintain this temperature was calculated using the formula:

$$R = \zeta_M \times A \times v_J \times c_p \times \Delta T_t$$

where A is the cross sectional area through the cylinder (= $1.25^2 \times \pi$), v_J the mean upward velocity in this segment, c_p the specific heat of argon taken as constant (Ref. 35) and ΔT_t the change in translational temperature from one segment to the next (Tables 9.1 and 9.2). The heat release rate is plotted for both argon throughput rates considered versus distance downstream in Figure 9.15. Each curve contains a maximum within the test region. The total "heat release" in the wake region

Table IX.1   Calculation of Apparent Heat Release in the Wake due to Convection of Non-Translational into Translational Energy.   Argon Flow Rate 13 1/min.

Downstream Position	Local Density D_i	Local Relat. Temperature $T_i = D_o/D_i \times$ $\frac{T_i}{T_o}$	Local Mass m_i = Volume $\times D_i$	Energy liberated in going from Posit. L-1) to Posit. i $m_i c_p (T_L - T_{L-1})$	Time Required to pass to section i: $\sum_{J=1}^{i} 1/v_J$	Local Velocity	Rate of Heat Release
2	1.0	1.0	3.15	0	3.8	533	0
3	1.0	1.0	3.15	0	5.9	433	0
4	0.91	1.1	2.87	0.29	8.0	533	155
5	0.71	1.41	2.24	0.63	10.0	473	298
6	0.53	1.89	1.67	0.57	12.5	440	251
7	0.49	2.04	1.54	0.11	14.8	410	45
	$(\times D_o)$	$(\times T_o)$	$(\times D_o)$	$(\times D_o T_o C_p)$	$(\times 10^{-3})$		$(\times D_o T_o C_p)$
[cm]	[g/cc]	[°K]	[g]	[cal]	[sec]	[cm/sec]	[cal/sec]

Total Heat Converted   42.8 cal/sec

Heat supplied by the arc to the gas: 160   cal/sec

List of Symbols:

D - density   M - mass C_p - specific heat at const. press.

T - temperature   v - velocity

Subscripts:

o - original   i - at position i

Table IX.2   Calculation of Apparent Heat Release in the Wake due to Conversion of Non-Translational into Translational Energy.   Argon Flow Rate 4.4 1/min.

Downstream Position	Local Density D_i	Local Relative Temperature $T_i = D_o/D_i \times T_o$	Local Mass $m_i = $ Volume x D_i	Energy liberated in going from posit. (i-1) to posit i $m_i c_p (T_i - T_{i-1})$	Time required to pass to section i: $\sum\limits_{J=1}^{i} 1/v_J$	Local Velocity	Rate of Heat Release
1	1.0	1.0	3.15	0	0.44	227	0
2	0.7	1.43	2.21	0.95	0.91	196	1.86
3	0.34	2.94	1.07	1.13	1.46	169	1.91
4	0.34	2.94	1.07	0	2.11	140	0
	(x D_o)	(x T_o)	(x D_o)	(x $D_o T_o c_p$)	(x 10^{-3})		(x $D_o T_o c_p$)
[cm]	[g/cc]	[°K]	[g]	[cal]	[sec]	[cm/sec]	[cal/sec]

Total Heat Converted   21.4 cal/sec

Heat supplied by the arc to the gas   94   cal/sec

List of Symbols:

D - density   M - mass c_p - specific heat at const. press.

T - temperature   v - velocity

Subscripts:

o - original   i - at position i
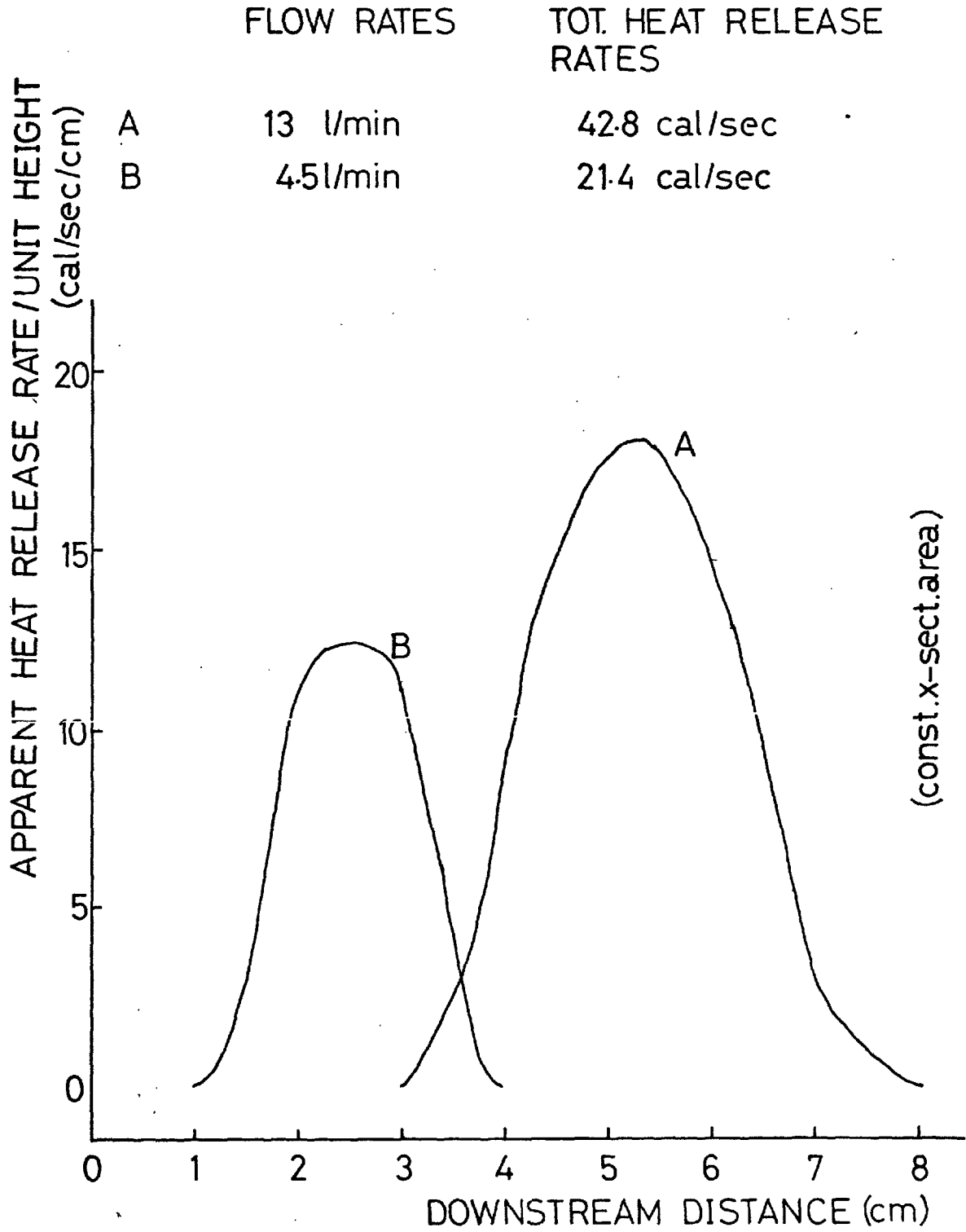
Fig. 9.15   APPARENT HEAT RELEASE VS. DOWNSTREAM
DISTANCE

determined from the area underneath each graph can be compared with the rate of heat supplied from the arc to the gas, heat losses to the burner having been deducted. In both cases the energy carried downstream in a non-translational form within the innermost two columns would amount to 25% or slightly less of the heat absorbed by the gas from the plasma, radiation losses being neglected. As can be seen from Figures 9.6 and 9.7 these innermost columns contain the largest flow velocities and the highest carrier gas throughput. This along with the tendency of hotter pockets to move towards the centre of the wake makes a figure of less than 25% of energy in a non-linear form in this region quite possible.

When the "heat release" rate is plotted versus time, rather than distance downstream, the positions of maxima for the high and low argon flow rates are found to coincide within experimental limits (Fig. 9.16). This suggests that the rate of energy conversion into a translational mode occurs on a constant time scale, independent of concentration, which is characteristic of a zero order rate law. From the present data no conclusions can be drawn about the temperature dependence of the above mentioned conversion rate. Although in terms of average values the heat transfer per unit volume to the faster gas flow is less than that to the slower flow, the energy transition is likely to occur in pockets of high temperature (including possible remains of the arc column) present under both flow conditions. The coincidence of the two "heat release" maxima gives support to this theory.

In practice both thermal eddy diffusion and energy transfer between different degrees of freedom may cause the density anomalies obtained from the analysis that takes account of ordinary convective heat transfer only. Eddy diffusion effects, however, appear to be most important in the outer wake regions, while the energy transfer into a translational mode predominates in the wake core.

APPARENT HEAT RELEASE RATE (cal/sec/cm)
/UNIT HEIGHT

FLOW RATES
A   13 l/min
B   45 l/min
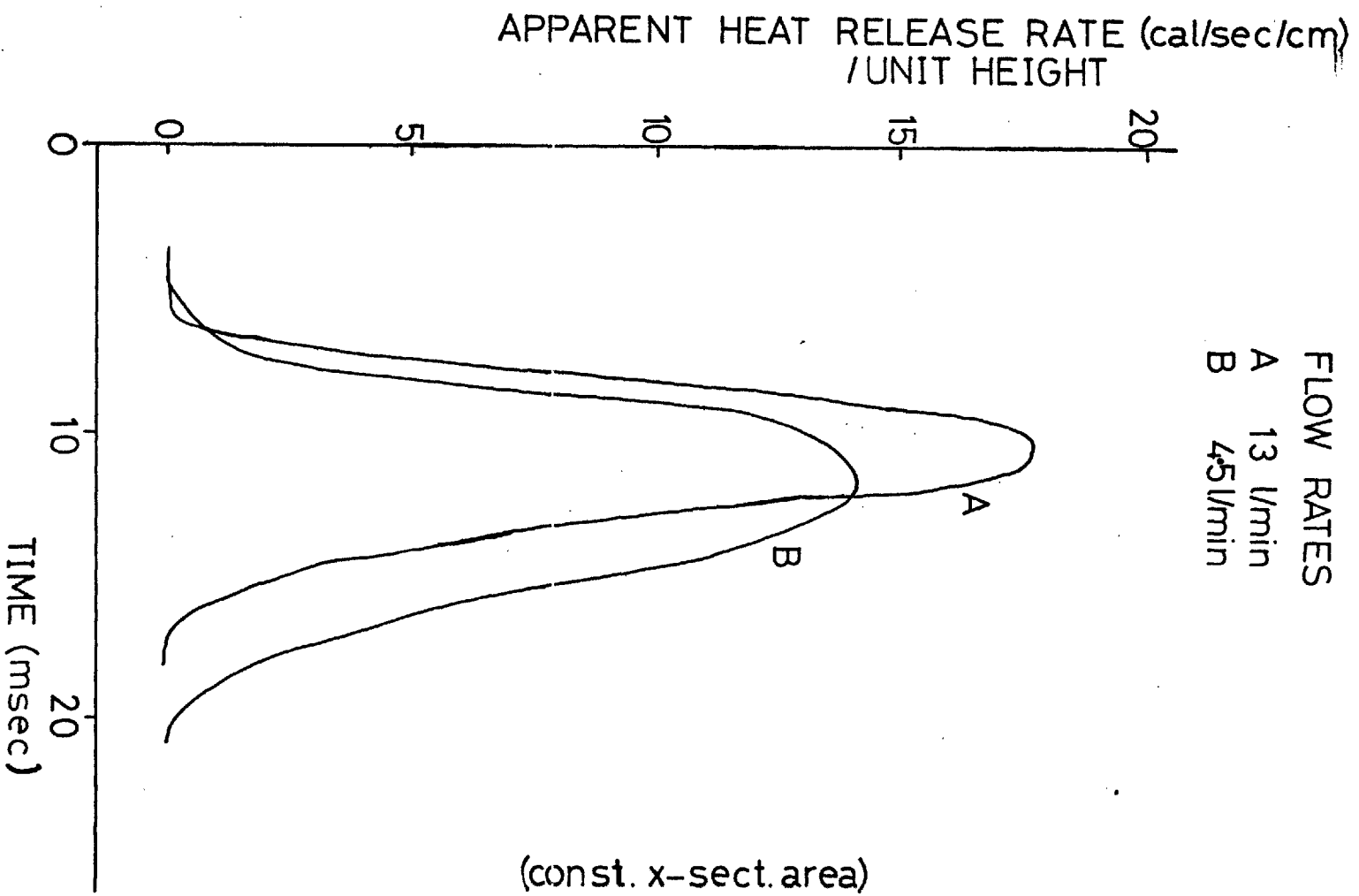
Fig. 9.16   APPARENT HEAT RELEASE RATE VS. TIME

(const. x-sect. area)

TIME (msec)

The presence of excited, ionized and possibly dissociated species in the core of the wake extending far into the downstream direction has important effects on the analysis of the distribution of physical properties in the wake as well as on the application of plasma jets to chemical and physical processing.

Any mathematical treatment of the plasma jet wake is not complete unless its equations contain terms allowing for the transfer of energy from non-translational to translational degrees of freedom. Simple fluid-dynamic considerations appear not to be sufficient at least in the inner core of the wake. Pockets of ionized and excited species far downstream would also explain the rapid reaction rates observed in the wake of plasma jets. Harrison and Weinberg (Ref. 14), for example, detected the formation of acetylene at the interface between the hot argon and methane-air mixture in electrically augmented flames. This indicates the presence of pockets of sufficiently excited argon to supply the energy required to facilitate this reaction. Alternatively, if the carrier gas is to take an active part in the reaction the reaction rate is further increased by the existence of species other than in their ground state of one or more of the reactants.

Heat transfer to particles or to solid surfaces is also greatly increased by the neutralisation of ionized species, by de-excitation and possible reassociation far downstream in the wake region. Simple heat transfer coefficient can therefore not be used in the modelling of systems incorporating plasma jets.

Chapter X

CONCLUSIONS

A promising plasma reactor configuration utilizes an arc spinning in an annulus under the influence of the interaction between the current in the plasma and an applied magnetic field. A carrier gas is pumped through the annulus to transfer the thermal power, dissociated, excited or ionized species from the arc to the downstream wake region. Because of the high by-pass ratio and the relatively slow mixing in the downstream region, the rotation rate of the arc must be tuned to the flow rate of the gas if the effects of the arc are to be distributed uniformly throughout the wake.

Theoretically, unless the arc is set to rotate through one revolution in the time required for the gas to pass a distance of 1 arc diameter down the nozzle, a rotating spiral staircase of hot gas in an atmosphere of cooler gas results in the region downstream of the electrodes. In practice this pattern is quickly broken up by the intense turbulence in the wake and only indications of some fragments of the spiral remain a few centimetres downstream of the nozzle.

This plasma jet configuration permits a variety of modes of introduction of reactants into its wake. They can either be mixed in with the carrier gas, which usually results in high electrical power dissipation in the arc, or they can be injected at the upper end of the nozzle, or allowed to be entrained into the wake from the surrounding atmosphere, depending on the aerodynamic configuration and use of the reactor.

The wake region was investigated using shadow and schlieren methods with the help of short duration photography (single and double exposure) and high speed cinephotography. A novel probe applying the phenomena of the corona discharge was used to map out regions of equal mixedness in

the test space. A schlieren velocimeter was devised and used to obtain
time averaged localized velocity distributions throughout the wake in
both the horizontal and vertical directions. Effects of averaging
along the optical path were corrected for by using a concentric ring
model.

The wake consists of a cylindrically symmetric cone whose spread
is inversely proportional to the gas flow rate through the nozzle. The
cone is made up of a large number of small pockets of gas of different
temperatures and compositions. Each pocket consists of a gas mixture
of uniform properties at its centre with slight refractive index and
therefore density gradients towards its edge. At the pocket boundary
itself these refractive index changes become abrupt.

The wake cone consists of two separate zones. The inner one is
made up of predominantly small pockets of gas present in very large
numbers and moving at very high turbulent velocities. The flow
properties in this region are dependent on the rotation rate of the arc
in the nozzle and its extent in the downstream direction is a function
of the flow velocity of the gas through the plasma jet. The pattern in
this inner region is relatively stable to induced draughts and little
entrainment appears to take place into this zone. It also contains
segments of remnants of arc columns in the form of excited and ionized
argon.

The region surrounding the inner core in the outside layers of the
wake cone and downstream of the fast flow regime consists of larger
pockets of lower number densities moving with much lower velocities.
The general flow pattern in this zone depends on the flow rate of the
gas through the plasma jet and is independent of events in the nozzle.
While the velocities in the inner regime are almost exclusively in the
upward direction, the slow moving region contains horizontal velocity

components as well as recirculating eddies. It is more susceptible

to outside influences and seems to be instrumental in most of the

entrainment of the surrounding gases into the wake.

As the onset of the outer region in the downstream direction is a

function of the carrier gas flow rate, the downstream distance after

which the outer gas is distributed throughout the wake region depends

on the gas velocity in the nozzle. A considerable amount of surrounding

stationary atmosphere is entrained in the immediate vicinity of the

nozzle into, probably, the outer layers of the wake cone. These outer

flows do not spread throughout the wake until reaching the zone past

the inner flow regime, when they are distributed with further entrained

gases throughout the wake. The relative entrainment rate in general

is inversely proportional to the volumetric flow rate through the plasma

jet.

The velocity vector distribution and the flow lines in the test

region were plotted for argon flow rates of 13 l/min and 4.4 l/min and

localized relative density distributions throughout the wake region

from 1 cm to 8 cm downstream of the nozzle were calculated for both

these cases.

A falling off in density in the fast moving inner regions with

distance from the nozzle, followed by a rise in density further down-

stream, was observed. Calculations show that this dip occurred at a

constant time interval of the order of a few milliseconds after the

argon left the plasma jet. This density distribution could be due to a

variety of reasons. It could be caused by a motion of cooler, heavier

gas pockets away from the wake centre (because of the centrifugal forces

due to the swirl of the gas introduced by the rotating arc) or by thermal

eddy diffusion resulting from a cooler centre of the wake of the plasma

jet immediately downstream of the nozzle, resulting from a cooling effect

of the cathode. Alternatively, pockets of gas containing non-translational energy in the form of excited or ionized argon or traces of entrained, dissociated air convert this energy into a translational form resulting in an apparent rise in gas temperature and reduction in density.

In order to assign areas of relative importance to these alternatives, values of relative turbulence energy for the vertical velocities were plotted throughout the wake region for both high and low flow rates. These distributions show that the fractional energy in turbulent motion, and therefore the eddy diffusion, is most important in the outer regions containing the shear layers between hot and cold gas flows. In the core of the wake which exhibits a density distribution reminiscent of that found in exothermic reactions "heat release" by energy transfer between different degrees of freedom seems to predominate.

This indicates the presence of ionized, excited and possibly dissociated species up to a distance of many centimetres downstream in the core of the wake, the extent of which depends on the carrier gas flow rate. This has important consequences on any analysis of the wake of the magnetically rotated arc as well as on the various uses of plasma jet in physical and chemical processing.

REFERENCES

1.   "Associating Plasma Jets with Hydrocarbon Combustion",

      F.J. Weinberg, Ind. Chim. Belg., 38 (1973), pp.2-5.

2.   "Technological Uses of Low Temperature Plasmas", J. Lawton,

      Physics in Technology, Sept. 1975, pp.190-197.

3.   "Plasma Chemical Reactions", V.J. Ibberson, High Temperature -

      High Pressure 1 (1969), pp.243-268.

4.   "Reactions of Coal in a Plasma Jet", R.L. Bond, W.R. Ladner and

      G.I.T. McConnell, Fuel, 14 (1966), pp.381-395.

5.   "Properties and Applications of Low Temperature Plasma",

      Plenary Lectures - Moscow 1965. Pure and Applied Chem., 13, 3 (1966)

6.   "The Application of Plasma to Chemical Processing", R.F. Baddon and

      R. Timmings, 1967, Pergamon Press.

7.   "Effect of N_2 containing Plasmas on Stability, NO Formation and

      Sooting of Flames", J.C. Hilliard and F.J. Weinberg, Nature, 259

      (1976), pp.556-557.

8.   "A Study of the Titanium Tetrachloride Oxidation in a Rotating

      Arc Plasma Jet", Ph.D. Thesis, University of London, I.M.H.

      Mahawilli, 1974.

9.   "The Role of Arc-Plasma in Metallurgy", A.R. Mos and W.J. Young,

      Powder Metallurgy, 1, 14 (1964), pp.261.

10.   "Boosting Flame Temperatures with the Electric Arc", Southgate,

      G.T., Chemical and Metallurgical Engineering, 31 (1924), p.16.

11.   "Flames Augmented by Electrical Power", Karlowitz, R.,

      Pure appl. Chem., 5, (1962), p.557.

12.   "Flame Arc Combination", J. Lawton, K.G. Payne and F.J. Weinberg,

      Nature, 193 (1962), p.736.

13. "Augmenting Flames with Electric Discharges", DCC Chen, J. Lawton and F.J. Weinberg, 10th Intern. Sympos. of Combustion, Combustion Institute, pp.743-754.

14. Flame Stabilisation by Plasma Jets, A.J. Harrison and F.J. Weinberg, Proc. Roy. Soc., 1971, A321, pp.95-103.

15. "Flames Augmented by Inductive Coupling of Electrical Energy", P.D. Johnston and J. Lawton, Nature, 230 (1971), 5292, pp.320-321.

16. "Recent Advances in Electric Arc Plasma Generation Technology", R.R. John and W.L. Bade, ARS (American Rocket Soc.) Journal, 31 (1961), 4.

17. "Heat Transfer from Augmented Flames and Plasma Jets based on Magnetically Rotated Arcs", J.B. Cox, A.R. Jones and F.J. Weinberg, Proc. Roy. Soc., 1971), A325, pp.269-289.

18. "Combustion Aerodynamics", Beer and Chigier, Applied Science Publishers Ltd., 1972.

19. "Industrial Flames", Vol. I, Measurements in Flames", Chedville and Braud, Edward Arnold, 1972.

20. "On the behaviour of enthalpy probes in fluctuating temperature environments", J.B. Cox and F.J. Weinberg, Journ. o. Phys. D (Appl. Phys), 4 (1971), pp.877.

21. "Optics of Flames", F.J. Weinberg, 1963, Butterworths.

22. "The Influence of Gas Streams and Magnetic Fields on Electric Discharges I and II. V.W. Adams, Min. of Aviation, C.P. No.743. H.M. Stationery Office, (1964).

23. "Discharge Heaters based on Magnetically Rotated Arcs", D.C.C. Chen and J. Lawton, Trans. Inst. Chem. Engrs, 46 (1968), T270.

24. "Arc motion in Magnetic Fields in the Presence of Gas Flow", J. Lawton, Journ. o. Phys. D. (Appl. Phys), 4 (1971), pp.1946-1957.

25. "Arcs with free Anode Roots in the Presence of Gas Flow and Magnetic Fields", J.F. Humphreys and J. Lawton, Journ. o. Phys. D (Appl. Phys), 5 (1972), pp.701-709.

26. "A Study of Electrically Augmented Combustion", Ph.D. Thesis, University of London, D.C.C. Chen, 1970.

27. Survey of Investigations of Electric Arc Interactions with Magnetic and Aerodynamic Fields", T.W. Myers, Aerospace Research Labs., Office of Aerospace Research - Wright Patterson AFB, Ohio, R ARL 66 0184 126P (Sept. 1966).

28. "A Multi-Purpose Spark Light Source System", R.J. North, Aerodyn. Divis., NPL/Aero/379.

29. "A Short-Duration Argon-Jet Spark Light Source System, R.J. North, Aerodyn. Divis., NPL/Aero/Note 1008.

30. "Fluid Mechanical Aspects of Discharge Reactors", Swithenbank, Plasma Processing of Materials, Electr. Chem. Techn. Group - Soc. of Chem. Ind., Oct. 1973, - Sheffield.

31. "Ionized Gases", von Engel, Oxford University Press, 1965.

32. "The Measurement of Velocity by applying Schlieren Interferometry to Doppler Shifted Light", M.J. Schwar and F.J. Weinberg, Proc. Roy. Soc., 1969, A311, pp. L/69-476.

33. "Measurement of Local Velocity of Shock and Detonation Waves by Schlieren Interferometry of Doppler Shifted Light", M.J.R. Schwar and J.B. Bowen, Journ. o. Phys., D 5, (1972), pp.1561-1575.

34. "Measurement of Shock Wave Velocity using the Doppler Principle", W. Merzkirch, W. Erdmann, Instit. of Thermo. & Fluiddynamik, Ruhr - Universitat D4630 Bochum, Fed. Rep. Germany, to be published.

35. "The T/D Properties of Argon Plasma in Local TDE 1-30 atm. $5 \to 60 \times 10^3\ ^oK$", R.G. Turner and W.E. Worsfold, AWRE REPORT No.020/69 (May 1969).

36. Private Communication, A.R. Jones, Department of Chemical Engineering and Chemical Technology, Imperial College, University of London.

37. "Initiation of Electrically Augmented Flames", I.J. Jagoda, F.J. Weinberg, Combustion and Flame, 19 (1972), p.305.

38. "The Determination of Arc Temperatures from Shock Velocities",
H. Edels and D. Whittaker, Proc. Roy. Soc., 240A, 1957, pp.54-66.

39. "Measuring the Mobility of Charged Aerosols by Schlieren
Interferometry of Doppler Shifted Light", M.J.R. Schwar, K.C. Thong
and F.J. Weinberg, J. Phys. D. Appl. Phys., 3 (1970), pp.1962-1966.

40. "Velocity Measurement by combining the Doppler Principle with the
Schlieren Method", M.J.R. Schwar and F.J. Weinberg, Nature, 221
(1969), p.357.

41. A Method of Correction of Astigmatism in Schlieren Systems,
R. Prescott and E.L. Gayhart, Applied Phys. Laboratory, Johns
Hopkins University, Journ. Aeron. Sciences, 18, (1951), p.69.

Appendix 1

DEPENDENCE OF AN EXPANDED VOLUME OF GAS ON THE DISTRIBUTION

OF THE ENERGY CAUSING THE EXPANSION

Consider a volume V of gas at temperature T_o. A quantity of energy E is passed onto a part of the volume of gas x, heating it to a temperature T_f. The remaining gas (V - x) stays at temperature T_o. Energy balance on volume x:

$$E = x \times \zeta \times \sigma \times (T_f - T_o)$$

where ζ is the density and σ the specific heat of the gas. Therefore:

$$T_f = E/x \times \zeta \times \sigma + T_o$$

If volume x after expansion becomes volume y and T_o and T_f are in [^{o}Abs.] then from the Ideal Gas Laws:

$$x/T_o = y/T_f = y/(E/x \times \zeta \times \sigma) + T_o$$

The final Total volume after expansion VH is:

$$VH = y + (V - x) = [x/T_o \times E/(x \times \zeta \times \sigma) + T_o] + (V - x)$$

$$VH = [E/\zeta \times \sigma \times T_o + x] + (V - x)$$

$$VH = E/\zeta \times \sigma \times T_o + V$$

The expression for VH is independent of x. This shows that the final

volume after expansion of a gas is independent of the fact whether

the energy causing the expansion is distributed uniformly throughout

the gas or whether it is concentrated on a fraction of the original

volume as long as the Ideal Gas Laws are observed and specific heat

of the gas remains constant over the temperature range considered.

COMPUTATION AND STATISTICAL ANALYSIS OF VERTICAL VELOCITIES

```
      PROGRAM VELOC  (INPUT,OUTPUT,TAPE5=INPUT,TAPE6=OUTPUT)
      COMMON L(10), M(10), VEL(10,400, VEL2(10,700)
      INTEGER D1,D2
      DIMENSION AV(10),AV2(10),KOU(10,40),KOU2(10,40)
C
C     SETTING THE ARRAYS TO ZERO
      DATA KOU/400*0/
      DATA KOU2 /400*0/
      DO 100   I=1,10
      L(I)=0
      M(I)=0
      DO 101 J=1,750
      VEL (I,J)  = 0.0
  101 CONTINUE
      DO 100  J=1,105
      VEL 2 (I,J) = 0.0
  100 CONTINUE
      K=0
      LMAX=0
      MMAX=0
      READ(5,9999) TITLE
 9999 FORMAT (1X,A10)
      WRITE(6,9999) TITLE
   11 K=K+1
      L(K)=0
      M(K)=0
C     DECIDING ON CALIBRATOR
      READ(5,1001) I4
  100 FORMAT (I1)
      IF (I4.EQ.2) GO TO 14
      IF(I4.EQ.3) GO TO 16
      IF(I4.EQ.4) GO TO 18
      IF(I4.EQ.5) GO TO 19
      CAL=1668./4.
      GO TO 15
   14 CAL=1668./8.
      GO TO 15
   16 CAL=1668./20.
      GO TO 15
   18 CAL=1668./40.
      GO TO 15
   19 CAL=1668/80.
   15 CONTINUE
   13 READ(5,1000)I1,I2,I3
 1000 FORMAT (3(1X,I4,1X))
C     CHECK FOR END OF RUN
      IF (I1.EQ.9) GO TO 10
C
C     CHECK FOR END OF POINT
      IF (I1.EQ.1) GO TO 11
C
C     CHECK FOR DIRECTION
      D1=I2-I1
      D2=I3-I2
      IF(D1.GT.D2) GO TO 12
C
C     DIRECTION 1 VELOCITY CALCULATION
      L(K)=L(K)+1
      L1=L(K)
```

```
      VEL(K,L1)=1.5*CAL/FLCAT(D2)/.85
      L(K)=L(K)+1
      L1=L(K)
      VEL(K,L1)=.82*CAL/FLCAT(D1)/.85
C
C     ESTABLISHING LIMITS FOR WRITING OUT VELOCITIES
      IF(L1.LE.LMAX) GO TO 31
      LMAX=L1
   31 CONTINUE
      GO TO 13
   12 CONTINUE
C
C     DIRECTION 2 VELOCITY CALCULATION
      M(K)=M(K)+1
      M1=M(K)
      VEL2(K,M1)=.82*CAL/FLCAT(D2)/.85
      M(K)=M(K)+1
      M1=M(K)
      VEL2(K,M1)=1.5*CAL/FLCAT(D1)/.85
C
C     ESTABLISHING LIMITS FOR WRITING OUT VELOCITIES
      IF(M1.LE.MMAX) GO TC 32
   32 CONTINUE
   10 CONTINUE
C
C
C     WRITING OUT VELOCITIES
C
C     DIRECTION 1
      WRITE (6,2001)
 2001 FORMAT (1X,20HVELOCITIES DIR.1)
      LMAX=LMAX+2
      WRITE(6,2000)((VEL(KK,LL),KK=1,10),LL=1,LMAX)
 2000 FORMAT (1X,10(F6.3,3X))
      WRITE  (6,2002)
 2002 FORMAT(1X,20HVELOCITIES DIR.2)
      MMAX=MMAX+2
      WRITE(6,2000)((VEL2(KK,LL),KK=1,10),LL=1,MMAX)
C
C     NUMBER OF READINGS TAKEN AT EACH POINT
      WRITE (6,3001)
 3001 FORMAT (29H DIR.1 READINGS AT EACH PCINT)
      WRITE (6,3000)(L(I),I=1,10)
      WRITE (6,3002)
 3002 FORMAT  (29H DIR.2 READINGS AT EACH FOINT )
      WRITE (6,3000)(M(I),I=1,10)
 3000 FORMAT (1X,10(I4,5X))
C
C     FIND AVERAGE VALUE AT EACH POINT
      DO 300 KK=1,K
C
C     FOR DIRECTION 1
      SUM=0.0
      J=L(KK)
      DO 400 LLL=1,J
      SUM=SUM+VEL(KK,LLL)
  400 CONTINUE
      AV(KK)=SUM/FLCAT(L(KK))
C
C     FOR DIRECTION 2
      SUM2 = 0.0
      J2=M(KK)
      DO 500  MM= 1,J2
      SUM2=SUM2+VEL2(KK,MM)
  500 CONTINUE
      AV2(KK)=SUM2/FLOAT(M(KK))
```

```
  300 CONTINUE
C
C      WRITING OUT AVERAGE AT EACH POINT
       WRITE  (6,4001)
 4001 FORMAT (13H AVERAGE DIR1 )
       WRITE(6,4000)(AV(JJ),JJ=1,K)
       WRITE (6,4002)
 4002 FORMAT (13H AVERAGE DIR2 )
       WRITE(6,4000)(AV2(JJ), JJ=1,K)
 4000 FORMAT (1X,10(F6.3,5X))
C
C      CALCULATION OF VEL HISTOGRAMS
       DO 20 KK=1,K
       J=L(KK)
       J2=M(KK)
C
C
C      SORTING INTO INTERVALS
C
C      DIRECTION 1
       DO 21 LL=1,J
       DO 22 I=1,40
       A=FLOAT(I) *.3
       IF(VEL(KK,LL).LT.A) GO TO 23
   22 CONTINUE
C
C      COUNTING UP ACCORDING TO INTERVALS
   23 KOU(KK,I) = KOU(KK,I)+1
   21 CONTINUE
C
C      DIRECTION2
       DO 26 MM=1,J2
       DO 24 I=1,40
       A=FLOAT(I)*.3
       IF(VEL2(KK,MM).LT.A) GO TO 25
   24 CONTINUE
C
C      COUNTING UP ACCORDING TO INTERVALS
   25 KOU2(KK,I)=KOU2(KK,I)+1
   26 CONTINUE
   20 CONTINUE
       CALL SUB (K, KOU, KOU2 )
       STOP
       END
C
C      CORRECTION OF VELOCITY HISTOGRAMS USING CONCENTRIC RING MODEL
C      CALCULATION OF AVERAGES AND STANDARD DEVIATIONS OF CORRECTED
C      DISTRIBUTIONS
C
       SUBROUTINE SUB (K, KOU, KOU2 )
       COMMON L(10), M(10), KOU(10,30), KOU2(10,40)
       DIMENSION A/A(10), AVAS(10), TI(10), TI2(10), TIT(10), AVCS(10),
      1AVCS2(10), KOU(10,40), KOU2(10,40), III(150), SIGMA(10),
      2SIGMA2(10), R(11), SR(11), AVC(10), AVC2(10)
C
C      SETTING THE ARRAYS TO ZERO (OR 1 FOR THE HISTOGRAM MARKERS)
       DATA III   /150*1 /
       DATA SIGMA /10*0.0/
       DATA SIGMA2/10*0.0/
       DATA AVC /10*0.0/
       DATA AVC2 /10*0.0/
C
C      READING RING SIZES
       I1 = K+1
       READ (5,8003)(R(I),I=1,11)
 8003 FORMAT (7(F6.3,5X)/4(F6.3,5X))
```

```
      DO 39  I=1,11
   39 SR(I)=R(I)**2
C
C     CORRECTION CF VELOCITY HISTOGRAMS USING CONCENTRIC RING MODEL
C
C     DIRECTION 1
      DO 41 I=1,40
      KOUC(1,I)=FLOAT(KOU(1,I))-SQRT(SR(1)-SR(2))
      KOUC(2,I)=(FLOAT(KOU(2,I))-FLOAT(KOU(1,I))*(SQRT(SR(1)-SR(3))-
     1SQRT(SR(2)-SR(3)))/SQRT(SR(2)-SR(3))
      IF (R(3).EQ.0.0) GO TO 40
      KOUC(3,I)=(FLOAT(KOU(3,I))-FLOAT(KOUC(1,I))*(SQRT(SR(1)-SR(4))-
     1SQRT(SR(2)-SR(4)))         -FLOAT(KOUC(2,I))*(SQRT(SR(2)-SR(4))-
     2SQRT(SR(3)-SR(4)))))/SQRT(SR(3)-SR(4))
      IF (R(4).EQ.0.0) GO TO 40
      KOUC(4,I)=(FLOAT(KOU(4,I))-FLOAT(KOUC(1,I))*(SQRT(SR(1)-SR(5))-
     1SQRT(SR(2)-SR(5)))         -FLOAT(KOUC(2,I))*(SQRT(SR(2)-SR(5))-
     2SQRT(SR(3)-SR(5)))         -FLOAT(KOUC(3,I))*(SQRT(SR(3)-SR(5))-
     3SQRT(SR(4)-SR(5))))/SQRT(SR(4)-SR(5))
      IF (R(5).EQ.0.0) GO TO 40
      KOUC(5,I)=(FLOAT(KOU(5,I))-FLOAT(KOUC(1,I))*(SQRT(SR(1)-SR(6))-
     1SQRT(SR(2)-SR(6)))         -FLOAT(KOUC(2,I))*(SQRT(SR(2)-SR(6))-
     2SQRT(SR(3)-SR(6)))         -FLOAT(KOUC(3,I))*(SQRT(SR(3)-SR(6))-
     3SQRT(SR(4)-SR(6)))         -FLOAT(KOUC(4,I))*(SQRT(SR(4)-SR(6))-
     4SQRT(SR(5)-SR(6))))/ SQRT(SR(5)-SR(6))
      IF (R(6).EQ.0.0) GO TO 40
      KOUC(6,I)=(FLOAT(KOU(6,I))-FLOAT(KOUC(1,I))*(SQRT(SR(1)-SR(7))-
     1SQRT(SR(2)-SR(7)))         -FLOAT(KOUC(2,I))*(SQRT(SR(2)-SR(7))-
     2SQRT(SR(3)-SR(7)))         -FLOAT(KOUC(3,I))*(SQRT(SR(3)-SR(7))-
     3SQRT(SR(4)-SR(7)))         -FLOAT(KOUC(4,I))*(SQRT(SR(4)-SR(7))-
     4SQRT(SR(5)-SR(7)))         -FLOAT(KOUC(5,I))*(SQRT(SR(5)-SR(7))-
     5SQRT(SR(6)-SR(7))))/SQRT(SR(6)-SR(7))
      IF (R(7).EQ.0.0) GO TO 40
      KOUC(7,I)=(FLOAT(KOU(7,I))-FLOAT(KOUC(1,I))*(SQRT(SR(1)-SR(8))-
     1SQRT(SR(2)-SR(8)))         -FLOAT(KOUC(2,I))*(SQRT(SR(2)-SR(8))-
     2SQRT(SR(3)-SR(8)))         -FLOAT(KOUC(3,I))*(SQRT(SR(3)-SR(8))-
     3SQRT(SR(4)-SR(8)))         -FLOAT(KOUC(4,I))*(SQRT(SR(4)-SR(8))-
     4SQRT(SR(5)-SR(8)))         -FLOAT(KOUC(5,I))*(SQRT(SR(5)-SR(8))-
     5SQRT(SR(6)-SR(8)))         -FLOAT(KOUC(6,I))*(SQRT(SR(6)-SR(8))-
     6SQRT(SR(7)-SR(8))))/SQRT(SR(7)-SR(8))
      IF (R(8).EQ.0.0) GO TO 40
      KOUC(8,I)=(FLOAT(KOU(8,I))-FLOAT(KOUC(1,I))*(SQRT(SR(1)-SR(9))-
     1SQRT(SR(2)-SR(9)))         -FLOAT(KOUC(2,I))*(SQRT(SR(2)-SR(9))-
     2SQRT(SR(3)-SR(9)))         -FLOAT(KOUC(3,I))*(SQRT(SR(3)-SR(9))-
     3SQRT(SR(4)-SR(9)))         -FLOAT(KOUC(4,I))*(SQRT(SR(4)-SR(9))-
     4SQRT(SR(5)-SR(9)))         -FLOAT(KOUC(5,I))*(SQRT(SR(5)-SR(9))-
     5SQRT(SR(6)-SR(9)))         -FLOAT(KOUC(6,I))*(SQRT(SR(6)-SR(9))-
     6SQRT(SR(7)-SR(9)))         -FLOAT(KOUC(7,I))*(SQRT(SR(7)-SR(9))-
     7SQRT(SR(8)-SR(9))))/SQRT(SR(8)-SR(9))
      IF (R(9).EQ.0.0) GO TO 40
      KOUC(9,I)=(FLOAT(KOU(9,I))-FLOAT(KOUC(1,I))*(SQRT(SR(1)-SR(10))-
     1SQRT(SR(2)-SR(10)))         -FLOAT(KOUC(2,I))*(SQRT(SR(2)-SR(10))-
     2SQRT(SR(3)-SR(10)))         -FLOAT(KOUC(3,I))*(SQRT(SR(3)-SR(10))-
     3SQRT(SR(4)-SR(10)))         -FLOAT(KOUC(4,I))*(SQRT(SR(4)-SR(10))-
     4SQRT(SR(5)-SR(10)))         -FLOAT(KOUC(5,I))*(SQRT(SR(5)-SR(10))-
     5SQRT(SR(6)-SR(10)))         -FLOAT(KOUC(6,I))*(SQRT(SR(6)-SR(10))-
     6SQRT(SR(7)-SR(10)))         -FLOAT(KOUC(7,I))*(SQRT(SR(7)-SR(10))-
     7SQRT(SR(8)-SR(10)))         -FLOAT(KOUC(8,I))*(SQRT(SR(8)-SR(10))-
     8SQRT(SR(9)-SR(10))))/SQRT(SR(9)-SR(10))
      IF(R(10).EQ.0.0) GO TO 40
      KOUC(10,I)=(FLOAT(KOU(10,I))-FLOAT(KOUC(1,I))*(SQRT(SR(1)-SR(11))-
     1SQRT(SR(2)-SR(11)))         -FLOAT(KOUC(2,I))*(SQRT(SR(2)-SR(11))-
     2SQRT(SR(3)-SR(11)))         -FLOAT(KOUC(3,I))*(SQRT(SR(3)-SR(11))-
     3SQRT(SR(4)-SR(11)))         -FLOAT(KOUC(4,I))*(SQRT(SR(4)-SR(11))-
     4SQRT(SR(5)-SR(11)))         -FLOAT(KOUC(5,I))*(SQRT(SR(5)-SR(11))-
```

```
     5SQRT(SR(6)-SR(11)))                -FLOAT(KOUC(6,I))*(SQRT(SR(6)-SR(11))-
     6SQRT(SR(7)-SR(11)))                -FLOAT(KOUC(7,I))*(SQRT(SR(7)-SR(11))-
     7SQRT(SR(8)-SR(11)))                -FLOAT(KOUC(8,I))*(SQRT(SR(8)-SR(11))-
     8SQRT(SR(9)-SR(11)))                -FLOAT(KOUC(8,I))*(SQRT(SR(9)-SR(11))-
     9SQRT(SR(1/)-SR(11))))/SQRT(SR(10)-SR(11))
  40 CONTINUE
C
C    DIRECTION 2
     KOUC2(1,I)=FLOAT(K)42(1,I))/SQRT(SR(1)-SR(2))
     KOUC2(2,I)=(FLOAT(KCU2(2,I))-FLOAT(KOUC2(1,I))*(SQRT(SR(1)-SR(3))
    1-SQRT(SR(2)-SR(3))))/SQRT(SR(2)-SR(3))
     IF(R(3).EQ.0.0) GC TC 41
     KOUC2(3,I)=(FLOAT(KOU2(3,I))-FLOAT(KCLC2(1,I))*(SQRT(SR(1)-SR(4))
    1-SQRT(SR(2)-SR(4)))                -FLOAT(KCUC2(2,I))*(SQRT(SR(2)-SR(4))
    2-SQRT(SR(3)-SR(4))))/SQRT(SR(3)-SR(4))
     IF(R(4).EQ.0.0) GO TC 41
     KOUC2(4,I)=(FLOAT(KOU2(4,I))-FLOAT(KCLC2(1,I))*(SQRT(SR(1)-ST(5))
    1-SQRT(SR(2)-SR(5)))                -FLOAT(KCUC2(2,I))*(SQRT(SR(2)-SP(5))
    2-SQRT(SR(3)-SR(5)))                -FLOAT(KCLC2(3,I))*(SQRT(SR(3)-SR(5))
    3-SQRT(SR(4)-SR(5))))/SQRT(SR(4)-SR(5))
     IF(R(5).EQ.0.0) GO TC 41
     KOUC2(5,I)=(FLOAT(KCU2(5,I))-FLOAT(KOUC2(1,I))*(SQRT(SR(1)-SR(6))
    1-SQRT(SR(2)-SR(6)))                -FLOAT(KCLC2(2,I))*( QRT(SR(2)-SP(6))
    2-SQRT(SR(3)-SR(6)))                -FLOAT(KCUC2(3,I))*(SQRT(SR(3)-SP(6))
    3-SQRT(SR(4)-SR(6)))                -FLOAT(KCLC2(4,I))*(SQRT(SR(4)-SP(6))
    4-SQRT(SR(5)-SR(6))))/SQRT(SR(5)-SR(6))
     IF (R(6).EQ.0.0)GO TC 41
     KOUC2(6,I)=(FLOAT(KCU2(6,I))-FLOAT(KCLC2(1,I))*(SQRT(SR(1)-SP(7))
    1-SQRT(SR(2)-SR(7)))                -FLOAT(KCLC2(2,I))*(SQRT(SR(2)-SR(7))
    2-SQRT(SR(3)-SR(7)))                -FLOAT(KCUC2(3,I))*(SQRT(SR(3)-SP(7))
    3-SQRT(SR(4)-SR(7)))                -FLOAT(KCUC2(4,I))*(SQRT(SR(4)-SR(7))
    4-SQRT(SR(5)-SR(7)))                -FLOAT(KCLC2(5,I))*( QRT(SR(5)-SP(7))
    5-SQRT(SR(6)-SP(7))))/SQRT(SR(6)-SR(7))
     IF (R(7).EQ.0.0) GO TC 41
     KOUC2(7,I)=(FLOAT(KOU2(7,I))-FLOAT(KCLC2(1,I))*(SQRT(SR(1)-SP(8))
    1-SQRT(SR(2)-SR(8))))                -FLOAT(KCLC2(2,I))*(SQRT(SR(2)-SP(8))
    2-SQRT(SR(3)-SR(8)))                -FLOAT(KCLC2(3,I))*(SQRT(SR(3)-SP(8))
    3-SQRT(SR(4)-SR(8)))                -FLOAT(KCLC2(4,I))*(SQRT(SR(4)-SF(8))
    4-SQRT(SR(5)-SR(8)))                -FLOAT(KCLC2(5,I))*(SQRT(SR(5)-SP(8))
    5-SQRT(SR(6)-SR(8)))                -FLOAT(KOUC2(5,I))*(SQRT(SR(6)-ST(8))
    6-SQRT(SR(7)-SR(8))))/SQRT(SR(7)-SR(8))
     IF(R(8).EQ.0.0) GO TC 41
     KOUC2(8,I)=(FLOAT(KCU2(8,I))-FLOAT(KCLC2(1,I))*(SQRT(SR(1)-SR(9))
    1-SQRT(SR(2)-SR(9)))                -FLOAT(KCLC2(2,I))*(SQRT(SP(2)-SP(9))
    2-SQRT(SR(3)-SP(9)))                -FLOAT(KCLC2(3,I))*( QRT(SR(2)-SP(9))
    3-SQRT(SR(4)-SR(9)))                -FLOAT(KCUC2(4,I))*(SQRT(SP(4)-SP(9))
    4-SQRT(SR(5)-SR(9)))                -FLOAT(KCLC2(5,I))*(SQRT(SR(5)-SR(9))
    5-SQRT(SR(6)-SR(9)))                -FLOAT(KCLC2(6,I))*(SQPT(SR(6)-SP(9))
    6-SQRT(SR(7)-SR(9)))                -FLOAT(KCLC2(7,I))*(SQRT(SR(7)-SP(9))
    7-SQRT(SR(8)-SR(9))))/SQRT(SR(8)-SR(9))
     IF(R(9).EQ.0.0) GO TC 41
     KOUC2(9,I)=(FLOAT(KCU2(9,I))-FLOAT(KCUC2(1,I))*( QRT(SR(1)-ST(10))
    1-SQRT(SR(2)-SR(10)))                -FLOAT(KCLC2(2,I))*(SQRT(SP(2)-ST(10))
    2-SQRT(SR(3)-SR(10)))                -FLOAT(KCLC2(3,I))*(SQPT(SR(3)-SR(10))
    3-SQRT(SR(4)-SR(10)))                -FLOAT(KCUC2(9,I))*(SQRT(SR(4)-SR(1/))
    4-SQRT(SR(5)-SR(10)))                -FLOAT(KCUC2(5,I))*(SQRT(SR(5)-SP(10))
    5-SQRT(SR(6)-SP(10)))                -FLOAT(KCUC2(6,I))*(SQRT(SR(6)-SP(10))
    6-SQRT(SR(7)-SR(10)))                -FLOAT(KCLC2(7,I))*(SQRT(SR(7)-SR(10))
    7-SQRT(SR(8)-SR(10)))                -FLOAT(KCLC2(8,I))*(SQRT(SR(8)-SR(10))
    8-SQRT(SR(9)-SR(10)))))SQRT(SR(9)-SR(10))
     IF(R(10).EQ.C.J) GO TC 41
     KOUC2(10,I)=(FLOAT(KCU2(10,I))-FLOAT(KOUC2(1,I))*(SQRT(SR(1)-SR(11
    1))-SQRT(SR(2)-SR(11)))                -FLOAT(KOUC2(2,I))*(SQRT(SR(2)-SR(11
    2))-SQRT(SR(3)-SR(11)))                -FLOAT(KOUC2(3,I))*(SQRT(SR(3)-SR(11
    3))-SQRT(SR(4)-SR(11)))                -FLOAT(KOUC2(4,I)) (SQRT(SR(4)-SR(11
```

```
      4))-SQRT(SR(5)-SR(11)))          -FLCAT(KOUC2(5,I))*(SQRT(SR(5)-SR(11
      5))-SQRT(SR(6)-SR(11)))          -FLCAT(KOUC2(5,I)) (SQRT(SR(6)-SR(11
      6))-SQRT(SR(7)-SR(11)))          -FLCAT(KOUC2(6,I))*(SQRT(SR(7)-SR(11
      7))=SQRT(SR(8)-SR(11)))          -FLCAT(KOUC2(7,I)) (AQRT(SR(8)-SR(11
      8))-SQRT(SR(9)-SR(11)))          -FLCAT(KOUC2(8,I)+(SQRT(SR(9)-SR(11
      9))-SQRT(SR(10)-SR(11))))/SQRT(SR(10)-SR(11)))
   41 CONTINUE
C
C     WRITING OUT CORRECTEC HISTOGRAMS
      WRITE (6,7010)
 7010 FORMAT (20H CORRECTEC HISTOGRAMS)
      WRITE (6,702)
  702 FORMAT (12H DIRECTICN 1)
      DO 42 KK=1,K
      WRITE (6,7002) KK
 7002 FORMAT (14H POINT NUMBER ,I2)
      DO 43 I=1,40
      I1=KOUC(KK,I)
      IF (I1.LE.0) GO TO 44
      IF (I1.GE.130) I1=130
      WRITE (6,7000) KCUC(KK,I),(III(II), II=1,I1)
 7000 FORMAT(1X,I3,3X,130(I1))
      GO TO 43
   44 WRITE (6,7000) KOUC(KK,I)
   43 CONTINUE
   42 CONTINUE
      WRITE (6,703)
  703 FORMAT (14H  DIRECTICN 2 )
      DO 45 KK=1,K
      WRITE (6,7002) KK
      DO 46 I=1,40
      I1 = KOUC2 (KK,I)
      IF (I1.LE.0) GO TO 47
      WRITE (6,7000) KOUC2 (KK,I),(III(II),II=1,I1)
      GO TO 46
   47 WRITE (6,7000) KOUC2 (KK,I)
   46 CONTINUE
   45 CONTINUE
C
C     COMPUTATION OF CORRECTED AVERAGES
      DO 50 KK=1,K
      SUM=0.0
      KSUM=0
      SUM2=0.0
      KSUM2=0
      DO 51 I=1,40
      IF(KOUC(KK,I).LT.0) KCUC(KK,I)=0
      IF(KOUC2(KK,I).LT.0) KOUC2(KK,I)=0
      SUM=SUM+FLOAT(KOUC(KK,I))*(FLOAT(I)*.3-.15)
      SUM2=SUM2+FLOAT(KOUC2(KK,I))*(FLOAT(I)*.3-.15)
      KSUM = KSUM + KOUC(KK,I)
      KSUM2 = KSUM2 + KOUC2(KK,I)
   51 CONTINUE
      IF(KSUM.EQ.0) KSUM=1
      AVC(KK) = SUM/FLOAT(KSUM)
      IF(KSUM2.EQ.0) KSUM2=1
      AVC2(KK) = SUM2/FLOAT(KSUM2)
   50 CONTINUE
C
C     WRITING OUT CORRECTED AVERAGE VELOCITIES
      WRITE (6,8001)
 8001 FORMAT (4JH CORRECTEC AVERAGE VELOCITIES DIRECTION 1 )
      WRITE (6,8000) (AVC(KK),KK=1,K)
 8000 FORMAT (1X,10(F6.3,5X)                   )
      WRITE (6,8002)
```

```
8002 FORMAT (40H CCRRECTEC AVERAGE VELOCITIES DIRECTION 2 )
     WRITE (6,8303) (AVC2(KK),KK=1,K)
C
C    CALCULATIONG STANDARD DEVIATICN CF VELOCITY DISTRIBUTION
C    IN EITHER DIRECTION
C
     DO 60   KK=1,K
     KOUCS=0
     SDIFX=0
     KOUCS2=0
     SDIFX2=0
     DO 61  J=1,40
     KOUCS=KOUCS+KCUC(KK,J)
     DIFX=(FLOAT(J)*.3-.15)-AVC(KK)
     SDIFX=SDIFX+DIFX**2*FLOAT(KCUC(KK,J))
     KOUCS2=KOUCS2+KOUC2(KK,J)
     DIFX2 =(FLOAT(J)*.3-.15)-AVC2(KK)
     SDIFX2=SDIFX2+DIFX2**2*FLOAT(KOUC2(KK,J))
  61 CONTINUE
     IF(KOUCS.EQ.0) KOUCS=1
     IF(KOUCS2.EQ.0) KOUCS2=1
     SIGMA(KK) =(SDIFX / FLOAT(KCUCS))**.5
     SIGMA2(KK) = (SDIFX2 / FLOAT(KOUCS2))**.5
  60 CONTINUE
C
C    WRITING OUT STANDARD DEVIATICNS IN EACH DIRECTION
     WRITE (6,9001)
9001 FORMAT(35H STANDARD DEVIATICNS DIRECTION 1 )
     WRITE (6,9300)(SIGMA(KK),KK=1,K)
9000 FORMAT (1X,10(F6.3,5X))
     WRITE (6,9302)
9002 FORMAT(35H STANDARD DEVIATICNS DIRECTION 2 )
     WRITE (6,9300) (SIGMA2(KK),KK=1,K)
C
C    CALCULATION CF RELATIVE TURBULENCE ENERGY FOR EITHER DIRECTION
     DO 59 I=1,K
     IF(SIGMA2(I).EQ.0.) SIGMA2(I)=1.
     IF(SIGMA(I).EG.0.) SIGMA(I)=1.
     TI(I)=1./(1.+(AVC(I)/SIGMA(I))**2)
     TI2(I)=1./(1.+(AVC2(I)/SIGMA2(I))**2)
  59 CONTINUE
     WRITE(6,8106)
C
C    WRITING OUT RELATIVE TURBULENCE ENERGIES
8106 FORMAT (26H RELATIVE TURBULENCE ENERGY )
     WRITE(6,8104)
8104 FORMAT (12H CIRECTION 1 )
     WRITE(6,8300)(TI(KK),KK=1,K)
     WRITE(6,3105)
8104 FORMAT (12H DIRECTION 2 )
     WRITE(6,8300)(TI2(KK),KK=1,K)
C
C    CALCULATION OF OVERALL STANDARD DEVIATION
     DO 53 KK=1,K
     DO 54 J=1,40
     JJ=(41-J)
     JJJ=40+J
     KOUJ=KUDC(KK,J)
     KOUC(KK,J)=KOUC2(KK,JJ)
     KOUC(KK,JJJ)=KOUJ
  54 CONTINUE
     KOUCS=J
     SDIFX=0
     DO 55 J=1,80
     KOUCS=KOUCS+KCUC(KK,J)
```

```
      DIFX=(FLOAT(J)*.3-12.15)-AVA(KK)
      SDIFX=SDIFX+DIFX**2*FLOAT(KCUC(KK,J))
   55 CONTINUE
      SIGMA(KK)=SQRT(SDIFX/FLOAT(KOUCS))
   53 CONTINUE
C
C     WRITING OUT OF OVERALL STANDARD DEVIATION
      WRITE(6,8110)
 8110 FORMAT (27H OVERALL STANDARD DEVIATION )
      WRITE(6,9000)(SIGMA(KK),KK=1,K)
C
C     CALCULATION OF OVERALL RELATIVE TURBULENCE ENERGIES
      DO 63 I=1,K
      IF(SIGMA(I).EC.0.) SIGMA(I)=1.
      TIT(I)=1./(1.+(AVA(I)/SIGMA(I))**2)
   63 CONTINUE
C
C     WRITING OUT OF OVERALL RELATIVE TURBULENCE ENERGIES
      WRITE(6,8112)
 8112 FORMAT (37H OVERALL RELATIVE TURBULENCE ENERGIES )
      WRITE(6,8000) (TIT(KK),KK=1,K)
      RETURN
      END
```

- 8 -

COMPUTATION AND STATISTICAL ANALYSIS CF HORIZONTAL VELOCITIES

```
      PRCGRAM VELCC2(INPUT,CUTPUT,TAPE5=INFLT,TAPE6=OUTPUT)
      COMMON L(10),VEL(1),900),VEL2(10,800),AV(10),AV2(10),M(10),
     1KOU(10,50),  KOUT(10,50),  R(11)  , SR(11),  KOUC(10,50),  AVC(10,
      DIMENSION III(150),  IIII(150)
      INTEGER O1,O2
C
C     SETTING THE ARRAYS TC ZERO
      DATA III  /150*1 /
      CO 1 I=1,8000
       VEL(I) = 0.0
       VEL2 (I) = 0.0
    1 CONTINUE
      CO 2 I=1,500
      KOU(I)=0
      KOUT(I) = 0
      KOUC(I) = 0
    2 CONTINUE
      CO 4 I=1,10
      AVC(I) = 0
      L(I)=0
      M(I)=0
    4 CONTINUE
      CO 3 I=1,11
      R(I)=0
      SR(I) = 0
    3 CONTINUE
      K=0
      LMAX=0
      MMAX=0
      READ (5,9999) TITLE
 9999 FORMAT (1X,410)
      WRITE(6,9999) TITLE
   11 K=K+1
      L(K)=0
      M(K)=0
C
C     DECIDING ON CALIBRATCR
      READ(5,1001) I4
 1001 FORMAT (I1)
      IF (I4.EQ.2) GO T6 14
      IF(I4.EQ.3)GO TO 30
      IF(I4.EQ.4) GO TO 17
      IF(I4.EQ.5) GC TO 18
      CAL=1665./4.
      GO TO 15
   14 CAL=1665./.8
      GO TO 15
   30 CAL=1665./20.
      GO TO 15
   17 CAL=1665./40.
      GO TO 15
   18 CAL=1665./80.
   15 CONTINUE
   13 READ(5,1000)I1,I2,I3
 1000 FORMAT (3(1X,I4,1X))
C
C     CHECK FOR END OF RUN
      IF (I1.EQ.9) GO TO 10
C
C     CHECK FCR END OF POINT
```

- 1 -

```
      IF (I1.EQ.1) GC TC 11
C
C     CHECK FOR DIRECTICN
      D1 = I2-I1
      D2 = I3-I2
      IF (D1.GT.D2) GO TJ 12
C
C     DIRECTION 1 VELCCITY CALCULATICN
      L(K)=L(K)+1
      L1=L(K)
      VEL(K,L1) = 1.5*CAL/FLOAT(D2)/.85
      L(K)=L(K)+1
      L1=L(K)
      VEL(K,L1)=.82*CAL/FLCAT(D1) /.85
C
C     ESTABLISHING LIMITS FCR WRITING CUT VELOCITIES
      IF(L1.LE.LMAX) GO TC 31
      LMAX=L1
   31 CONTINUE
      GO TO 13
   12 CONTINUE
C
C     CIRECTION 2 VELCCITY CALCULATICN
      M(K)=M(K)+1
      M1=M(K)
      VEL2(K,M1)=.82*CAL/FLCAT(D2)/.85
      M(K)=M(K) +1
      M1 =M(K)
      VEL2(K,M1)= 1.50* CAL /FLOAT(D1)/.85
C
C     ESTABLISHING LIMITS FCR WRITING CUT VELOCITIES
      IF (M1.LE.MMAX) GC TC 32
      MMAX=M1
   32 CONTINUE
      GO TO 13
C
C     WRITING OUT VELOCITIES
C
C     DIRECTION 1
      WRITE (6,2001)
 2001 FORMAT (1X,20HVELCCITIES DIR.1)
      LMAX=LMAX+2
      WRITE(6,2000)((VEL(KK,LL),KK=1,10),LL=1,LMAX)
 2000 FORMAT (1X,10(F6.3,3X))
      WRITE (6,2002)
 2002 FORMAT(1X,20HVELCCITILS DIR.2)
      MMAX=MMAX+2
      WRITE(6,2000)((VEL2(KK,LL),KK=1,10),LL=1,MMAX)
C
C     NUMBER OF READINGS TAKEN AT EACH PCINT
      WRITE (6,3001)
 3001 FORMAT (29H DIR.1 READINGS AT EACH PCINT)
      WRITE (6,3000)(L(I),I=1,10)
      WRITE (6,3002)
 3002 FORMAT  (29H DIR.2 READINGS AT EACH PCINT )
      WRITE (6,3000)(M(I),I=1,10)
 3000 FORMAT (1X,10(I4,5X))
C
C     FIND AVERAGE VALUE AT EACH POINT
      DO 300 KK=1,K
C
C     FOR DIRECTION 1
      SUM=0.0
      J=L(KK)
      DO 400 LLL=1,J
```

```
        SUM=SUM+VEL(KK,LLL)
  400 CONTINUE
        AV(KK)=SUM/FLOAT(L(KK))
C
C       FOR DIRECTION 2
        SUM2 = 0.0
        J2=M(KK)
        DO 500  MMM= 1,J2
        SUM2=SUM2+VEL2(KK,MMM)
  500 CONTINUE
        AV2(KK)=SUM2/FLOAT(M(KK))
  300 CONTINUE
C
C       WRITING OUT AVERAGE AT EACH POINT
        WRITE   (6,4001)
 4001 FORMAT (13H AVERAGE DIR1 )
        WRITE(6,4000)(AV(JJ),JJ=1,K)
        WRITE (6,4002)
 4002 FORMAT (13H AVERAGE DIR2  )
        WRITE(6,4000)(AV2(JJ), JJ=1,K)
 4000 FORMAT (1X,10(F6.3,5X))
   10 CONTINUE
        DO 70  KK=1,K
        J3=M(KK)
        DO 70  MM=1,J3
        LL=L(KK)+MM
        VEL(KK,LL)=-VEL2(KK,MM)
   70 CONTINUE
C
C    CALCULATION OF VELOCITY HISTOGRAMS
        DO 20 KK=1,K
        J=L(KK)+M(KK)
C
C       SORTING INTO INTERVALS
        DO 21 LL=1,J
        DO 22 I=1,50
        A=-5.0+FLOAT(I)*.2
        IF(VEL(KK,LL).LT.A) GO TO 23
   22 CONTINUE
C
C       COUNT UP ACCORDING TO INTERVALS
   23 KOU(KK,I) = KOU(KK,I)+1
   21 CONTINUE
   20 CONTINUE
        DO 130  KK=1,K
        WRITE  (6,6002)  KK
 6002 FORMAT (14H POINT NUMBER ,I2)
        DO 32 I=1,50
        I1=KOU  (KK,I)
        IF (I1.EQ.0) GO TO  35
        WRITE (6,6000) KOU(KK,I),(III(II),II=1,I1)
 6000 FORMAT (1X,I3,3X,130(I1))
        GO TO  32
   35 WRITE   (6,6000) KOU (KK,I)
   32 CONTINUE
  130 CONTINUE
C
C       READING RING SIZES
        I1=K+1
        READ(5,8003)(R(I),I=1,11)
 8003 FORMAT (7(F6.3,5X) / 4(F6.3,5X))
        DO 39 I=1,11
   39 SR(I)=R(I)**2
C
C       CORRECTION OF VELOCITY HISTOGRAMS USING CONCENTRIC RING MODEL
```

```
      DO 41 I=1,50
      KOUC(1,I)=FLOAT(KCU(1,I))/SQRT(SR(1)-SR(2))
41    CONTINUE
      DO 71 I=1,50
      E=(-4.9+FLOAT(I)*.2)*R(2)/R(1)
      DO 72 J=1,50
      A=-5.0+FLOAT(J)*.2
      IF(B.LT.A)GO TO 73
72    CONTINUE
73    KOUT(1,J)=KOUC(1,I)+KCUT(1,J)
71    CONTINUE
      DO 74 I=1,50
      KOUC(2,I)=(FLOAT(KOU(2,I)) - FLOAT(KCUT(1,I))*(SQRT(SR(1)-SR(3))
     1-SQRT(SR(2)-SR(3))))/ SQRT(SR(2)-SR(3)  )
74    CONTINUE
      DO 88 I=1,50
      KOUT(1,I)=0
88    CONTINUE
      DO 77 I=1,50
      DO 77  KK=1,2
      E=(-4.9+FLOAT(I)*.2)*R(3)/R(KK)
      DO 75 J=1,50
      A=-5.0+FLOAT(J)*.2
      IF(B.LT.A) GO TO 76
75    CONTINUE
76    KOUT(KK,J)= KCUC(KK,I) + KOUT(KK,J)
77    CONTINUE
      DO 80 I=1,50
      KOUC(3,I)=(FLOAT(KOU(3,I))-FLOAT(KCUT(1,I))*(SQRT(SR(1)-SR(4))-
     1SQRT (SR(2)-SR(4)))-FLOAT(KOUT(2,I))*(SQRT(SR(2)-SR(4))-SQRT
     2 (SR(3)-SR(4)))) /SQRT(SR(3)-SR(4))
80    CONTINUE
      IF(R(4).EQ.0.0) GO TO 40
      DO 89 I=1,50
      KOUT(1,I)=0
      KOUT(2,I)=0
89    CONTINUE
      DO 84 I=1,50
      DO 84 KK=1,3
      E=(-4.9+FLOAT(I)*.2)*R(4)/R(KK)
      DO 82 J=1,50
      A=-5.0+FLOAT(J)*.2
      IF(B.LT.A)GO TO 83
82    CONTINUE
83    KOUT(KK,J)=KCUC(KK,I)+KOUT(KK,J)
84    CONTINUE
      DO 91 I=1,50
      KOUC(4,I)=(FLOAT(KOU(4,I))-FLOAT(KOUT(1,I))*(SQRT(SR(1)-SR(5))-
     1SQRT(SR(2)-SR(5)))-FLOAT(KOUT(2,I))*(SQRT(SR(2)-SR(5))-SQRT
     2(SR(3)-SR(5)))-FLOAT(KOUT(3,I))*(SQRT(SR(3)-SR(5))-SQRT(SR(4)-
     3SR(5))))/ SQRT(SR(4)-SR(5))
91    CONTINUE
      DO 90 I=1,50
      KOUT (1,I)=0
      KOUT(2,I) =0
      KOUT (3,I)=0
90    CONTINUE
      IF (R(5).EQ.0.0) GO TO 40
      DO 95 I=1,50
      DO 95 KK=1,4
      E=(-4.9+FLOAT(I)*.2)*R(5)/R(KK)
      DO 93 J=1,50
      A=-5.0+FLOAT(J)*.2
      IF(B.LT.A) GO TO 94
93    CONTINUE
```

```
   94 KOUT(KK,J)= KCUC(KK,I)+KOUT(KK,J)
   95 CONTINUE
      CO 112 I=1,50
      KOUC(5,I)=(FLCAT(KOU(5,I))-FLCAT(KCUT(1,I))*(SQRT(SR(1)-SR(6))-
     1SQRT(SR(2)-SR(6)))-FLCAT(KOUT(2,I))*(SQRT(SR(2)-SR(6))-SQRT
     2(SR(3)-SR(6)))-FLCAT(KOUT(3,I))*(SQRT(SR(3)-SR(6))-SQPT(SR(4)-
     3SR(6)))-FLOAT(KOUT(4,I))*(SQRT(SR(4)-SR(6))-SQRT(SR(5)-SR(6))))
     4/ SQRT(SR(5)-SR(6))
  112 CONTINUE
      DO 113 I=1,50
      KOUT(1,I)=0
      KOUT(2,I)=0
      KOUT(3,I)=0
      KOUT(4,I)=0
  113 CONTINUE
      IF(R(6).EQ.0.0) GO TO 40
      CO 114 I=1,50
      DO 114 KK=1,5
      B=(-4.9+FLOAT(I)*.2)*R(6)/R(KK)
      CO 115 J=1,50
      A=-5.0+FLOAT(J)*.2
      IF(B.LT.A) GO TO 116
  115 CONTINUE
  116 KOUT(KK,I)= KCUC(KK,I)+KOUT(KK,I)
  114 CONTINUE
      DO 118 I=1,50
      KOUC(6,I)=(FLCAT(KOU(6,I))-FLCAT(KOUT(1,I))*(SQRT(SR(1)*SR(7))-
     2SQRT(SR(2)-SR(7)))-FLCAT(KOUT(2,I))*(SQRT(SR(2)-SR(7))*SQRT
     3(SR(3)-SR(7)))-FLCAT(KOUT(3,I))*(SQRT(SR(3)-SR(7))-SQPT(SR(4)
     4-SR(7)))-FLOAT(KCUT(4,I))*(SQRT(SR(4)-SR(7))-SQRT(SR(5)-SR(7)))
     5-FLOAT(KOUT(5,I))*(SQRT(SR(5)-SR(7))- SQRT(SR(6)-SR(7))))/
     6SQRT(SR(6)-SR(7))
  118 CONTINUE
      CO 119 I=1,50
      DO 119 KK=1,5
      KOUT(KK,I)=0
  119 CONTINUE
      IF(R(7) .EQ.0.0) GO TO 40
      CO 121 I=1,50
      DO 121 KK=1,6
      B=(-4.9+FLOAT(I)*.2)*R(7)/R(KK)
      CO 123 J=1,50
      A=-5.0+FLOAT(J)*.2
      IF(B.LT.A) GO TO 124
  123 CONTINUE
  124 KOLC(KK,I)=KOUC(KK,I)+KOUT(KK,I)
  121 CONTINUE
      DO 122 I=1,50
      KOUC(7,I)=(FLCAT(KOU(7,I))-FLCAT(KOUT(1,I))*(SQPT(SR(1)-SR(8))-
     1SQRT(SR(2)-SR(8)))-FLCAT(KOUT(2,I))*(SQRT(SR(2)-SR(8))-SQRT
     2(SR(3)-SR(8)))-FLCAT(KOUT(3,I))*(SQRT(SR(3)-SR(8))-SQRT(SR(4)-
     3SR(8)))-FLOAT(KOUT(4,I))*(SQRT(SR(4)-SR(8))-SQRT(SR(5)-SR(8)))
     4-FLCAT(KOUT(5,I))*(SQRT(SR(5)-SR(8))-SQRT(SR(6)-SR(8)))-FLOAT
     5(KOUT(6,I))*(SQRT(SR(6)-SR(8))-SQRT(SR(7)-SR(8))))/SQPT(SR(7)-
     6SR(8))
  122 CONTINUE
      CO 993 I=1,50
      DO 993 KK=1,6
      KOUT(KK,I)=0
  993 CONTINUE
      IF(R(8).EQ.0.0) GO TO 40
      CO 994 I=1,50
      CO 994 KK=1,7
      B=(-4.9+FLOAT(I)*.2)*R(8)/R(KK)
      DO 125 J=1,50
```

- 5 -

```
      A=-5.0+FLOAT(J)*.2
      IF(B.LT.A) GO TO 126
  125 CONTINUE
  126 KOUT(KK,I)=KOUC(KK,I)+KOUT(KK,I)
  994 CONTINUE
      DO 127 I=1,50
      KOUC(8,I)= (FLOAT(KCU(8,I))-FLOAT(KOUT(1,I))*(SQRT(SR(1)-SR(9))-
     1SQRT(SR(2)-SR(9)))-FLOAT(KOUT(2,I))*(SQRT(SR(2)-SR(9))-SQRT(SR(3)
     2-SR(9)))-FLOAT(KOUT(3,I))*(SQRT(SR(3)-SR(9))-SQRT(SR(4)-SR(9)))-
     3FLCAT(KOUT(4,I))*(SQRT(SR(4)-SR(9))-SQRT(SR(5)-SR(9)))-FLCAT(KOUT
     4(5,I))*(SQRT(SR(5)-SR(9))-SQRT(SR(6)-SR(9)))-FLOAT(KOUT(6,I))*
     5(SQRT(SR(6)-SR(9))-SQRT(SR(7)-SR(9)))-FLOAT(KOUT(7,I))*(SQRT
     6(SR(7)-SR(9))-SQRT(SR(8)-SR(9))))/ SQRT(SR(8)-SR(9))
  127 CONTINUE
      DO 128 I=1,50
      DO 128 KK=1,7
      KOUT(KK,I)=0
  128 CONTINUE
      IF(R(9).EQ.0.0) GO TO 40
      DO 995 I=1,50
      DO 995 KK=1,8
      B=(-4.9+FLOAT(I)*.2)*R(9)/R(KK)
      DO 129 J=1,50
      A=-5.0+FLOAT(J)*.2
      IF(B.LT.A) GO TO 136
  129 CONTINUE
  136 KOUT(KK,I)=KOUC(KK,I)+KOUT(KK,I)
  995 CONTINUE
      DO 131 I=1,50
      KOUC(9,I)=(FLCAT(KOU(9,I))-FLCAT(KOUT(1,I))*(SQRT(SR(1)-SR(10))-
     1SQRT(SR(2)-SR(10)))-FLOAT(KOUT(2,I))*(SQRT(SR(2)-SR(10))-SQRT(SR(3
     2)-SR(10)))-FLCAT(KOUT(3,I))*(SQRT(SR(3)-SR(10))-SQRT(SR(4)-SR(10))
     3)-FLOAT(KOUT(4,I))*(SQRT(SR(4)-SR(10))-SQRT(SR(5)-SR(10)))-FLCAT(
     4KOUT(5,I))*(SQRT(SR(5)-SR(10))-SQRT(SR(6)-SR(10)))-FLCAT(KOUT(6,I)
     5) *(SQRT(SR(6)-SR(10))-SQRT(SR(7)-SR(10)))-FLCAT(KOUT(7,I))*(SQRT
     6(SR(7)-SR(10))-SQRT(SR(8)-SR(10)))-FLCAT(KOUT(8,I))*(SQRT(SR(8)-
     7SR(10))-SQRT(SR(9)-SR(10))))/SQRT(SR(9)-SR(10))
  131 CONTINUE
      DO 132 I=1,50
      DO 132 KK=1,7
      KOUT(KK,I)=0
  132 CONTINUE
      IF(R(10).EQ.0.0)GO TO 40
      DO 996 I=1,50
      DO 996 KK=1,9
      B=(-4.9+FLOAT(I)*.2)*R(10)/R(KK)
      DO 133 J=1,50
      A=-5.0+FLOAT(J)*.2
      IF(B.LT.A) GO TO 134
  133 CONTINUE
  134 KOUT(10,I)=KOUC(KK,I)+KOUT(KK,I)
  996 CONTINUE
      DO 135 I=1,50
      KOUC(10,I)=(FLOAT(KOU(10,I))-FLCAT(KOUT(1,I))*(SQRT(SR(1)-SR(11))-
     1SQRT(SR(2)-SR(11)))-FLOAT(KOUT(2,I))*(SQRT(SR(2)-SR(11))-SQRT(SR(3
     2)-SR(11)))-FLCAT(KOUT(3,I))*(SQRT(SR(3)-SR(11))-SQRT(SR(4)-SR(11))
     3)-FLCAT(KOUT(4,I))*(SQRT(SR(4)-SR(11))-SQRT(SR(5)-SR(11)))-FLCAT(
     4KOUT(5,I))*(SQRT(SR(5)-SR(11))-SQRT(SR(6)-SR(11)))-FLCAT(KOUT(6,I)
     5)*(SQRT(SR(6)-SR(11))-SQRT(SR(7)-SR(11)))-FLCAT(KOUT(7,I))*(SQRT
     6(SR(7)-SR(11))-SQRT(SR(8)-SR(11)))-FLCAT(KOUT(8,I))*(SQRT(SR(8)-
     7SR(11))-SQRT(SR(9)-SR(11)))-FLOAT(KOUT(9,I))*(SQRT(SR(9)-SR(11))-
     8SQRT(SR(10)-SR(11))))/SQRT(SR(10)-SR(11))
  135 CONTINUE
   40 CONTINUE
    C
```

```fortran
C       WRITING OUT CORRECTEC HISTOGRAMS (ROT. VELOCS. NOT YET CONSID.)
        WRITE (6,2000)
 2000 FORMAT (21H CORRECTED HISTOGRAMS )
        DO 150 KK=1,K
        WRITE (6,2001)  KK
 2001 FORMAT (13H PCINT NUMBER ,I2)
        DO 151  I=1,50
        I1=KOUC(KK,I)
        IF(I1.LE.0) GC TO 152
        IF(I1.GT.130) I1=130
        WRITE (6,2002) KOUC(KK,I),(III(II),II=1,I1)
 2002 FORMAT (1X,I3,3X,130(I1))
        GC TO 151
  152 WRITE(6,2002) KOUC(KK,I)
  151 CONTINUE
  150 CONTINUE
C
C       SUBTRACTING -VE FROM +VE PART OF HISTCGRAM
        DO 210 J=1,25
        DO 210 KK=1,K
        IP=25+J
        IN=26-J
        KOUT(KK,J)=(KCUC(KK,IP)-KOUC(KK,IN))
  210 CONTINUE
C
C       WRITING OUT HISTOGRAMS OF VEL+MINUSVEL-
        WRITE(6,7010)
 7010 FORMAT(30H HISTOGRAMS OF VEL+ MINUS VEL- )
        DO 42 KK=1,K
        WRITE(6,7002) KK
 7002 FORMAT(14H POINT NUMBER  ,I2)
        DO 43 I=1,25
        I1= KOUT(KK,I)
        IF(I1.EQ.0) GO TO 44
        IF(I1.LT.0) GC TO 45
        IF(I1.GT.130) I1=130
        WRITE(6,7000)KOUT (KK,I),(III(II),II=1,I1)
 7000 FORMAT (1X,I3,3X,130(I1))
        GO TO 43
   44 WRITE(6,7000) KOUT(KK,I)
        GO TO 43
   45 J1=-I1
        WRITE(6,7010) KOUT(KK,I),(IIII(II),II=1,J1)
   43 CONTINUE
   42 CONTINUE
C
C       COMPUTATION CF CORRECTED AVERAGES
        DO 50 KK=1,K
        SUM=0.0
        KSUM=0
        DO 51 I=1,25
        SUM=SUM+FLOAT(KOUT(KK,I))*(-.1+FLOAT(I)*.2)
        KSUM=KSUM+IABS(KOUT(KK,I))
   51 CONTINUE
        AVC(KK)=SUM /FLOAT(KSUM)
   50 CONTINUE
C
C       COMPUTATION CF CORRECTED AVERAGE S
        WRITE(6,8001)
        WRITE(6,8000)(AVC(I),I=1,K)
 8001 FORMAT (20H CORRECTED AVERAGES  )
 8000 FORMAT(1X,10(F6.3,5X))
        STOP
        END
```

                                        -   7   -